Transport Properties of Divertor Edge Plasmas Measured with Multi-Spectral Imaging

by

Bryan Lee Linehan

Submitted to the Department of Physics
in partial fulfillment of the requirements for the degree of

DOCTOR OF PHILOSOPHY IN PHYSICS

at the

MASSACHUSETTS INSTITUTE OF TECHNOLOGY

June 2024

Authored by: Bryan Lee Linehan
                 Department of Physics
                 April 29th, 2024

Certified by: Earl S Marmar
                 Senior Research Scientist, Thesis Supervisor

Accepted by: Lindley Winslow
                 Associate Department Head of Physics

Transport Properties of Divertor Edge Plasmas Measured with Multi-Spectral Imaging

by

Bryan Lee Linehan

Submitted to the Department of Physics
on April 29th, 2024 in partial fulfillment of the requirements for the degree of

DOCTOR OF PHILOSOPHY IN PHYSICS

ABSTRACT

The transport of heat and particles in the boundary of a tokamak is not sufficiently understood for the purposes of constructing a pilot nuclear reactor. Improving numerical and theoretical understanding is inhibited by traditional boundary diagnostics that provide sparse and inflexible spatial coverage. In this thesis, multi-spectral imaging of helium line ratios (HeMSI) was used to create 2D poloidal maps of T_e and n_e in the TCV divertor. These are the first plasma boundary measurements to provide continuous 2D coverage of T_e and n_e for arbitrary magnetic geometries. These measurements were validated against co-local Thomson scattering measurements in diverted plasmas. HeMSI showed good agreement with Thomson scattering in the common flux region (CFR) of ionizing plasma for both majority helium and majority deuterium plasmas. Having validated this powerful new tool, HeMSI was used to investigate the effects of flux expansion in the TCV divertor for plasmas in the conduction limited regime. Increasing poloidal flux expansion is expected to lower the temperature of the divertor target by increasing the plasma volume and connection length of the magnetic field line between the core and target. These benefits are observed in the conduction limited regime but not in the partially detached regime. The 2D poloidal maps of T_e and n_e, in concert with other measurements, were used to calculate the ionization rate of He and D, the E $\times$ B drift velocity, Spitzer heat conduction, and parallel flow in 2D. This allowed for heat transport to be locally resolved into conduction, parallel convection, and drift convection components. Similarly, particle transport was categorized into drift and parallel components. These calculations demonstrate that in relatively cool plasmas ($T_e < 30\text{eV}$), drifts compose a significant amount of the heat and particle transport. This violates the assumptions of simple two-point modeling and demonstrates the importance of accounting for drifts in modeling. Drifts may explain the boundary's lack of sensitivity to poloidal flux expansion in the partially detached regime. Lastly, the anomalous heat and particle transport coefficients, $\chi_\perp$ and $D_\perp$, were calculated by enforcing local power and particle balance. Values of $\chi_\perp$ close to the separatrix ($\rho < 1.005$), and values of $D_\perp$ were consistent with standard modeling practices. However, $\chi_\perp$ measurements sufficiently far into the CFR ($\rho > 1.005$) exceeded typical modeling assumptions by two orders of magnitude. This implies that boundary codes will underestimate the radial temperature falloff length. This is shown to be true in a comparison of T_e measurement to simulations performed with the SOLPS-ITER code. This brings into question the validity of the assumption of diffusive heat transport in the far CFR.

Thesis supervisor: Earl S Marmar
Title: Senior Research Scientist

The impediment to action advances action.

What stands in the way becomes the way.

- Marcus Aurelius

Acknowledgments

I arrive at the end of my doctoral studies aware that I have been blessed with immeasurable support from family, mentors, and friends. Thus, I offer my deepest thanks here.

To begin, I wish to recognize my parents, Kim and Mark Linehan, for their unconditional love and support. Their tireless work on behalf of my brother and myself has allowed us both to thrive. I also thank my brother, Kevin Linehan, for his constant support and companionship.

I thank my mentors, Basil Duval, Earl Marmar, and Jim Terry. It has been a long journey, and they have all put a great deal of effort into my development as a scientist. I am grateful for their patience, dedication to teaching, and the wealth of expertise that they have shared with me. I am fortunate to have been able to learn from them. I do not think such mentorship can be repaid; it is only passed on. I will strive to do so. Furthermore, I thank my other committee members, Brian LaBombard and Joseph Formaggio, for lending their expertise.

I am grateful to my partner and closest friend, Brooke Zampell. Your listening ear and stalwart companionship helped me be my best every day. I am also deeply grateful for all the support the whole Zampell family has offered during my studies.

Many thanks to my friend and fellow graduate student Artur Perek, with whom I worked closely during this PhD on multi-spectral imaging. Our friendship was forged under the stress of many long nights at the lab performing calibrations and preparing for experiments. I could not have wished for a better comrade with whom to have shared the work.

I would like to thank my many friends at MIT and EPFL, with whom I have thoroughly enjoyed this journey. A special thanks to those in my cohort: Aaron Rosenthal, Kevin Montes, Julian Picard, Francesco Sciortino, Filippo Bagnato, and Lorenzo Martinelli.

Lastly, I owe a great deal of thanks to scientists and more senior students at EPFL and MIT: Christian Theiler, Olivier Février, Stefano Coda, Yanis Andrebe, Bob Mumgaard, Holger Reimerdes, Alex Tinguely, and Adam Kuang.

Contents

List of Figures

14

List of Tables

Chapter 1

Introduction

1.1 Thermonuclear Fusion

The last 200 years of human existence have witnessed an unprecedented technological boom. While 800,000 years passed between humanity's first campfire [1] and Thomas Savery's invention of the commercial steam engine in 1698, in the last 100 years, humanity has gone from the first electric power plant to the mass adoption of smartphones. These technological leaps are a cornerstone of modern civilization. However, these advancements have spurred anthropogenic climate change. The byproducts of carbon-based energy sources pollute the atmosphere, trapping heat and raising the global temperature. These trends can be seen in Figure 1.1 which shows the global average of the CO_2 mole fraction in the atmosphere as measured by the National Oceanic and Atmospheric Administration (NOAA) [2][3], and the variation in the yearly average temperature as measured by NASA's Goddard Institute for Space Studies (NASA/GISS) [4][5]. The existential threat posed by climate change demands the development of new carbon-free energy sources. One candidate energy source and the topic of this thesis is nuclear fusion.
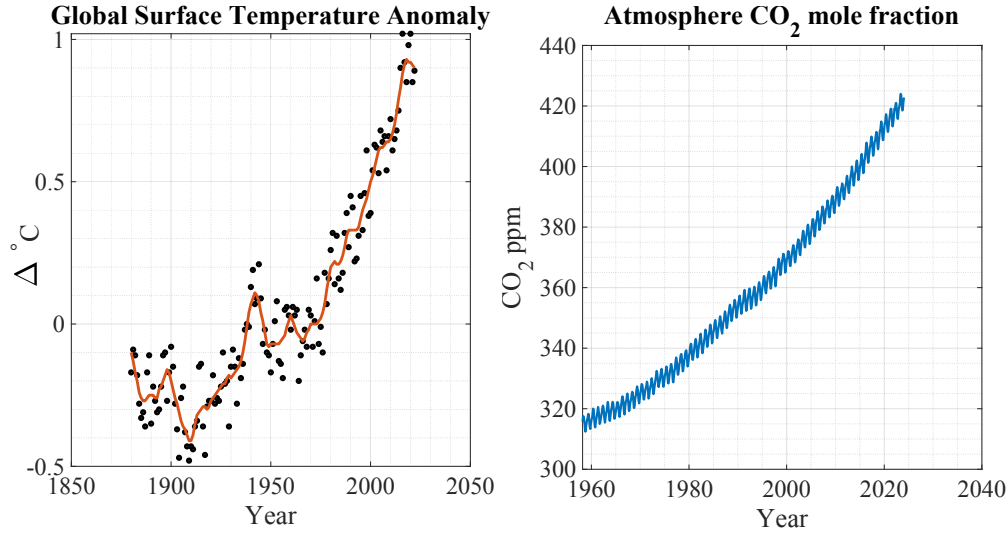
Figure 1.1: Left) The difference in the yearly average global surface temperature from the long-term average taken from 1951 to 1980 [4][5]. Right) The global average of the mole fraction of CO_2 in the atmosphere since NOAA began making measurements in 1958.

Nuclear fusion denotes the process of combining atomic nuclei into new assortments of nuclei and neutrons. In these reactions, while energy is conserved, mass is not. The difference in mass, mass deficit, is converted into kinetic energy in accordance with the mass-energy equivalency principle, i.e., $\Delta E = \Delta m c^2$. Therefore, kinetic energy is gained when the total mass of the reaction's products is less than the mass of the reactants. For example, deuterium and tritium have masses of $(2 - 0.000994)m_p$ and $(3 - 0.006284)m_p$, respectively, where $m_p = 1.67 \times 10^{-27}$kg is the mass of the proton. When fused, as shown in Figure 1.2, they produce an alpha particle, $_2\text{He}^4$, with mass $(4 - 0.027404)m_p$, and a neutron with mass $(1 + .001378)m_p$ [6].

$$_1\text{D}^2 + {}_1\text{T}^3 = \text{He}^4 + \text{n}^1 + 17.6\text{MeV} \tag{1.1}$$

The result is a mass deficit of 0.01875 m_p, which is equivalent to 17.6 MeV. This energy manifests as kinetic energy; the alpha particle carries 3.5 MeV and the neutron 14.1 MeV. The distribution of the energy between neutron and alpha particle is set by conservation of momentum.
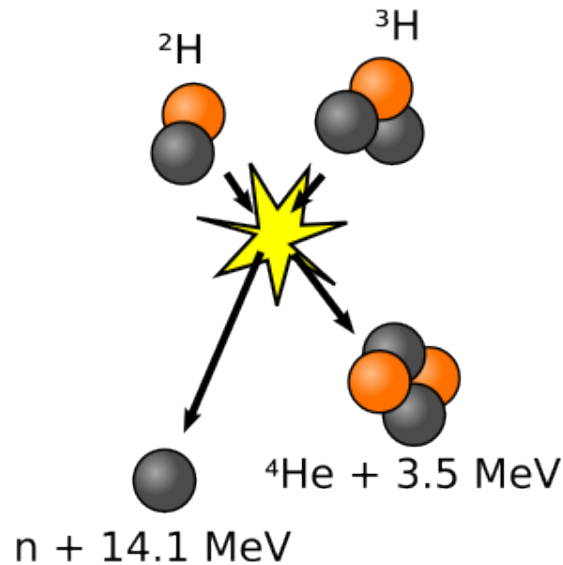
Figure 1.2: Deuterium-Tritium fusion diagram by n.d. Public domain, via Wikimedia Commons, https://commons.wikimedia.org/wiki/File:D-t-fusion.png

The goal of nuclear fusion research is to regulate this deuterium and tritium reaction so that the released kinetic energy may be converted to electricity. The conversion is accomplished by stopping the released 14 MeV neutrons in a "blanket" material that surrounds the tokamak's vessel. The neutrons transfer their energy to the blanket which is used to heat water, generate steam, and turn a turbine [6], [7]. However, positively charged nuclei repel one another via the long-range Coulomb force, and nuclei will not begin to attract each other via the nuclear strong force until they are within several femtometers (10^{-15} m) of each other. Even if two nuclei have sufficient energy to overcome the Coulomb potential, the probability of a fusion collision, as opposed to a glancing Coulomb collision, is extremely small. Thus, producing fusion energy at a scale relevant to energy production requires confining the nuclei within an environment in which they undergo frequent collisions with sufficient energy to fuse. These requirements demand that the nuclei be suspended in a quasineutral ionized gas, a plasma, at extremely high temperatures and pressures, greater than 15 keV (200 million °C) and 7 atmospheres.

Extraordinary countermeasures are required to confine plasma at the pressures relevant to fusion production. In nature, these conditions and sustained fusion power are achieved only within stars. Stars are confined by their own gravitational pull as they undergo a continuous fusion reaction. The energy released from the fusion reaction maintains a star's temperature while it continuously emits blackbody (electromagnetic) radiation, which in turn supports life on Earth.

Lacking the ability to manufacture a solar mass, controlled nuclear fusion power poses a considerable and ongoing challenge for human engineering. There are two primary methods for accomplishing it: heating and confining a plasma within a magnetic field, known as magnetic confinement fusion (MCF), or compressing a plasma with lasers, known as inertial confinement. This thesis focuses exclusively on MCF and its implemen-

tation with a device known as a tokamak.

1.2 Magnetic Confinement

In a magnetic field, charged particles execute *gyro-orbits* as a result of the magnetic force:

$$\vec{F} = m\frac{d\vec{v}}{dt} = q\vec{v} \times \vec{B} \tag{1.2}$$

For a constant magnetic field of $\vec{B}(r) = B_o\hat{e}_z$ a charged particle's trajectory with initial velocity $v_o = v_\perp\hat{e}_x + v_{||}\hat{e}_z$ is:

$$\vec{v}(t) = \begin{bmatrix} v_\perp \cos(\omega_g t) \\ -\frac{|q|}{q}\sin(\omega_g t) \\ 0 \end{bmatrix} + \begin{bmatrix} 0 \\ 0 \\ v_{||} \end{bmatrix} \tag{1.3}$$

$$\vec{r}(t) = \begin{bmatrix} \rho_g \sin(\omega_g t) \\ \rho_g \cos(\omega_g t) \\ 0 \end{bmatrix} + \begin{bmatrix} x_g \\ y_g \\ v_{||}t \end{bmatrix} \tag{1.4}$$

$$\omega_g = |\frac{qB}{m}| \tag{1.5}$$

$$\rho_g = \frac{v_\perp}{\omega_g} \tag{1.6}$$

The quantities ω_g and ρ_g are known as the gyrofrequency and gyroradius, respectively. The center of an orbit, known as the guiding center, is $\vec{r}_{gc} = \begin{bmatrix} x_{gc} \\ y_{gc} \\ v_{||}t \end{bmatrix}$. The appropriateness of the term "guiding center" should be clear from Eqs 1.3 and 1.4. As seen in the equations, the charged particles freely stream along the magnetic field lines, while the motion perpendicular to the magnetic field line, i.e., the guiding center, averages to zero over the period of the orbit. Of course, this terminology would be of little relevance if this were only the case for a constant magnetic field. It is the fact that charged particles follow guiding centers for the complicated magnetic fields produced in confinement devices that merits the terminology and allows magnetic fields to confine plasmas effectively.

For the conditions of a magnetic confinement device, it can be assumed that

$$\frac{\rho_g|\boldsymbol{\nabla}B|}{B} << 1\frac{1}{B}\frac{dB}{dt} << \omega_g \tag{1.7}$$

$$\frac{1}{B}\frac{\partial B}{\partial t} << \omega_g \tag{1.8}$$

Eqs 1.7 and 1.8 state that a charged particle observes little variation in the magnetic field over the diameter and period of its gyro-orbit. Thus, even though a magnetic field may be changing as a particle moves in space, the magnetic field will appear constant to an individual charged particle on the timescale of the gyrofrequency, and the orbits will have plenty of time to recenter themselves to the new local magnetic field and continue to freestream along the field's new direction. Consequently, it should be expected that the charged particles will follow the magnetic field lines to the lowest order. The crucial question is then to calculate the first-order corrections to the guiding centers, so that the trajectory of a charged particle may be expressed as:

$$\vec{R}(t) = \vec{R}_{GC}(t) + \epsilon \vec{\rho}_g(t) \tag{1.9}$$

$$\vec{V}(t) = \vec{V}_{GC}(t) + \vec{v}_g(t) \tag{1.10}$$

$$\tag{1.11}$$

Where $\vec{R}_{GC}(t)$ and $\vec{V}_{GC}(t)$ represent the movement of the particle's guiding center resulting from averaging the particle motion over several gyro-orbits, and $\rho_g(t)$ and $v_g(t)$ are the gyrating radius and velocity. It is required when averaged over one gyro-orbit that $< \rho_g(t) >= 0$ and $< v_g(t) >= 0$.

As a simple, but non-trivial, example of guiding center analysis, suppose a force is applied to a charged particle in a magnetic field such that:

$$\vec{F} = m\vec{a} = q\vec{v} \times \vec{B} + \vec{F}_{ext} \tag{1.12}$$

To solve for the trajectory, define $u = v - \frac{\vec{F} \times \vec{B}}{qB^2}$. Then, by substitution into Eq 1.12:

$$m\frac{\mathrm{d}u}{\mathrm{d}t} = (F \cdot \hat{e}_z)\hat{e}_z + u \times \vec{B} \implies m\frac{\mathrm{d}u_z}{\mathrm{d}t} = (F \cdot \hat{e}_z) \tag{1.13}$$

$$m\frac{\mathrm{d}u_\perp}{\mathrm{d}t} = qu_\perp \times \vec{B} \tag{1.14}$$

Eq 1.13 is now of the same form as Eq 1.2. Thus, Eq 1.15 and 1.4 becomes:

$$\vec{v}(t) = \begin{bmatrix} v_\perp \cos(\omega_g t) \\ -\frac{|q|}{q}\sin(\omega_g t) \\ 0 \end{bmatrix} + \begin{bmatrix} 0 \\ 0 \\ F \cdot \hat{e}_z t \end{bmatrix} v_{||} + \frac{\vec{F} \times \vec{B}}{qB^2} \tag{1.15}$$

$$\vec{r}(t) = \begin{bmatrix} \rho_g \sin(\omega_g t) \\ \rho_g \cos(\omega_g t) \\ 0 \end{bmatrix} + \begin{bmatrix} x_g \\ y_g \\ v_{||} t + \frac{F}{2} \cdot \hat{e}_z t^2 \end{bmatrix} + \frac{\vec{F} \times \vec{B}}{qB^2} t \tag{1.16}$$

In Eq 1.15, $\vec{V}_{GC} = (F \cdot \hat{e}_z)\hat{e}_z t + \frac{\vec{F} \times \vec{B}}{qB^2}$. The component of the guiding center velocity perpendicular to the magnetic field is termed the drift velocity, $\vec{V}_{GC\perp}$. Such drifts are the result

of electric fields perpendicular to the magnetic field lines, or can be viewed as spawning from the centrifugal force observed when following a curved magnetic field line in a non-inertial frame. Drifts also result from spatial variations in the magnetic field or temporal variations in the magnetic field and perpendicular forces. The net result is that:

$$\vec{V}_{GC\perp} = V_{\text{E}\times\text{B}} + V_{\boldsymbol{\nabla}B} + V_{\kappa} + V_{p} \tag{1.17}$$

$$V_{\text{E}\times\text{B}} = \frac{\vec{E} \times \vec{B}}{B^2} \tag{1.18}$$

$$V_{\boldsymbol{\nabla}B} = -m\frac{v_{\perp}^2}{2qB^3}\boldsymbol{\nabla}B \times \vec{B} \tag{1.19}$$

$$V_{\kappa} = -m\frac{v_{\perp}^2}{qB^2}\hat{b} \cdot \boldsymbol{\nabla}\hat{b} \times \vec{B} V_p = -\frac{m}{qB^2}\frac{\text{d}}{\text{dt}} \times B \tag{1.20}$$

In Eq 1.17, $V_{\text{E}\times\text{B}}$ (read "E cross B drift") is the result of a perpendicular electric force, $V_{\boldsymbol{\nabla}B}$ (grad B drift) is the result of variations in the magnetic field's strength, V_{κ} (curvature drift) is the result of curving magnetic field lines, and v_p is the result of temporal variations.

While a magnetic field constrains the movements of charged particles in the directions perpendicular to the field, movements parallel to the field are unaffected. Consequently, plasmas are very good conductors of heat in the direction parallel to the magnetic field, so the temperature gradients along a magnetic field line in steady-state conditions will be small. This has a great practical consequence for designing a MCF reactor. The reactor must sustain a fusion reaction at temperatures around 200 million °C, while the temperature of the device's surface is kept below its materials' melting points. Tungsten has the highest melting point of any solid at 3422 °C. Therefore, the parallel heat conductivity of plasma and material limitations require that the portion of the plasma undergoing fusion must not be confined to field lines that intersect any part of the MCF device.

The intuitive response for closing the field lines is to confine the plasma in the circular magnetic field of a toroid, i.e.:

$$B(R) = \frac{\mu_o I n}{2\pi R}\hat{e}_{\phi} \implies \tag{1.21}$$

$$B(R) = \frac{B(a)a}{R}e_{\phi} \tag{1.22}$$

Where n is the number of turns, I is the current, a is some arbitrary radial position and R is the radial position inside the torus. While intuitive, this approach is unsuccessful. The ∇B and curvature drifts cause electrons and ions to drift in opposite directions which induces an electric field. The E×B drift then causes both electrons and ions to drift radially outward. This outward drift prevents a purely toroidal field from confining a plasma.

To achieve confinement, the magnetic field must have both a toroidal and poloidal component. This is the basis of the tokamak's design.

A tokamak is a torus-shaped MCF device that confines the plasma in a toroidally symmetric magnetic field that has both a toroidal and poloidal component. The toroidal component is driven by electromagnetic toroidal field coils. The poloidal component is driven by the plasma's own current. The plasma current is initially produced via induction from

the increasing current run through a solenoid transformer at the center of the torus, and can be sustained with radio waves after the period of induction. These essential elements of a tokamak are illustrated in Figure 1.4.

Combining the toroidal and poloidal fields produces magnetic field lines that orbit both the major and minor axes of the torus. The orbits in the poloidal plane (around the minor axis) reside on toroidally symmetric two-dimensional surfaces known as flux surfaces. As required by toroidal symmetry, these surfaces are nested about the center of the plasma in the poloidal plane. An example of such a magnetic field line's trajectory and the contour of its flux surface in the poloidal plane is shown in Figure 1.3. The poloidal orbit of the particles assuages the effects of the drifts directed along the major radial direction, $\hat{e}_R$. To understand this result, consider two points on the same flux surface: one at the position of maximum major radius and the other at the minimum. The drifts moving outward in major radius push the particle at the position of the maximum major radius away from the plasma center, but the drifts at the minimum major radius push the particle toward the center of the plasma. Thus, as a particle undergoes an orbit in the poloidal plane it is pushed both towards and away from the plasma center. In this way, the effects of drifts in major radial position "cancel" over the orbit of the particle.
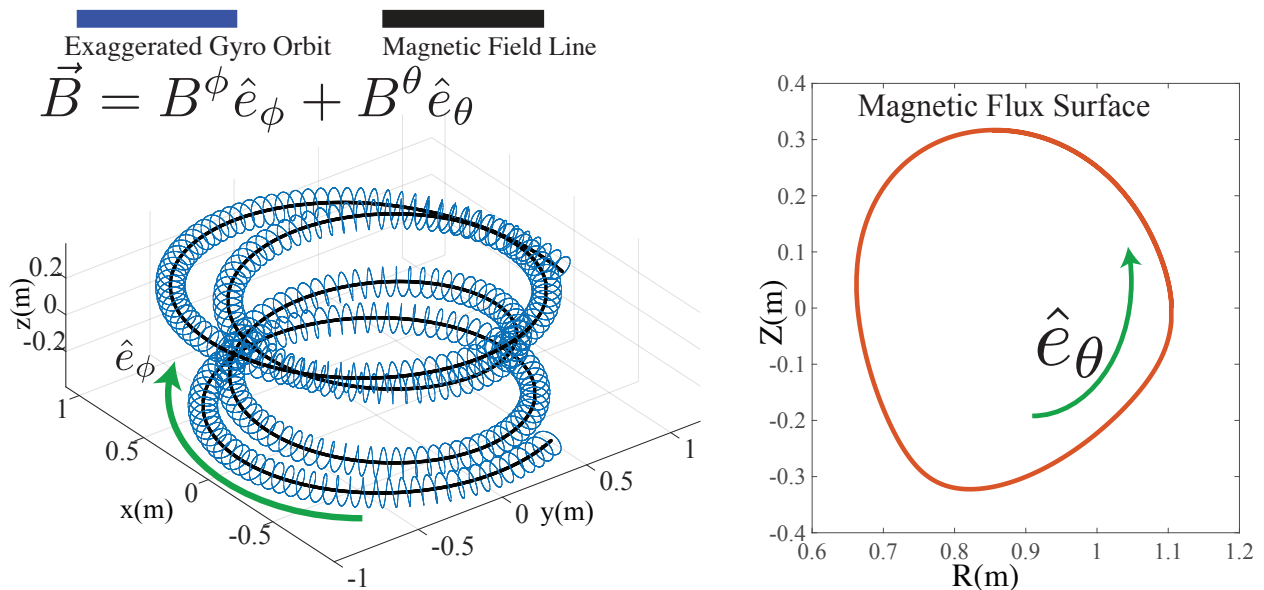
Figure 1.3: Left) 3D path of magnetic field line in a tokamak. Right) The projection of the magnetic field line's trajectory into the poloidal plane.
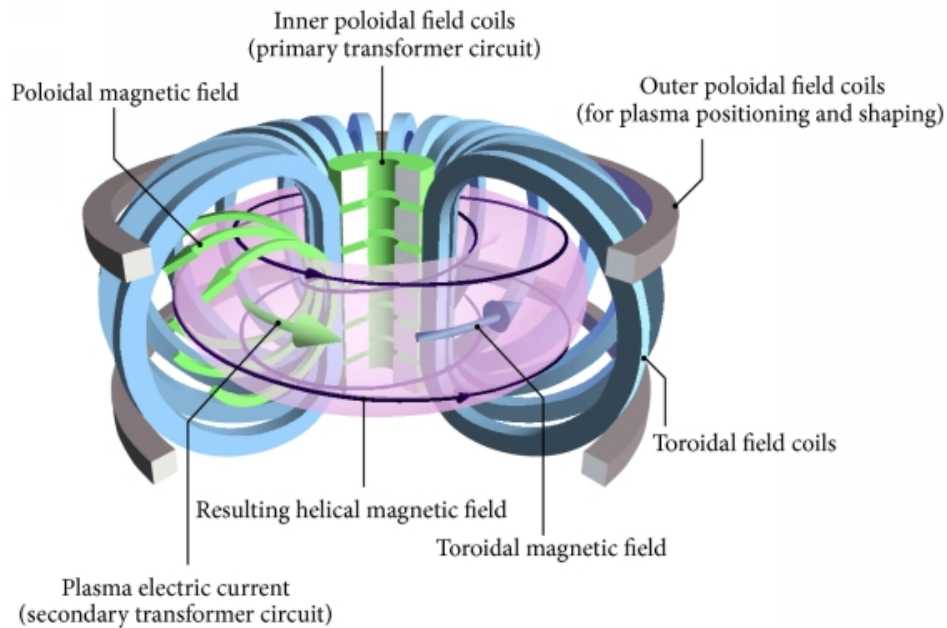
Figure 1.4: Schematic of a tokamak. The toroidal field coils are shown in blue, and the toroidal field they produce is represented by the blue arrow. The volume of the plasma is outlined in purple, and the green arrow within it represents the electric current. The current is driven by the central solenoid, which acts as a transformer in accordance with Faraday's law. The plasma current creates a poloidal magnetic field, which is represented in the figure by the green arrows outside the purple plasma. Image taken from [8] licensed under CC BY 4.0 and available at https://commons.wikimedia.org/wiki/File:Schematic-of-a-tokamak-chamber-and-magnetic-profile.jpg

1.3 Tokamak Boundary Research and Motivation

The performance of tokamaks has improved steadily over several decades. However, several challenges still must be overcome if commercial electric power from tokamaks is to be realized. One such challenge, and central to this thesis, is the power and particle exhaust problem facing tokamaks. The anatomy of a tokamak can be parsed into two regions: the core and the boundary. The core refers to the flux surfaces with magnetic field lines that close without intersecting the vessel, and the boundary describes the flux surfaces with field lines that do intersect the vessel. In the core, the plasma is heated to the temperature and pressure needed to produce fusion energy. The magnetic force confines the plasma, counteracting the pressure force of the plasma. However, this confinement is imperfect. Drifts and collisions cause the plasma to diffuse into the boundary. These open field lines transport both the plasma and heat to the vessel's surface. The heat transport perpendicular to the flux surfaces is signifcantly less than that from parallel transport. Thus, the boundary plasma is much cooler than that of the core where the fusion energy is produced, so it is feasible to mitigate its interaction with the reactor surface to be within

26

material constraints.

A future tokamak reactor will employ a diverted magnetic configuration to accomplish heat and particle exhaust. In this configuration, the magnetic field lines transition from closed to open at a separatrix. The open field lines divert the plasma and heat escaping the core to target plates in the divertor chamber, which are spatially removed from the core (see Figure 1.5). Unabated, the parallel heat flux reaching the plates in a tokamak reactor will exceed $1\,\mathrm{GW\,m^{-2}}$ [9] [10]. However, material limitations require that the heat flux be less than $10\,\mathrm{MW\,m^{-2}}$. Consequently, the divertor chamber conditions must be manipulated to ensure that the heat exhaust is dispersed onto a wider area of the vessel through atomic radiation, interactions with neutrals, and cross-field transport. This mitigation of the heat must be achieved while maintaining sufficient particle exhaust.
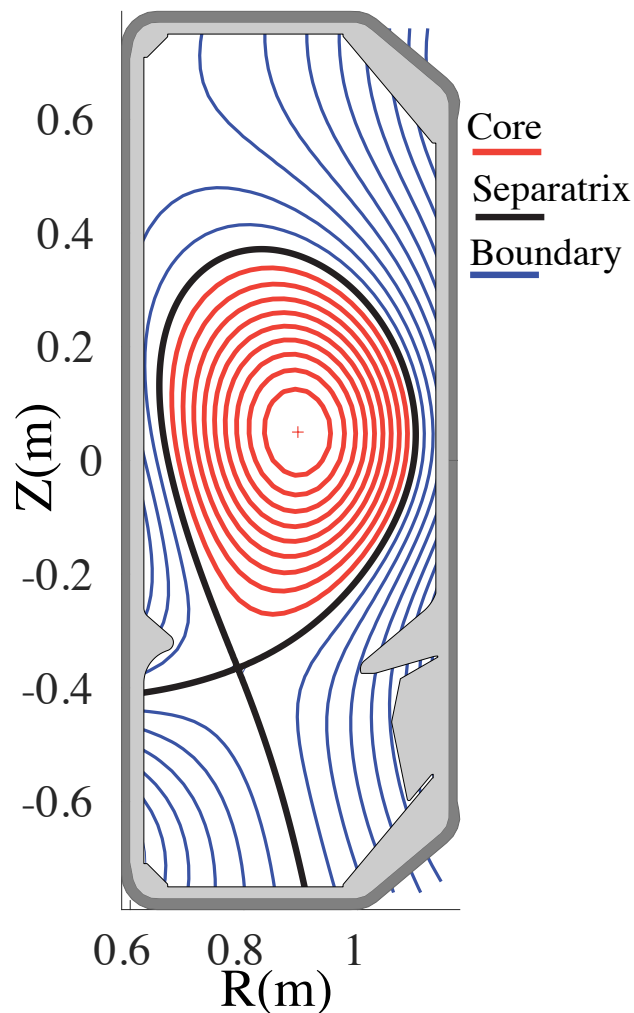
Figure 1.5: The magnetic geometry of diverted plasma in a tokamak. The red flux surface denotes the plasma core where the fusion energy is produced. These field lines are closed. The black flux surface denotes the magnetic separatrix where the field lines transition from closed to open. The plasma boundary, the region of open field lines, is represented by the blue flux surfaces.

To design a future solution to this problem, the dynamics of the plasma must be accurately understood and predicted by numerical models. However, despite the classical nature of plasma physics, current understanding and modeling are insufficient for confidentally projecting out a heat exhaust solution. For this reason, experimental tokamak reactors are employed across the world to further progress and validate plasma theoretical and computational research.

Accurate and comprehensive measurements are critical to advancing this research. Unfortunately, mechanical constraints limit the spatial coverage of traditional tokamak diagnostics in the plasma boundary. For example, the electron temperature, T_e, and electron density, n_e, are two critical plasma parameters. However, the diagnostic coverage of T_e and n_e in the plasma boundary is limited to a relatively sparse collection of Thomson scattering or Langmuir probe measurements. Thomson scattering measurements are confined to the one-dimensional path of their lasers, and Langmuir probe measurements (when non-invasive) occur at the surface of the vessel. This is particularly problematic for exhaust research because the magnetic geometry of the plasma boundary plays a key role in the exhaust performance and can be extensively shaped. Figure 1.6 demonstrates this shortcoming by showing three different magnetic configurations studied at the *Tokamak à Configuration Variable* (TCV) [11]–[14] and the spatial coverage of the Thomson scattering and Langmuir probe measurements.

Spectrally filtered cameras have the advantage of being able to view entire large areas of the plasma boundary. With the assumption of toroidal symmetry, these spectral images can be tomographically inverted into measurements of the emissivity in the poloidal plane. However, the quantitative insights that can be drawn from a single emissivity profile are limited due to the sensitivity of the emission to several factors. Boundary plasmas do not exist in local thermal equilibrium (LTE), so, in theory, the temperatures and densities of all species involved in the creation of the emission need to be modeled. For the emission discussed in this work, the amount of emissivity is sensitive to three factors: the density of the emitting atom, the density of the bombarding electrons, and the temperature of the electrons. Consequently, while spectral emission can be resolved over a large spatial area with one camera, its interpretation requires equally large diagnostic coverage of T_e and n_e. This has historically limited the efficacy of spectral imaging diagnostics.

The creation of measurement methodologies that exceed the spatial limitations of traditional diagnostics motivates this work. This thesis centers on the development and implementation of multi-spectral imaging techniques using systems with a novel polychromator design, TCV's Multispectral Advanced Narrowband Tokamak Imaging System (MANTIS) diagnostics [15]. These MANTIS cameras' polychromator design allows them to image up to 10 individual spectral lines simultaneously over the same tangential view of the divertor chamber of a tokamak. The images are absolutely calibrated, and by assuming toroidal symmetry, the images are tomographically inverted to create 2D poloidal emissivity maps.

This thesis work leveraged these MANTIS cameras to create the first 2D poloidal maps of T_e and n_e in the divertor. For this work, three He I lines, 728.2 nm ($3\,^1S \rightarrow 2\,^1P$), 667.8 nm ($3\,^1D \rightarrow 2\,^1P$), and 706.5 nm ($3\,^3S \rightarrow 2\,^3P$), were imaged. These images were inverted into poloidal emissivity profiles. Then, the ratios of emissivities at each point in the poloidal grid were independently regressed to T_e and n_e values using a collisional-

radiative model (CRM) for He I emission. This diagnostic process will be referred to as helium multi-spectral imaging (HeMSI) throughout the rest of this thesis. These HeMSI measurements were validated in experiments against co-local measurements of T_e and n_e via Thomson scattering.

In the second part of this thesis work, these powerful new measurements were used in experiments on TCV studying the effects of magnetic geometry on heat exhaust performance. The poloidal field strength was varied for several single-null L-mode plasmas resulting in a scan of poloidal flux expansion (defined in Chapter 4). With the ability to resolve T_e and n_e throughout the poloidal plane, several conclusions could be drawn. First, the neutral densities and ionization rates of He, He^+, and D were resolved from their spectral images of atomic emission, which were all simultaneously captured with MANTIS. Furthermore, drift velocities were calculated in 2D with the assistance of floating potential measurements from the Langmuir probes at the vessel's surface. These auxiliary calculations allowed for 2D calculations of heat and particle transport throughout the divertor volume and demonstrated the current shortcomings of simple 1D plasma boundary models and transport assumptions in modeling.

In all, this thesis work has added a powerful new diagnostic tool to the field of plasma exhaust research and used that tool to perform a novel analysis of the effects of magnetic geometry on plasma exhaust. These results benefit the field and serve as a template for future analysis.
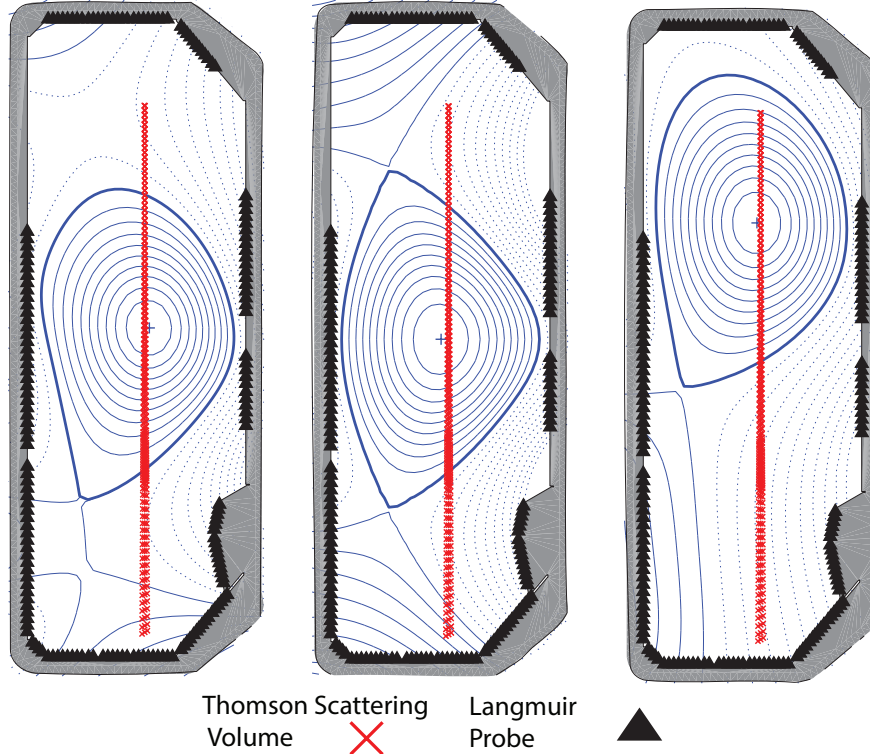
Figure 1.6: Magnetic reconstructions from three TCV discharges. These images illustrate the wide range of magnetic geometries explored at TCV and the amount of plasma volume in the boundary that lacks T_e and n_e diagnostic coverage from Thomson scattering and Langmuir probes.

1.4 Thesis Outline

The presentation of this thesis will proceed as follows. Chapter 2 focuses on the implementation and hardware of the polychromator-based multi-spectral imaging systems used in this thesis. The chapter discusses:

- The work done to improve the optics of these systems

- The calibration methodology

- The tomographic inversion methodology

Chapter 3 reports on the HeMSI methodology and the results of the validation experiments. The results are:

- HeMSI showed good agreement with Thomson scattering when employing the Goto atomic rates in a collisional radiative model (CRM) but not the ADAS atomic rates.

- HeMSI is accurate for the case of an ionizing plasma, $T_e > 10\mathrm{eV}$.

- HeMSI measurements for $T_e < 10\text{eV}$ cannot be reconciled with current atomic models. The inability to make measurements at $T_e < 10\text{eV}$ is attributed to a lack of physical understanding and not the uncertainties of the HeMSI measurements.

Chapter 4 reports on the application of HeMSI to experiments in which the poloidal flux expansion of the divertor was varied. The results of this experiment are:

- Poloidal flux expansion does not benefit the plasma exhaust performance as expected from simple 1D modeling in the detached regime. However, it does produce lower temperatures at the divertor plate prior to detachment while in the conduction-limited regime. This demonstrates that the onset of detachment is a non-linear process.

- The drift fluxes are calculated in 2D. The poloidal drifts are shown to be much larger for smaller flux expansion, but cross-field drifts are shown to be more important in the cases of larger flux expansion.

- The direction of the toroidal field has a significant impact on the T_e and n_e profile shapes.

- The anomalous cross-field heat transport coefficient $\chi_\perp$ is shown to be much larger than what is customarily used in modeling and assumed to be unphysical. This implies that the assumption of cross-field heat transport being diffusive is incorrect.

- T_e and n_e profiles from the Scrape-Off Layer Plasma Simulation code (SOLPS) are compared to HeMSI measurements. The simulated T_e profiles are shown to have a significantly smaller fall-off length than that of the measurements. This discrepancy is consistent with anomalously large values of $\chi_\perp$ calculated in the poloidal flux expansion experiments.

Finally, Chapter 5 reflects on how multi-spectral imaging and HeMSI can be leveraged in future work, and on how the diagnostic can be improved in the future.

Chapter 2

MSI and MANTIS Diagnostics

2.1 History of Spectral Cameras in Tokamaks

As described in Chapter 1.1, the development of a plasma exhaust solution requires experimental measurements to validate plasma therotical and numerical models. However, many traditional diagnostics, e.g., Langmuir probes, Thomson scattering, and spectrometers, offer limited coverage. Spectral cameras offer the ability to observe spectral emission over a large portion of the plasma. Assuming toroidal symmetry, these spectral images can be tomographically inverted into local emissivity measurements in the poloidal plane.

Researchers have utilized spectral images and produced emissivity maps from these images since the 1990s [16]–[21]. However, the earliest such measurements were limited to one filtered camera per diagnostic port [17]–[19]. Thus, repeated shots were required in order to analyze different spectral lines for the same scenario. This is unideal because it requires more discharges, which are quite expensive, and because it requires the further assumption that repeated discharges remain similar. This is a strong assumption due to the differences in wall-conditioning over time and fluctuations in the magnetic equilibrium. Furthermore, the quantitative insight that can be gathered from a single emissivity profile is limited. Spectral emission is sensitive to at least the temperature and density of the emitting species and the species with which it is colliding. Therefore, extracting 2D quantitative information on the background plasma from the emission requires more than one 2D emissivity profile. More recently, beam splitters have been utilized as a way of producing multiple spectral images through one viewing pupil [16]. However, by design, beam splitters "throw away" light, so they are inherently limited by their inefficient use of light.

2.2 Polychromator Multi-Spectral Imaging Systems

In this thesis work, a polychromator-based multi-spectral imaging system was used for the first time which circumvented previous limitations of spectral camera diagnostics. Polychromators filter light via the repeated reflection of light off of bandpass filters and mirrors. Light enters the optical system and is relayed to a dielectric filter where a select wavelength is passed through to a detector. The out-of-band light is reflected back

into the system and relayed again, in an identical manner. This process repeats itself for each filter in the system. The optical layout is illustrated in Figure 2.2. The advantage of this design is that it creates multiple simultaneous images from a single view without splitting the light. The design of the polychromator imaging systems used in this thesis originated from the polychromator system used for the Thomson scattering diagnostic on DIII-D [22]. Later, it was adapted for the motional stark effect (MSE) diagnostic on Alcator C-MOD [23]. In these previous works, only the total intensity of the light arriving at the detector was recorded. During his Ph.D. thesis work on MSE diagnostics, Bob Mumgaard proposed that the MSE polychromator be outfitted with cameras and converted into a visible imaging system. This thesis work began with this proposal.

As the first part of this thesis work, a four-channel MSE polychromator was repurposed for the imaging of visible light along the plasma boundary. This system, known as the multi-spectral imaging system (MSI), was tested on Alcator C-MOD and then installed on TCV in 2017. This was the first instance of a polychromator system being operated on tokamaks and was reported in *Linehan 2018* [24]. Figure 2.1 shows examples of images taken with the MSI on TCV and C-MOD.

The multispectral imaging research was conducted within a collaboration between MIT, the Swiss Plasma Center at École Polytechnique Fédérale de Lausanne (EPFL), where TCV is located, and the Dutch Institute for Fundamental Energy Research (DIFFER). As part of the collaboration, DIFFER contributed a 10-channel Multispectral Advanced Narrowband Tokamak Imaging System (MANTIS) diagnostic [15]. The initial MANTIS system replaced the MSI in 2018. The design of the MANTIS system was reported on in *Perek 2018* [15]. In 2020, MIT and DIFFER both contributed 6-channel MANTIS systems, which allowed for coverage of the whole vessel. The data analysis presented in the following chapters focuses on data collected with the 10-channel MANTIS system. MANTIS's camera detectors operated at 200 frames per second with 12 bits of dynamic range and the pixels were square in shape. The gain and exposure times were adjusted dynamically to avoid overexposure. However, work to improve the polychromator design began with the MSI diagnostic. This is discussed in the next section.

2.3   Ghosting and Filter Quality

At the beginning of this thesis work, the images suffered from an artifact known as ghosting. Ghosting refers to a detector seeing multiple instances of the same image. This artifact was immediately observed in the original MSI system. However, the appearance of the artifact was dependent not only on the wavelength of the light but also the optical filters preceding the ghosting image's filter. Testing on the optical bench revealed that the artifact vanished when specific optical filters were replaced by mirrors. This demonstrated that the optical filters were reflecting the light at multiple planes rather than only on the surface of the filter. This is a shortcoming of soft-coated dielectrics which reflect light at multiple planes within the filter's width. The soft-coated dielectric filters were replaced with hard-coated filters which reflected all the light at the surface of the filter. This removed the ghosting artifacts. Hard-coated filters also had a transmission efficiency of 95% which was twice that of soft-coated filters. The bandpass of these filters were 1.2 nm and
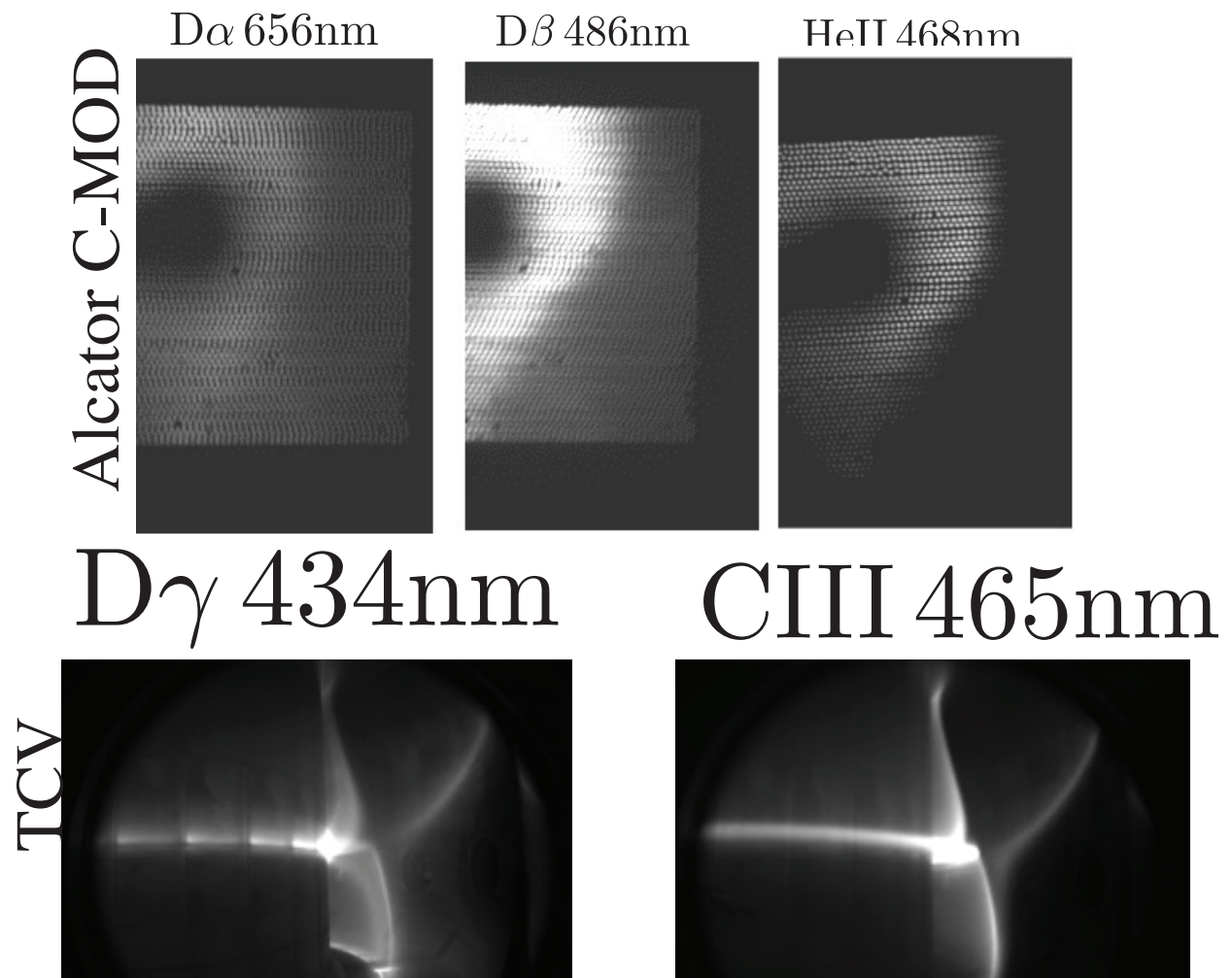
Figure 2.1: Example images from MSI on C-MOD and TCV. On C-MOD the light was relayed to polychromator with a coherent fiber bundle.
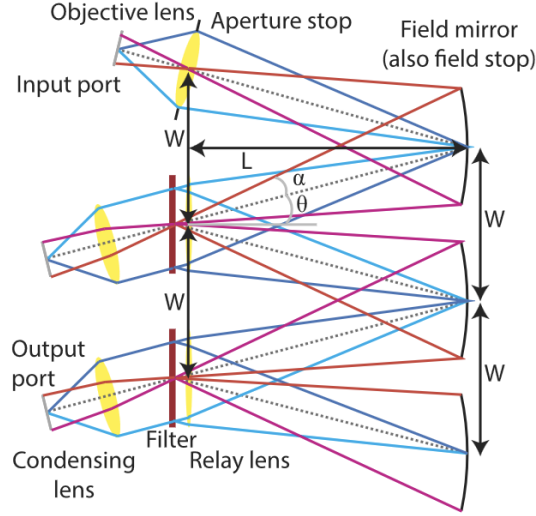
Figure 2.2: Optical layout for polychromator-based imaging system. Figure used with permission from [23]

they had OD6 blocking. Figure 2.4 shows examples of images taken with the 10-channel MANTIS system using final filter specifications.

2.4   System Calibration

The absolute brightnesses of the images are calibrated using an integrating sphere coupled to a broadband lamp. The spectral radiance of the broadband light at the output of the integrating sphere, the transmission of the band-pass filters, and their respective uncertainties are assumed to be known from the data provided by their manufacturers. The uncertainty in the radiance of the lamp was given as 3%. The filters' transmission profiles were provided at 0.05 - 0.1 nm increments about their band-passes with each transmission having an uncertainty of $< 1\%$.

   When observing a brightness source with MANTIS, the counts per second measured by a pixel, p_i, is related to the radiance of the source by:

$$p_i = \int_\Omega \int_A \int_\nu \alpha_i(\nu) B(\nu) f(\nu) d\nu da d\omega = \Omega_i A_i \int_\nu \alpha_i(\nu) B(\nu) f(\nu) d\nu \qquad (2.1)$$

Where A_i is the area of the sphere viewed by the pixel, Ω_i is the solid angle subtended by the aperture of the optics about the area being viewed, $\alpha_i(\nu)$ is an efficiency coefficient incorporating the quantum-efficiency of the detector and transmission of the optical system, $f(\nu)$ is the transmission of the band-pass filter, and $B(\nu)$ is the radiance of the source. $B(\nu)$ and $\alpha_i(\nu)$ are assumed to be constant about the center-wavelength, ν_o, of the 1.2 nm

458 nm   **465 nm**

Filter Order 1
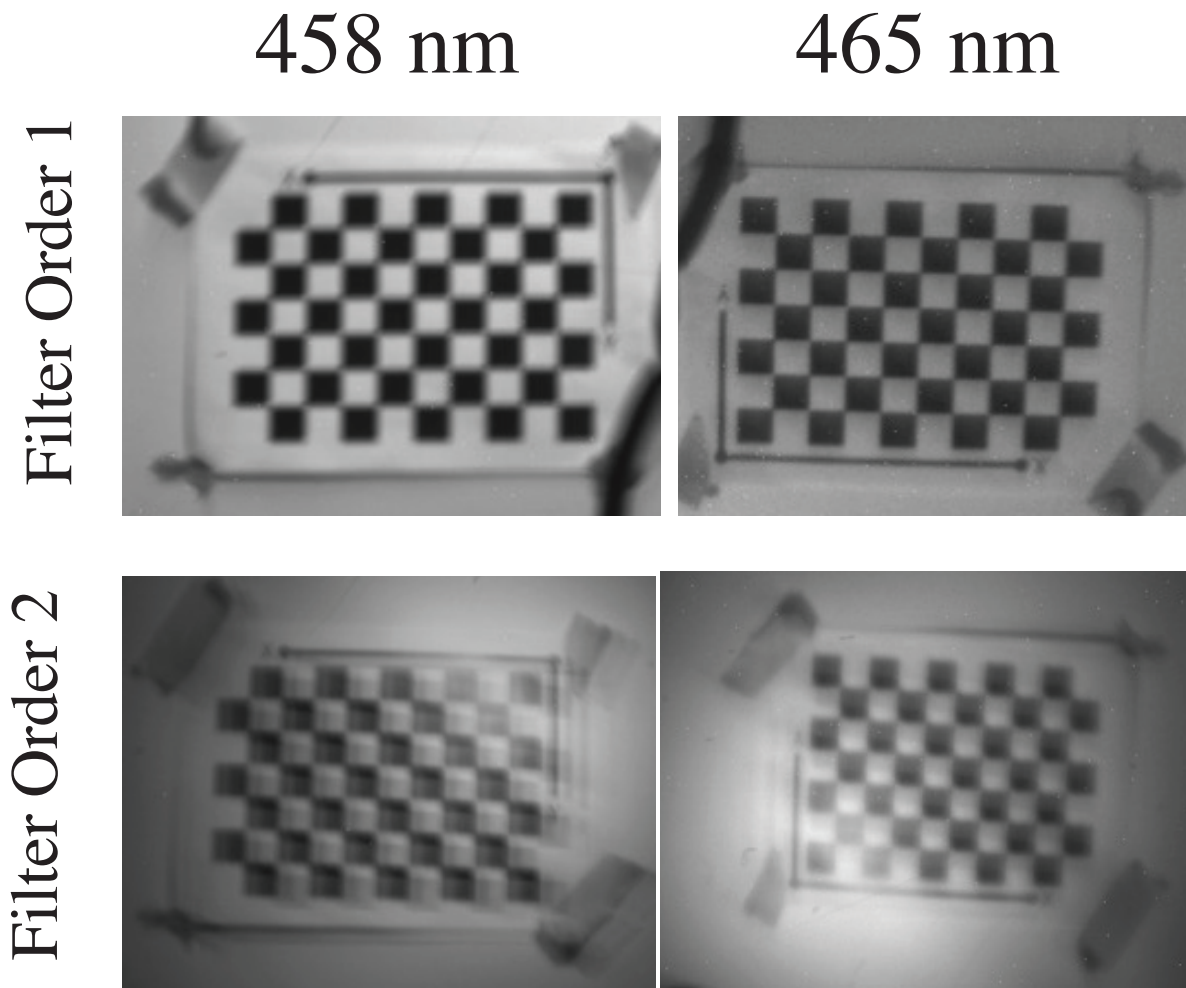
Filter Order 2

Figure 2.3: Example of ghosting viewed by MSI system with soft-coated filters. The center wavelengths of filter order 1 are, in order: 397 nm, 656 nm, 458 nm, and 465 nm. For filter order 2 they are: 397 nm, 434 nm, 458 nm, and 465 nm. Thus, the introduction of the 434 nm filter is producing a ghost artifact to the filters down the line.

He I 728 nm | He I 706 nm | He I 667 nm | $D\gamma$ 434nm | $D\epsilon$ 397 nm

$D\alpha$ 656 nm | C III 465 nm | He II 468 nm | He I 501 nm | He I 587 nm
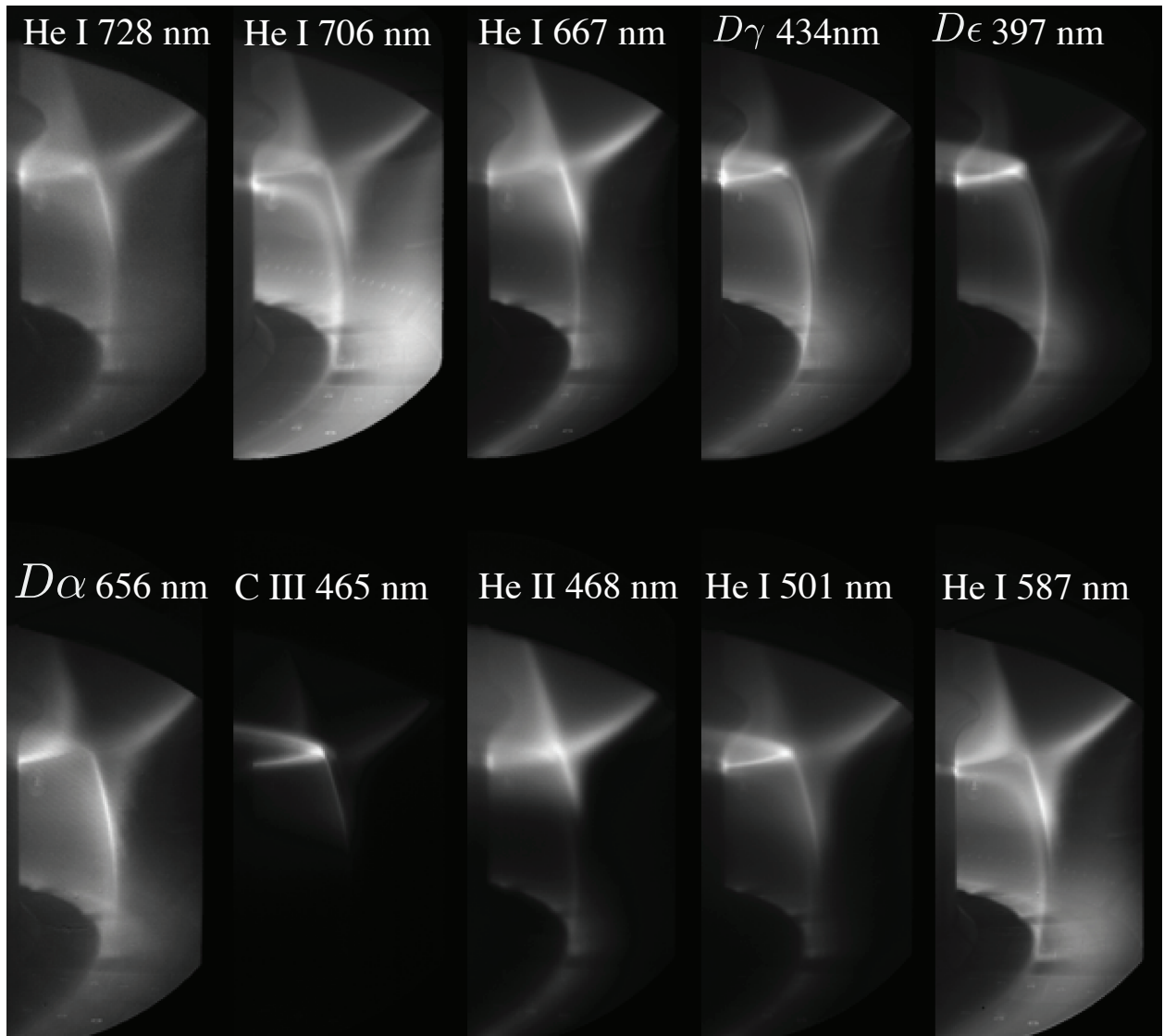
Figure 2.4: Example of a single capture by the 10-channel MANTIS system.
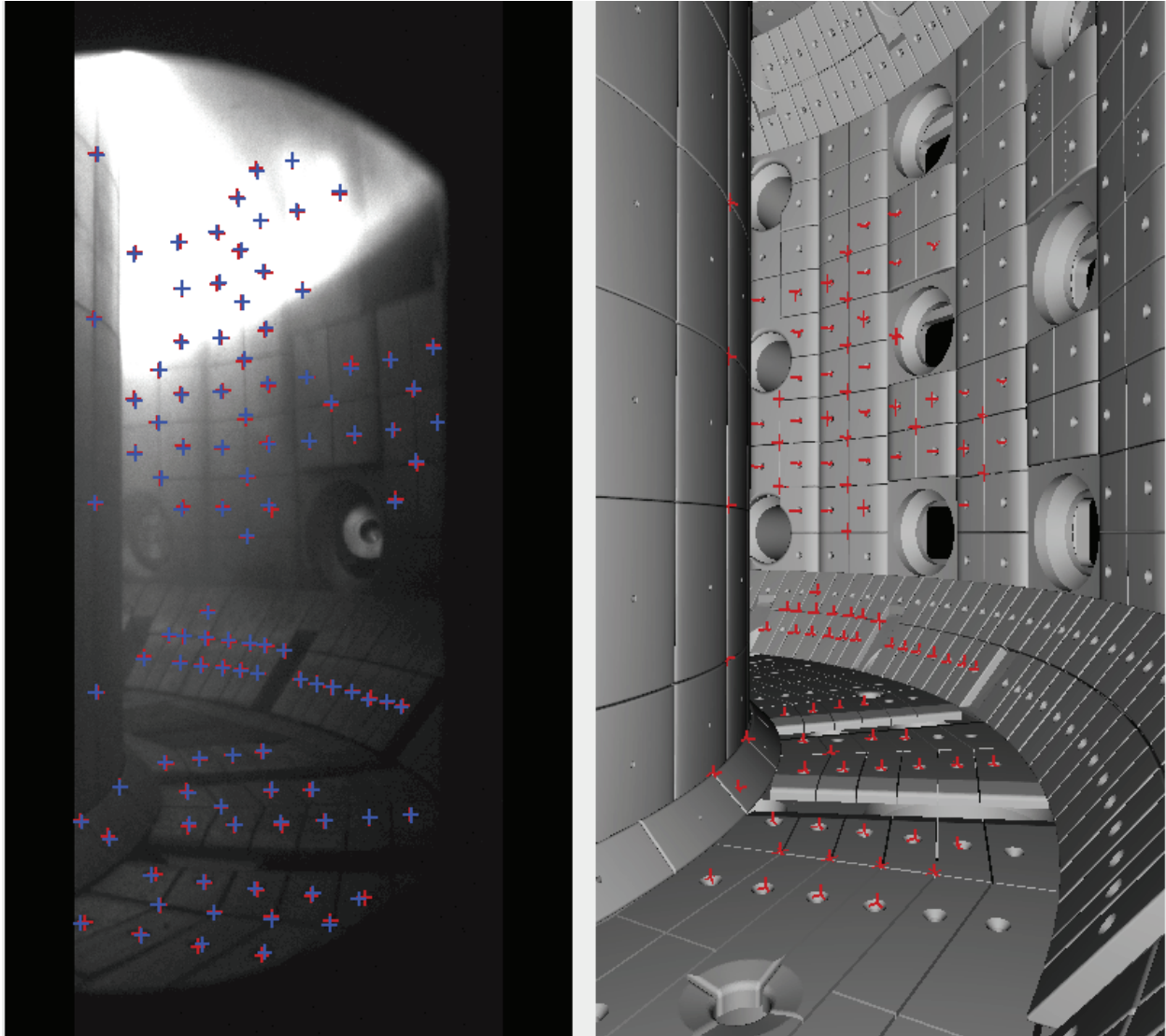
Figure 2.5: Red crosses show the point matching done between vessel and image to perform registration. The blue crosses show the location of the real points from the fitted camera model. The image's exposure and contrast were altered to better show in print; this is the cause of the saturated pixels at the top of the image.

wide band-pass of the filter. Therefore:

$$p_i = \alpha_i(\nu_o)B(\nu_o)\Omega_i A_i F \tag{2.2}$$

$$F \equiv \int_{\nu_o-\delta\nu}^{\nu_o+\delta\nu} f(\nu)d\nu \tag{2.3}$$

The calibration factor γ_i for the pixel is then defined as:

$$\frac{1}{\gamma_i} \equiv \frac{p_i}{B(\nu_o)F} = \Omega_i A_i \alpha_i(\nu_o) \tag{2.4}$$

Now, instead of a broadband source, assume a monochromatic source of light, $L^m(\nu_o)$, is input into the system. The signal per second on the pixel, p_i^m, is then:

$$p_i^m = \alpha(\nu_o)\Omega_i A_i L^m(\nu_o)f(\nu_o) \tag{2.5}$$

$$\tag{2.6}$$

This permits the measurement of $L^m(\nu_o)$ via the calibration factor, γ_i, i.e.:

$$\frac{\gamma_i}{f(\nu_o)}p_i^m = L^m(\nu_o) \tag{2.7}$$

2.5   Inversion of the Images

The emissivity of a plasma, $\epsilon(\vec{r})$, has dimensions of $(\frac{\text{photons}}{\text{s}\cdot\text{m}^3})$. The counts per second recorded by a pixel, c_i, is related to the emissivity, which is assumed constant in time, by:

$$p_i^m = f(\nu_o)\alpha(\nu_o)) \int_\Omega \int_T \int_A \int_l \epsilon(\vec{r})/(4\pi)d\Omega dA dl = f(\nu_o)\alpha(\nu_o)\Omega_i A_i \int_L \epsilon(\vec{r})dl \tag{2.8}$$

Where l is the length along the pixel's line-of-sight. In integrating over $d\Omega$ and da it has been implicitly assumed that plasma emission is isotropic, and that the rays are pencil thin, i.e., $\epsilon(\vec{r})$ is constant for a given value of l. Applying the system calibration:

$$\frac{\gamma_i}{f(\nu_o)}p_i^m = \int_L \epsilon(\vec{r})dl \tag{2.9}$$

When inverting the images, ϵ is assumed to be toroidally symmetric, i.e., $\epsilon(\vec{r}) = \epsilon(r, z)$. By discretizing in the poloidal plane, Eq 2.9 becomes

$$b_i \equiv \frac{\gamma_i}{f(\nu_o)}p_i^m = \sum_j ds_{(i,j)}\epsilon_j \tag{2.10}$$

$$\rightarrow \vec{b} = K \cdot \vec{\epsilon} \tag{2.11}$$

where $K_{(i,j)} = ds_{(i,j)}$ is the geometric transfer matrix. This matrix represents the length of the ith ray subtending the jth voxel. For the tomographic inversions performed in this

work, the images were down-sampled by a factor of 4 (factor of 2 along the detectors' rows and columns). The software Calcam was used to register the cameras' positions and create the geometric transfer matrices [25]. The down-sampled images each contained approximately 10^5 pixels, whereas the inversion grid contained 14549 or 50000 polygons. Therefore, the reconstruction problem was over-determined and no external regularization was required to reconstruct the emissivities. As the $K_{(i,j)}$'s were large and non-sparse matrices, calculating the pseudo-inverse of the K's for the purpose of inverting the images was unfeasible. Instead of using the pseudo-inverse, the SART algorithm [26] was used to iteratively solve for $\vec{\epsilon}$.

2.6 Camera Registration

In this thesis, each pixel's line of sight is assumed to be represented by a pencil thin ray. The brightness measured by each pixel represents a line integrated measurement through the plasma as discussed in the previous section (2.5). Thus, to interpret these images quantitatively, the trajectory of each pixel's line of sight must be known. To determine each pixel's trajectory, several features within an image are matched to their real-world points in order to determine a camera model. The fitting of this camera model then determines each pixel's line of sight. This fitting process is performed by the calcam tool box [25].

Chapter 3

HeMSI Diagnostic

This chapter describes the measurement of 2D poloidal profiles of T_e and n_e via multi-spectral imaging of helium lines (HeMSI) at TCV and the experiments performed to validate the profiles against co-local divertor Thomson scattering measurements. The content of this chapter was published in *Linehan 2023* [27].

3.1 Helium Plasma Spectroscopy History

The application of helium line-ratios as a T_e and n_e diagnostic was first proposed by Cunningham in 1955 [28]. Helium line-ratio spectroscopy (HLRS) has since become an effective plasma diagnostic and has been utilized in multiple plasma experiments including: **AUG** [29], [30], **Magnum** [31], **PISCES-A** [32], **W7X** [33], [34], **TEXTOR** [35], **LHD** [36], **MAP-II** [37], [38], **H-1** [39], **TJ-II** [40], **MAST** [41], **Nagdis-II** [42], **RFX** [43], **COMPASS** [44], **JT-60** [45], and **JET** [46].

The work presented here is innovative in that it was the first application of HLRS in a tokamak that incorporated 2D poloidal emissivity profiles. Traditional HLRS methodologies in tokamaks have utilized a localized He gas puff. The advantage of the gas puff methodology is that it requires neither the inversion of images nor the consideration of recombination processes. However, the methodology is limited in its spatial coverage and is inherently perturbative. While HeMSI requires image inversions and consideration of recombination processes, this innovative approach produces 2D T_e and n_e profiles with unprecedented spatial coverage. Furthermore, HeMSI requires viewing multiple lines simultaneously with sufficient resolution to permit inversion. Thus, HeMSI has only now been made feasible for a tokamak experiment with the introduction of the MANTIS diagnostics at TCV.

3.2 Helium Collisional-Radiative Model

A collisional-radiative model (CRM) describes the evolution of atomic or molecular state populations within a background plasma. In diagnostic applications, CRMs are used to forward-model atomic emissions from plasma parameters, including T_e and n_e, so that

they may be determined by fitting the predictions to spectroscopic measurements. Collisional-radiative modeling originated in *Bates 1962* [47], and has since been thoroughly described in several works. The general theory of CRMs is presented in *Fujimoto 2004* [48] and *Summers 2006* [49]. The original derivation of metastable resolved He CRMs was first given in *Fujimoto 1979* [50]. More recent explanations of the helium CRMs can be found in *Goto 2003* [51], *Muñoz-Burgos 2012* [52], and *Zholobenko 2018* [33], [34].

Quantitatively, a CRM is a system of first-order differential rate equations. The helium collisional model utilized in this work accounts for: radiative decay ($A_{i \to j}$), electron impact excitation and deexcitation ($q_{i \to j}^e$), electron impact ionization (S_i^e), three-body recombination (α_i), radiative recombination (β_i), and dielectronic recombination (β_i^d). The three recombination processes will be referred to collectively as electron-ion recombination (EIR). The system of equations defining the He CRM is given in Eq 3.1, and a description of each term in Eq 3.1 is given in Table 3.1.

n_e	electron density
T_e	electron temperature
$n_{\text{He,He}^+}$	neutral He, or He$^+$ density
n_i	density of the ith He atomic state
$q_{i \to j}^e(T_e)$	electron impact (de-)excitation rate coefficient from n_i to n_j
$S_i^e(T_e)$	electron impact ionization rate coefficient from n_i to He$^+$
$\alpha_i(T_e, n_e), \beta_i(T_e), \beta_i^d(T_e)$	three-body, radiative, and dielectronic recombination rate coefficients
$A_{i \to j}$	Einstein spontaneous emission coefficients ($A_{i \to j} = 0$ for $i \geq j$)

Table 3.1: Description of parameters included in Eq 3.1

$$\frac{dn_i}{dt} = \sum_{j \neq i}(A_{j \to i} + n_e q_{j \to i}^e)n_j - (\sum_{j < i} A_{i \to j} + \sum_{j \neq i} n_e q_{i \to j}^e + n_e S_i^e)n_i + n_{\text{He}^+} n_e (\alpha_i + \beta_i + \beta_i^d)$$

(3.1)

A key result of collisional-radiative modeling is that the populations of many excited states can be approximated as residing in a quasi-static equilibrium (QSE) with the background plasma, i.e., $\frac{dn_i}{dt} = 0$. In regards to Eq 3.1, QSE means that the population of such an excited state becomes solely a function of T_e, n_e, n_{He^+}, and the populations of ground and metastable helium states. The timescale, relaxation time, for an atomic state of helium to reach QSE is given by [53]:

$$\tau_{\text{relax}}^i = \frac{1}{(\sum_{j<i} A_{i \to j} + \sum_{j \neq i} n_e q_{i \to j}^e + n_e S_i^e)}$$

(3.2)

In this work, all excited states including metastables will be assumed to be in QSE. The metastable state 2^3S cannot decay through a radiative dipole transition and is the slowest to relax. Therefore, τ_{relax}, which is defined here as the relaxation time for all states, is given by

$$\tau_{\text{relax}} \equiv \tau_{\text{relax}}^{2^3S} = \frac{1}{(n_e q_{2^3S \to j}^e + n_e S_{2^3S}^e)}$$

(3.3)

In regards to HeMSI and following from Eq 3.3, the criterion for QSE to be applicable to neutral helium traversing the divertor is:

$$\frac{\lambda^{\text{pol}}_{(T_e,n_e)}}{v_{\text{He}}} << \tau_{\text{relax}} \tag{3.4}$$

$\lambda^{\text{pol}}_{(T_e,n_e)}$ is the length scale in the poloidal plane over which T_e and n_e vary, and v_{He} is the velocity of the helium atoms. In this work, helium atoms are assumed to be at the temperature of the walls, $\approx 300\,\text{K}$. Figure 3.1a depicts the relaxation time and the average distance traveled in the poloidal plane by helium atoms at $300\,\text{K}$ in one τ_{relax} interval. In the context of TCV, $\lambda^{\text{pol}}_{(T_e,n_e)} \approx 2$ cm, and $n_e > 2 \times 10^{18}\,\text{m}^{-3}$ along the leg of an L-mode plasma. Therefore, looking at Figure 3.1a, an assumption of QSE for the metastable helium states is justified for the plasmas analyzed in this work.

Setting $\frac{dn_i}{dt} = 0$ for all but the 1^1S state, Eq 3.1 simplifies to:

$$n(p) = r_0(p)n_e n_{\text{He}^+} + r_1(p)n_e n(1^1\text{S}) \tag{3.5}$$

Where p indexes an excited state of helium, the $r_0(p)$ and $r_1(p)$ are coefficients determined by T_e and n_e, and $n(X)$ denotes the number density of species X.

The emissivity produced from the $n_i \to n_j$ transition (with units $\frac{\text{photons}}{s \cdot m^3}$) is given by:

$$\epsilon_{i \to j}(t) = A_{i \to j} n_i(t) \tag{3.6}$$

Combining Eqs 3.5 and 3.6 yields:

$$\epsilon^{\text{He}}_{i \to j} = A_{i \to j} r_1(i) n_{\text{He}(1^1\text{S})} n_e + A_{i \to j} r_0(i) n_{\text{He}^+} n_e \tag{3.7}$$

Adjusting the notation going forward, the $A_{ij}r(i)$ terms are relabeled as *photon emissivity coefficients* (PEC) in accordance with the terminology of *Summers 2006* [49], and it is assumed that $n_{\text{He}} \approx n_{\text{He}(1^1\text{S})}$. Thus, Eq 3.7 becomes:

$$\epsilon^{\text{He}}_{i \to j} = n_{\text{He}} n_e \text{PEC}^{\text{i} \to \text{j}}_{\text{Excit}} + n_{(\text{He}^+)} n_e \text{PEC}^{\text{i} \to \text{j}}_{\text{Recom}} \tag{3.8}$$

Eq 3.8 shows that Helium emission is driven by two processes, electron impact excitation (EIE) which corresponds to the $n_{\text{He}} n_e \text{PEC}^{\text{i} \to \text{j}}_{\text{Excit}}$ term and electron ion recombination (EIR) which corresponds to the $n_{(\text{He}^+)} n_e \text{PEC}^{\text{i} \to \text{j}}_{\text{Recom}}$ term. In this work, it will be assumed the EIE emission dominates. Motivation for this assumption is seen in Figure 3.1b wherein it can be seen that:

$$\frac{\text{PEC}_{\text{Recom}}}{\text{PEC}_{\text{Excit}}} << 1 \qquad (T_e > 2\,\text{eV}) \tag{3.9}$$

It is assumed in this work that n_{He^+} is not large enough to overcome the disparity between $\text{PEC}_{\text{Recom}}$ and $\text{PEC}_{\text{Excit}}$. Therefore, the emissivity of He I line can be approximated as:

$$\epsilon^{\text{He}}_{i \to j} \approx n_{\text{He}} n_e \text{PEC}^{\text{i} \to \text{j}}_{\text{Excit}} \tag{3.10}$$

3.2.1 Fitting Data to Forward Model

Measurements of T_e and n_e are inferred by matching the observed relative intensities of He I lines to CRM predictions. Using Eq 3.10, the line-ratios can be expressed as

$$r_{ab} = \frac{\epsilon_a}{\epsilon_b} \approx \frac{\text{PEC}^{\text{a}}_{\text{Excit}}}{\text{PEC}^{\text{b}}_{\text{Excit}}} \tag{3.11}$$

In these HeMSI validation experiments, 4 He I lines, 728 nm, 706 nm, 668 nm, and 587 nm were observed. The fitted T_e and n_e were determined by performing a least squares regression between the measured He I line ratios and the predictions of the CRM being scanned over the T_e and n_e parameter space, i.e.:

$$(T_e, n_e)_{\text{fit}} = \arg\min \sum_i (1 - \frac{r_i^{\text{obs}}}{r_i^{\text{model}}(T_e, n_e)})^2 \tag{3.12}$$
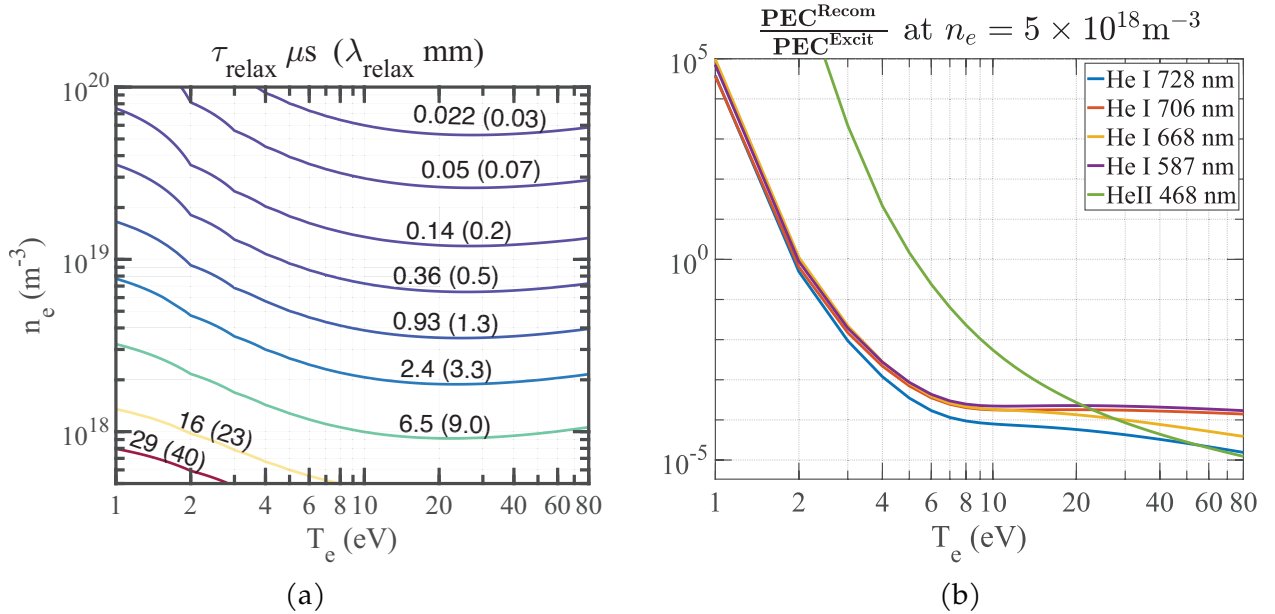
Figure 3.1: 3.1a): Relaxation time, τ_{relax}, and the average distance traveled in the poloidal plane during that time, λ_{relax}, by neutral helium atoms at $300K$ and in a 1.4 T magnetic field. 3.1b): Ratio of $\text{PEC}_{\text{Recom}}$ to $\text{PEC}_{\text{Excit}}$ as a function of T_e at $5 \times 10^{18} \text{m}^{-3}$.

3.2.2 Sources of Atomic Rates

	G-CRM	A-CRM
References describing CRM	[33], [34], [51]	[52]
$A_{i \to j}$ source	[54]	[55]
$q^e_{i \to j}(T_e)$ source	[33], [34], [56]	[57]
$S^e_i(T_e)$ source	[33], [34], [56]	[56], [58]
$\alpha_i(T_e, n_e), \beta_i(T_e), \beta^d_i(T_e)$ source	See Ref. within [50]	[57], [59]
Includes effects of magnetic field	Yes	No

Table 3.2: References to the two CRMs and the rates they employ.

The efficacy of collisional radiative modeling is constrained by the accuracy of the atomic rates. Two different helium CRM codes which utilize different sources of atomic data were used in the analysis of the HeMSI measurements. The first code [33], [34], [51] has been dubbed the Goto code (in reference to *Goto 2003* [51]) in the literature and will be denoted as G-CRM. The second code [52] makes use of cross-sections and computational routines available from the *Atomic Data Analysis Structure* (ADAS) database and will be denoted as A-CRM. Table 3.2 summarizes the data sources implemented by these codes. G-CRM uses electron impact excitation and ionization cross-sections from *Ralchenko et al* [56] for states $n \leq 4$, uses scaling laws for $5 \leq n \leq 20$ [33], [34], and assumes that states $21 \leq n \leq 26$ are described by a Saha-Boltzmann equilibrium. A-CRM implements electron impact excitation cross-sections from *Ballance et al.* [57] but ionization cross-sections from *Ralchenko et al* [56]. For completeness, it is noted that G-CRM accounts for the mixing of singlet and triplet atomic states by a finite magnetic field and A-CRM does not account for a magnetic field. However, the effects of the magnetic field at TCV's 1.4 T field are negligible.

The predicted line ratios of excitation-driven emission for $\frac{3^1 S \to 2\ ^1 P}{3^1 D \to 2\ ^1 P}$, i.e., $\mathrm{Lrt}(\frac{728\mathrm{nm}}{668\mathrm{nm}})$, and $\frac{3^3 S \to 2\ ^3 P}{3^1 D \to 2\ ^1 P}$, i.e., $\mathrm{Lrt}(\frac{728\mathrm{nm}}{668\mathrm{nm}})$, by G-CRM at $B = 1.4\mathrm{T}$ and by A-CRM are shown in Figure 3.2. Direct comparisons of G-CRM at $B = 1.4\mathrm{T}$ to A-CRM and to G-CRM at $B = 0$ are shown in Figure 3.3. As will be discussed in Section 3.6, G-CRM was found to produced T_e and n_e measurements in good agreement with those of Thomson scattering, whereas A-CRM was found to systematically overestimate the temperature. The root of this overestimation by A-CRM is that A-CRM predicts $\mathrm{Lrt}(\frac{728\mathrm{nm}}{706\mathrm{nm}})$'s that are $\sim 15\%$ smaller for a given T_e than what is observed and predicted by G-CRM. Due to this disparity in performance, only HeMSI measurements produced with G-CRM are presented in Section 3.6 and are the focus of this work. Both codes are noted here as both are still employed frequently in plasma research. For works employing and related to G-CRM, see [33], [34], [36]–[39], [42], [45], [50], [51], [60]–[80] and for those employing, and related to A-CRM, see [29], [30], [52], [57], [81]–[86].
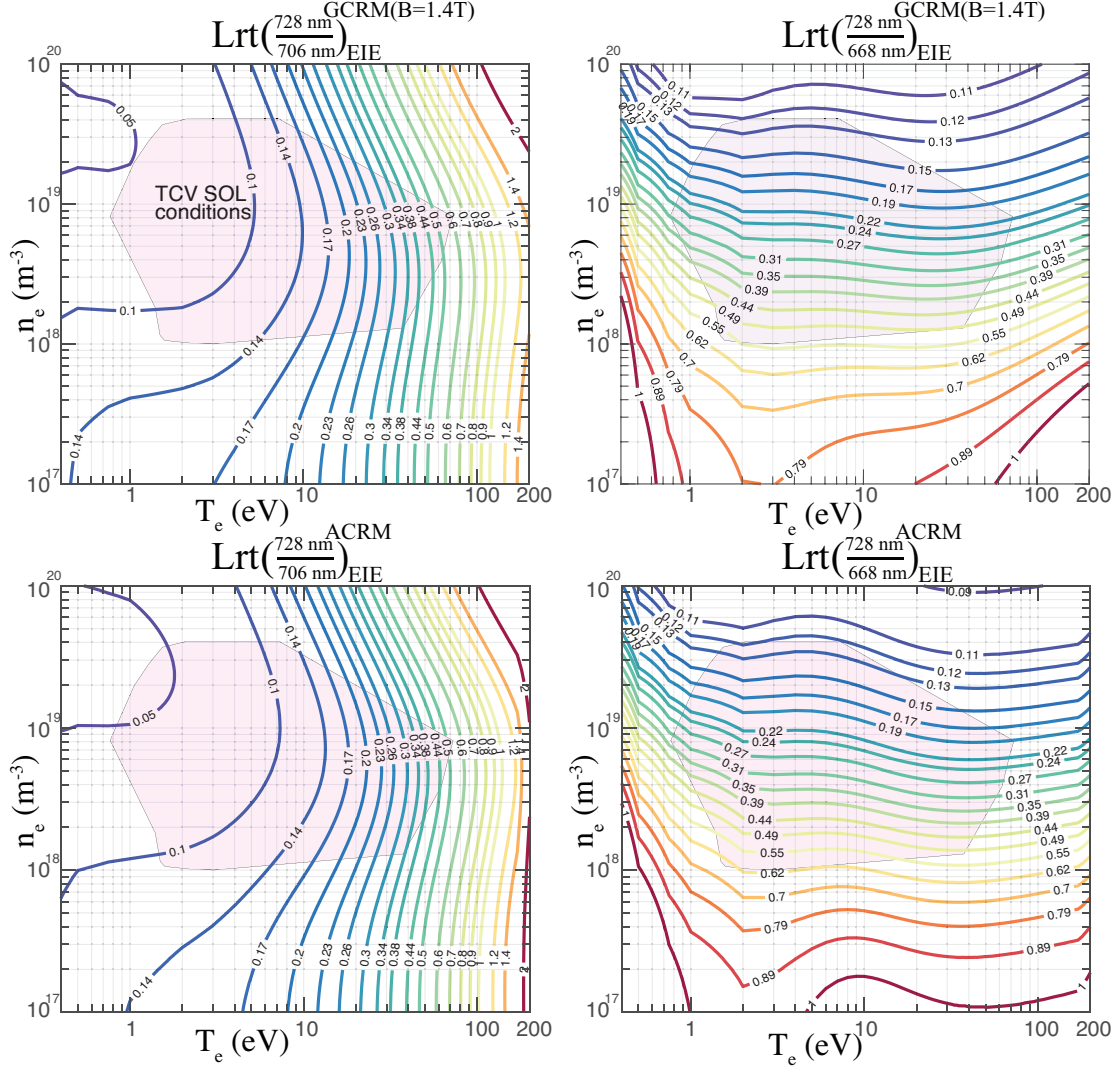
Figure 3.2: Contour plots of $\mathrm{Lrt}(\frac{728\text{nm}}{706\text{nm}})$ and $\mathrm{Lrt}(\frac{728\text{nm}}{668\text{nm}})$ for EIE driven emission for G-CRM at $B = 1.4$T and A-CRM.

3.3 A Qualitative Description of the Multi-spectral Images and Emissivities

In order to better contextualize the HeMSI measurements, a montage of He I, He II (468 nm), and C III (465 nm) images (all simultaneously imaged with MANTIS) and their inversions over the course of a density ramp are shown in Figure 3.4. The C III line is displayed because it is a low-temperature indicator. It sharply transitions from emitting to non-emitting for TCV densities, $n_e \approx 1 \times 10^{19}$, at $T_e \sim 8\,\text{eV}$ [14], [87]. In Section 3.6, it will be shown that HeMSI produces accurate measurements for ionizing plasma conditions. The C III line can be used to validate this criterion when HeMSI is applied independent of Thomson scattering in the future. Note that the plasma equilibrium in Figure 3.4 differs from that used in the validation experiments (See Figure 3.5), and was chosen for this
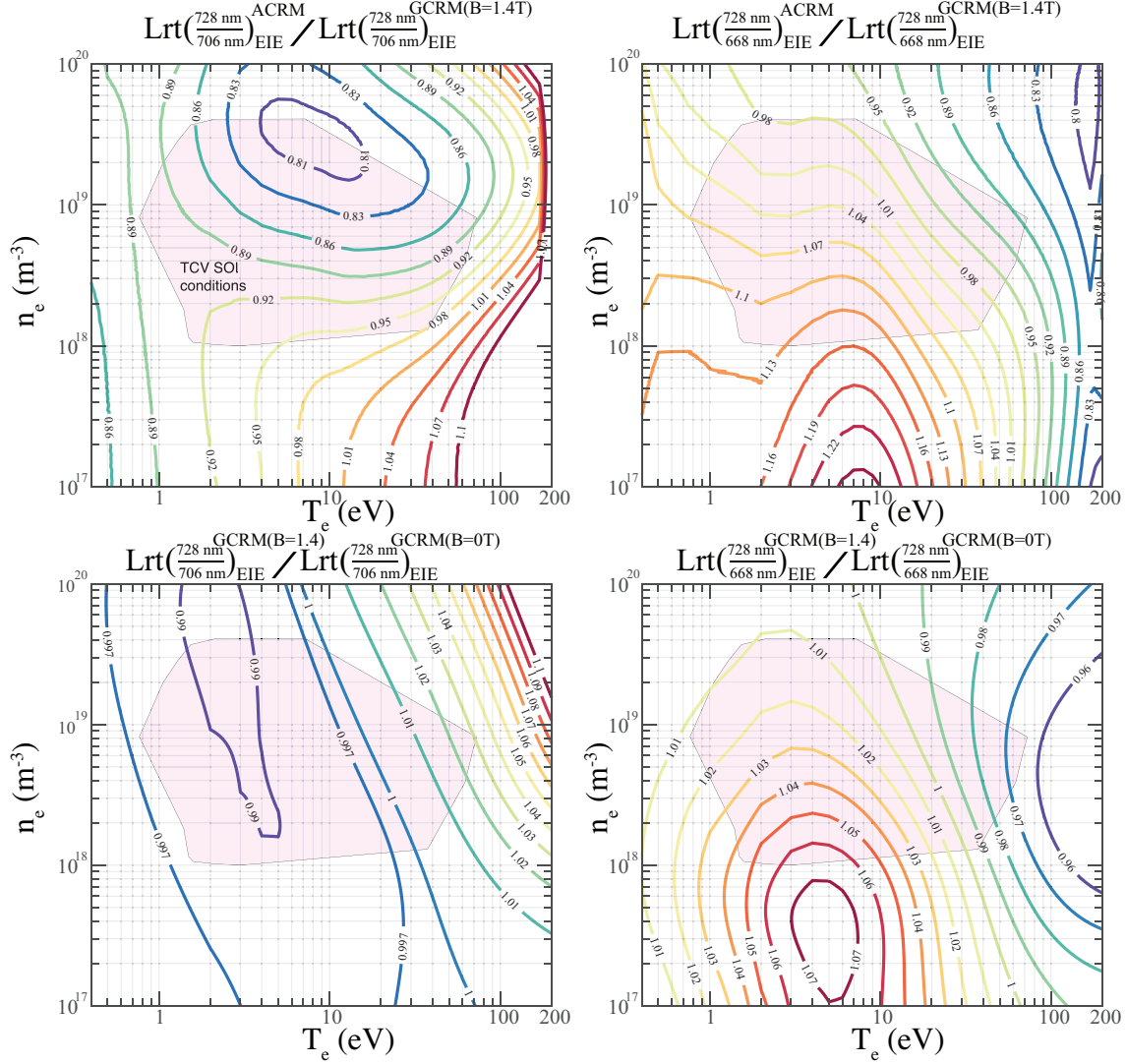
Figure 3.3: Ratio of predicted line-ratios from G-CRM at $B = 1.4$ to A-CRM and G-CRM at $B = 0$.

qualitative description because it shows a larger portion of the plasma boundary.

During the start of the density ramp in Figure 3.4, $0.7s < t < 1.1s$, all lines emit along the whole length of the divertor leg with emission concentrated along the separatrix and common flux region. As the density is increased, the helium emission in the common flux region progressively diminishes downstream. This change coincides with the retraction of the C III and He II emission fronts from the outer target towards the X-point, implying T_e is falling downstream. While the emission of the He I lines in the common flux region recedes with falling T_e, He I begins to emit within the private flux region. From $t > 1.3$ s, a new He II emission front emerges from the target moving towards the X-point, while the emergent He I emission front in the private flux region travels cross-field towards the separatrix. The disappearance and reemergence of emission fronts suggest that different atomic processes are producing each front.

As will be shown in Section 3.6, HeMSI gives good agreement with Thomson scattering measurements for the He I emission produced during $0.7s < t < 1.1s$ when the plasma can still be described as ionizing. However, when $T_e < 10$eV in deuterium plasmas, as it is for $t > 1.3$, the helium CRM's predictions of the 728nm to 706nm line-ratio diverge from the observed line ratios. In Section 3.6, it is shown that this emission at low T_e cannot be explained by EIE or EIR indicating the existence of competing processes outside the CRM. Note that non-ionizing majority helium plasmas were not observed as the helium plasmas would disrupt before a sufficiently low T_e could be reached. If a scenario with significant EIR were reached, the 468 nm He II line would have been used to constrain the amount of He I emission driven by EIR.
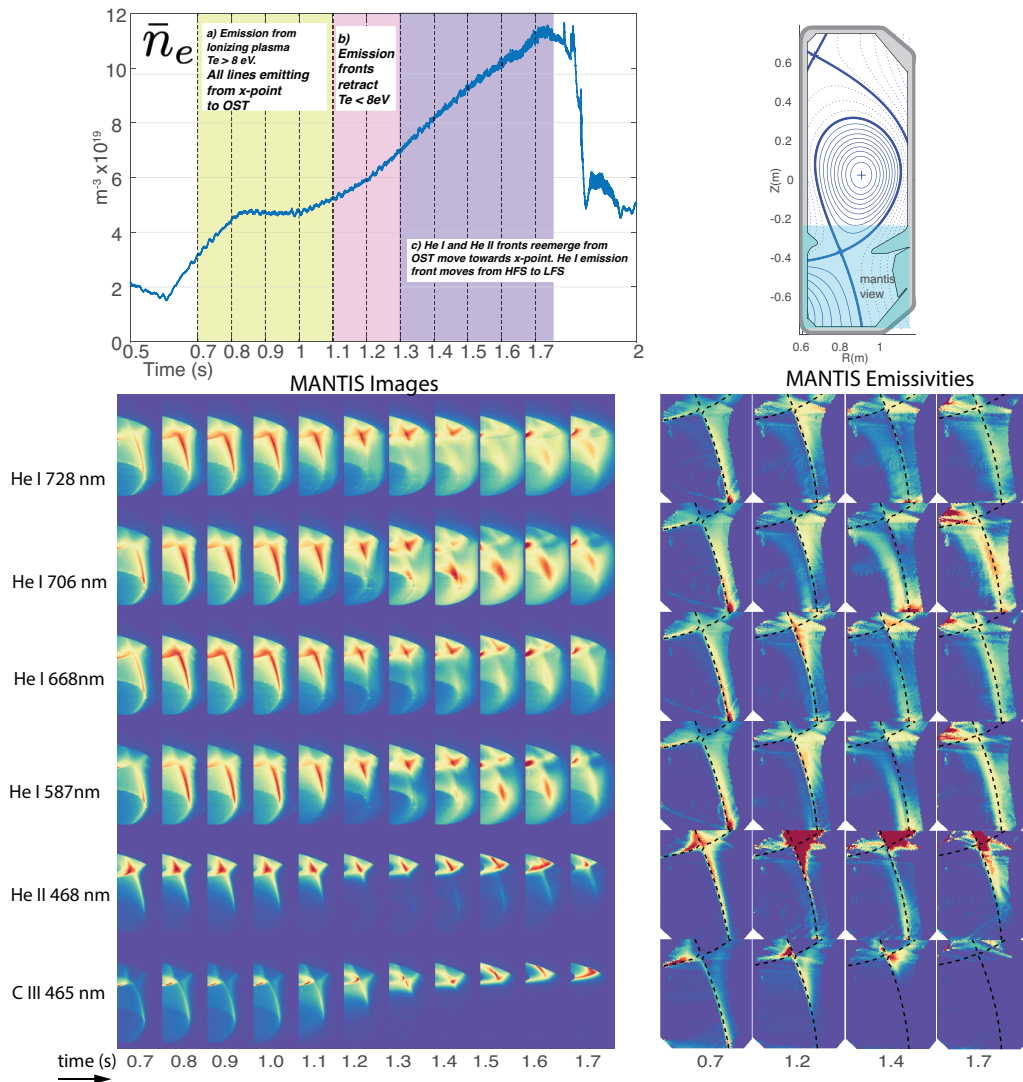
Figure 3.4: Montage of He I, He II, and C III images and emissivities during a density ramp of deuterium plasma. See Section 3.3.

3.4 Experimental Setup

A series of L-mode plasmas with the same single-null magnetic geometry (see Table 3.3) was performed to compare HeMSI measurements to divertor Thomson scattering measurements. See [88] for information on the divertor Thomson scattering system. In order to maximize the spatial cross-coverage of both diagnostics, the plasma geometry was shaped such that the outer divertor leg of the separatrix was nearly parallel to the Thomson scattering laser's path. During a discharge, the plasma was brought to a specified value of line-averaged density. While maintaining this specified density, the position of the outer target was moved between discreet points about the Thomson scattering laser's path. This sweep produced 2D profiles of Thomson scattering T_e and n_e measurements. The 2D HeMSI measurements were acquired during the entire shot. The cameras operated at 200 Hz with exposure times dynamically adjusting between 0.2 ms to 5.0 ms to prevent saturation. Divertor spectrometers which viewed the divertor leg were utilized for the purpose of cross-checking the MANTIS measurements [89]. The emissivity profiles measured by MANTIS were found to accurately predict the brightness observations of the divertor spectrometers. Furthermore, the divertor spectrometers confirmed that there was negligible spectral contamination within the MANTIS filters' spectral bands. A poloidal cross-section displaying the magnetic equilibrium and diagnostic coverage is shown in Figure 3.5.

Discharges were conducted for majority deuterium and majority helium plasmas. In deuterium plasmas at TCV, there is sufficient He emission for HeMSI due to the use of a helium glow between shots to clean the vessel. Nevertheless, for the validation experiments, additional helium was seeded during the ramp to the target density to increase the signal strength. Observing plasmas of both species was important for investigating the importance of different atomic mechanisms. Several works have reported photon-excitation, which is not accounted for in this work, as a factor in observed discrepancies between measurements and He CRMs' predictions [29], [36], [64], [67]–[69], [71], [90]. A majority helium plasma should exacerbate this effect if it is significant in the TCV divertor. It was found that HeMSI gave similar results for ionizing deuterium and helium plasmas supporting the decision to neglect photon-excitation.

Benchmarking discharges were performed for both toroidal field directions. The two field-directions engender distinct n_e and T_e profile shapes about the separatrix [91], [92]. Observing plasmas in both field-directions tested whether HeMSI could resolve the changes in profiles. In this work, *'forward field'* refers to a discharge in which B_t is directed clockwise when looking from above (∇-B drift favorable to H-mode), and *'reverse field'* refers to a discharge in which B_t is directed counter-clockwise (∇-B drift unfavorable to H-mode).

During the experimental campaign, divertor baffles were installed and removed periodically [12], [93], [94]. The change to the vessel's poloidal cross-section due to the 'long' low-field-side baffles is shown in Figure 3.5. The presence of baffles increased the neutral compression within the divertor [12], [93], [94]. A gas injection system was also installed into the low-field-side baffle, and used to produce a localized gas puff of helium into deuterium plasmas. Localized gas puffs allowed the application of the HeMSI technique under conditions in which the need for an inversion was removed. The results from this

methodology are reviewed in Section 3.6.4. As expected, the puff and inversion methodologies produced similar agreement with Thomson scattering. A difference in the results of the two methodologies would have implied an error in the application of HeMSI. Thus, the results from both methodologies are shown to demonstrate that the two applications are consistent with each other.
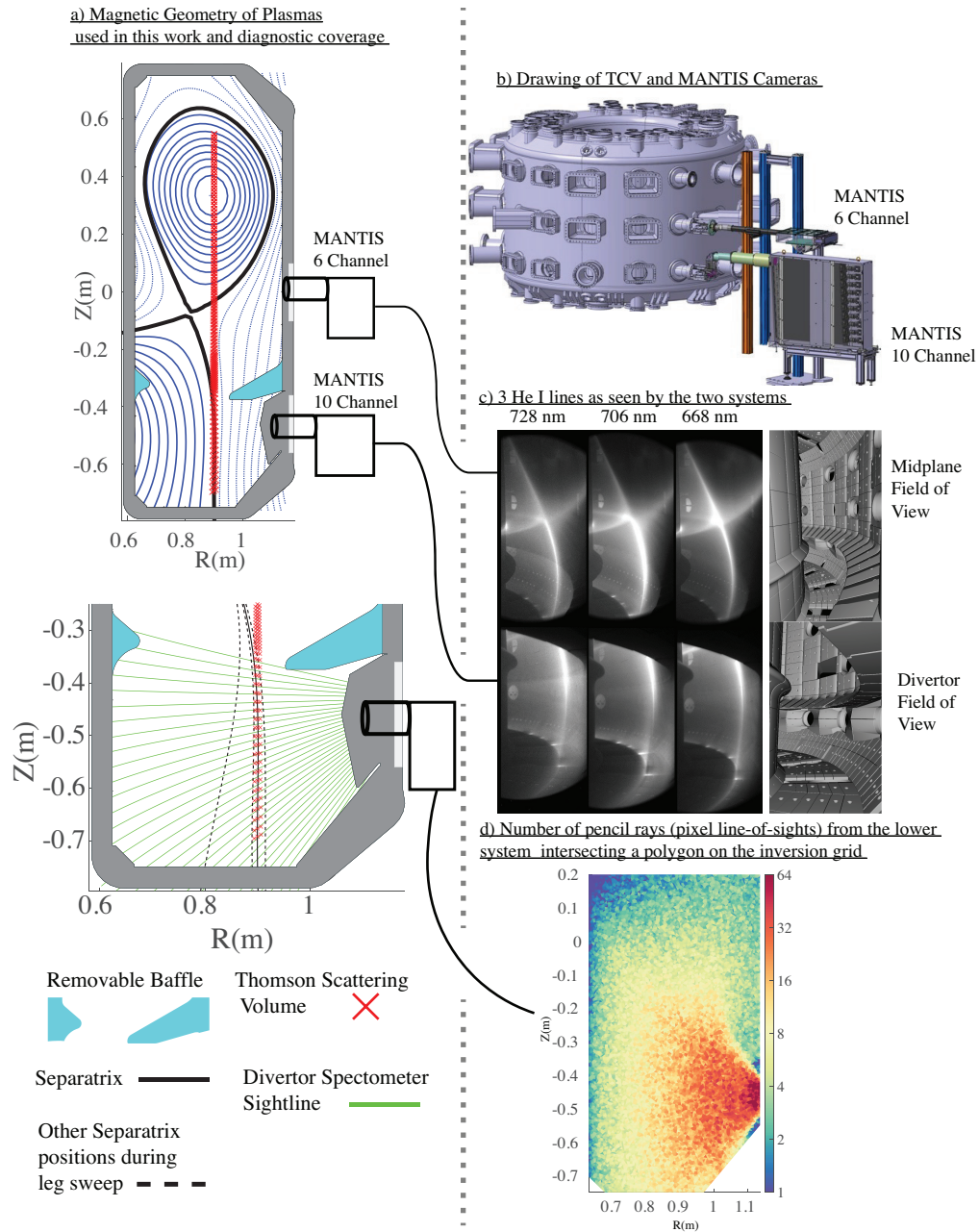
Figure 3.5: a) Display of the poloidal cross-sections of the magnetic configuration used in the experiments and the TCV vessel. The top plot displays the whole vessel cross-section, while a magnification of the divertor region is shown below it. The dotted black lines in the magnified divertor drawing indicate the different positions through which the outer divertor leg was swept. The modification of the vessel's profile due to the baffle is shown in blue. Also indicated on the cross-section are the poloidal locations of the MANTIS cameras, Thomson scattering volumes, and spectrometer lines of sight. b) Drawing of TCV and the MANTIS cameras. c) Example images, which have been normalized, from three helium lines taken during the experiments, and a synthetic view produced from the calcam software [25]. d) Number of pixels whose line of sight intersects a given triangle of the inversion grid.

51

3.5 Comparison Methodology

To facilitate the comparison between the T_e and n_e measurements from HeMSI and Thomson scattering, all measurements were parsed into a discrete (ρ, Z) bin with ρ defined as:

$$\rho(\psi) = \sqrt{1 - \frac{\psi}{\psi_o}} \tag{3.13}$$

ψ denotes the poloidal magnetic flux such that $\psi = 0$ at the separatrix and ψ_o is the flux at the magnetic axis. Both sets of measurements were spatially and temporally averaged within these (ρ, Z) bins. Each co-temporal set of HeMSI images generates a set of T_e and n_e measurements spanning the whole (ρ, Z) space of interest. However, successive Thomson scattering measurements were required to discern T_e and n_e profiles for comparison with the inherently 2-D HeMSI results. Therefore, only the time-averaged Thomson scattering and HeMSI measurements were compared. The data were averaged over time intervals in which $\bar{n}_e$ was held constant. The temporal variations within the HeMSI measurements were driven primarily by sawtooth oscillations in the core plasma. This variation was negligible compared to the spatial gradients of T_e and n_e. The binned profiles were used to compare the two measurements. In order to present these comparisons, the HeMSI and Thomson scattering measurements are presented together in 1-D plots versus a ρ axis. In these plots, the error bars assigned to the HeMSI measurements correspond to the average absolute deviation within each (ρ, Z) bin such that the width of the error bar is 2 standard deviations of the average value.

Examples of HeMSI profiles compared to Thomson profiles are shown in the bottom two panels of Figure 3.6. The steps of averaging the data for the comparison are illustrated in Figure 3.7. The top two plots in Figure 3.6 display the time-averaged 2D HeMSI measurements. In Section 3.6, the results from other discharges will be presented in the same format as Figure 3.6.

Figure 3.6: Discharge #1. Reverse field helium plasma with $\bar{n}_e = 8 \times 10^{19}\,\mathrm{m}^{-3}$ and an unbaffled divertor. HeMSI evaluations are shown with and without inclusion of 587 nm line.

1   Measurements between -0.5 m < z < -0.4 m
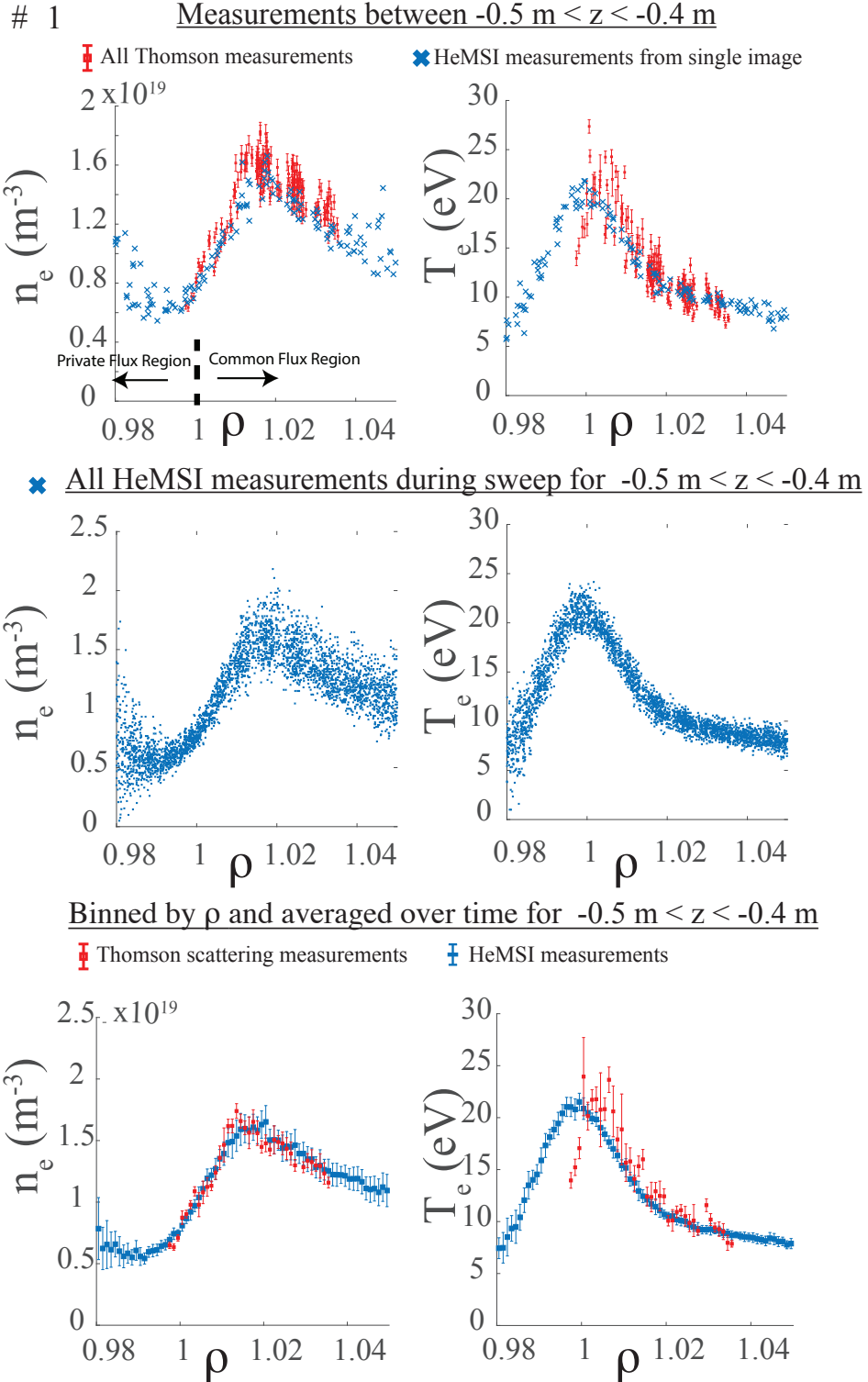
Figure 3.7: Depiction of data shown in Figure 3.6 before and after averaging. The top row displays HeMSI measurements from a single image between $-0.5 \leq z \leq -0.4$ in blue. The Thomson scattering measurements acquired during the entire leg sweep in this spatial range are shown in red. The second row shows each HeMSI measurement within $-0.5 \leq z \leq -0.4$ that was collected during the leg sweep. The last row shows both measurements binned onto a single ρ axis with bin sizes of $\delta\rho = .001$. The error bars were estimated from the standard-deviation within each bin.

3.6   Results and Discussion

The principal conclusions of this work are as follows. First, when employing G-CRM, HeMSI demonstrated consistently good agreement with Thomson scattering at the separatrix and in the common flux region, but intermittent agreement in the private flux region for:

- majority helium plasmas

  - $5 \text{ eV} \leq T_e \leq 60 \text{ eV}$
  - $2 \times 10^{18} \text{ m}^{-3} \leq n_e \leq 3 \times 10^{19} \text{ m}^{-3}$

- majority deuterium plasmas

  - $10 \text{ eV} \leq T_e \leq 40 \text{ eV}$
  - $2 \times 10^{18} \text{ m}^{-3} \leq n_e \leq 3 \times 10^{19} \text{ m}^{-3}$

For deuterium plasmas with $T_e < 10$ eV, HeMSI overestimated T_e with respect to Thomson scattering. This overestimation was due to the measurements of $\text{Lrt}(\frac{728\text{nm}}{706\text{nm}})$ which were 2 to 3 times larger than would be expected for $T_e < 10$ eV. However, in this colder regime, the HeMSI measurements of n_e remained in good agreement with those of Thomson scattering. Disagreements in the private flux region were characterized primarily by an overestimation of n_e by HeMSI. This overestimation was driven by measurements of $\text{Lrt}(\frac{728\text{nm}}{668\text{nm}})$ being 2 to 3 times lower than expected.

   To elaborate on these results, HeMSI and Thomson scattering measurements from six individual discharges are presented (see Table 3.3). The discussion of these discharges follows in Sections 3.6.1 - 3.6.1 with each emphasizing a salient feature of the HeMSI measurements. After presenting these individual discharges, the HeMSI measurements will be shown in aggregate as functions of T_e and n_e Thomson scattering measurements. This method reveals how the accuracy of HeMSI changes with local plasma conditions. Lastly, the HeMSI measurements from a localized gas puff into a majority deuterium plasma are demonstrated to be consistent with the measurements produced by inverting entire images.

3.6.1   Individual HeMSI Poloidal Maps Compared to Thomson Scattering

Two types of figures will be referenced in the following discussion of individual discharges. The first, which was described in Section 3.5, directly compares 2D profiles of T_e and n_e from HeMSI and Thomson scattering. The second compares observed line ratio profiles $\text{Lrt}(\frac{728\text{nm}}{706\text{nm}})$ and $\text{Lrt}(\frac{728\text{nm}}{668\text{nm}})$ against synthetic profiles constructed by forward modeling the Thomson scattering measurements with G-CRM. This comparison is shown for $-0.5 \text{ m} \leq z \leq -0.4 \text{ m}$ for five discharges in Figure 3.15.

Ref #	Fuel	$\bar{n}_e(10^{19}\text{m}^{-3})$	w 587nm	B_T direction	Divertor Type	Figure
#1	helium	8	yes	*rf*	unbaffled	3.6
#2	deuterium	2	no	*rf*	unbaffled	3.8
#3	helium	2.5 (with X2 heating)	yes	*rf*	unbaffled	3.9 - 3.11
#4	helium	7	no	*ff*	unbaffled	3.12
#5	deuterium	3	yes	*rf*	baffled	3.13
#6	deuterium	6.5	no	*rf*	baffled	3.14

Table 3.3: Description of the discharges that are individually presented in this paper. *rf* denotes that B_T is in the reverse field direction (unfavorable to H-mode access), and *ff* denotes that B_T is in the forward field direction (favorable to H-mode access). Note that these are different shots than those considered in Chapter 4.

HeMSI accurately reproduces Thomson scattering measurements for both deuterium and helium ionizing plasmas

Discharges #1 and #2 were majority helium and majority deuterium discharges, respectively. Although the species differed, both discharges were performed in the reverse field configuration, without baffles, and had similar T_e and n_e profiles. In Figures 3.6 and 3.8, the HeMSI measurements from both discharges are seen to be in excellent agreement with the Thomson scattering measurements. In discharge #2, Thomson scattering and HeMSI agree in both the common and private flux regions over the ranges of $10\text{ eV} \leq T_e \leq 40\text{ eV}$ and $2 \times 10^{18}\text{ m}^{-3} \leq n_e \leq 5 \times 10^{18}\text{ m}^{-3}$. Similar agreement is also observed in #1 over the ranges of $10\text{ eV} \leq T_e \leq 20\text{ eV}$ and $1 \times 10^{19}\text{ m}^{-3} \leq n_e \leq 1.5 \times 10^{19}\text{ m}^{-3}$. However, in #1, the Thomson scattering measurements were only collected in the common flux region.

Figure 3.15's first two rows contain the measured and synthetic $\text{Lrt}(\frac{728\text{nm}}{706\text{nm}})$ and $\text{Lrt}(\frac{728\text{nm}}{668\text{nm}})$ profiles from discharges #1 and #2. As would be expected from the similar T_e and n_e measurements, the two sets of observed ratios are similar to each other across the two discharges and both sets are in agreement with their synthetic counterparts. This gives confidence that the CRM correctly describes helium emission in the boundary of an ionizing plasma.
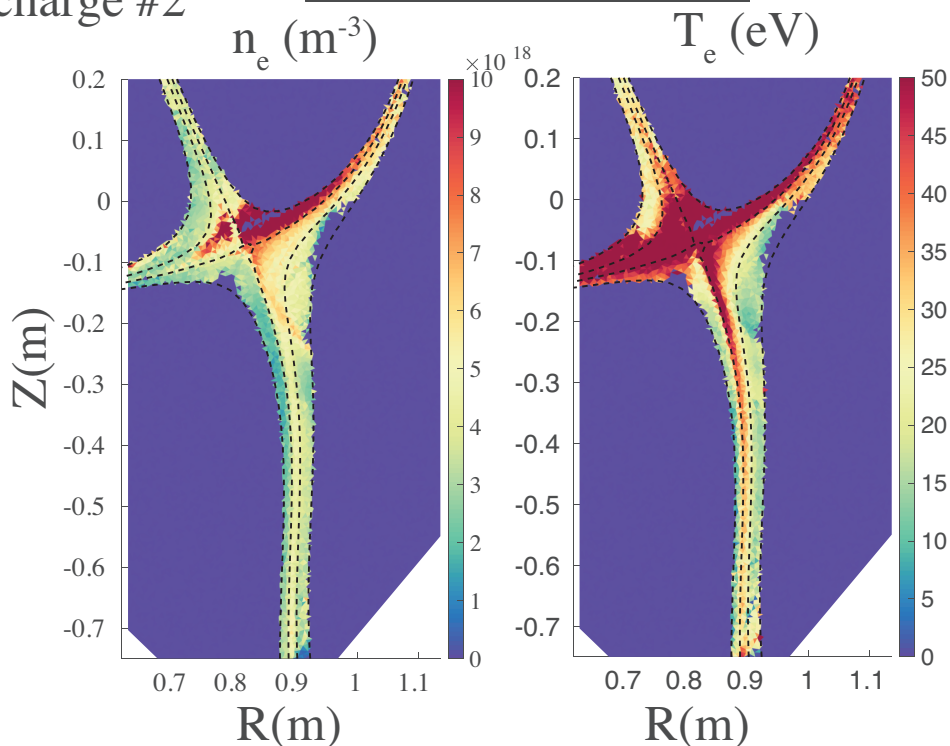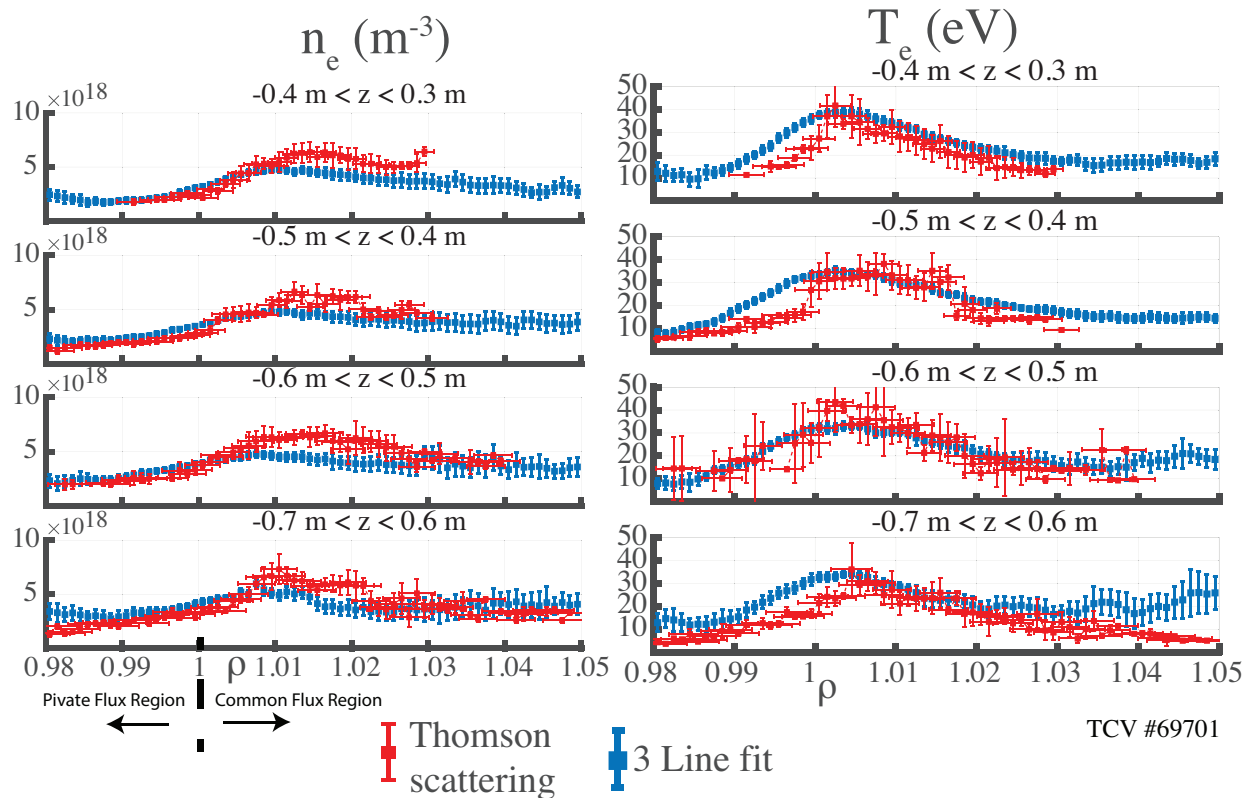
Figure 3.8: Discharge #2. Reverse field deuterium plasma with $\bar{n}_e = 2 \times 10^{19}\mathrm{m}^{-3}$ and an unbaffled divertor. HeMSI evaluations did not include the 587 nm line.

HeMSI's sensitivity to T_e

The sensitivity of HeMSI to changes in T_e will be highlighted here. During discharge #3, X2 electron cyclotron heating (ECH) was applied to the plasma at three different levels of input power, 1800 kW, 1200kW, and 600 kW. Accounting for the Ohmic heating, the resultant total heating powers were 1890 kW, 1290kW, and 820 kW, respectively. This is the only discharge discussed here that utilized auxiliary heating. For reference, the shots without auxiliary heating featured approximately 300 kW of Ohmic heating power. The HeMSI and Thomson measurements for the three levels of ECH input power are shown in Figures 3.9 (1800 kW), 3.10 (1200kW), and 3.11 (600kW).

The discreet modulation of the X2 input power gives a clear demonstration of HeMSI's T_e sensitivity because the HeMSI and Thomson scattering measurements move in unison with the changing heating power. For example, the peak temperature drops for both measurements from $\sim 60\text{eV}$ to $\sim 40\text{eV}$ when the X2 power is decreased from 1800 kW to 1200 kW. Furthermore, the T_e profile is much broader for the 1800 kW and 1200 kW levels of input power than it is for the 600 kW level and the other Ohmic discharges. The $-0.6 \leq z \leq -0.5$ region in Figure 3.10 (1200kW) clearly illustrates this broadening. In all, the HeMSI measurements accurately resolve the T_e profiles about the separatrix for ionizing plasmas.
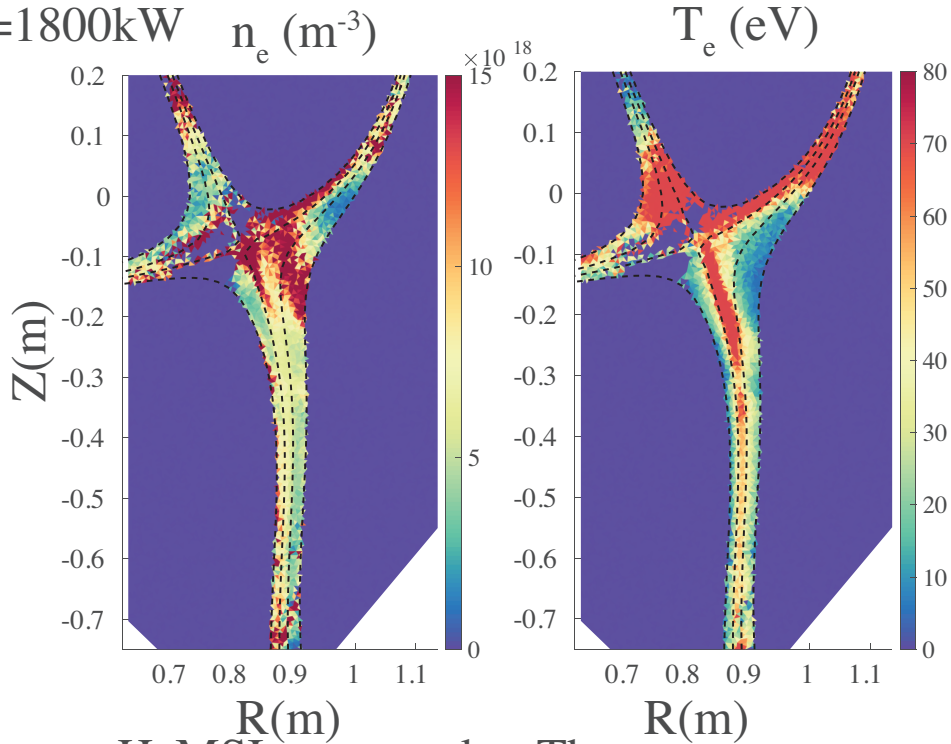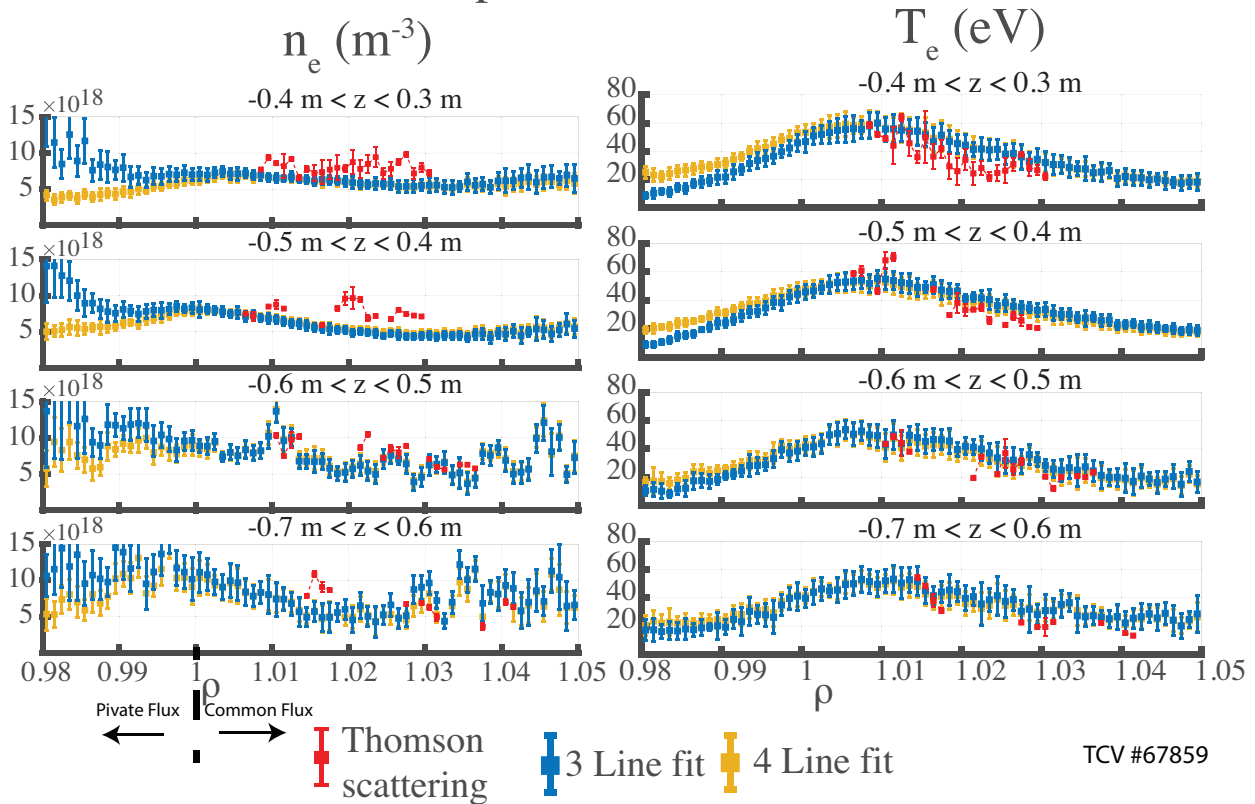
Figure 3.9: Discharge #3. Reverse field helium plasma with $\bar{n}_e = 2.5 \times 10^{19} \text{m}^{-3}$ with 1800 kW of X2. HeMSI evaluations are shown with and without inclusion of 587 nm line.
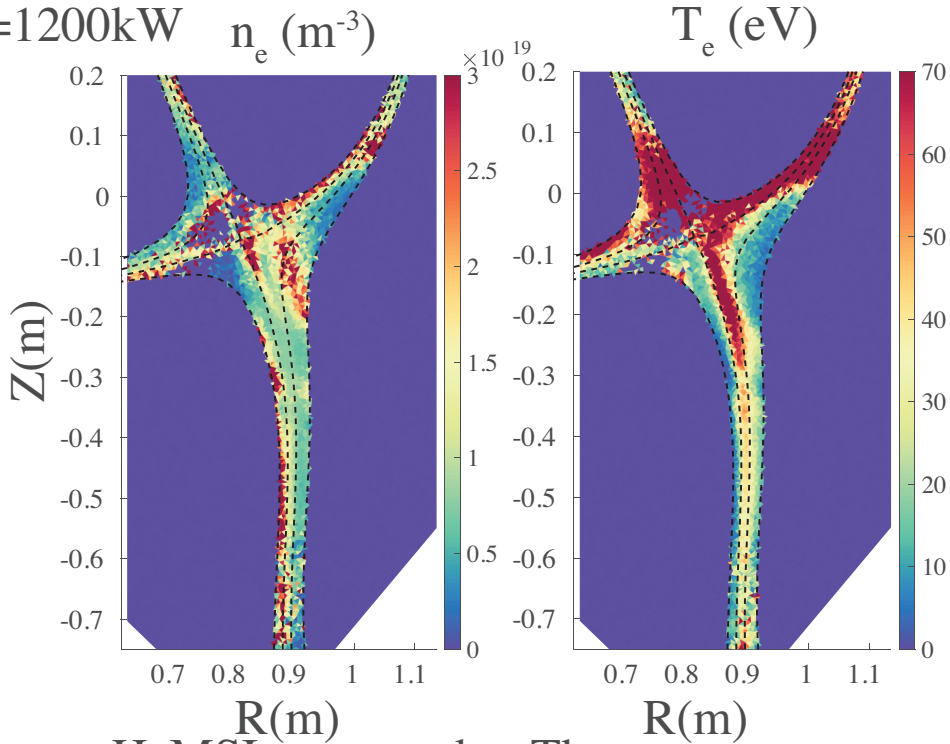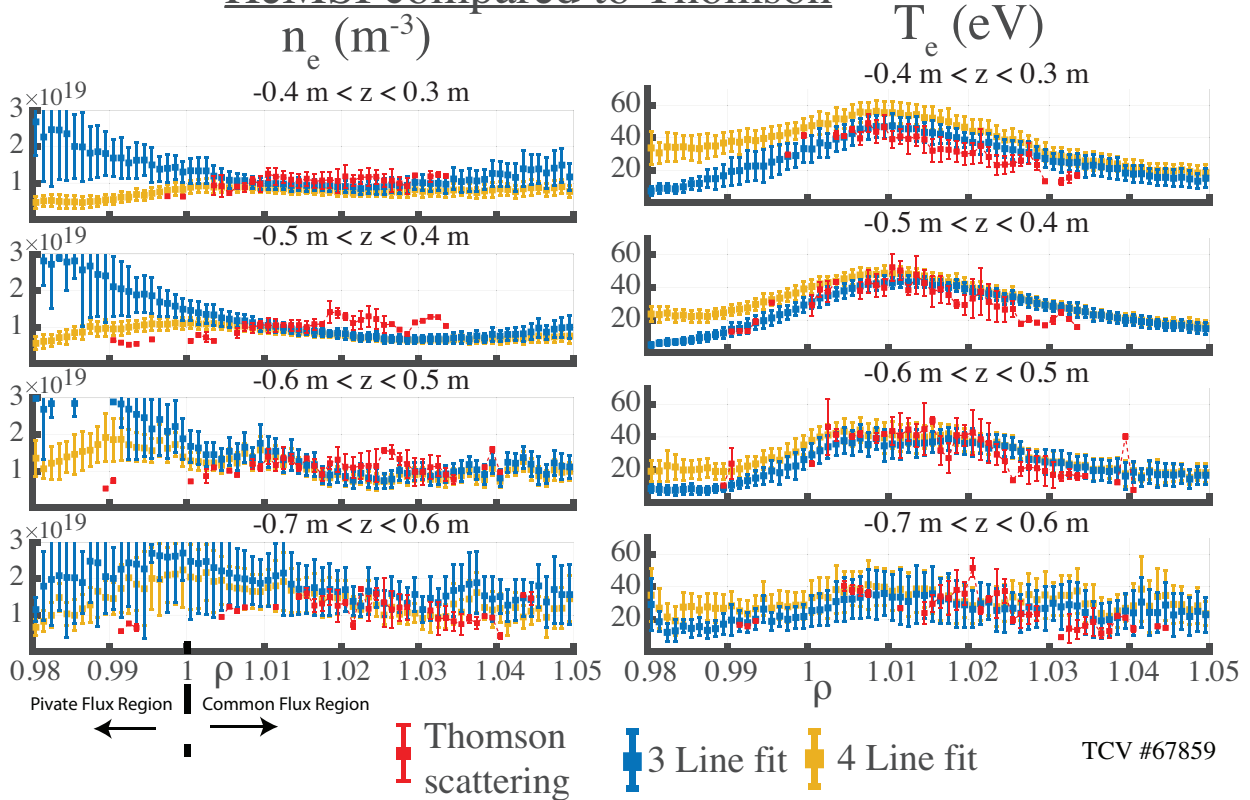
Figure 3.10: Discharge #3. Reverse field helium plasma with $\bar{n}_e = 2.5 \times 10^{19}\,\mathrm{m^{-3}}$ with 1200 kW of X2. HeMSI evaluations are shown with and without inclusion of 587 nm line.
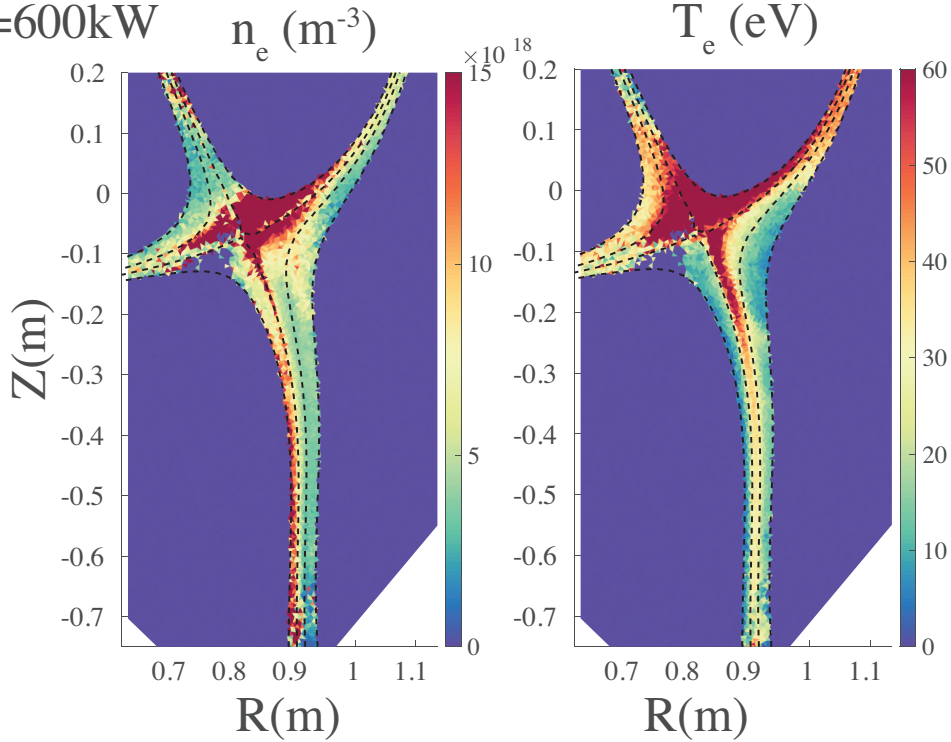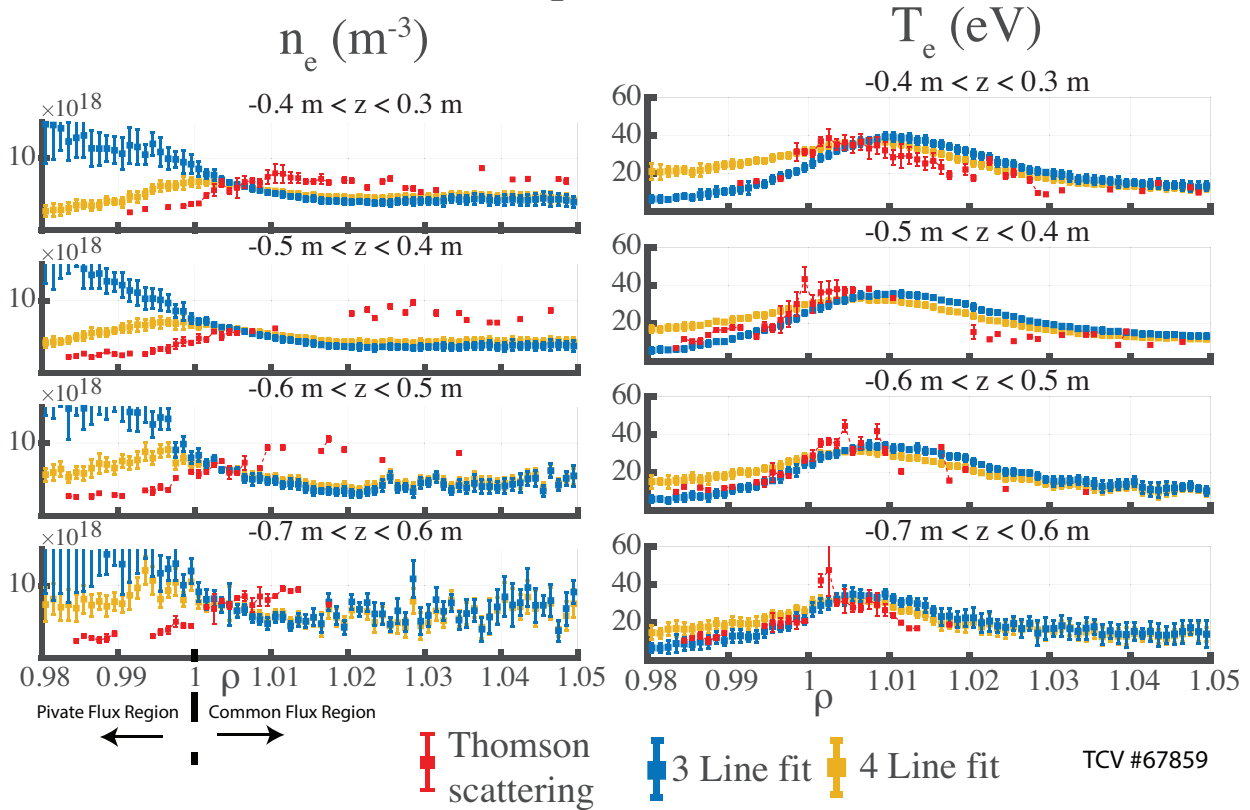
Figure 3.11: Discharge #3. Reverse field helium plasma with $\bar{n}_e = 2.5 \times 10^{19} \, \text{m}^{-3}$ with 600 kW of X2. HeMSI evaluations are shown with and without inclusion of 587 nm line.

HeMSI resolves the effects of changing the B_t direction on the T_e and n_e profiles

In the section above, HeMSI was shown to capture the changes in the T_e profile caused by application of X2 heating. In this subsection, HeMSI is shown to resolve changes to the n_e and T_e profiles resulting from different B_t directions. The reverse field direction of B_t produces a distinct n_e and T_e profile shape from the forward field direction for sufficiently low temperature [91], [92]. Forward field discharges have n_e profiles that peak at the separatrix, $\rho = 1.0$, and their T_e profiles fall off in a nearly linear manner going from the separatrix into the common flux region. For sufficiently low temperature, reverse field discharges have n_e peaks well into the common flux region at $\rho > 1.01$, and their T_e profiles are concave. The two Ohmic reverse field shots previously described, #1, and #2 (Figures 3.6, 3.8), exemplify these reverse field characteristics. Discharge #4 was performed in forward field. As shown in Figure 3.12, HeMSI resolves the translation of the n_e profile while remaining in excellent agreement with the Thomson scattering measurements in the common flux region. The change in the T_e profile is also resolved by HeMSI, and HeMSI matches the T_e measurement from Thomson scattering in the private and common flux regions.

Comparing the $\mathrm{Lrt}(\frac{728\mathrm{nm}}{706\mathrm{nm}})$ and $\mathrm{Lrt}(\frac{728\mathrm{nm}}{668\mathrm{nm}})$ profiles for both field directions in Figure 3.15 reveals stark differences. In the forward field case (row 3 and discharge #4), $\mathrm{Lrt}(\frac{728\mathrm{nm}}{668\mathrm{nm}})$ linearly increases from the separatrix into the common flux region while $\mathrm{Lrt}(\frac{728\mathrm{nm}}{706\mathrm{nm}})$ decreases linearly in the common flux region. In the reverse field cases (all other rows), $\mathrm{Lrt}(\frac{728\mathrm{nm}}{668\mathrm{nm}})$ has a local minimum in the common flux and a concave $\mathrm{Lrt}(\frac{728\mathrm{nm}}{706\mathrm{nm}})$ profile going from the separatrix into the common flux region. These subtle but resolved changes in the emission profiles and in the T_e and n_e profiles establish confidence in the inversion methodology and spatial resolution of HeMSI.
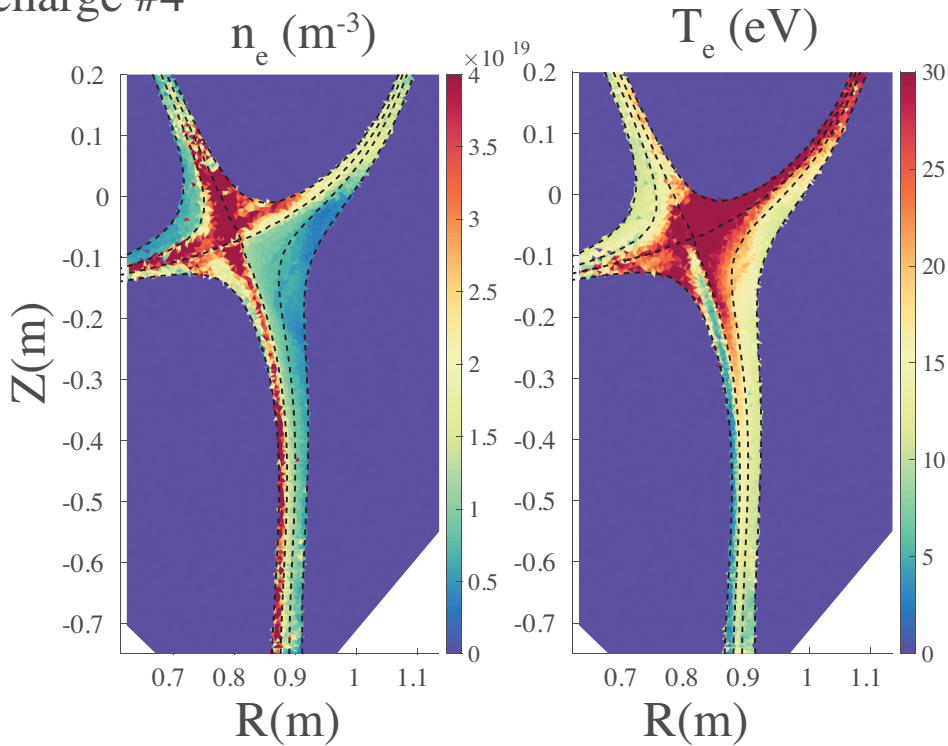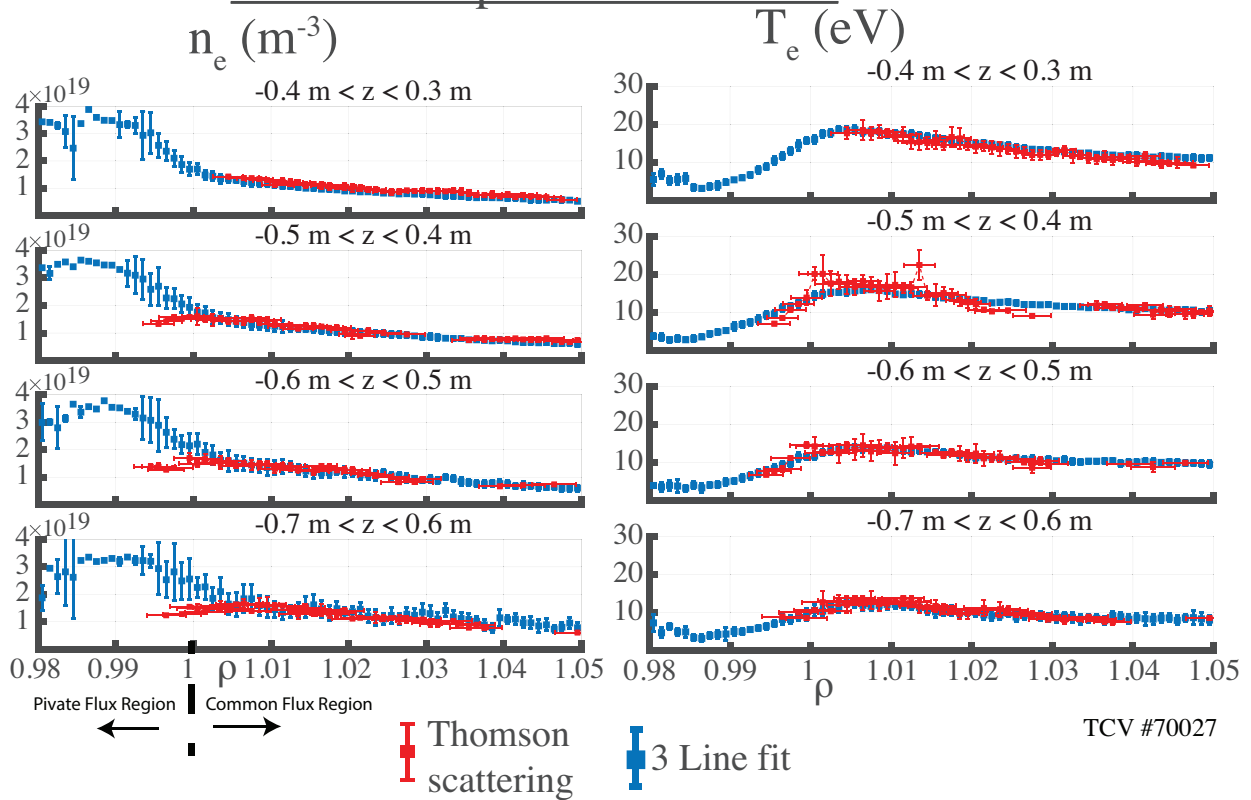
Figure 3.12: Discharge #4. Forward field helium plasma with $\bar{n}_e = 7 \times 10^{19}\,\mathrm{m}^{-3}$ and an unbaffled divertor. HeMSI evaluations do not include 587 nm line.

HeMSI measurements with baffled divertor

The presence of a divertor baffle increases the neutral density within the divertor volume [93]. Nonetheless, HeMSI and Thomson scattering measurements compared similarly for baffled and unbaffled conditions. The measurements from discharge #5, a baffled discharge, are an example of this result. As depicted in Figure 3.13, HeMSI and Thomson scattering maintain good agreement in the common flux region and inconsistent agreement in the private flux region in this baffled discharge. This is consistent with the non-baffled results.
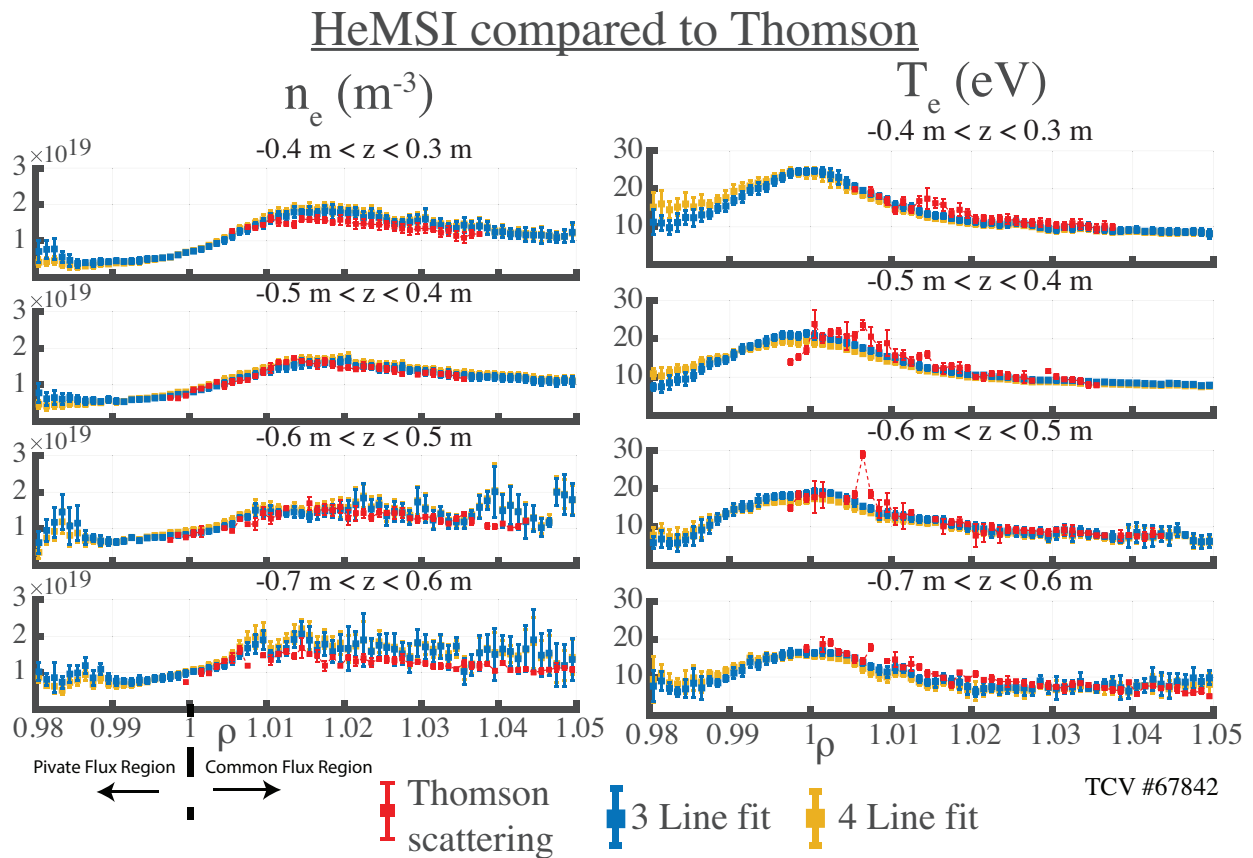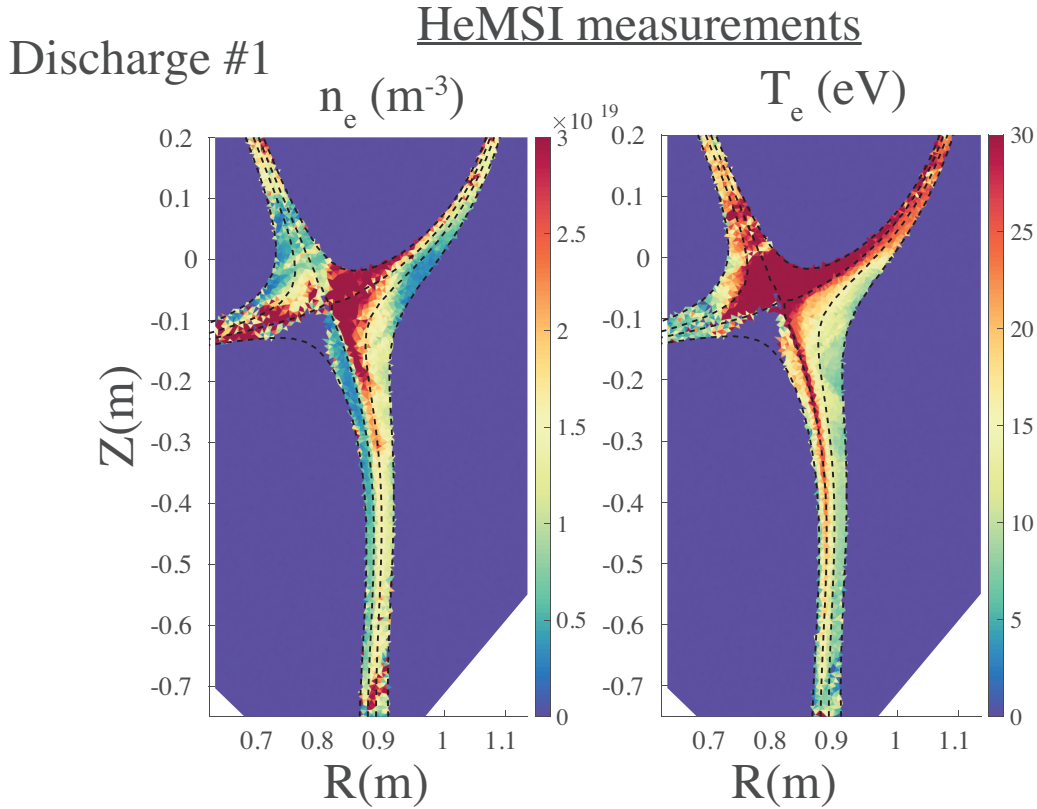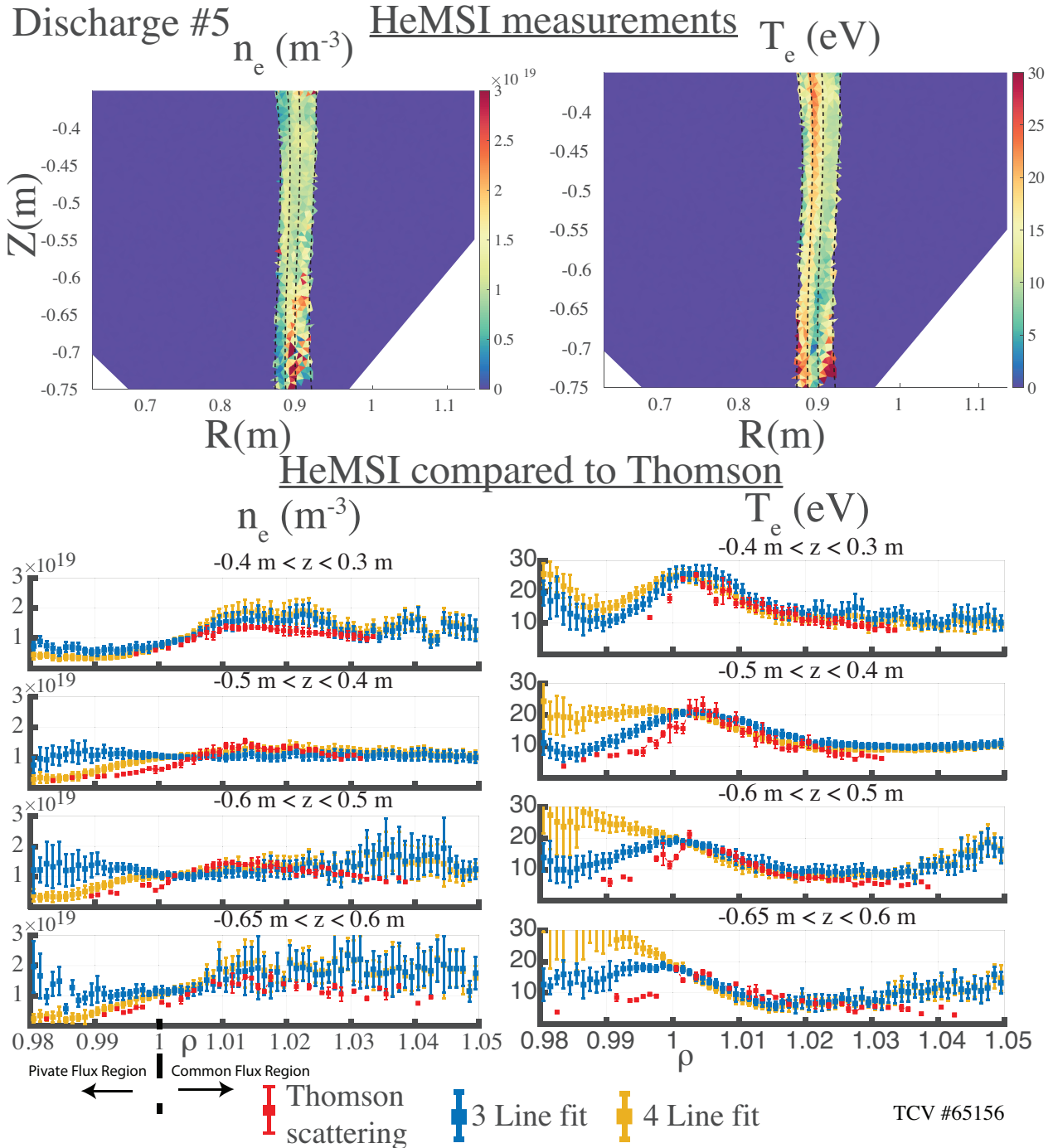
Figure 3.13: Discharge #5. Reverse field deuterium plasma with $\bar{n}_e = 3 \times 10^{19} \, \mathrm{m}^{-3}$ and a baffled divertor. HeMSI evaluations are shown with and without inclusion of 587 nm line.

Disagreement between n_e measurements in the private flux region

Inconsistent agreement was observed between HeMSI and Thomson scattering measurements of n_e in the private flux region. The disagreement was observed in all forward field shots but not all reverse field discharges. For example, discharges #4 (Figure 3.12) and #5 (Figure 3.13), forward field and reverse field, respectively, exhibited this disagreement. Like all forward field discharges, the disagreement was seen throughout the whole private flux region in discharge #4; in the reverse field case, #5 , the disagreement is present in the private flux for $z < -0.4$ m. On the other hand, discharge #2 (Figure 3.8) manifests good agreement throughout the private flux for both T_e and n_e measurements.

The line-ratio profiles of discharges #4 and #5 are shown in rows 3 and 4 of Figure 3.15, respectively. Therein, the measurements of $\mathrm{Lrt}(\frac{728nm}{668nm})$ are seen to be the source of the disagreement. For both discharges, the synthetic $\mathrm{Lrt}(\frac{728nm}{668nm})$ profiles increase as they cross the separatrix going into the private flux region. However, the observed $\mathrm{Lrt}(\frac{728nm}{668nm})$ profile in the forward field discharge is decreasing at this junction while that of the reverse field discharge is flat. Note that the synthetic and observed $\mathrm{Lrt}(\frac{728nm}{706nm})$ profiles in both discharges are in fair agreement. The intermittent agreement in the reverse field cases and no agreement in the forward field cases for the private flux region is not currently understood.

Deuterium plasmas for $T_e < 10\,\mathrm{eV}$

Discharge #6 demonstrates the disagreement observed between HeMSI and Thomson scattering for deuterium plasmas with $T_e < 10\,\mathrm{eV}$. As displayed in Figure 3.14, HeMSI greatly overestimates Thomson scattering's measurements of T_e in the region where $T_e < 10$, i.e, $z < -0.4$ m. However, $T_e \approx 10\,\mathrm{eV}$ for $-0.4\mathrm{m} < \mathrm{z} < -0.3\mathrm{m}$ and in this region, Thomson and HeMSI agree for both measurements. The ratio profiles within the region of disagreement for discharge #6 are shown in row 5 of Figure 3.15. These profiles reveal that in the $T_e < 10\,\mathrm{eV}$ regime the measurements of $\mathrm{Lrt}(\frac{728nm}{706nm})$ are three times larger than the synthetic ratio. The larger $\mathrm{Lrt}(\frac{728nm}{706nm})$ ratios cause the fitted T_e's to be much higher than the actual T_e. This behavior was observed in all deuterium plasmas with $T_e < 10$. Curiously, while the CRM fails to produce agreement with T_e for $T_e < 10\mathrm{eV}$, the n_e measurements compare favorably to those of Thomson scattering. This is because the fit of n_e is strongly dependent on $\mathrm{Lrt}(\frac{728nm}{668nm})$ and only weakly dependent on $\mathrm{Lrt}(\frac{728nm}{706nm})$ for $n_e > 1 \times 10^{19}\mathrm{m}^{-3}$. This discrepancy will further be discussed in the next section.
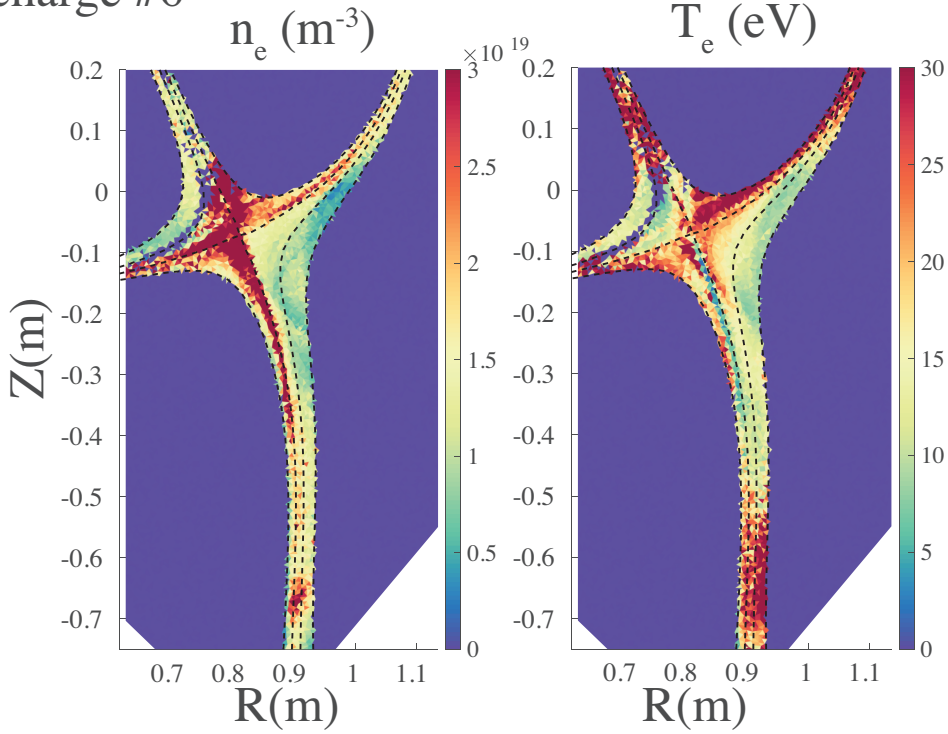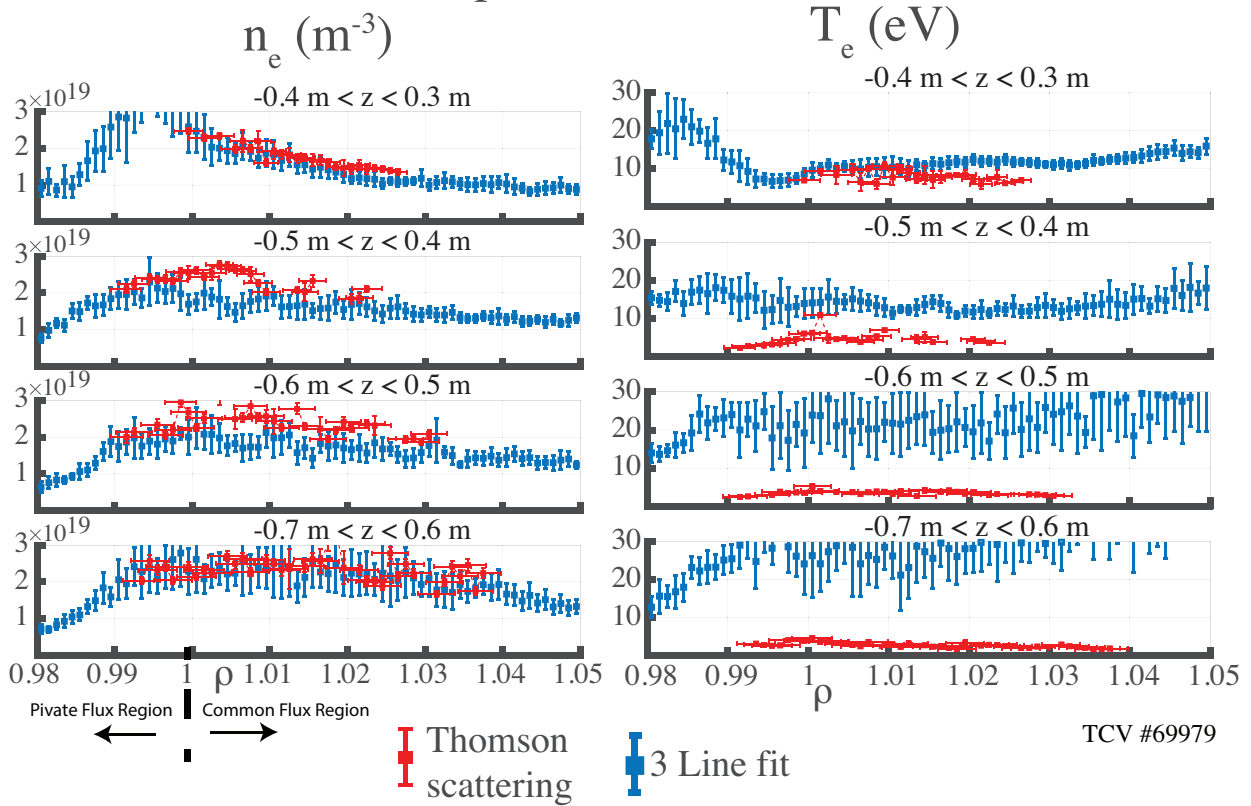
Figure 3.14: Discharge #6. Reverse field deuterium plasma with $\bar{n}_e = 6.5 \times 10^{19}\,\mathrm{m}^{-3}$ and an unbaffled divertor. HeMSI evaluations do not include 587 nm line.

3.6.2 Empirical Trends

In this section, the HeMSI measurements in the common flux region are presented in aggregate. For each discharge, the HeMSI and Thomson scattering measurements in the common flux region were binned then averaged on (ρ, z). For each averaged HeMSI measurement, a corresponding Thomson scattering measurement was produced by linearly interpolating on the averaged Thomson scattering profile. In this section, the line-ratio measurements and HeMSI T_e and n_e measurements are presented as a function of these interpolated T_e and n_e Thomson scattering values. Measurements in the private flux region are omitted because HeMSI has poor precision in this region. All figures discussed in this section are segmented into majority helium and majority deuterium cases.

Beginning this overview, Figure 3.16 presents the $\mathrm{Lrt}(\frac{728\mathrm{nm}}{706\mathrm{nm}})$ and $\mathrm{Lrt}(\frac{728\mathrm{nm}}{668\mathrm{nm}})$ measurements versus the Thomson scattering measured T_e and n_e. As expected, the measured $\mathrm{Lrt}(\frac{728\mathrm{nm}}{706\mathrm{nm}})$'s are primarily a function of T_e and the measured $\mathrm{Lrt}(\frac{728\mathrm{nm}}{668\mathrm{nm}})$'s are primarily a function of n_e. Note that the two ratios change smoothly over the parameter space.

Next, Figure 3.17 presents the average fractional differences between HeMSI and Thomson scattering T_e and n_e measurements. As seen in Figure 3.17, the HeMSI measurements of T_e are in strikingly good agreement with those of Thomson scattering for $T_e > 10\,\mathrm{eV}$. Moreover, for majority helium plasmas, this good agreement continues for $T_e < 10\,\mathrm{eV}$. The HeMSI measurements of n_e are in generally good agreement with Thomson scattering for $10\mathrm{eV} < T_e < 20\mathrm{eV}$ and $n_e < 1.75 \times 10^{19}\mathrm{m}^{-3}$. For $21\mathrm{eV} < T_e < 26\mathrm{eV}$, there is a 20% systematic difference in the n_e measurements between HeMSI and Thomson scattering for both helium and deuterium plasmas.

Similar to Figure 3.17, Figure 3.18 displays the average fractional difference between the measured $\mathrm{Lrt}(\frac{728\mathrm{nm}}{706\mathrm{nm}})$ and $\mathrm{Lrt}(\frac{728\mathrm{nm}}{668\mathrm{nm}})$ ratios and those synthetically produced via Thomson scattering. The disagreements in n_e from Figure 3.17 are seen in Figure 3.18 to correspond to observations of $\mathrm{Lrt}(\frac{728\mathrm{nm}}{668\mathrm{nm}})$ that are 20% smaller than what would be expected from G-CRM. The disagreement in $\mathrm{Lrt}(\frac{728\mathrm{nm}}{706\mathrm{nm}})$ measurements for deuterium plasmas with $T_e < 10\,\mathrm{eV}$ correspond to $\mathrm{Lrt}(\frac{728\mathrm{nm}}{706\mathrm{nm}})$ observations that are 2 to 3 times smaller than what are expected.

The discrepancies at $T_e < 10\,\mathrm{eV}$ are further explored in Figure 3.19 which displays 1D box plots of $\mathrm{Lrt}(\frac{728\mathrm{nm}}{706\mathrm{nm}})$ and $\mathrm{Lrt}(\frac{728\mathrm{nm}}{668\mathrm{nm}})$ measurements versus the parameter to which they are most sensitive. On top of these box plots, the $\mathrm{Lrt}(\frac{728\mathrm{nm}}{706\mathrm{nm}})$ and $\mathrm{Lrt}(\frac{728\mathrm{nm}}{668\mathrm{nm}})$ predictions by G-CRM are plotted for constant n_e's and T_e's, respectively. The solid lines show predictions of the ratios for emission that is completely EIE driven, while the dashed lines correspond to emission that is driven entirely by EIR. These box plots contain the same data that was shown in Figure 3.18, but allow for trends to be more easily inferred. In particular, they highlight the disagreement observed for deuterium plasmas with $T_e < 10\,\mathrm{eV}$.

Prior to viewing Figure 3.19, it could have been reasonably suspected that the disagreement for deuterium plasmas at $T_e < 10\,\mathrm{eV}$ is caused by the omission of EIR in the fitting. However, assuming only EIR and EIE contribute to the emission, any $\mathrm{Lrt}(\frac{728\mathrm{nm}}{706\mathrm{nm}})$ measurement must fall between what would be produced by fully EIE or fully EIR emission, i.e., between the solid and dashed lines in in Figure 3.19. However, in Figure 3.19, the observed $\mathrm{Lrt}(\frac{728\mathrm{nm}}{706\mathrm{nm}})$ is not only outside these bounds, but outside these bound on the side of the EIE bound, i.e., $\mathrm{Lrt}(\frac{728\mathrm{nm}}{706\mathrm{nm}})_{\mathrm{obs}} > \mathrm{Lrt}(\frac{728\mathrm{nm}}{706\mathrm{nm}})_{\mathrm{EIE}} > \mathrm{Lrt}(\frac{728\mathrm{nm}}{706\mathrm{nm}})_{\mathrm{EIR}}$. Thus, including EIR emission

would only make the discrepancy between HeMSI and Thomson scattering worse.

3.6.3 Further Discussion of Deuterium Plasmas with $T_e < 10\,\mathrm{eV}$

The results for deuterium plasmas with $T_e < 10\,\mathrm{eV}$ demonstrate that a physical process outside the current He CRM (Eq 3.1) is perturbing the atomic populations of helium. This is consistent with the results from other He-H plasma experiments [37], [64], [66], [76], [95], [96]. In these reports, it was concluded or conjectured that molecular assisted recombination (MAR) or molecular assisted dissociation (MAD) processes were significantly affecting the He emission. It was shown in [66], [95] that deuterium can completely quench He^+ EIR processes for $1\,\mathrm{eV} \lesssim T_e \lesssim 6\,\mathrm{eV}$. In [37] and [76], the addition of H_2 into a helium plasma was observed to perturb the ratios of singlet to triplet states, i.e., $\mathrm{Lrt}(\frac{728\mathrm{nm}}{706\mathrm{nm}})$ but not greatly perturb singlet-singlet or triplet-triplet ratios. These results are consistent with the measurements reported here. Extending the CRM to this regime is beyond the scope of this work. However, note the sharp increase in $\mathrm{Lrt}(\frac{728\mathrm{nm}}{706\mathrm{nm}})$ as T_e falls below $10\mathrm{eV}$ in Figure 3.19 demonstrating that $\mathrm{Lrt}(\frac{728\mathrm{nm}}{706\mathrm{nm}})$ remains sensitive to T_e for $T_e < 10\,\mathrm{eV}$. This observation suggests that a more complete CRM would facilitate HeMSI measurements of T_e and n_e in this regime.

Irrespective of T_e and n_e diagnostic applications, understanding the helium spectral measurements in this regime may be of general interest to boundary physics. For example, the missing mechanism for helium emission could imply a collisional process that affects the transport of helium ash in the boundary. Furthermore, understanding molecular processes is key to understanding detachment in TCV [97]. HeMSI measurement may assist with this understanding should molecular processes prove to be the missing components of the CRM.
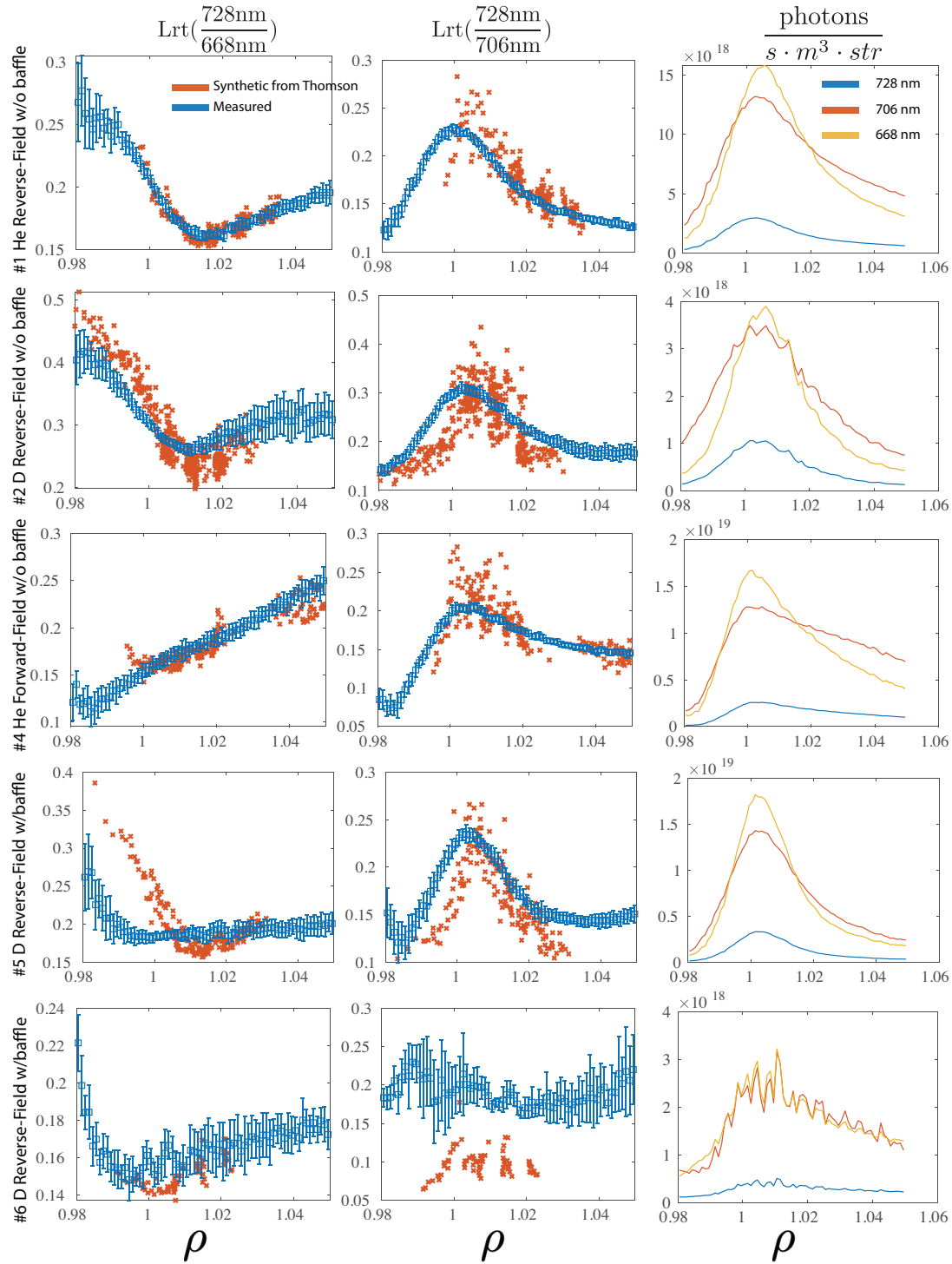
Figure 3.15: Each row displays line-ratio profiles from a different discharge for $-0.5\text{m} < z < -0.4\text{m}$. This presentation shows how the measurements of helium line ratios compare to the predictions created by applying G-CRM to the T_e and n_e Thomson scattering measurements.
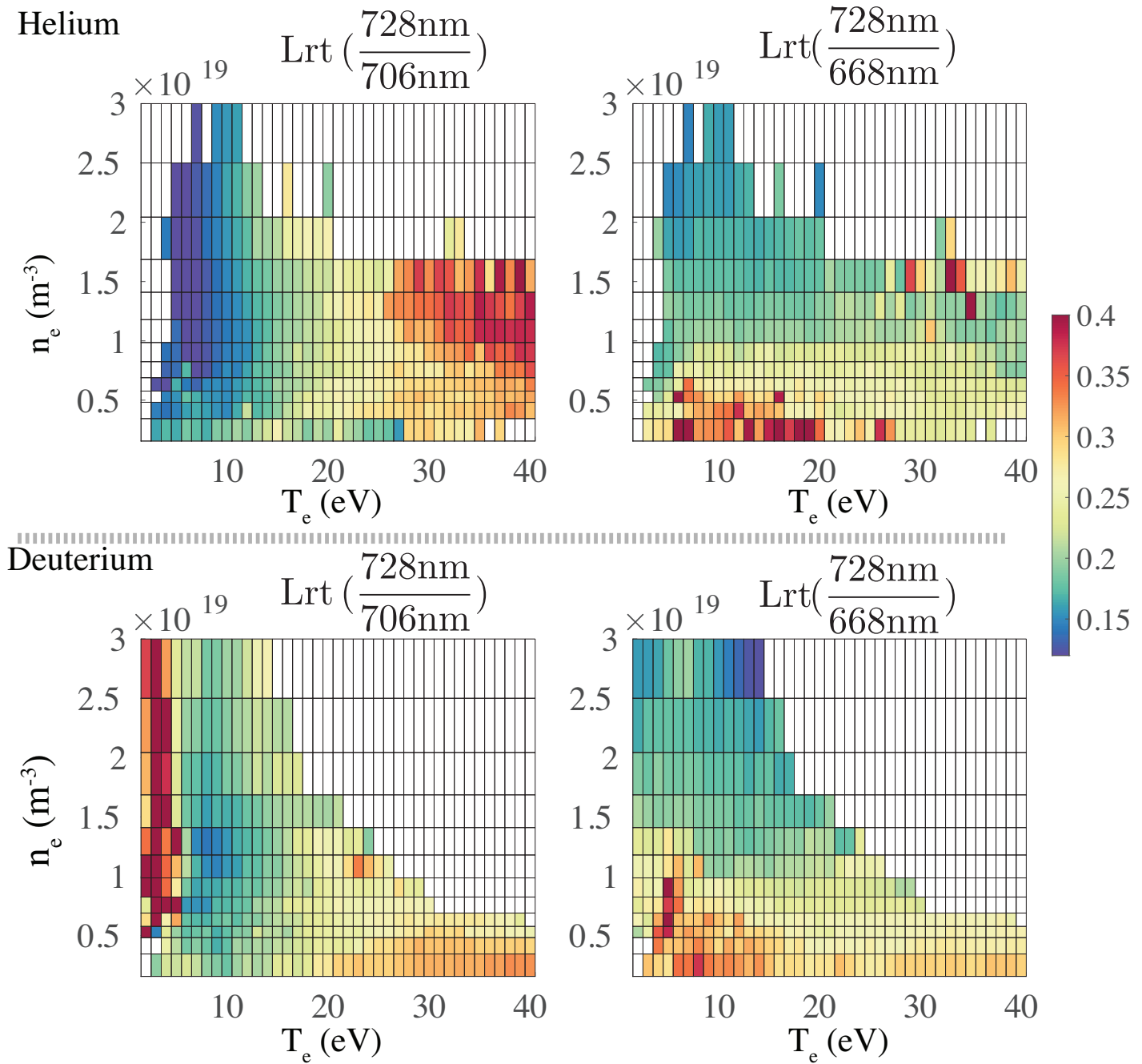
Figure 3.16: Average $\mathrm{Lrt}(\frac{728\mathrm{nm}}{706\mathrm{nm}})$ and $\mathrm{Lrt}(\frac{728\mathrm{nm}}{668\mathrm{nm}})$ measured at a given Thomson scattering value of T_e and n_e. Measurements restricted to the separatrix and common flux region.
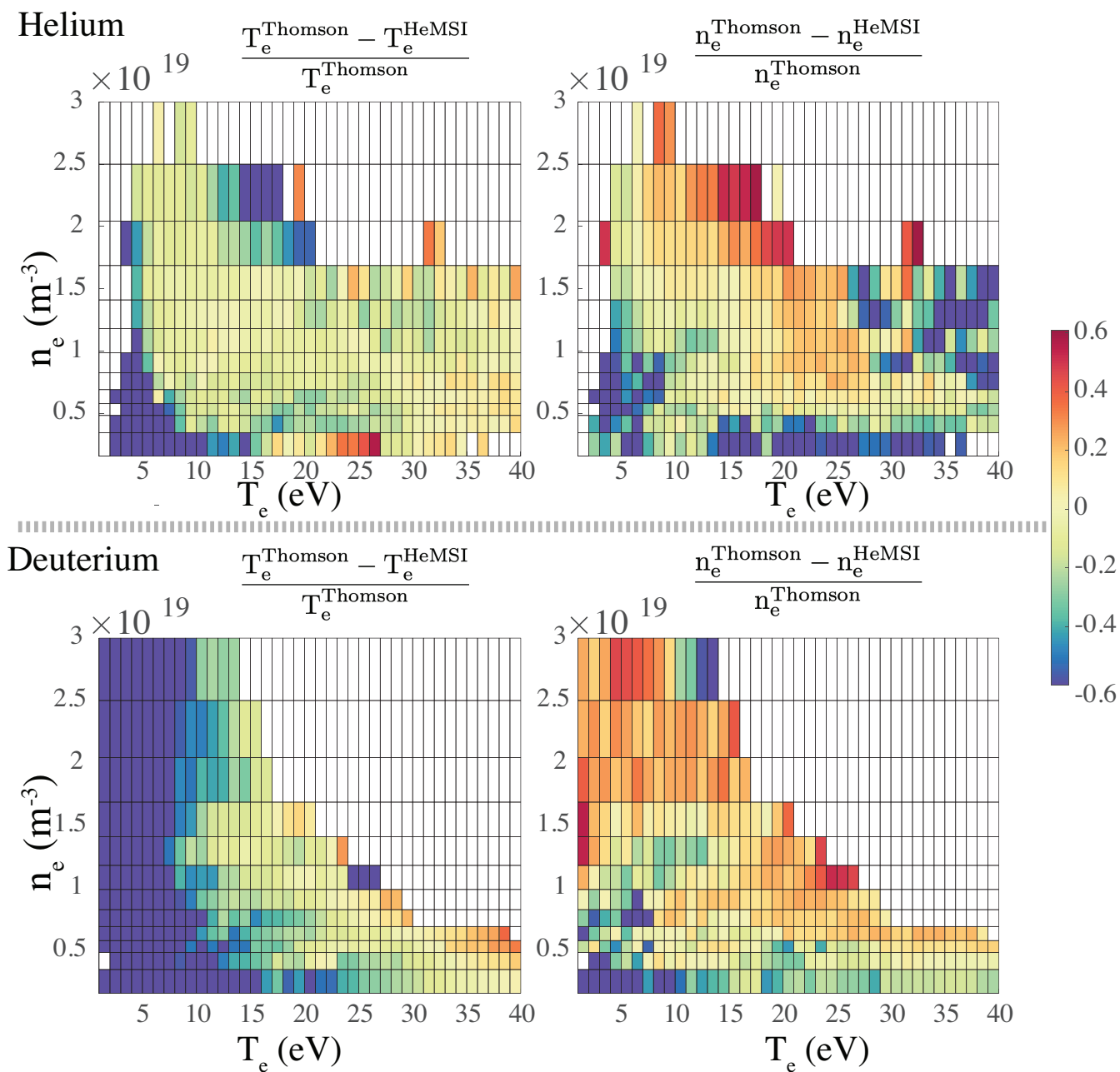
Figure 3.17: Comparison of T_e and n_e measured by HeMSI using G-CRM to that of Thomson scattering. Measurements restricted to the separatrix and common flux region.
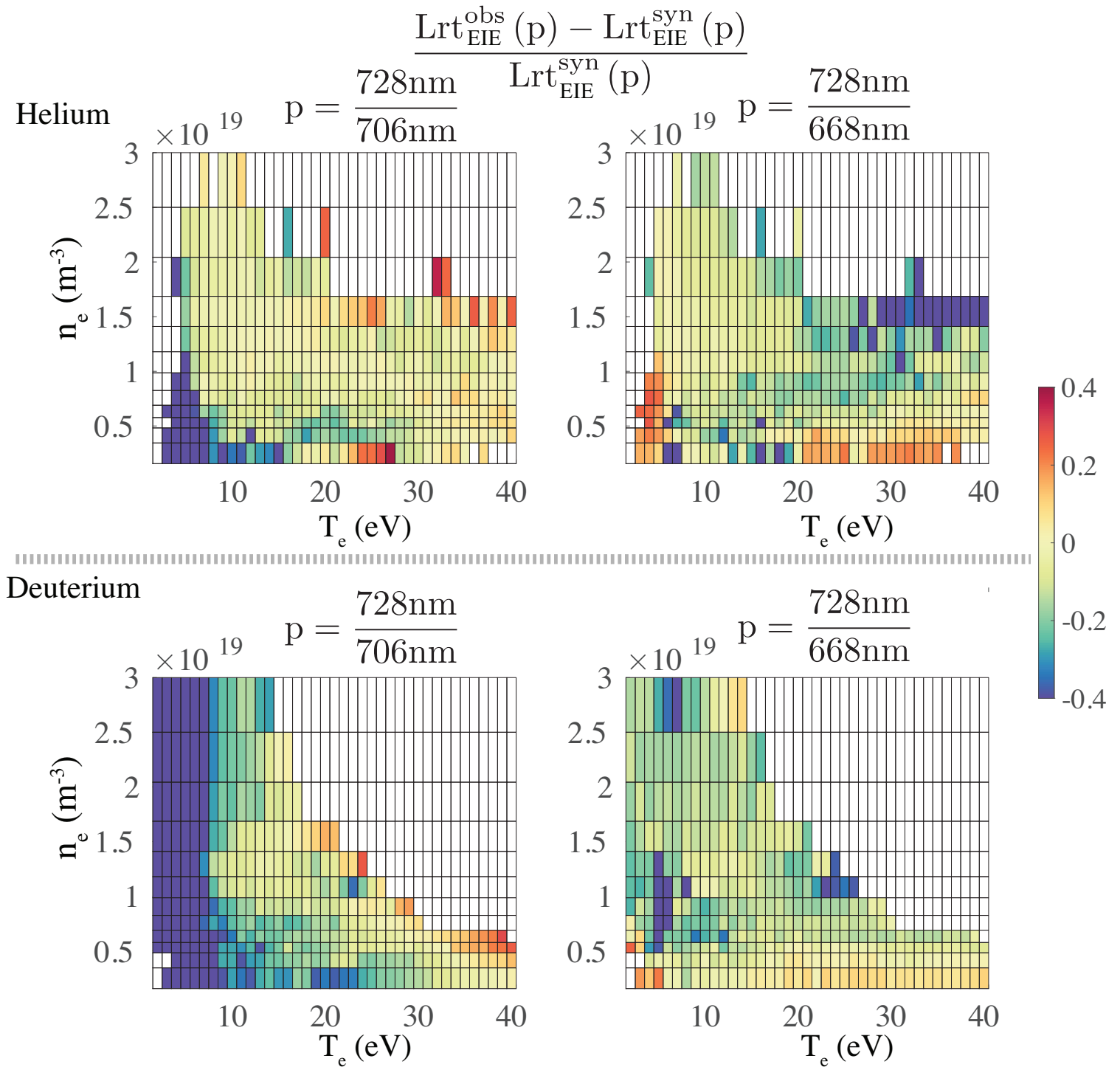
Figure 3.18: Comparison of $\text{Lrt}(\frac{728\text{nm}}{706\text{nm}})$ and $\text{Lrt}(\frac{728\text{nm}}{668\text{nm}})$ measurements to the expectation of an ionizing plasma produced from G-CRM and Thomson scattering measurements. Measurements restricted to the separatrix and common flux region.
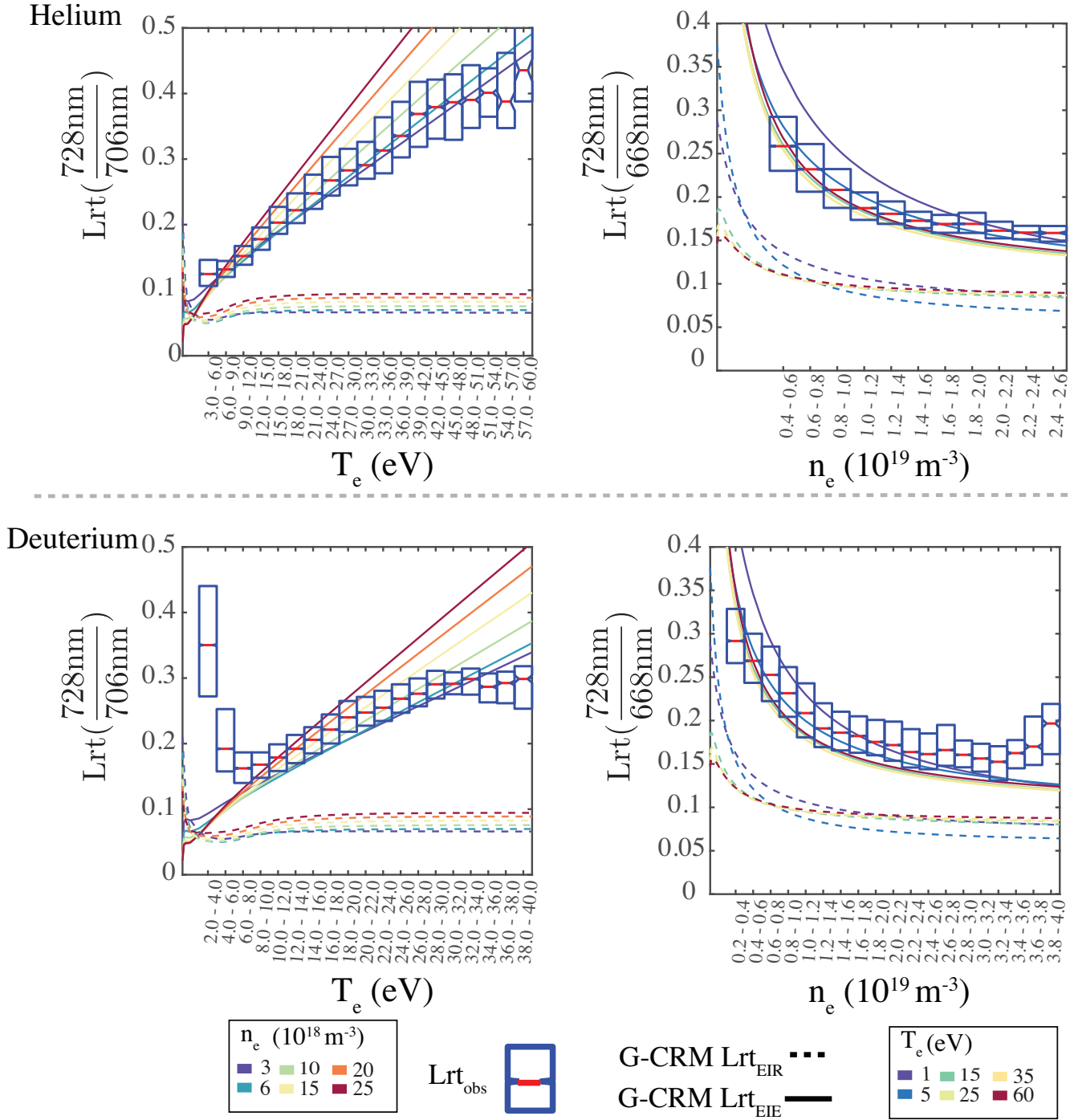
Figure 3.19: Box plots of $\mathrm{Lrt}(\frac{728\mathrm{nm}}{706\mathrm{nm}})$ and $\mathrm{Lrt}(\frac{728\mathrm{nm}}{668\mathrm{nm}})$ measurements versus the parameter to which they are most sensitive. The solid and dashed lines are produced by forward-modeling the line ratios with G-CRM. The solid line depicts the ratio of the EIE component, $\mathrm{Lrt_{EIE}}$, whilst the dashed line depicts the ratio of the EIR component, $\mathrm{Lrt_{EIR}}$.

3.6.4 Gas Puff Images

Ref #	Fuel	$\bar{n}_e(10^{19}\mathrm{m}^{-3})$	w 587nm	$\vec{v}_{\nabla B} \cdot \hat{z}$	Divertor Type	Figure
#7	deuterium	2	yes	rf	baffled	3.20
#8	deuterium	3	no	rf	baffled	3.21

Table 3.4: Description of discharges that are presented in this paper which applied HeMSI to a localized helium puff sent into a deuterium plasma.

HeMSI measurements were also performed for localized gas puffs made into deuterium plasmas. Using a localized puff removed the need for an image inversion because the emission could be approximated as local. The results of the gas puff analysis were consistent with that from the inverted data. Good agreement was seen in the common flux region, but the agreement became worse near the separatrix going towards the private flux region. Two examples are shown in Figures 3.20 and 3.21. The consistency between HLRS methodologies further bolsters confidence in the measurements made via inversion
.
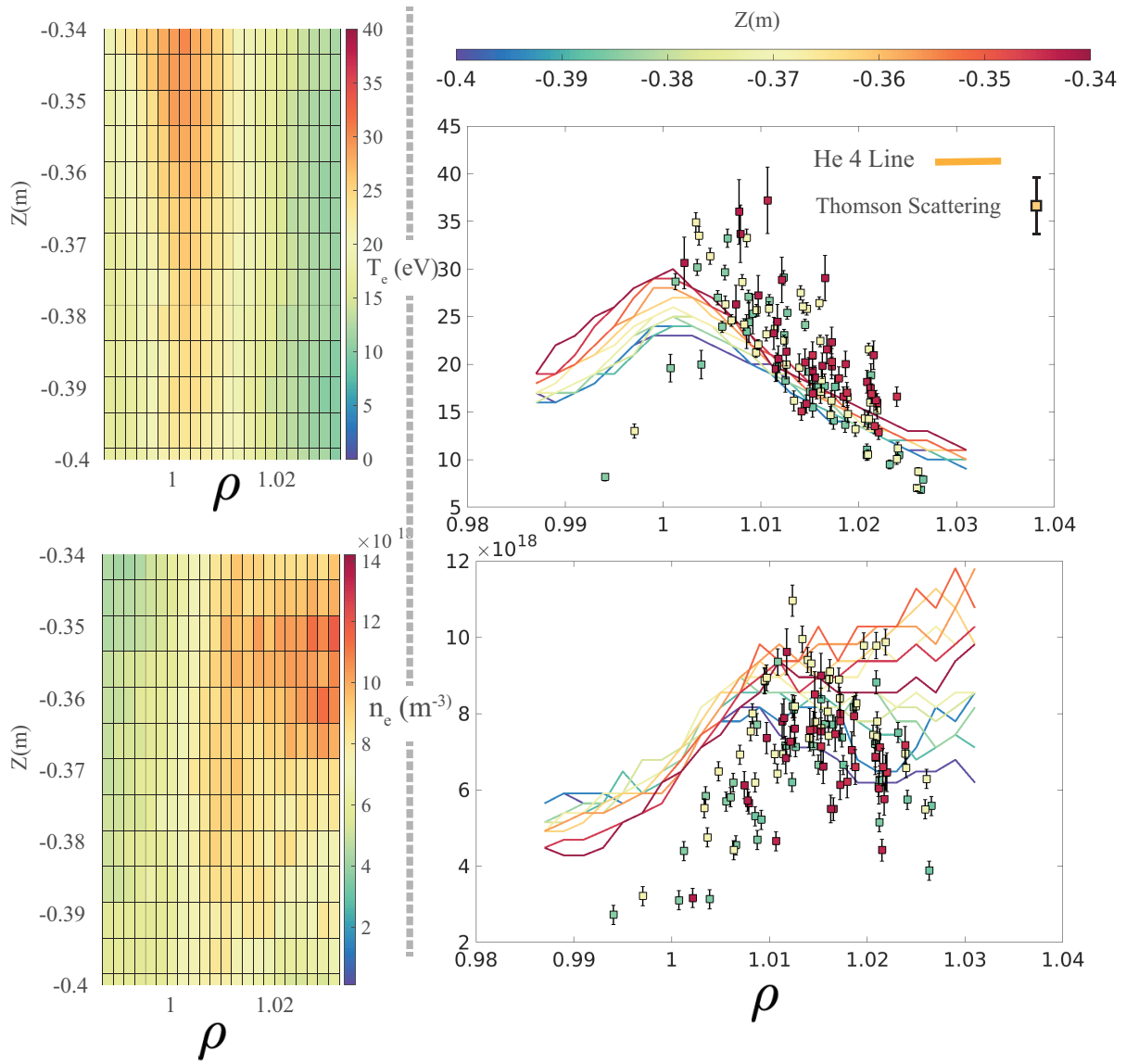
Figure 3.20: Comparison of HeMSI data collected from a localized puff into a reverse field deuterium plasma at $\bar{n}_e = 2 \times 10^{19} \mathrm{m}^{-3}$. HeMSI fits include 587 nm line.
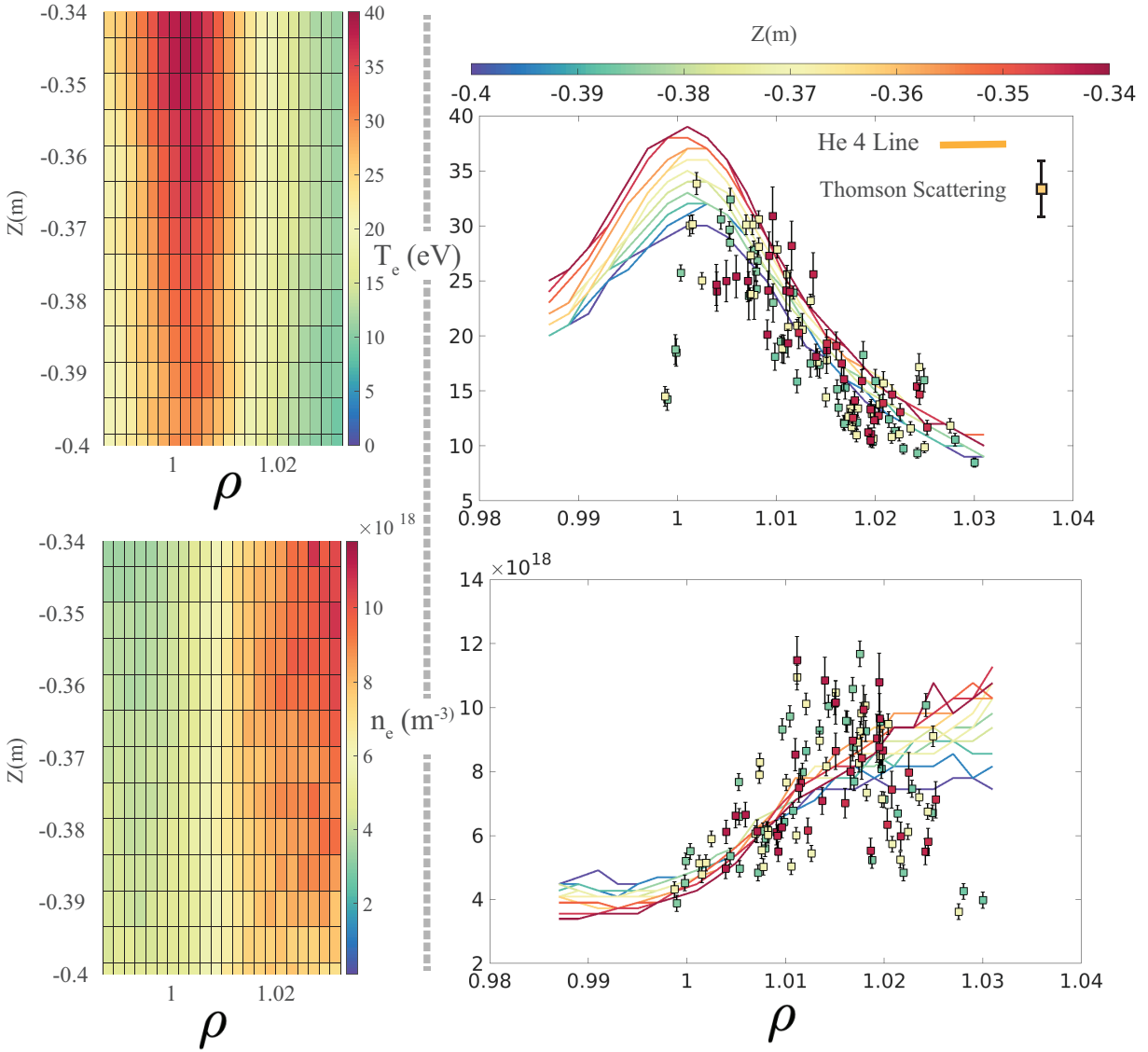
Figure 3.21: Comparison of HeMSI data collected from a localized puff into a reverse field deuterium plasma at $\bar{n}_e = 3 \times 10^{19} \mathrm{m}^{-3}$. HeMSI fits include 587 nm line.

In conclusion, these innovative measurements provide unprecedented diagnostic coverage of T_e and n_e in the divertor. In the next chapter, this powerful tool is used to perform a novel analysis of the effects of flux expansion in a tokamaks divertor.

Chapter 4

Flux Expansion Study

This chapter describes the first application of HeMSI to the study of the effect divertor magnetic geometries have on the divertor plasma. HeMSI is applied to 7 lower single-null Ohmically heated L-mode plasmas. Four are in forward field and three are in reverse field. Forward (reverse) field denotes that the ion $\boldsymbol{\nabla} B$ drift is directed from the core to (away from) the active x-point. All the discharges were designed to maintain a consistent separatrix shape. At the same time, the strength of the poloidal field was varied, resulting in a scan of poloidal flux expansion (defined in Section 4.2) along the outer divertor leg. Two-point modeling (2PM) [98] indicates that increasing poloidal flux expansion should lower the target temperature, facilitating detachment along the outer leg. However, in *Theiler 2017* [14], poloidal flux expansion was shown not to affect the detachment threshold of L-mode reverse field plasmas. This work aims to expand upon these previous results by applying HeMSI to L-mode plasmas residing in the conduction-limited regime immediately before partial divertor detachment for both field directions.

In this work, the 2D T_e and n_e maps from HeMSI along the outer divertor leg are coupled with plasma potential measurements from Langmuir probes at the vessel floor to calculate the electric potential and, by corollary, the E × B drift velocities in 2D. Then, by estimating the upstream velocity from measurements reported in *Tsui 2022* [99] and measurements of the neutral ionization rate in 2D, the plasma's parallel velocities are calculated along individual flux surfaces. Thus, particle and power transport are quantified into drift, convection, and conduction components in 2D. Transport resolved in 2D was recently reported in [100] using a vertical reciprocating probe. Unique to this work is the performance of the analysis with HeMSI and the variation in magnetic geometry.

This chapter is organized as follows. **Section 4.1** defines flux expansion and introduces the 2PM. **Section 4.2** describes the plasma discharges and the diagnostics. Then, **Section 4.3** reviews the local conservation equations applied to each flux tube to calculate the plasma potential and transport properties from the HeMSI measurements. **Section 4.4** presents the methodologies used to fit the 2D HeMSI profiles and resolve the local derivatives.

The results are presented in **Section 4.5** over several subsections. **Section 4.5.1** shows that poloidal flux expansion does not affect the C-III emission front or the ion flux to the plate. These measurements are typical indicators of detachment. This is in agreement with previous TCV results [14]. **Section 4.5.2** discusses the 2D T_e and n_e measured during the

conduction-limited regime. In the conduction-limited regime, increasing poloidal flux expansion lowers the temperature at the outer target as expected qualitatively from the 2PM. The effects of both toroidal field direction and poloidal flux expansion are observed to influence the T_e and n_e profiles. Double-peaked density profiles are also observed and their appearance is shown to be sensitive to both poloidal flux expansion and the toroidal field direction. In **Section 4.5.3**, the calculated parallel flows and drifts are presented. In **Section 4.5.4**, the total power flux through an annulus within the outer divertor plasma is found to be constant along the outer leg, i.e., not dependent upon the height of the annulus. However, a significant portion of the power flux is relayed through convection. Bolometric losses are shown to increase with poloidal flux expansion. **Section 4.5.4** discusses the power and particle balances in 2D. Large power losses along the separatrix are balanced by the large influx of power observed farther into the common flux region (CFR). **Section 4.5.4** reports the calculated particle and heat transport coefficients ($D_\perp$ and $\chi_\perp$) assuming $D_\perp$ and $\chi_\perp$ are constant in the SOL. The calculations of $D_\perp$ fall within the usual values used by modelers, but the values of $\chi_\perp$ in the far CFR exceed expectations by two orders of magnitude. Finally, **Section 4.6** discusses the results and concludes the chapter.

4.1 Poloidal Flux Expansion

The definition of poloidal flux expansion arises from the conservation of poloidal flux, which states:

$$(B_\theta dA)_{\text{OMP}} = B_\theta\left(\rho, s\right) dA\left(\rho, s\right) \tag{4.1}$$

$$(B_\theta R dr)_{\text{OMP}} = B_\theta\left(\rho, s\right) R\left(\rho, s\right) dr\left(\rho, s\right) \tag{4.2}$$

where OMP refers to the outer-midplane, B_θ is the poloidal field, ρ is a flux coordinate, s is an arclength parameter along the flux surface, R is the major radial position, and dr is the distance between neighboring flux surfaces in the poloidal plane. By definition, poloidal flux expansion, f_x, is the ratio of the infinitesimal distance between neighboring flux surfaces at a specific point along a flux contour and the infinitesimal distance at the OMP, i.e.:

$$f_x(\rho, s) \equiv \frac{\mathrm{d}r\left(\rho, s\right)}{\mathrm{d}r_{\text{OMP}}} = \frac{B_{\theta\,\text{OMP}} R_{\text{OMP}}}{B_\theta(\rho, s) R(\rho, s)} \tag{4.3}$$

Both the length of the magnetic field line between the OMP and the vessel and the plasma volume of the divertor are functions of f_x. To see these effects, define s_p to be the arclength traversed along a flux surface away from the OMP towards the target. Then, the length of a flux tube and the volume between two flux surfaces are:

$$s(\rho, s_p) = \int_0^{s_p} \frac{B}{B_\theta} ds_\theta = \int_0^{s_p} f_x \frac{R(\rho, s_\theta) B}{B_{\theta\,\text{OMP}} R_{\text{OMP}}} ds_\theta \tag{4.4}$$

$$\approx \frac{RB}{B_{\theta\,\text{OMP}} R_{\text{OMP}}} \int_0^{s_p} f_x(\rho, s_\theta) ds_\theta \tag{4.5}$$

$$dV(\rho) = \int_0^{s_p^{\text{target}}} 2\pi R(s) dr(s) ds_\theta = dr_{\text{OMP}} \int_0^{s_p^{\text{target}}} 2\pi R(s) f_x(\rho, s_\theta) ds_\theta \tag{4.6}$$

In the above, it was assumed that $RB \approx RB_\phi$. Figure 4.1 illustrates the effect of f_x on the plasma volume, while Figure 4.2 shows the connection length between the target and OMP, $L(\rho)$, for each of the four magnetic geometries in Figure 4.1. Figure 4.2 also shows how f_x varies along the separatrix.

The SOL of a reactor will need to reside in a partially detached regime. This requires lowering the SOL's temperature below 5 eV so that a substantial amount of the SOL's momentum and power can be dispersed via elastic collisions with neutral atoms in the divertor chamber [98]. As can be observed in Eq 4.6, increasing flux expansion facilitates this by increasing the plasma volume which increases the amount of neutrals with the SOL. The benefit of increasing the length of the magnetic field line is expected from the two-point model (2PM) [98]. The 2PM assumes that election heat conduction as described by Spitzer conductivty is the dominant form of heat transport and ignores variations in the strength of the magnetic field. From these assumptions, it follows that:

$$q_{||} = -\kappa_o T_e^{\frac{5}{2}} \frac{\mathrm{d}T_e}{\mathrm{d}s} \tag{4.7}$$

$$\implies T(s)^{\frac{7}{2}} = T_u^{\frac{7}{2}} - \frac{7}{2} \frac{q_{||} s}{\kappa_o} \tag{4.8}$$

Where T_u is the temperature at the OMP and s specifies a distance from the OMP to a position along the field line. Thus, Eqs 4.4 and 4.8 show that increasing flux expansion also benefits the SOL's exhaust performance by increasing the length over which the heat is conducted.

4.2 Experiment

The effects of changing the connection length and the divertor plasma volume were investigated in seven Ohmically heated L-mode discharges: four in forward field and three in reverse field. The magnitudes of B_t and I_p were 1.4 T and 170 kA, respectively. The targeted shape of the separatrix was identical for each shot, but the strength of the poloidal field varied, resulting in different values of poloidal flux expansion.

Four lower single-null magnetic geometries were explored. The values of poloidal flux expansion on the separatrix at the target for these four shapes were 2.5, 4, 6, and 11 (see Figure 4.1).
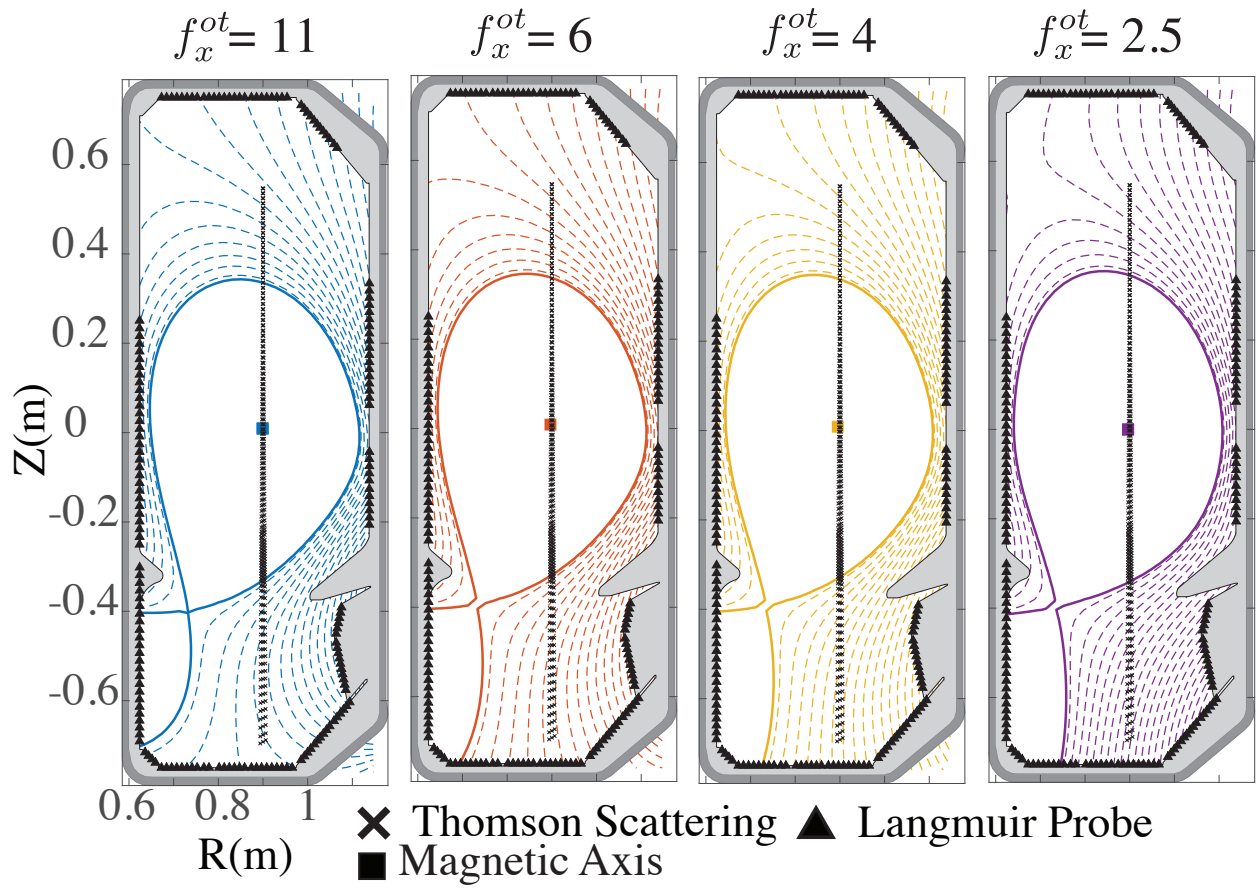
Figure 4.1: Magnetic equilibrium reconstructions for different flux expansions. The solid line indicates the separatrix. Flux surfaces are spaced $\Delta\rho = 0.02$.
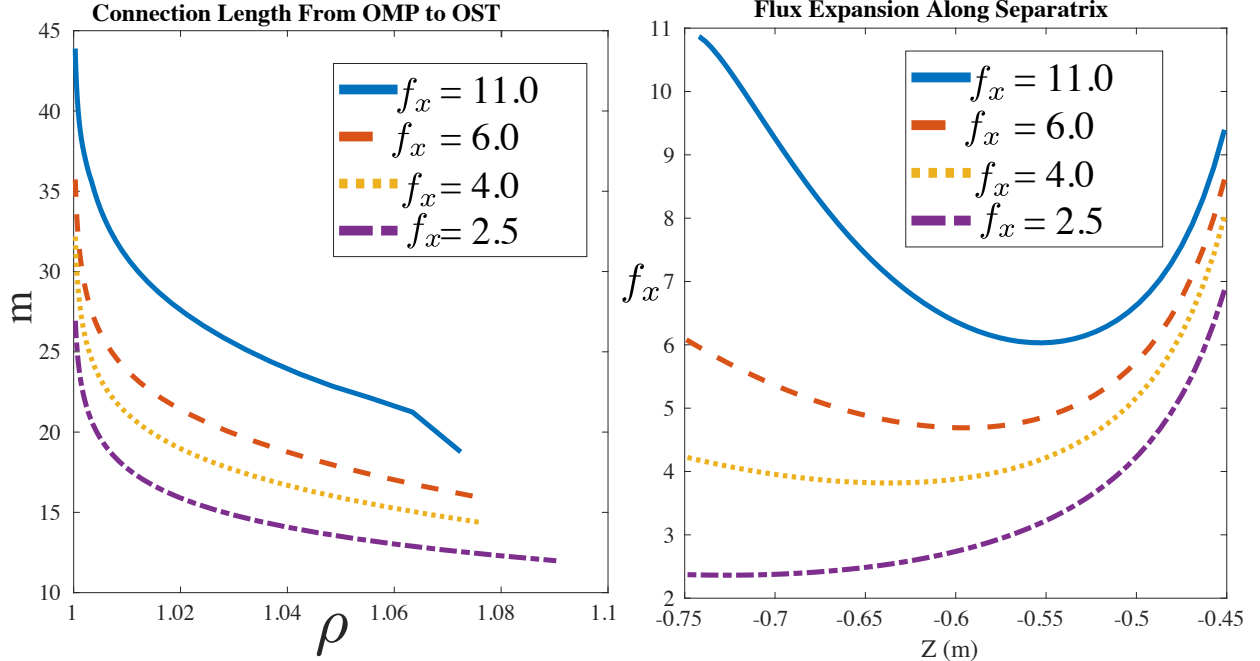
Figure 4.2: Left: Connection length from outer mid-plane (OMP) to outer strike point (OST) target versus normalized flux value for each magnetic equilibrium examined. Right: Flux expansion at the separatrix for each magnetic equilibrium as a function of height in the vessel.

Each discharge is partitioned into two periods. First, a density plateau of $\bar{n}_e = 3.5 \times 10^{19} m^{-3}$ was reached for a period of 150 ms. During this period, all discharges exhibited significant $\nabla_{||} T_e$ along the divertor leg. Consequently, the plasmas reside in the conduction-limited regime (the high-recycling regime) [98]. Then, a density ramp was performed over 0.8 s, leading to a partially-detached state. Figure 4.3 shows time traces of $\bar{n}_e$ and the Ohmic heating power.

The HeMSI analysis was validated for ionizing plasmas in the CFR [27]. Therefore, the HeMSI analysis is confined to the conduction-limited phase of the discharges. The detachment phase is investigated using ion flux measured by the probes at the plate and the temperature-sensitive C-III front. Increasing f_x lowers the temperature at the target in the conduction-limited regime. However, during detachment, the C-III front and Langmuir probe measurements are insensitive to variations in f_x. The lack of variation during detachment is consistent with previous TCV studies [14].

A list of the discharges can be viewed in Table 4.1, and a list of plasma parameters during the conduction-limited regime for those shots can be viewed in Table 4.2. The shots considered in this chapter are different from those reported in Chapter 3.
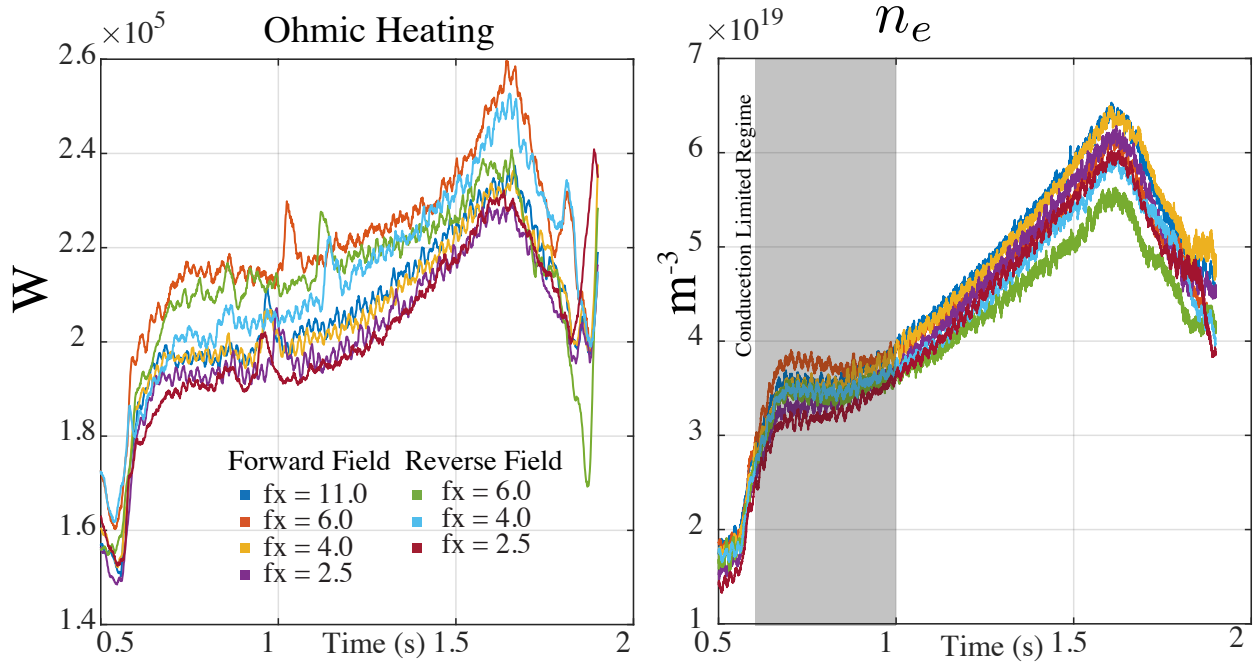
Figure 4.3: Time traces of Ohmic heating power and $\bar{n}_e$ for each discharge discussed.

$I_p = 170kA$| $P_{ohm} \approx 200$ kW | $\bar{n}_e \approx 3.5 \times 10^{19} m^{-3}$		
Forward Field B_ϕ = -1.4 T		
Ref #	f_x at OT	TCV ref #
1	11	72016
2	6	72014
3	4	72020
4	2.5	71969
Reverse Field B_ϕ = 1.4 T		
Ref #	f_x at OT	TCV ref #
5	6	71975
6	4	72022
7	2.5	71973

Table 4.1: Details of discharges used in flux expansion study. Note that these are different shots than those considered in Chapter 3.

Parameter	Range
T_e	5 - 35 eV
n_e	2-10 ($\times 10^{18}$ m^{-3})
$\ln \Lambda$	10-13.5
$\sqrt{\frac{T}{m_e}}$	9 - 26 ($\times 10^5 \frac{\text{m}}{\text{s}}$)
$\sqrt{\frac{T}{m_d}}$	2 - 4 ($\times 10^4 \frac{\text{m}}{\text{s}}$)
$\lambda_{ee} \sim \frac{T^2}{n}$	0.02-9 m
$\lambda_{ii} \sim \frac{T^2}{n}$	0.03-12 m
$\nu^*_{SOL,e} = \frac{L}{\lambda_{ee}}$	12-20 (for $\lambda_{ee} \sim 2m$ at the separatrix)

Table 4.2: Ranges of plasma parameters on the outer divertor leg during the time of density plateau at $\bar{n}_e \approx 3.5 \times 10^{19} m^{-3}$.

The diagnostics used to assess the power and particle transport along the outer divertor leg are listed in Table 4.3. Section 4.4 describes the data analysis unique to this work.

Diagnostic	Measurement	Ref
HeMSI / MANTIS	2D profiles of T_e, n_e, and ion densities	[15], [27], [101]
Thomson scattering	Upstream T_e, n_e	[88]
Wall mounted Langmuir probes	Downstream T_e, n_e, $j_\parallel$	[102]
Bolometery	2D profiles of radiated power	[103]
IR thermography	$q_\parallel$ radial profile along the outer target	[104]

Table 4.3: List of diagnostics used in this study.

4.3 Theory

This work is concerned with plasma transport in the outer divertor volume and how it is affected by flux expansion and toroidal field direction. The aim is to quantify the transport into parallel, drift, and anomalous components. The measurements used to accomplish this task are the 2D measurements of T_e, n_e, n_D, n_{He}, radiated power (Q_{rad}), and the 1D floor probe measurements of floating potential (V_{float}), and parallel current when V = 0 ($j_0^\parallel$). The spatial coverage of the 2D T_e and n_e from HeMSI maps allows the calculation of the first and second derivatives of T_e and n_e. Section 4.4 discusses the methodology of extracting derivatives from the maps.

This analysis makes the following simplifying assumptions:

- the plasma resides in an equilibrium $\frac{\partial}{\partial t} = 0$

- $T_e = T_i = T$

- $n_e = n_i = n$

- B $\approx B^\phi$

- cross-field momentum losses are negligible

It is assumed that plasma transport along the outer leg is determined by the steady-state Braginskii fluid equations [105]. There are five equations to consider: conservation of charge, Ohm's law, conservation of parallel ion momentum, particle continuity, and conservation of energy. These equations are solved in the order listed in Table 4.4. Each equation is discussed individually below.

Step	Equation	Requires	Result
0	Measurements	-	T,n, $n_{\mathrm{D,He}}$, $j_0^{\parallel}$,V_{float},Q_{rad}
1	Charge Continuity	$j_0^{\parallel}$	$j^{\parallel}$
2	Ohm's Law	T,n,$j_0^{\parallel}$, V_{float}	V, $\mathbf{E}$
3	Ion Momentum Conservation	$\mathbf{E}$,T,n	$v_{\parallel}$
4	Continuity	$\mathbf{E}$,$v_{\parallel}$,T,n,$n_{\mathrm{D,He}}$	$D_{\perp}$
5	Energy Conservation	$\mathbf{E}$,$v_{\parallel}$,T,n,	$\chi_{\perp}$

Table 4.4: Analysis Steps

4.3.1   Step 1: Charge Continuity Equation

Conservation of charge requires that:

$$\boldsymbol{\nabla} \cdot \mathbf{j} = 0 \tag{4.9}$$

$$\boldsymbol{\nabla} \cdot \mathbf{j}_{\parallel} = -\boldsymbol{\nabla} \cdot \mathbf{j}_{\perp} \tag{4.10}$$

$$B\frac{\partial}{\partial s}\left(\frac{j_{\parallel}}{B}\right) \approx -\frac{\partial}{\partial z}j_{\perp} \tag{4.11}$$

The perpendicular current can be expressed as [106]

$$\mathbf{j}_{\perp} = \boldsymbol{\nabla} \times \mathbf{K} + \left(p_{\parallel} + p_{\perp} + m_i n v_{\parallel}^2\right) \frac{\mathbf{B} \times \boldsymbol{\nabla} B}{B^3} \tag{4.12}$$

where $\mathbf{K} = -\frac{p_{\perp}}{B^2}\mathbf{B}$ and $p_e + p_i = 2p_e = p$

$$\mathbf{j}_{\perp} = \boldsymbol{\nabla} \times \mathbf{K} + \left(2p + m_i n v_{\parallel}^2\right) \frac{\mathbf{B} \times \boldsymbol{\nabla} B}{B^3} \tag{4.13}$$

$$\tag{4.14}$$

Only the divergence of $\mathbf{j}$ is relevant to this analysis. Thus, $\boldsymbol{\nabla} \times \mathbf{K}$ can be ignored, and the effective current, $\widetilde{\mathbf{j}}$, can be approximated as:

$$\widetilde{\mathbf{j}}_{\perp} = \left(2p + m_i n v_{\parallel}^2\right) \frac{\mathbf{B} \times \boldsymbol{\nabla} B}{B^3} \tag{4.15}$$

Now the assumption $B \approx B^{\phi} = \frac{B_o R_o}{R}$ is applied to Eq 4.15. The quantity RB^{ϕ} is constant throughout the vessel, and this is emphasized via the 'o' subscript in $R_o B_o$. Consequently:

$$\boldsymbol{\nabla} B \approx \boldsymbol{\nabla} \frac{B_o R_o}{R} = -\frac{B_o R_o}{R^2} \hat{R} = -\frac{B}{R} \hat{R} \tag{4.16}$$

$$\frac{\mathbf{B} \times \boldsymbol{\nabla} B}{B^3} \approx -\frac{1}{B^3} \frac{B^2}{R} \hat{\phi} \times \hat{R} = \frac{\hat{Z}}{B_o R_o} \tag{4.17}$$

$$-\boldsymbol{\nabla} \cdot \mathbf{j}_\perp \approx -\frac{\partial}{\partial z} j_\perp \approx \frac{1}{B_o R_o} \frac{\partial}{\partial z} \left(4p + m_i n v_\parallel^2 \right) \tag{4.18}$$

$$B \frac{\partial}{\partial s} \left(\frac{j_\parallel}{B} \right) \approx -\frac{1}{B_o R_o} \frac{\partial}{\partial z} \left(4p_e + m_i n v_\parallel^2 \right) \tag{4.19}$$

$$\frac{j_\parallel}{B} = \frac{j_{o\parallel}}{B_o} - \int_{\text{target}}^z \frac{1}{B} \frac{1}{B_o R_o} \frac{\partial}{\partial z} \left(4p_e + m_i n v_\parallel^2 \right) ds \tag{4.20}$$

In Eq 4.20, $v_\parallel$ is yet unknown. Reciprocating probe measurements presented in [99] showed parallel Mach numbers of approximately $M = 0.5$ in the divertor leg for plasma configurations similar to those of this work, so $v_\parallel^2$ is approximated as $v_\parallel^2 \approx \frac{1}{2} \frac{T_e}{m_i}$. Consequently:

$$\frac{j_\parallel}{B} = \frac{j_{o\parallel}}{B_o} - \int_{\text{target}}^z \frac{1}{B} \frac{1}{B_o R_o} \frac{\partial}{\partial z} \left(4.5 p_e \right) ds \tag{4.21}$$

We assume that parallel flows are below the sound speed, $0 < m_i n v_\parallel^2 < 2v p_e$. The following analysis is only concerned with the quantity $\frac{j_\parallel}{\sigma_{sp}}$ which makes a $\sim 10\%$ contribution to the parallel electric field. Thus, the approximation that $v_\parallel^2 \approx \frac{1}{2} \frac{T_e}{m_i}$ will only affect the parallel electric field calculation by at most a few percent.

4.3.2 Step 2: Ohm's Law

Ohm's law states that the parallel electric field is given by

$$E_\parallel = -\frac{0.71}{e} \frac{\partial T_e}{\partial s} - \frac{1}{e n_e} \frac{\partial p_e}{\partial s} + \frac{j_\parallel}{\sigma_{sp}} \tag{4.22}$$

Assuming no cross-field current, the voltage along a field line a parallel distance l from the target is

$$V(\rho, l) = -\int_{\text{floor}}^l E_\parallel(\rho, s) ds + V(\rho, 0) \tag{4.23}$$

The voltage at the entrance to the sheath at the floor, $V(\rho, 0)$, is given from sheath theory [98]:

86

$$V(\rho, 0) = V_{\text{float}} - \frac{0.5T_{\text{e}}}{e} \ln\left(4\pi\frac{m_e}{m_i}\right) \tag{4.24}$$

Where V_{float} and T_{e} are taken from measurements made by Langmuir probes embedded in the outer target. As a result,

$$V(\rho, l) = -\int_{\text{floor}}^{l} E_{||}(\rho, s)ds + V_{\text{float}} - \frac{0.5T_{\text{e}}}{e} \ln\left(4\pi\frac{m_e}{m_i}\right) \tag{4.25}$$

$$\mathbf{E}(\rho, l) = -\mathbf{\nabla}V(\rho, l) \tag{4.26}$$

4.3.3 Step 3: Single Fluid Parallel Momentum

This section follows similar discussions given in [107], [108]. The plasma is treated as a single fluid with isotropic pressure, and neutral friction is ignored. However, specific to this work, the cross-field velocity will be assumed to be zero. Thus, the total pressure, static plus dynamic, is assumed to be constant along each flux surface, so solving for the fluid velocity is a one-dimensional problem. Beginning at the most general relation and assuming equilibrium, momentum conservation of a single fluid states that:

$$-\mathbf{\nabla}p = m_i\mathbf{\nabla}\cdot(n_{\text{e}}\mathbf{vv}) = m_i\left(n_{\text{e}}\mathbf{v}\cdot\mathbf{\nabla}\right)\mathbf{v} + \mathbf{v}\left(\mathbf{\nabla}\cdot n_{\text{e}}\mathbf{v}\right) \tag{4.27}$$

To reduce Eq 4.27, covariant and contravariant notation will be used. Since pressure balance is assumed to be satisfied along each flux surface, a specific coordinate system will be defined for each flux surface with $\{y, x, \phi\}$ where y is an arclength parameter of a flux surface, x is a cross-field coordinate, and ϕ is the toroidal angle. This is a Frenet-Serret coordinate system, further described in Apendix .1. Its metric is given by:

$$g_{ij} = \begin{pmatrix} (1-\kappa_y x)^2 & 0 & 0 \\ 0 & 1 & 0 \\ 0 & 0 & R^2 \end{pmatrix} \tag{4.28}$$

Of course, $x = 0$ along each flux surface for which y is specifically defined. Expanding Eq 4.27 with these conventions yields:

$$-\mathbf{\nabla}p = m_i n_{\text{e}}\left(v^y\nabla_y + v^\phi\nabla_\phi\right)\mathbf{v} + \mathbf{v}\left(\mathbf{\nabla}\cdot n_{\text{e}}\mathbf{v}\right) \tag{4.29}$$

To solve for parallel momentum balance, the assumption shall be made that $e_{||} = \hat{\phi} = \frac{e_\phi}{R}$. Now expanding the covariant derivatives in Eq 4.29:

$$-\frac{\partial p}{\partial \phi}e^\phi = m_i n_{\text{e}}v^y\frac{\partial v^\phi}{\partial y} + m_i n_{\text{e}}v^y\Gamma^\phi_{yy}v^y + m_i n_{\text{e}}v^y\Gamma^\phi_{\phi y}v^\phi$$
$$+ m_i n_{\text{e}}v^\phi\Gamma^\phi_{y\phi}v^y + \Gamma^\phi_{\phi\phi}v^\phi + v^\phi\left(\mathbf{\nabla}\cdot n_{\text{e}}\mathbf{v}\right)$$

Where Γ_{bc}^a are the Christoffel symbols of the second kind. Their values are

$$\Gamma_{\phi y}^\phi = \Gamma_{y\phi}^\phi = \frac{1}{R}\frac{\mathrm{d}R}{\mathrm{d}y} \tag{4.30}$$

$$\Gamma_{\phi\phi}^\phi = 0 \tag{4.31}$$

$$\Gamma_{yy}^\phi = 0 \tag{4.32}$$

The plasma fluid velocity is the sum of its parallel velocity and three drift components: the E × B drift, the ion ∇B drift, and the ion curvature drift.

$$\mathbf{v} = \mathbf{v}_{||} + \mathbf{v}_{E\times B} + \mathbf{v}_{\nabla B} + \mathbf{v}_k \tag{4.33}$$

Where the drift terms are given by

$$\mathbf{v}_{E\times B} = \frac{\mathbf{E}\times\mathbf{B}}{B^2} \tag{4.34}$$

$$\mathbf{v}_k = \frac{nm_i v_{||}^2}{eB^3}\mathbf{B}\times B\cdot\nabla\left(\frac{\mathbf{B}}{B}\right) \approx sign(B)\frac{m_i v_{||}^2}{eRB}\hat{Z} \tag{4.35}$$

$$v_{\nabla B} = \frac{\mathbf{B}\times\nabla p}{enB^2} \tag{4.36}$$

Thus, v^y is given by

$$v^y = v^{||}\frac{B^\theta}{B} + \mathbf{v}_{E\times B}^y + \mathbf{v}_{\nabla B}^y + v_k^y \tag{4.37}$$

It follows then that:

$$-\frac{\partial p}{\partial s} = m_i n_e v^y \frac{\partial v^{||}}{\partial y} + m_i n_e \frac{v^{||}}{R}\frac{\mathrm{d}R}{\mathrm{d}y}v^y \tag{4.38}$$

$$+v^{||}\left(\left(B\frac{\partial}{\partial s}\frac{n_e v^{||}}{B}\right) + \nabla\cdot n_e\mathbf{v}_{E\times B} + \nabla\cdot n_e\mathbf{v}_{\nabla B} + \nabla\cdot n_e\frac{m_i^2 v_{||}^2}{eRB}\hat{Z}\right) \tag{4.39}$$

The divergences of the fluxes resulting from each velocity are given below. It is assumed $B = \frac{R_o B_o}{R}\hat{\phi}$.

$$\nabla\cdot n_e\mathbf{v}_{||} = B\frac{\mathrm{d}}{\mathrm{d}s}\frac{n_e v_{||}}{B} \tag{4.40}$$

$$\nabla\cdot(n_e\mathbf{v}_{E\times B}) = \nabla n_e\cdot\mathbf{v}_{E\times B} + n_e\nabla\cdot\frac{\mathbf{E}\times\mathbf{B}}{B^2} \tag{4.41}$$

$$= \nabla n_e\cdot\mathbf{v}_{E\times B} + n_e\left(\frac{\nabla R}{R}\cdot\mathbf{v}_{E\times B}\right) \tag{4.42}$$

To evaluate $\nabla \cdot n v_{\nabla B}$ note that

$$\nabla \cdot n_e v_{\nabla B} = \nabla \cdot \frac{\mathbf{B} \times \nabla p}{eB^2} \tag{4.43}$$

$$= \nabla \cdot \left(-\nabla \times \left(\frac{p}{eB^2}\mathbf{B} \right) + \frac{2p}{eB^3}\mathbf{B} \times \nabla B + \frac{p}{eB^2}\nabla \times \mathbf{B} \right) \tag{4.44}$$

$$= \nabla \cdot \left(\frac{2p}{eB^3}\mathbf{B} \times \nabla B \right) \approx \nabla \cdot \left(\frac{2p_e}{eB_oR_o}\hat{z} \right) = \frac{2}{eB_oR_o}\frac{dp_e}{dz} \tag{4.45}$$

Finally, the divergence of the flux from the curvature drift is

$$\nabla \cdot n_e \mathbf{v}_k = sign(B)\frac{2m_i v_{||}}{eRB}\frac{ds}{dz}\frac{dv_{||}}{ds} \tag{4.46}$$

Thus, the relationship for parallel momentum balance becomes

$$-\frac{\partial p}{\partial s} = \left(v^y\frac{B}{B^\theta} + v^{||} + \frac{2m_i v_{||}^2}{eRB}\frac{\partial s}{\partial Z} \right) m_i n_e \frac{\partial v^{||}}{\partial s} \tag{4.47}$$

$$+ m_i v^{||} \left(v^{||}\frac{\partial n_e}{\partial s} - \frac{n_e v^{||}}{B}\frac{\partial B}{\partial s} + n_e\frac{1}{R}\frac{dR}{dy}v^y + \nabla \cdot n_e\mathbf{v}_{E\times B} + \nabla \cdot n_e\mathbf{v}_{\nabla B} \right) \tag{4.48}$$

$$+ m_i v^{||} \left(sign(B)\frac{m_i v_{||}^2}{eRB}\frac{\partial n_e}{\partial z} \right) \tag{4.49}$$

Eq 4.47 is solved numerically in this work. This requires choosing a boundary condition, discussed in Section 4.4.6. It must be noted that Eq 4.47 has a singularity at $\left(v^y\frac{B}{B^\theta} + v^{||} + \frac{2m_i v_{||}^2}{eRB}\frac{\partial s}{\partial z} \right) = 0$ for $v_{||} \neq 0$. The curvature term is relatively small, so the parallel velocity at which this singularity is reached can be approximated by

$$v_*^{||} = -\frac{1}{2}\frac{B^\theta}{B}\left(\mathbf{v}_{E\times B}^y + \mathbf{v}_{\nabla B}^y \right) \tag{4.50}$$

4.3.4   Step 4: Particle Continuity

Continuity of particles states:

$$\nabla \cdot \left(n\mathbf{v}_{||} + n\mathbf{v}_{E\times B} + n\mathbf{v}_{an} \right) = S_p, \tag{4.51}$$

where S_p is the source of particles given from ionization, and $\mathbf{v}_{an}$ is the velocity associated with anamolous particle transport:

$$n\mathbf{v}_D = -D_\perp\nabla n \tag{4.52}$$

In this work, the diffusion coefficient, $D_\perp$, is assumed to be constant in space.

4.3.5 Step 5: Energy Conservation

Heat fluxes from conduction and convection are considered here. Assuming the plasma is sufficiently collisional, heat conduction is described by Spitzer conductivity [98]:

$$\mathbf{q}_{\text{sp}} = -\kappa_{o,e} T_e^{\frac{5}{2}} \frac{dT_{i,e}}{ds} \hat{s} - \kappa_{o,i} T_i^{\frac{5}{2}} \frac{dT_i}{ds} \hat{s} \tag{4.53}$$

For $T_e = T_i$, $\frac{\kappa_{o,e}}{\kappa_{o,i}} \approx 30$, so it is assumed that

$$\mathbf{q}_{\text{sp}} \approx -\kappa_{o,e} T_e^{\frac{5}{2}} \frac{dT_{i,e}}{ds} \hat{s} \tag{4.54}$$

For $T_e = T_i$, the convected heat flux is given by

$$\mathbf{q}_{\text{conv}} = \left(5 n_e T_e + \frac{1}{2} m_i n_e v^2 \right) \mathbf{v} \tag{4.55}$$

Both anomalous heat conduction and convection will also be considered. Anomalous heat conduction is given by:

$$\mathbf{q}_\chi = -\chi_\perp n \boldsymbol{\nabla} T_e \tag{4.56}$$

And anomalous heat convection by:

$$\mathbf{q}_D = -\left(5 T_e + \frac{1}{2} m_i v^2 \right) D_\perp \boldsymbol{\nabla} n_e \tag{4.57}$$

Note that $\mathbf{v}_{\text{D}}$ has been ignored in calculating v^2 since parallel flow is assumed to dominate. Accounting for these heat fluxes, energy conservation is given by:

$$\boldsymbol{\nabla} \cdot \mathbf{q} = \boldsymbol{\nabla} \cdot \mathbf{q}_{\text{sp}} + \boldsymbol{\nabla} \cdot \vec{q}_{\text{conv}} + \boldsymbol{\nabla} \cdot \vec{q}_{\text{anomalous}} + \boldsymbol{\nabla} \cdot \vec{q}_D = Q_{\text{rad}} + Q_{\text{Sion}} \tag{4.58}$$

$$\tag{4.59}$$

Where the source terms are Q_{rad}, radiation losses, and Q_{Sion}, the energy lost due to ionizations.

4.4 Methodology

The HeMSI analysis is confined to the region defined by $-0.45m \leq z \leq -0.65m$ and $1 \leq \rho \leq 1.03$ (see Figure 4.4). The parameter ρ is the square root of the normalized poloidal magnetic flux, ψ, given by

$$\rho(\psi) = \sqrt{\frac{\psi_{\text{axis}} - \psi}{\psi_{\text{axis}}}}$$

Thus, $\rho = 1$ on the separatrix.

Approximately 30 sets of multi-spectral images were acquired for each discharge during the 150 ms conduction-limited period. Apart from minor changes in the magnetic equilibrium, the plasma conditions are assumed to be constant during this period. Each polygon in the poloidal map to which HeMSI ascribes a T_e and n_e was mapped to a flux coordinate and an arclength value at each time to account for small changes in the magnetic equilibrium during this interval. The coordinates used here are ρ and x, which is the distance from the separatrix following a path normal to the flux surfaces. The arclength parameters are s, the distance along the magnetic field from the outer-midplane (OMP), and y, the distance along the flux surface in the poloidal plane from the OMP. The parameters s, y, and x have dimensions of length. Figure 4.4 shows the values of parameters s, ρ, x for each polygon in the poloidal plane for a given time and discharge, and Figure 4.5 provides a sketch of the coordinates and their directions. Note that y and s are related by $\frac{B_y}{B}|ds| = |dy|$. The coordinates are listed in Table 4.5.
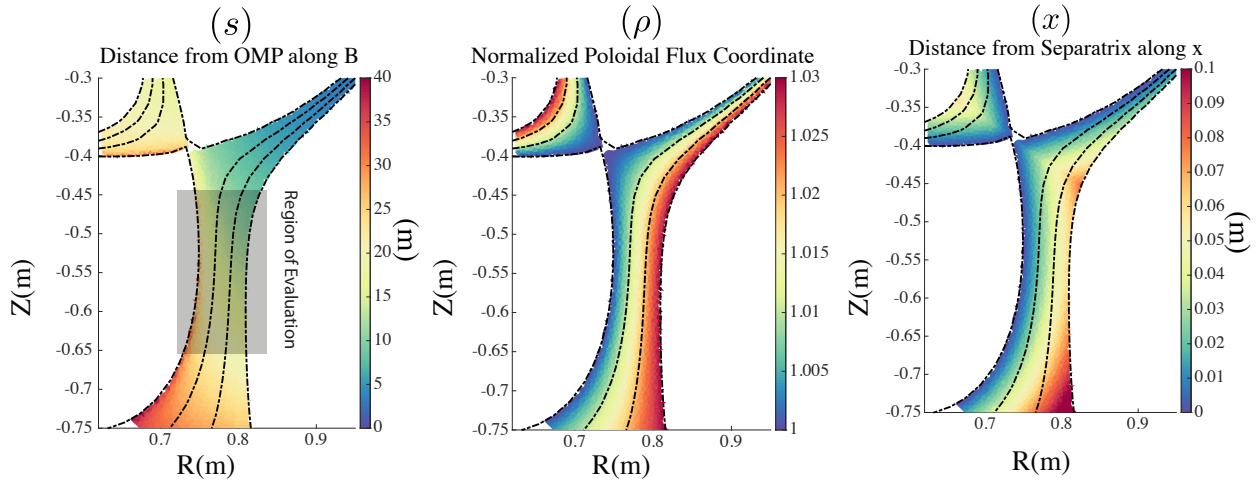
Figure 4.4: Poloidal maps displaying the value of coordinate parameters s,ρ,x in space at a given time for Discharge #1 . The region in which the transport equations are solved is noted in the plot of s.

4.4.1 Coordinates

	Coordinates
s	Distance along a magnetic field line from outer-midplane (OMP) (m)
y	Distance along poloidal flux surface from OMP (m)
x	Distance from separatrix following path normal to flux surfaces (m)
ρ	Square root of normalized poloidal flux $\rho(\psi) = \sqrt{\frac{\psi_\mathrm{axis} - \psi}{\psi_\mathrm{axis}}}$
R	Major Radius location (m)
Z	Height above vessel floor (m)

Table 4.5: Coordinates used in analysis
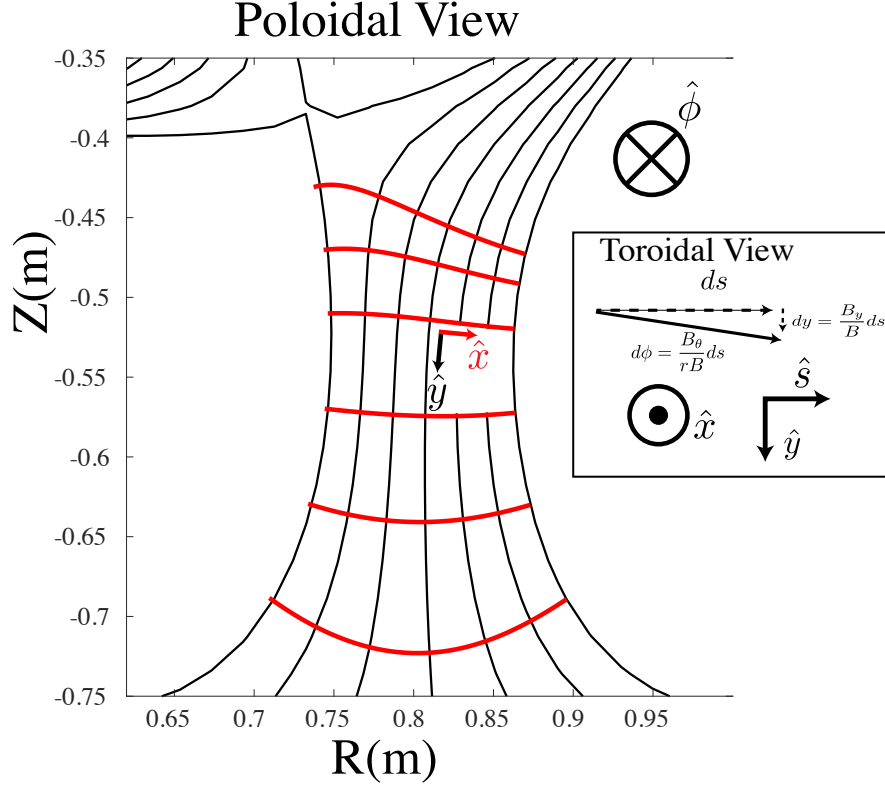
Figure 4.5: Drawing of the coordinate system used to parameterize the 2D profiles along and across flux surfaces.

4.4.2 Fitting T_e, n_e, and p_e along $\hat{s}$

To fit the T_e, n_e, and p_e profiles along the s coordinate, the data were binned into 15 flux tubes of width $\delta\rho = .002$ over $1 \leq \rho \leq 1.03$ and $-0.45m \leq z \leq -0.65m$ (see Figure 4.5). The data from each flux tube were then fit with a spline. The spline fits for T_e, p_e, and n_e were constrained with the following criteria:

- T_e: A three-knot cubic spline was used to fit $T_e(s)$ along each flux tube, and $\frac{dT_e(s)}{ds} < 0$ was enforced. The Thomson scattering and Langmuir probe ρ profiles were interpolated to give upstream and downstream constraints on $T_e(s)$. Lastly, $T_e(s)$ was forced to approach a constant value as $s \to 0$. An example of these fits are shown in Figures 4.6 and 4.7.

- n_e: A two-knot quadratic spline was used to fit $n_e(s)$.

- p_e: A three-knot quadratic spline was used to fit $p_e(s)$. The Thomson scattering profiles were used to constrain the upstream values. It was assumed that $\frac{dp_e(s)}{ds} < 0$.

Examples of T_e fits along s are shown in Figures 4.6 and 4.7.
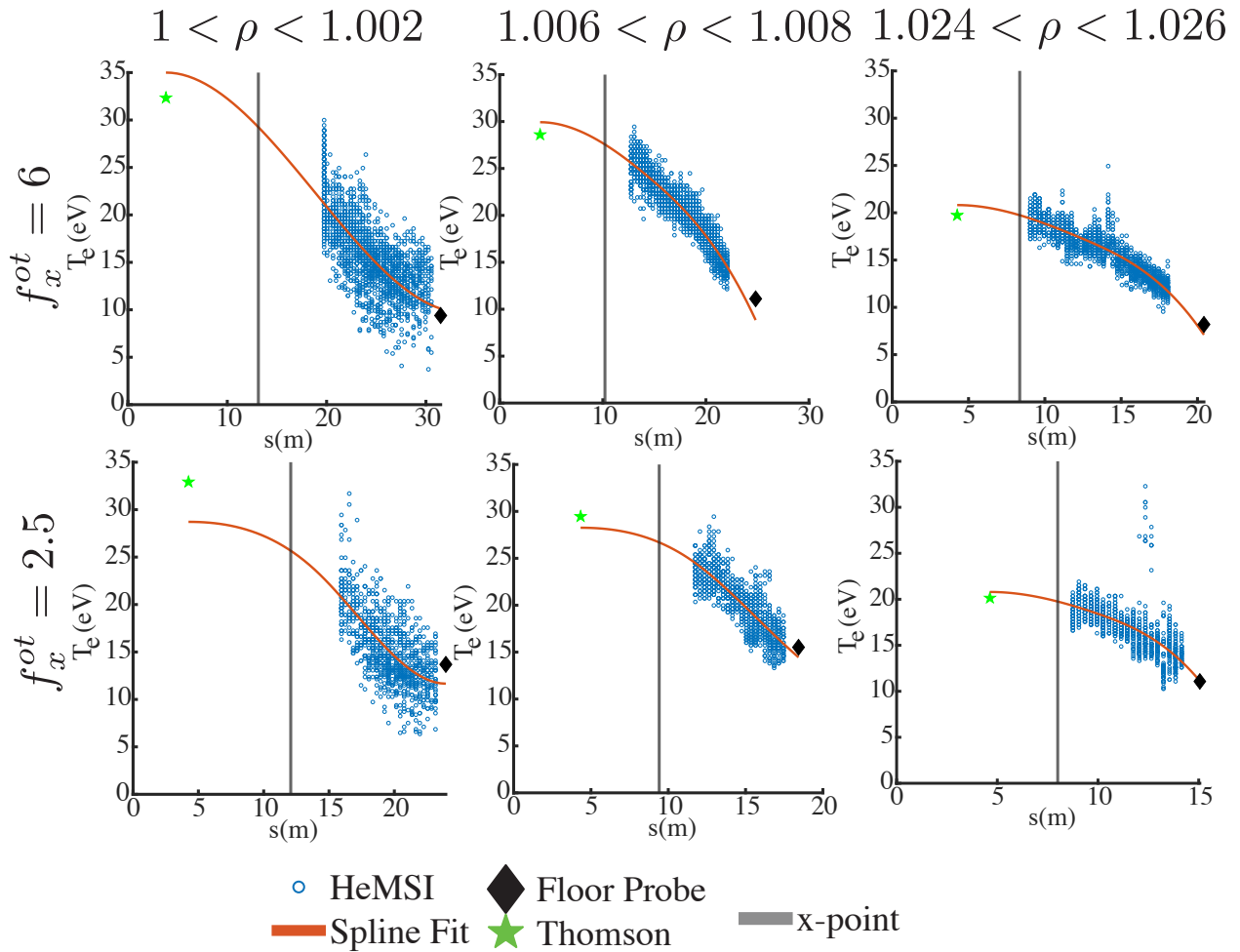
Figure 4.6: Examples of fits of $T_e(s)$ for different flux surfaces in two forward field shots. *Blue markers*: measurements from HeMSI. *Orange line*: the spline fit used in this work. *Grey dashed line*: location of minimum B^θ which approximates the location of the x-point. *Black diamond*: interpolated downstream value from Langmuir probes. *Green star*: interpolated upstream value from Thomson Scattering.
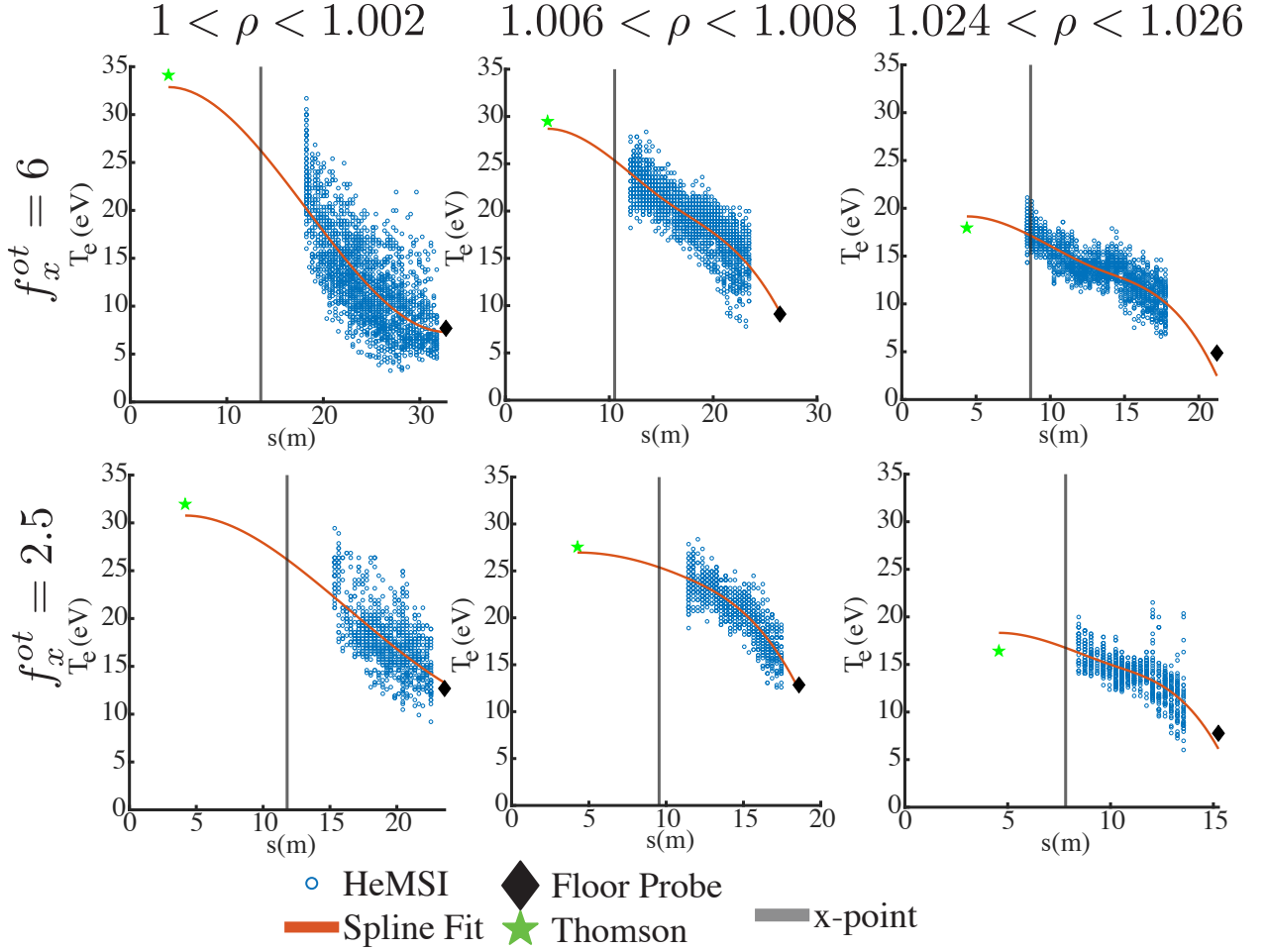
Figure 4.7: Examples of fits of $T_e(s)$ for different flux tubes in two reverse field shots. *Blue markers*: measurements from HeMSI. *Orange line*: the spline fit used in this work. *Grey dashed line*: location of minimum B^θ which approximates the location of the x-point. *Black diamond*: interpolated downstream value from Langmuir probes. *Green star*: interpolated upstream value from Thomson Scattering.

4.4.3 Fitting T_e, n_e, and p_e along $\hat{x}$

To fit the T_e, n_e, and p_e profiles along the x coordinate, the data were binned between two x-contours that intercepted the separatrix 1 cm apart in z. The ansatz used to fit the $T_e(x)$ and $p_e(x)$ profiles is (see Fig. 6):

$$F(x) = A\left(e^{\frac{-(x-x_o)}{\lambda_1}} - e^{\frac{-(x-x_o)}{\lambda_2}}\right) + B \tag{4.60}$$

The ansatz used to fit the $n_e(x)$ profiles for forward field shots is:

94

$$n_e(x) = Ae^{\frac{-(x-x_o)}{\lambda_1}} + Be^{\frac{-(x-x_o)}{\lambda_2}} + C \qquad (4.61)$$

The reverse field discharges exhibited double-peaked density profiles in the volume of the divertor, so a simple exponential profile would not fit the data. In this case the $n_e(x)$ profile is estimated by taking $\frac{T_e(x)}{p_e(x)}$.
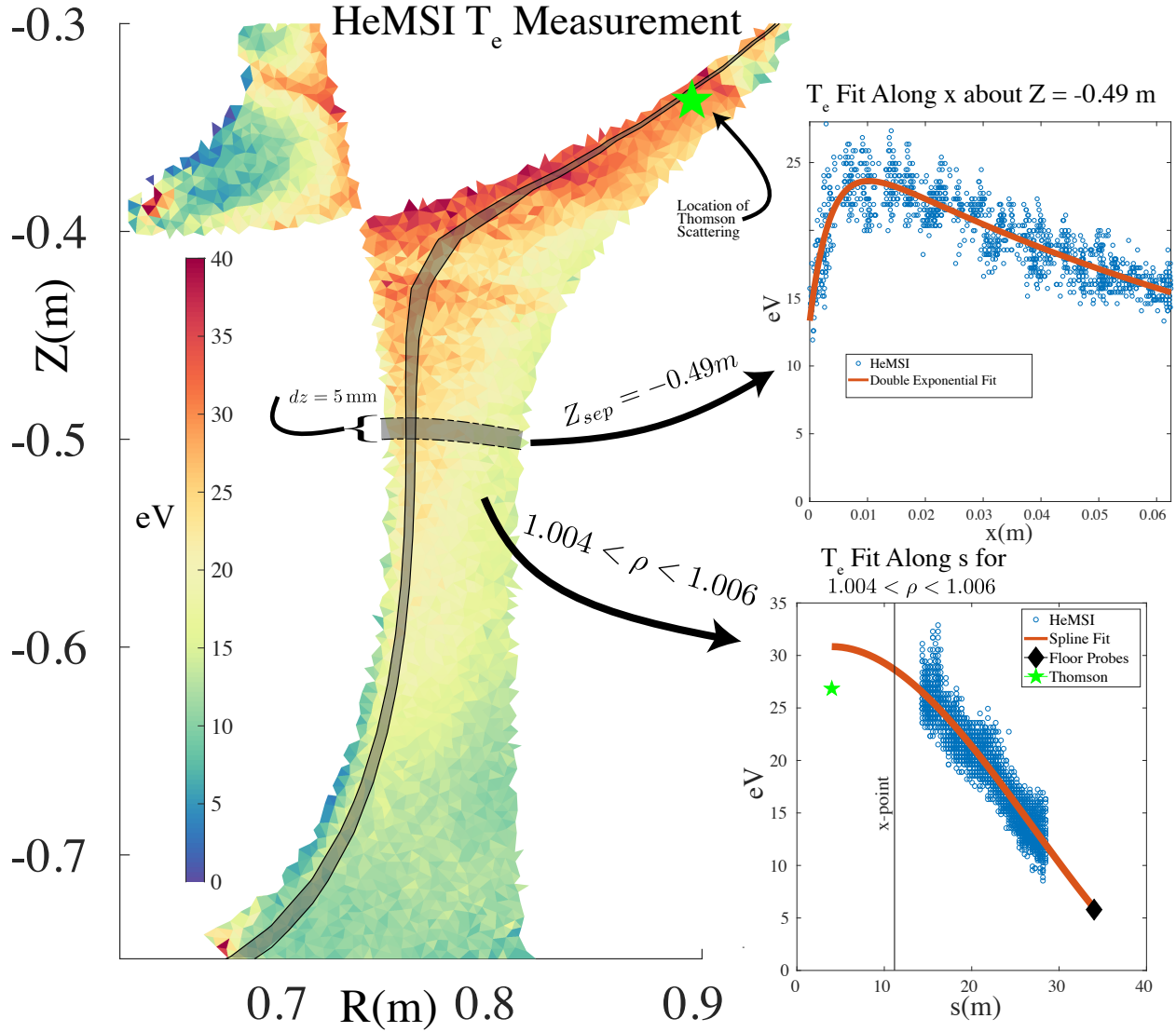
Figure 4.8: Illustration of how the data were binned and fit. The T_e poloidal map represents data taken at a specific time during the conduction limited interval of discharge #1 ($f_x = 11$). The gray ribbons show examples of cross-field binning and flux surface-aligned binning. The fits along x and s are displayed for each highlighted region. The fitted data utilizes HeMSI data collected over all frames.

4.4.4 Fitting Calculated Quantities

When derivatives of calculated quantities were needed, such as $\frac{dV}{dr}$ for calculating E_r or $\frac{dv_{||}}{dx}$ for evaluating $\nabla \cdot n_e v_{||}$, the profiles were also fit with splines. The splines where chosen such that the profiles were smooth when inspected by eye.

4.4.5 Estimating the Electric Potential at the Divertor Plate

Solving for the plasma potential along the leg, as described in Section 4.3, requires the Langmuir probe measurements of $j_0^{||}$, V_{float}, T_e and p_e at the plate. Poor spatial resolution for the lowest flux expansion cases hampered the profile fits. However, as can be seen in Figures 4.9 and 4.10, $j_0^{||}$ and V_{float} varied weakly with flux expansion, so a single spline fit was used to approximate $j_0^{||}$ and V_{float} for each field direction irrespective of flux expansion. The quantities T_e and p_e from the probes were fit individually for each discharge. The lack of spatial coverage for the lowest flux expansion in these cases could not be alleviated. However, only the absolute values of T_e and p_e are needed to set the boundary condition, not their derivatives. Hence, the estimations given by the spline are sufficient for this analysis.
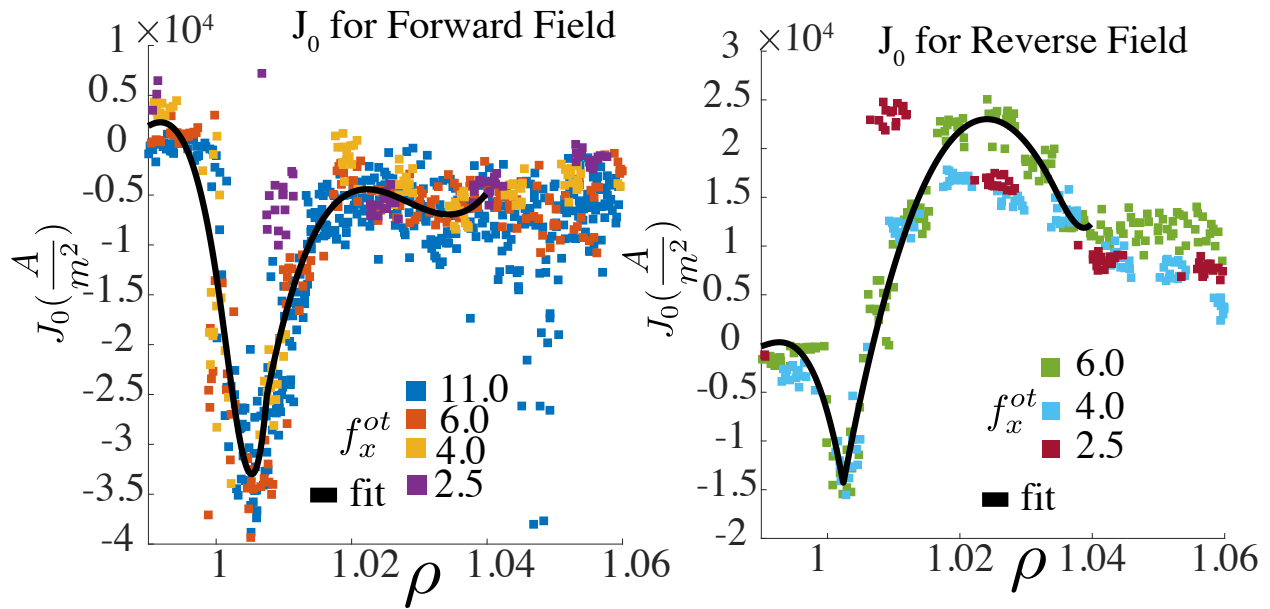
Figure 4.9: The current collected by floor Langmuir probes when the probes are biased to 0 V, $j_0^{||}$, for forward and reverse field cases. Each scattered point is color-coded by the discharge's flux expansion. The black line denotes the spline fit used in the analysis for all cases of the noted field direction.

.
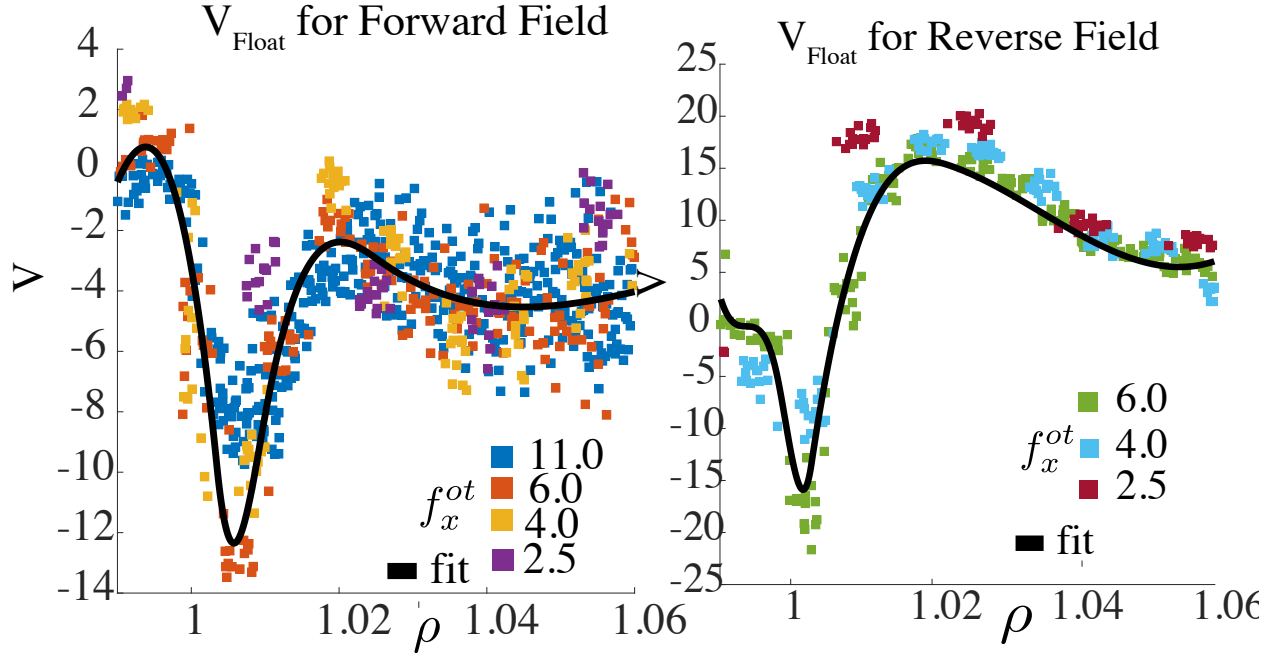
Figure 4.10: The floating voltage of the Langmuir probes for the forward and reverse field cases. Each point is color-coded by the the discharge's flux expansion. The black line denotes the spline fit used in the analysis for all cases of the noted field direction.

.

4.4.6 Assumptions of Fluid Mass and Z_{eff}

The plasma was fueled with deuterium gas. However, the neutral helium density in the scrape-off layer was comparable to the density of neutral deuterium in the SOL. To account for this, a mean ion mass of 3 amu was used in the fluid analysis, and z_{eff} was assumed to be 1.5. The rates of deuterium and helium ionization were measured, and an example of the data is shown in Figure 4.11. The ionization rates were measured by using 2D emissivity maps of He I , He II, and Balmer $3 \rightarrow 2$, the HeMSI $T'_e s$ and $n'_e s$, and electron impact ionization rates from Goto for He and ADAS foror He^+ and D. The figure shows that neutral deuterium and neutral helium are ionized at comparable rates. However, singly ionized helium, He^+, is further ionized at a much slower rate. Thus, the plasma is composed primarily of singly charged ions.

4.4.7 Choosing a Boundary Value for the Fluid Velocity

In the 2PM, the plasma flow at the OMP is assumed to be zero. However, this is an inaccurate assumption as Pfirsch-Schülter flows can be large [109]. Recently, *Tsui 2022* [99] reported parallel mach number profiles for L-mode single-null plasmas in TCV for reverse and forward field discharge with a $f_x^{ot} = 4$. It will be assumed here that the profiles for these shots resemble those reported in *Tsui 2022* [99]. However, enforcing these profiles at the top of the divertor for each discharge results in some flux tubes reaching the singularity at $v_{\parallel}*$, as discussed in Section 4.3.3. Therefore, the boundary value was found by
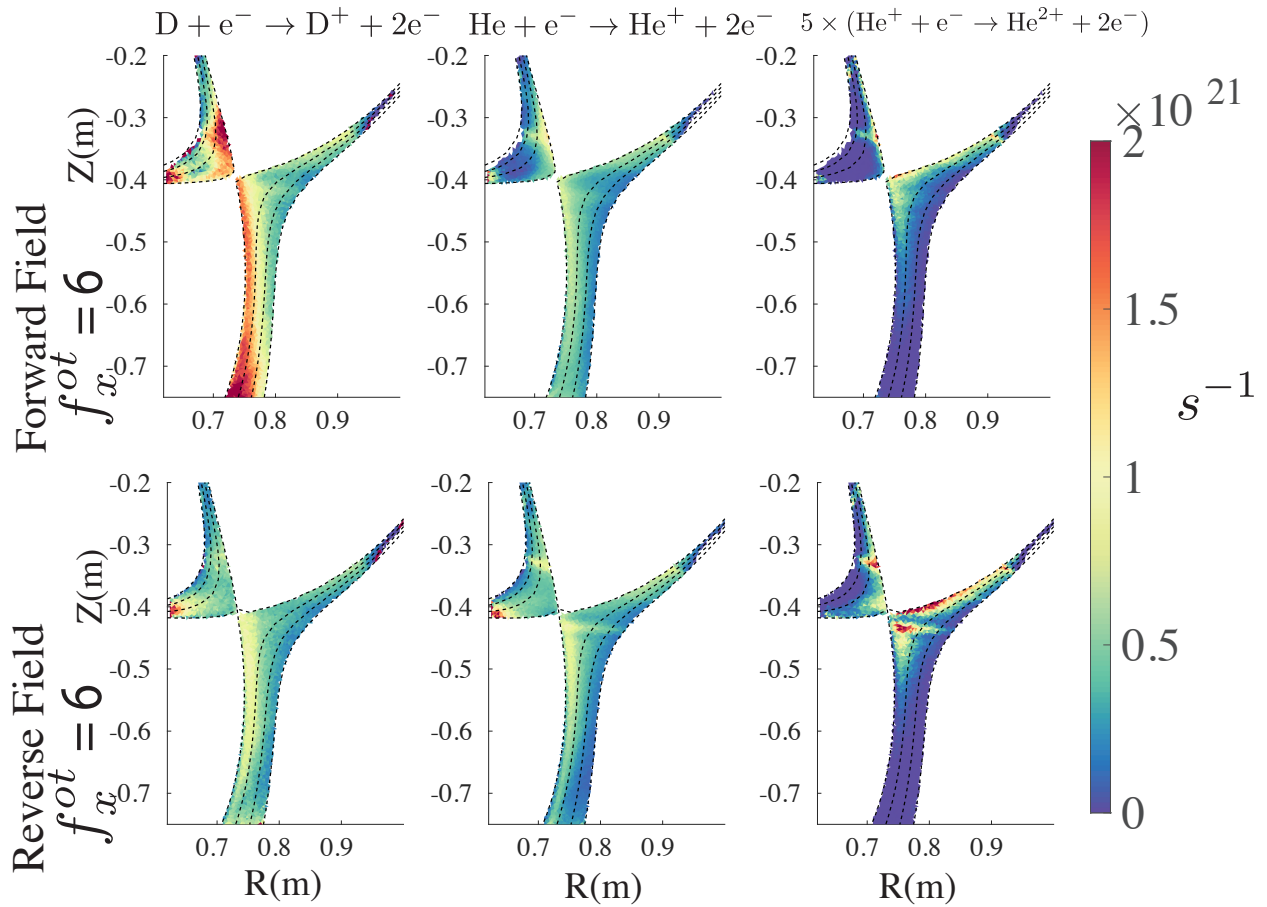
Figure 4.11: Examples of measurements of ionization rates of deuterium, neutral helium, and singly ionized helium. Note that the plots of $He^+ + e \rightarrow He^{2+} + 2e$ are multiplied by 5.

choosing the velocity at the the bottom of the flux tube, $v_b(\rho)$ that projected to the value at the top of the flux tub nearest to that reported in *Tsui 2022* [99]. Values between 0.1 M and 1 M were checked in increments of 0.05 M. The boundary value was enforced at the bottom of the divertor to guarantee $v^{\parallel}$ was directed towards the target and did not exceed 1 M. The profiles that produced the closest match and were used for the calculation are shown in Figure 4.12.
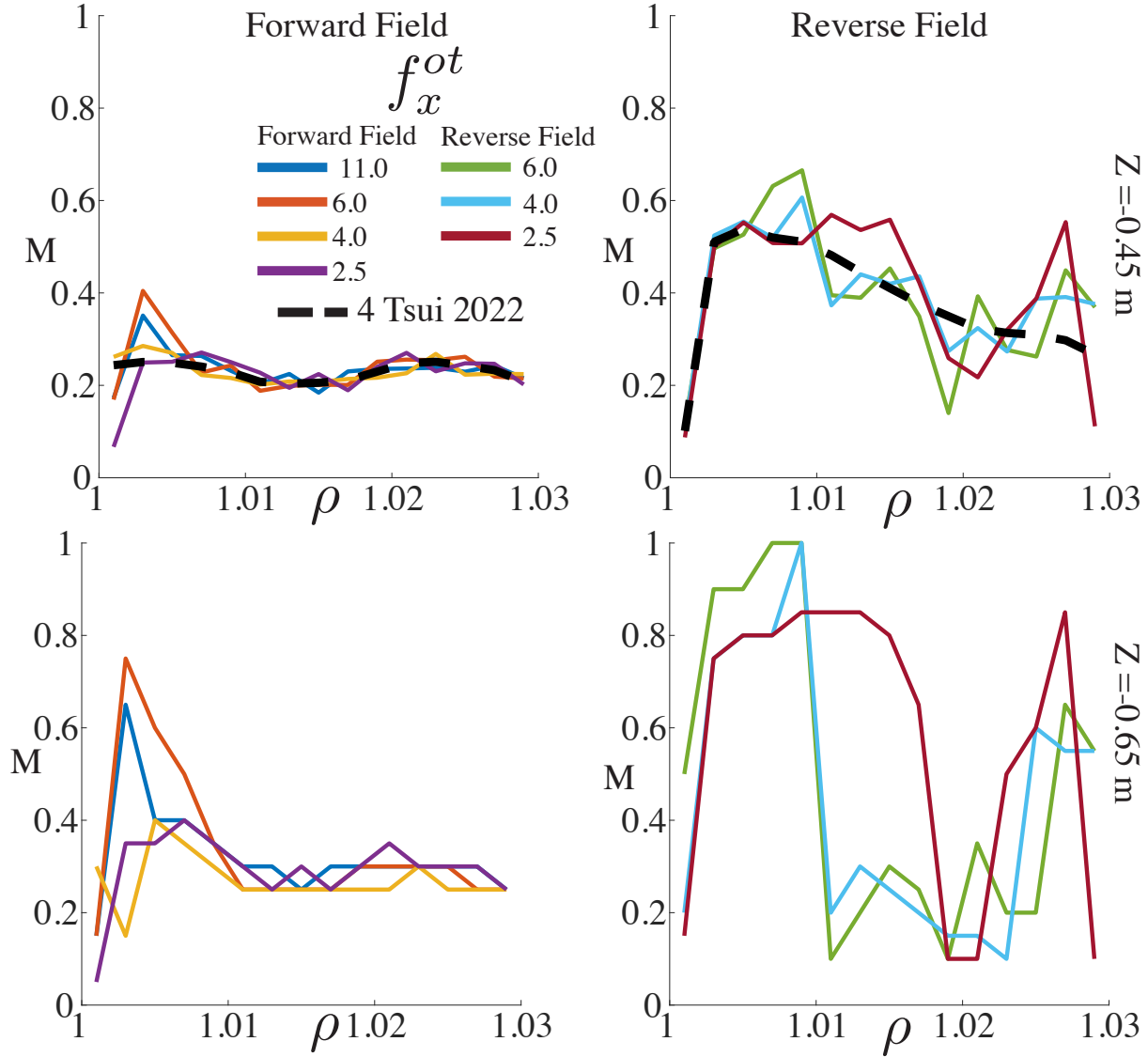
Figure 4.12: Mach number profiles calculated for each flux surface in the discharges at the top and bottom of the analysis region.

4.4.8 Anomalous Transport Ansatzes

Eqs 4.52 and 4.56 attempt to capture the effects of anomalous transport via simple diffusion ansatzes. The parameters $\chi_{\perp}$ and $D_{\perp}$ are correction factors to the steady-state Bragniskii equations weighted by the local derivatives of density and temperature. They are

intended to capture the time-averaged effects of fast scale turbulent and filamentary transport. Within the current paradigm of edge modeling, the values of $\chi_\perp$ and $D_\perp$ are typically set between $0.1\frac{m^2}{s} - 10\frac{m^2}{s}$, and are often chosen to be constant in space [110]. While this may be the current practice, it must be noted that reciprocating probe measurements in the main chamber of Alcator C-MOD demonstrated decades ago that $D_\perp$ grew from $0.1\frac{m^2}{s}$ to $10\frac{m^2}{s}$ when moving from the separatrix into the common flux region [111][112][113]. However, $\chi_\perp$ was observed to be roughly constant in space.

The continued use of fixed $\chi_\perp$ and $D_\perp$ seems to be driven primarily by convenience. In current practice, $\chi_\perp$ and $D_\perp$ are treated as two scalar parameters that can be tuned to match upstream or downstream profiles.

This analysis will solve for $\chi_\perp$ and $D_\perp$ under the assumption that they are constant. This is done for the purpose of simplifying this analysis and is justified because it mimics the assumptions of current model implementations. Furthermore, any inference of $\chi_\perp$ and $D_\perp$ will have significantly large uncertainties. This is due to the inherent uncertainty in approximating derivatives of measurements and the fact that $\vec{v}$ is not directly measured. The inferences of $\chi_\perp$ and $D_\perp$ should be interpreted with respect to their orders of magnitude. Their measurement here is a test if the anomalous transport along the outer leg is of the same order of magnitude as assumed by current modeling practices for TCV.

4.5 Results

4.5.1 Detachment Indicators

The C-III Emission Location

Plasma temperatures below 5 eV are needed for neutral ion collisions to remove significant momentum from exhaust plasma [98], which is required for detachment. The 465 nm C-III line ceases to emit at a slightly higher temperature, between 8-12 eV [14][114]. Thus, the presence or absence of C-III emission is a detachment indicator [14]. The distance the front has retracted from the target is assumed to correlate with lower target temperatures.

Figures 4.13 and 4.14 show the spatial distribution of the C-III emission for forward and reverse fields, respectively. In both figures, the top row displays the plasmas in a conduction-limited regime, before the retraction of the C-III front. In contrast, the bottom rows show the plasmas in a partially detached regime, after the retraction of the C-III front away from the target.

To calculate the height of the emission front above the target, the grid cells between $1.002 < \rho < 1.01$ were binned and averaged by the cells' vertical position. The front was determined to be located at the position at which this average emissivity fell below $8 \times 10^{19} \frac{\text{photons}}{m^3 s}$. The threshold $8 \times 10^{19} \frac{\text{photons}}{m^3 s}$ is approximately the value of the emissivity right below the x-point at the end of the density ramp, at which point the leg has fully retracted.

Using this criterion, Figure 4.15 shows the height of the C-III front for the discharges as a function of $\bar{n}_e$. Increasing poloidal flux expansion does not correlate with a lower $\bar{n}_e$ threshold for retraction of the front. This agrees with the previous reports on reverse field

L-mode discharges [14] and demonstrates that the behavior is the same for forward field L-modes.

The location of the C-III front is insensitive to the poloidal flux expansion. However, the shape of the 2D profile of C-III does exhibit sensitivity to flux expansion in the conduction-limited regime. In the forward field case, the location of the peak C-III emissivity travels significantly down the leg towards the target with increasing poloidal flux expansion. In reverse field, the peak is at the target for the case of the smallest value of poloidal flux expansion but is translated upward for the with increasing poloidal flux expansion.
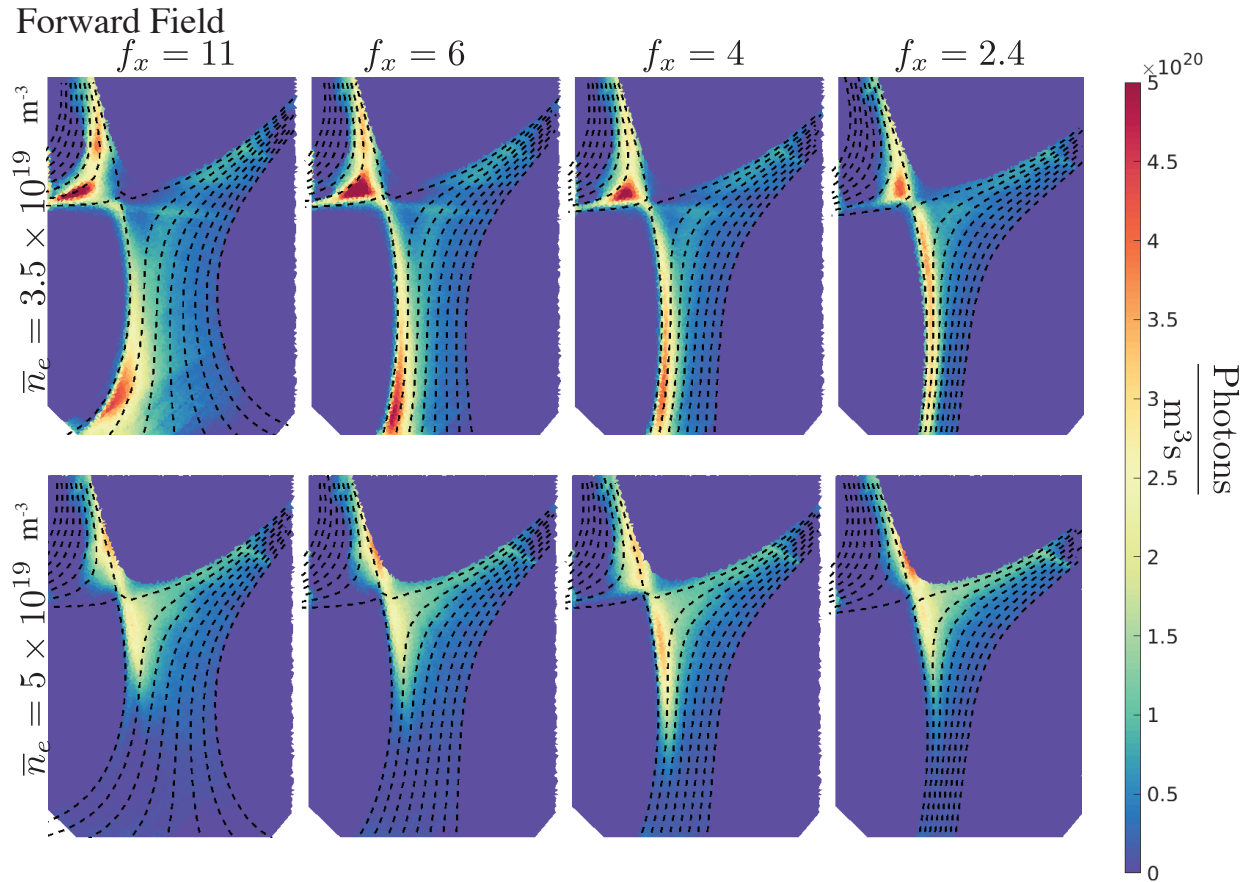
Figure 4.13: C-III fronts for forward field cases at two line-average densities. The top row displays the fronts for $\bar{n}_e = 3.5 \times 10^{19}$. At this density, the plasma resides in a conduction-limited regime, and the front has not yet retracted from the target. The bottom row depicts the fronts for $\bar{n}_e = 5.0 \times 10^{19}$. The plasma is now partially detached, and the front has receded from the outer-strike point.
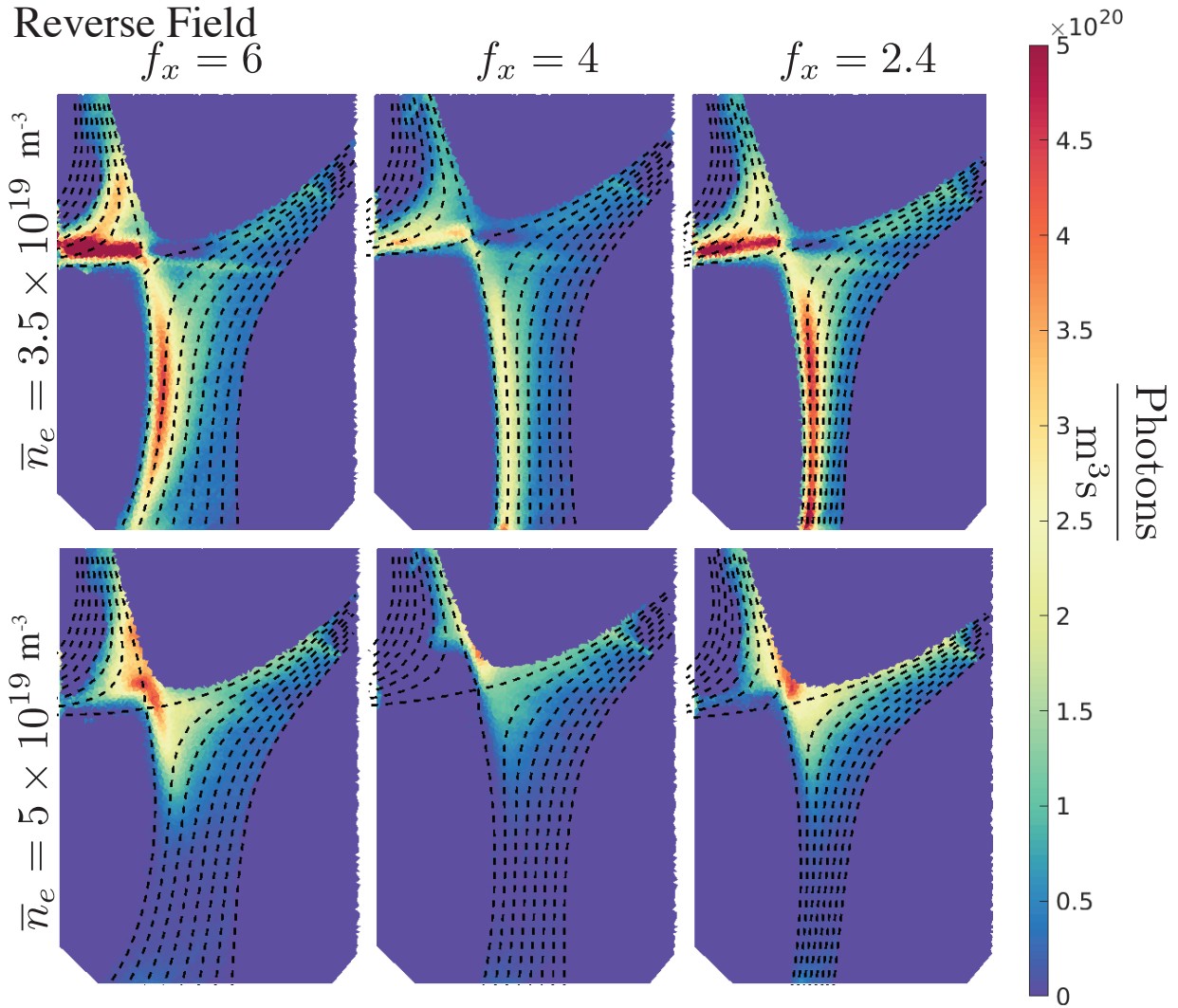
Figure 4.14: C-III fronts for reverse field cases at two line-average densities. The top row displays the fronts for $\bar{n}_e = 3.5 \times 10^{19}$. At this density, the plasma resides in a conduction-limited regime, and the front has not yet retracted from the target. The bottom row depicts the fronts for $\bar{n}_e = 5.0 \times 10^{19}$. The plasma is now partially detached, and the front has receded from the outer-strike point.
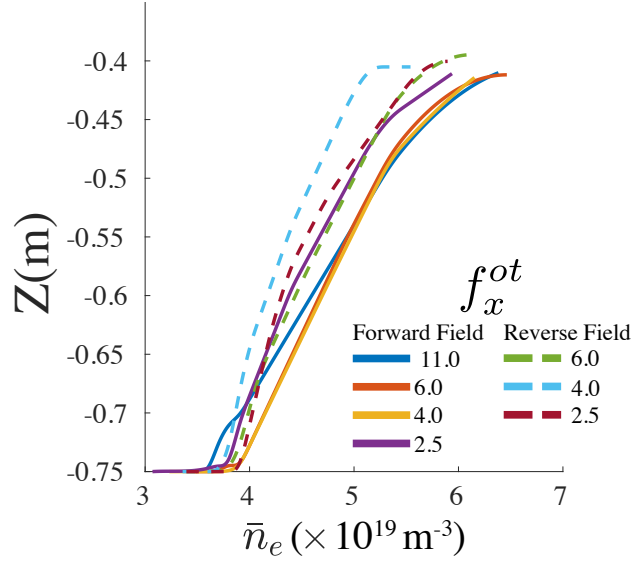
Figure 4.15: The location of the C-III emission fronts versus line-averaged density.

Ion Flux During Detachment

A rollover of the ion flux to the target is typically ascribed to ions being removed from the plasma bulk by recombination processes, indicating that the plasma has fully detached. Figure 4.16 shows the ion fluxes to the walls. The ion flux to the target rolls over in the reverse field cases and plateaus in the forward field cases at $\bar{n}_e$'s above $\sim 5 \times 10^{19} m^{-3}$. However, the key observation regarding the effect of flux expansion is that the $\bar{n}_e$ threshold for a plateau or rollover does not correlate with f_x. Again, this is consistent with *Theiler 2017* [14].

The presence of a rollover in the reverse field cases, but not in the forward field cases, suggests the poloidal drifts play a significant role in determining the fluxes to the outer target. In the reverse field cases, the poloidal components of the diamagnetic and E × B drifts are directed away from the outer target, in the counter-clockwise direction. Thus, in the reverse field cases, the rollover may occur because the parallel velocity has been sufficiently dampened by friction such that the drift-driven component dominates. In the forward field cases, the opposite occurs, as the poloidal drift assists the flow in reaching the outer target despite the increasing neutral friction.

103
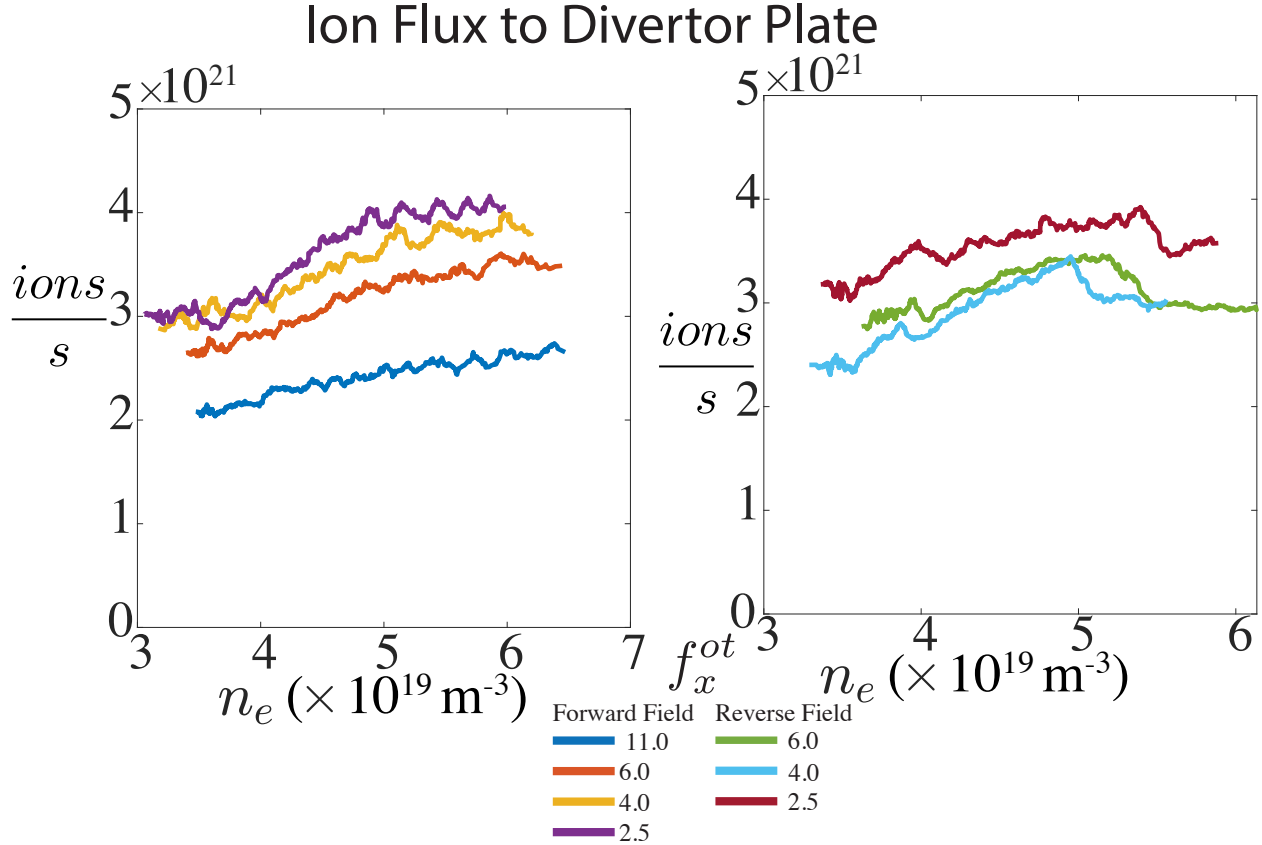
Figure 4.16: Ion flux to divertor plate as a function of line-averaged density.

4.5.2 HeMSI T_e and n_e Profiles During Conduction-Limited Regime

In stark contrast to the partially detached regime, poloidal flux expansion significantly impacts the outer leg in the conduction-limited regime. This is clear in the T_e and n_e profiles shown in Figures 4.17 - 4.18. As can be seen within these figures, T_e systematically falls as f_x^{ot} increases. The largest difference is observed when comparing the forward field $f_x^{ot} = 11$ case to the $f_x^{ot} = 2.5$ forward field case, which exhibit values of 5 eV and 15 eV at the plate, respectively.

The shapes of the n_e profiles differ significantly when the field direction is changed. The forward field discharges have n_e profiles peaked at the separatrix, while the reverse field discharges have local density peaks farther into the CFR. This result is shown in Figure 4.19, in which HeMSI measurements of n_e and p_e are shown along ρ for -0.50 $<$z(m)$<$-0.49. Note the large scatter in n_e at $\rho = 1$ observed in Figure 4.19. The density at the separatrix for the reverse field discharges fluctuates over the 150 ms period of acquisition. Thus, the existence of a second n_e peak at the separatrix fluctuates in the reverse field discharges. While n_e exhibits large fluctuations at $\rho = 1$, note that there is no such scatter in the p_e profiles. Furthermore, the p_e profiles are also translated away from the separatrix into the CFR in the reverse field cases. As will be shown in the analysis in Section 4.5.3, the radial shifting of the profiles is consistent with the direction of the radial component of the E $\times$ B drift. In reverse field, it points from the separatrix into the CFR, while in

forward field it points from the CFR towards the separatrix.

The double-peaked profiles observed in the reverse field plasmas do not extend to the bottom of the divertor. Probe and HeMSI measurements show this in Figure 4.18. At the bottom of the divertor, the effects of the radial drifts have pushed the n_e peak out to $\rho = 1.02$. Curiously, while HeMSI observes only single peaks in the n_e profiles for the forward field discharges, Langmuir probes observe a double peak at the plate for $f_x^{ot} = 6$. Thus, the existence and location of multiple peaks in the density profiles are sensitive to both field direction and poloidal flux expansion.
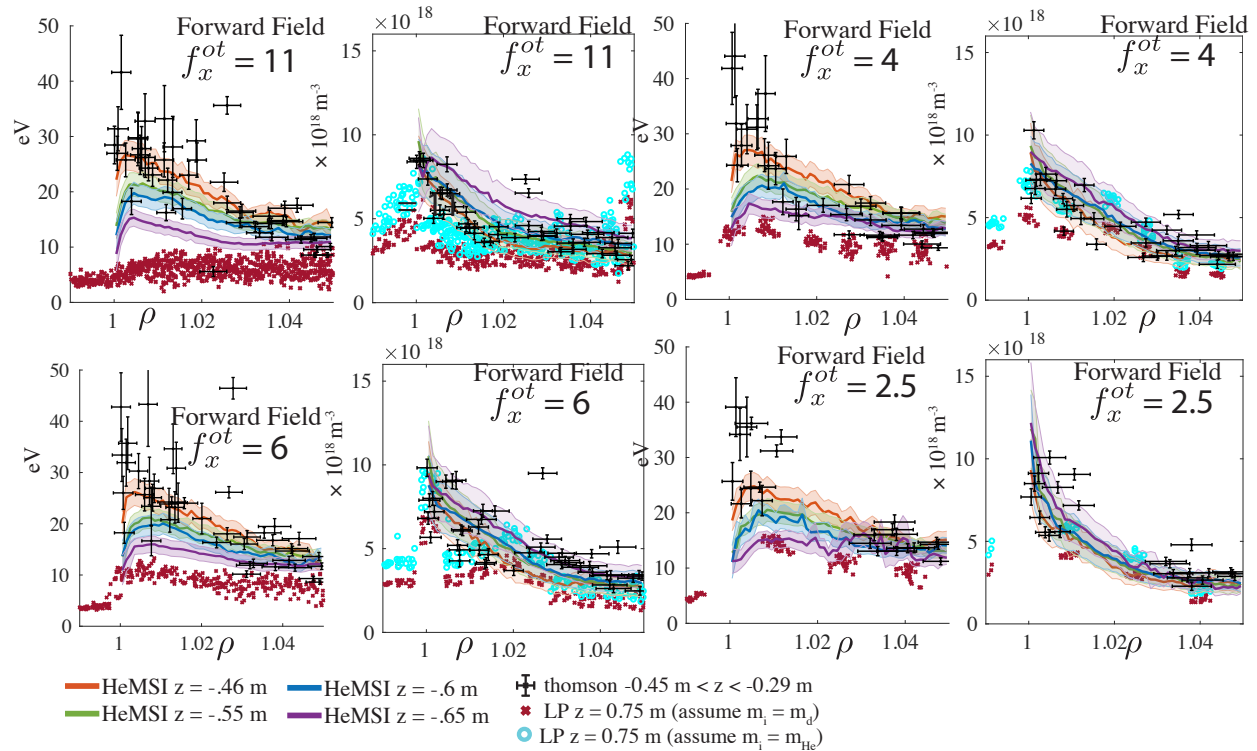
Figure 4.17: Electron temperature and density profiles from HeMSI, Thomson scattering, and Langmuir probes for forward field discharges. Langmuir probe density measurements are shown for the assumption of D^+ ions and He^+ ions moving at their respective sound speeds.
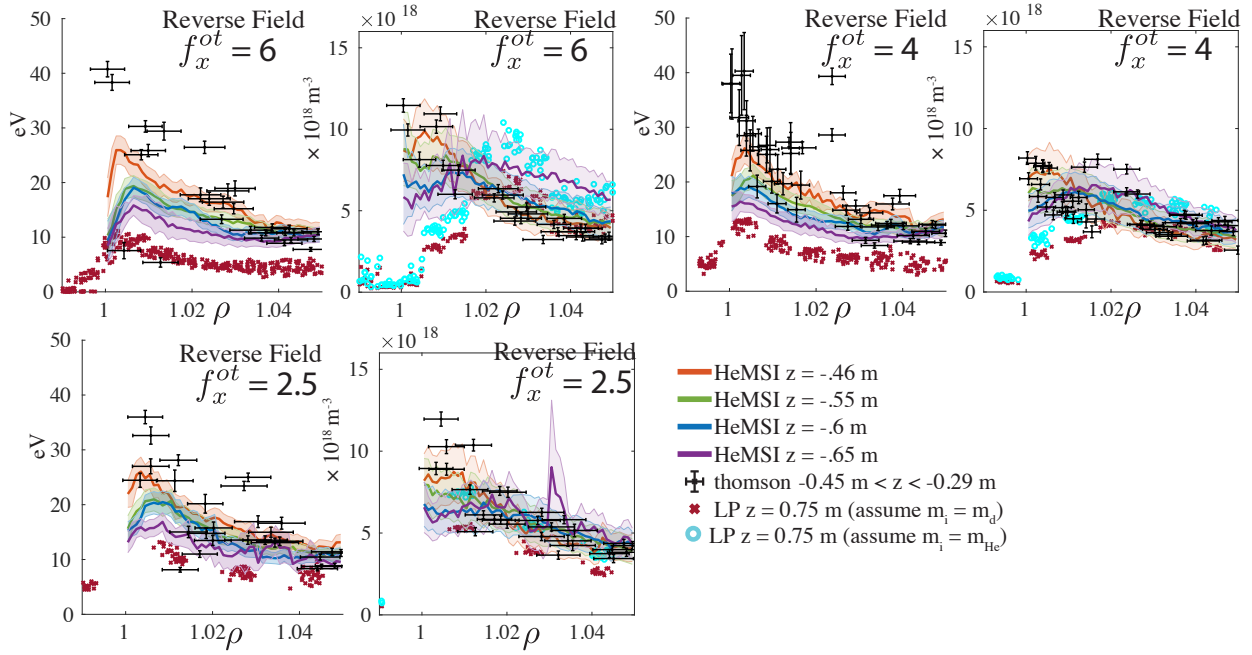
Figure 4.18: Electron temperature and density profiles from HeMSI, Thomson scattering, and Langmuir probes for reverse field discharges. Langmuir probe density measurements are shown for the assumption of D^+ ions and He^+ ions moving at their respective sound speeds.
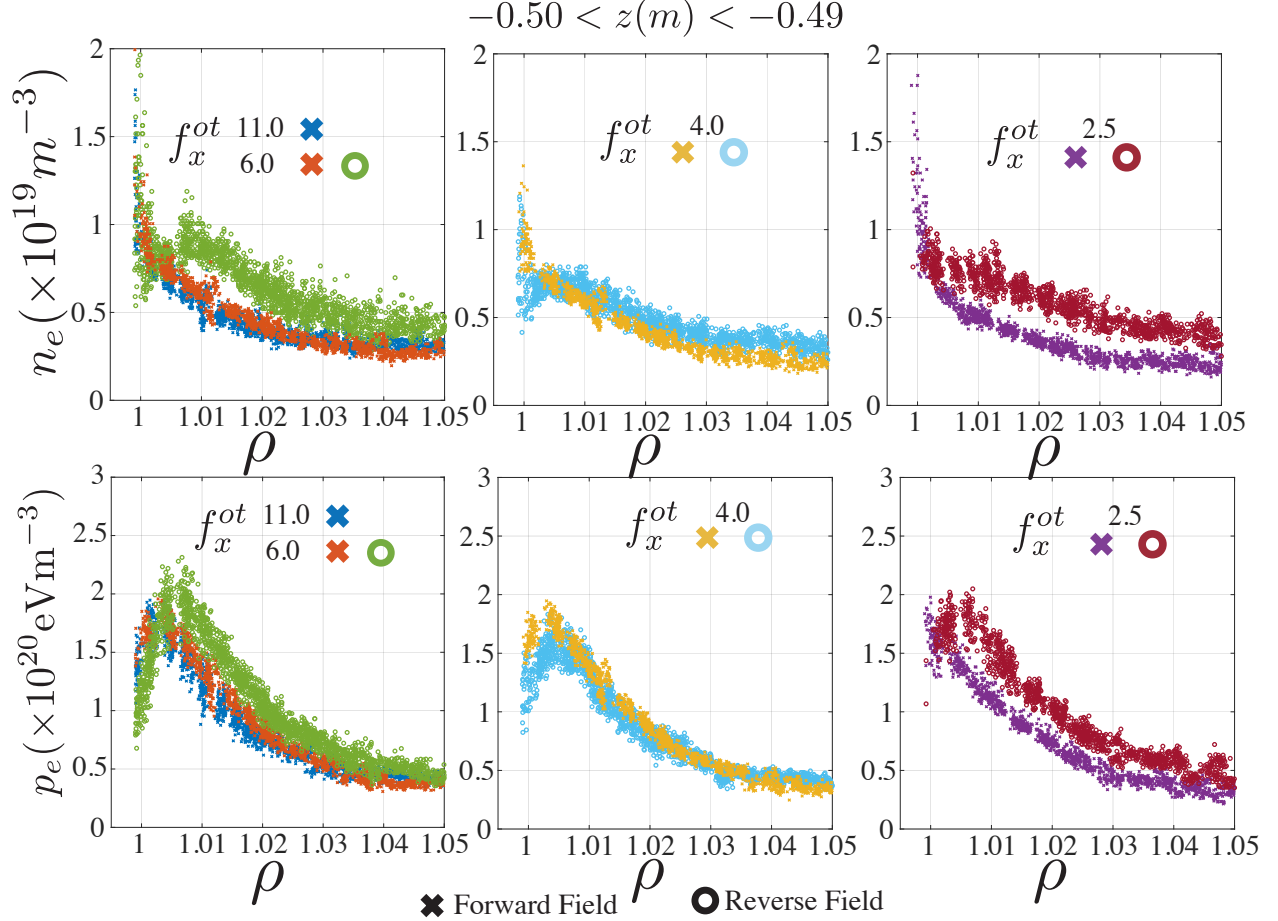
Figure 4.19: HeMSI measurements of p_e and n_e for $-0.50 < z(m) < -0.49$. The profiles highlight the effects of the radial drift.

4.5.3 Calculated Parallel and Drift Velocities

The inferred velocities in the poloidal plane are shown as vector plots in Figures 4.20 and 4.22. These total velocities are calculated by summing the drift velocities with the projection of the parallel velocity into the poloidal plane. As can be observed within the figures, each discharge has at least one shear layer between $1 < \rho < 1.03$. For the forward field discharges, the net velocity along the flux surface is away from the plate near the separatrix and switches to being towards the plate further out in the common flux region. The situation is the opposite for the reverse field discharges. Figures 4.21 and 4.23 display the $\hat{y}$ component of the total poloidal velocity along with the $\hat{y}$ component of the parallel and drift velocities for the regions highlighted in blue in Figures 4.20 and 4.22. These figures show that the drift velocities near the separatrix dominate the poloidal transport. Further into the CFR, the drifts and parallel flow are of the same order. The largest drift velocities, and consequently the largest net total poloidal velocities, are observed for the case of $f_x^{ot} = 4$ in forward field and $f_x^{ot} = 2.5$ in reverse field. The discharges with $f_x^{ot} = 11$ and $f_x^{ot} = 6$ have the smallest drift and net velocities. Thus, poloidal flow along flux surfaces tends to decrease with increasing flux expansion.

This result is expected, considering that the floating potential tends to be a function of flux surface and field direction. To see this, approximate Eq 4.22 as $E_{||} = -\frac{0.71}{e}\frac{\partial T_e}{\partial s}$, then Eq 4.23 is approximately

$$V(\rho, y) \approx -\frac{0.71}{e}(T_e(\rho, y) - T_e(\rho, y_{\text{floor}})) + V_{\text{float}} + \frac{0.5 T_e(\rho, y_{\text{floor}})}{e} \ln\left(4\pi\frac{m_e}{m_i}\right) \qquad (4.62)$$

The separation of neighboring flux surfaces goes as

$$dr(\rho, y) = f_x(\rho, y)dr_{\text{OMP}}$$

Thus, the radial electric field, E^x, and $v_{\text{E}\times\text{B}}^y$ go as $\sim \frac{1}{f_x}$. There is also a trend for the E^y and $v_{\text{E}\times\text{B}}^x$ to increase with flux expansion. These results are shown in Figures 4.24 and 4.25.
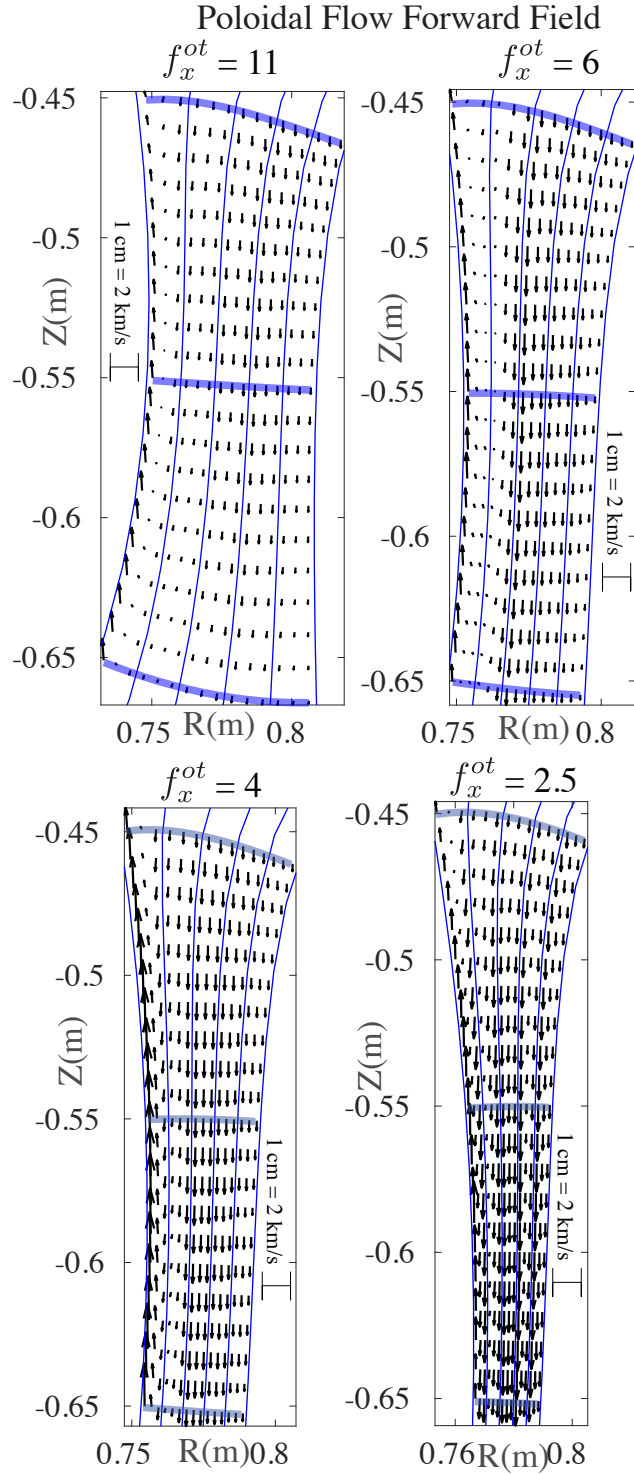
Figure 4.20: Total plasma fluid velocity projected into the poloidal plane for forward field shots. The blue cross-field lines highlight the data shown in Figure 4.21.

Figure 4.21: The parallel velocity projected into the poloidal plane and the $\hat{y}$ component of the $v_{\nabla B}$ and $v_{E \times B}$ drifts for forward field discharges. The sum of these three terms is also shown, which is approximately the net plasma velocity along the flux surface since the curvature drift is negligible. The projection of the local sound speed is also shown for reference. The poloidal projection is given by multiplying the parallel component by $\frac{B}{B^\theta}$.
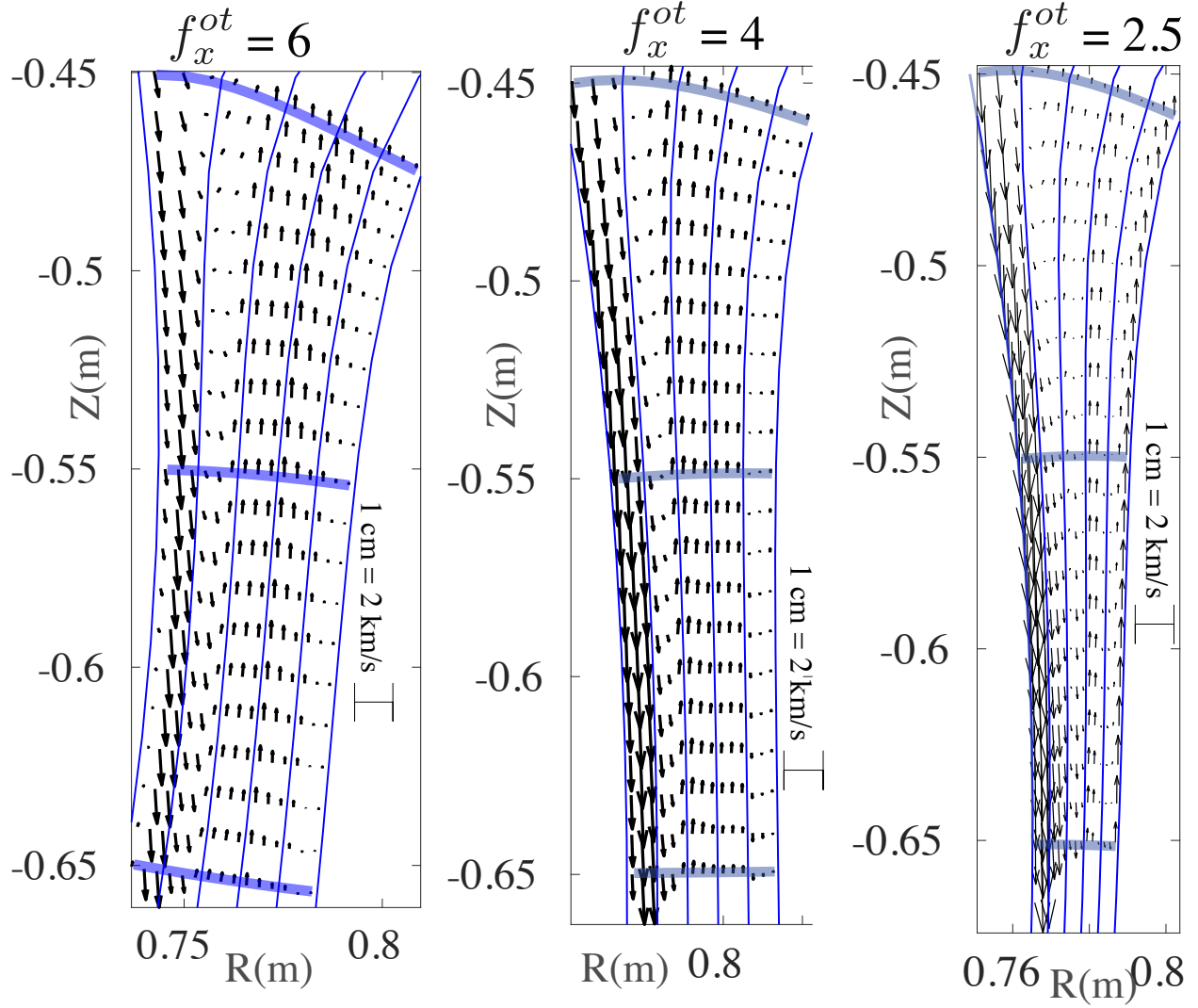
Figure 4.22: Total plasma fluid velocity projected into the poloidal plane for reverse field shots. The blue cross-field lines highlight the data shown in Figure 4.23.

Velocity along Flux Surface in Reverse Field
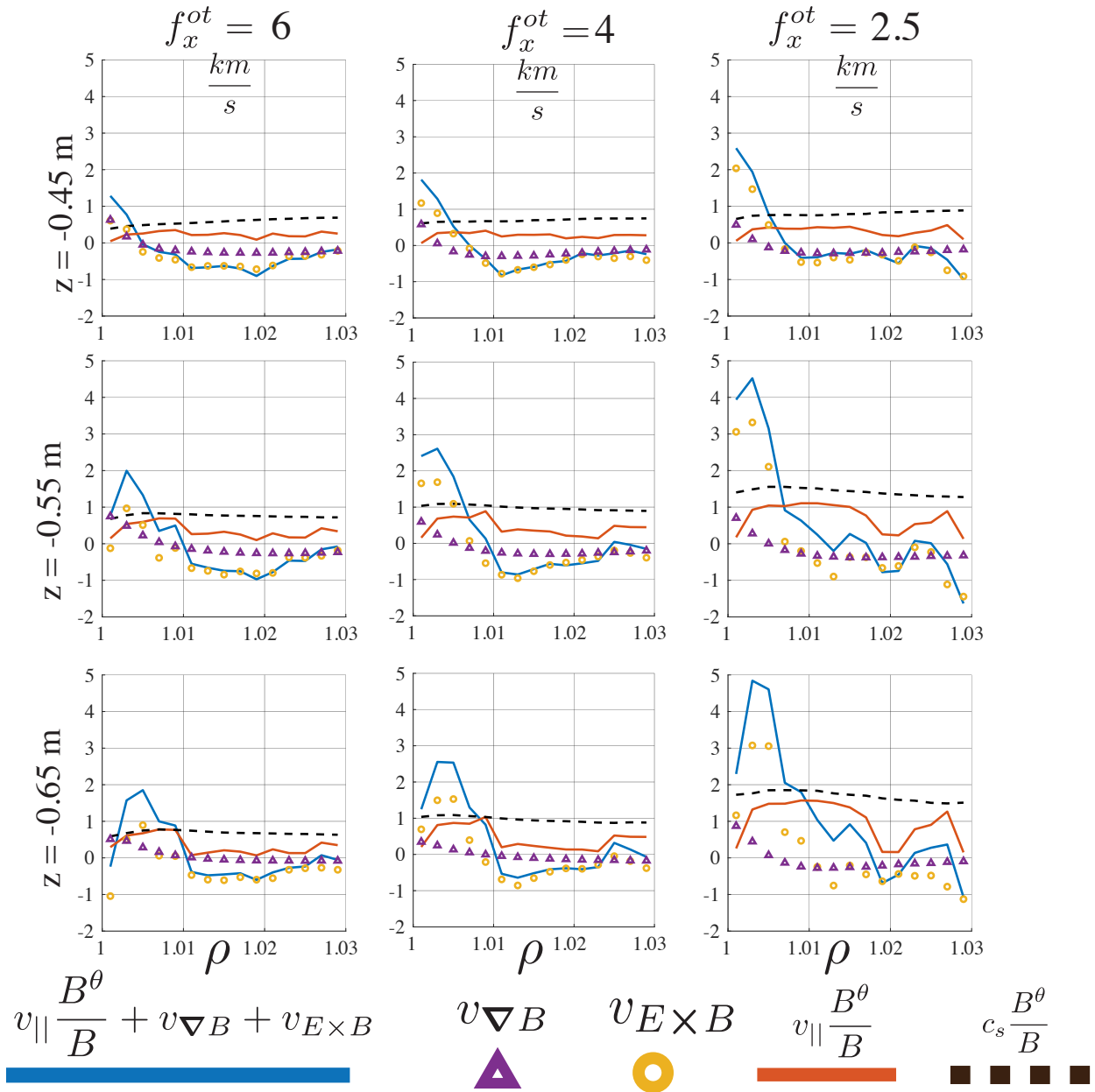
Figure 4.23: The parallel velocity projected into the poloidal plane and the $\hat{y}$ component of the v_{gradB} and $v_{\mathrm{E\times B}}$ drifts for reverse field discharges. The sum of these three terms is also shown, which is approximately the net plasma velocity along the flux surface since the curvature drift is negligible. The projection of the local sound speed is also shown for reference. The poloidal projection is given by multiplying the parallel component by $\frac{B}{B^\theta}$.

Figure 4.24: The electric potential and electric field for forward field discharges of $f_x^{ot} = 11$ and $f_x^{ot} = 2.5$.

Electric Potential and Field in Reverse Field
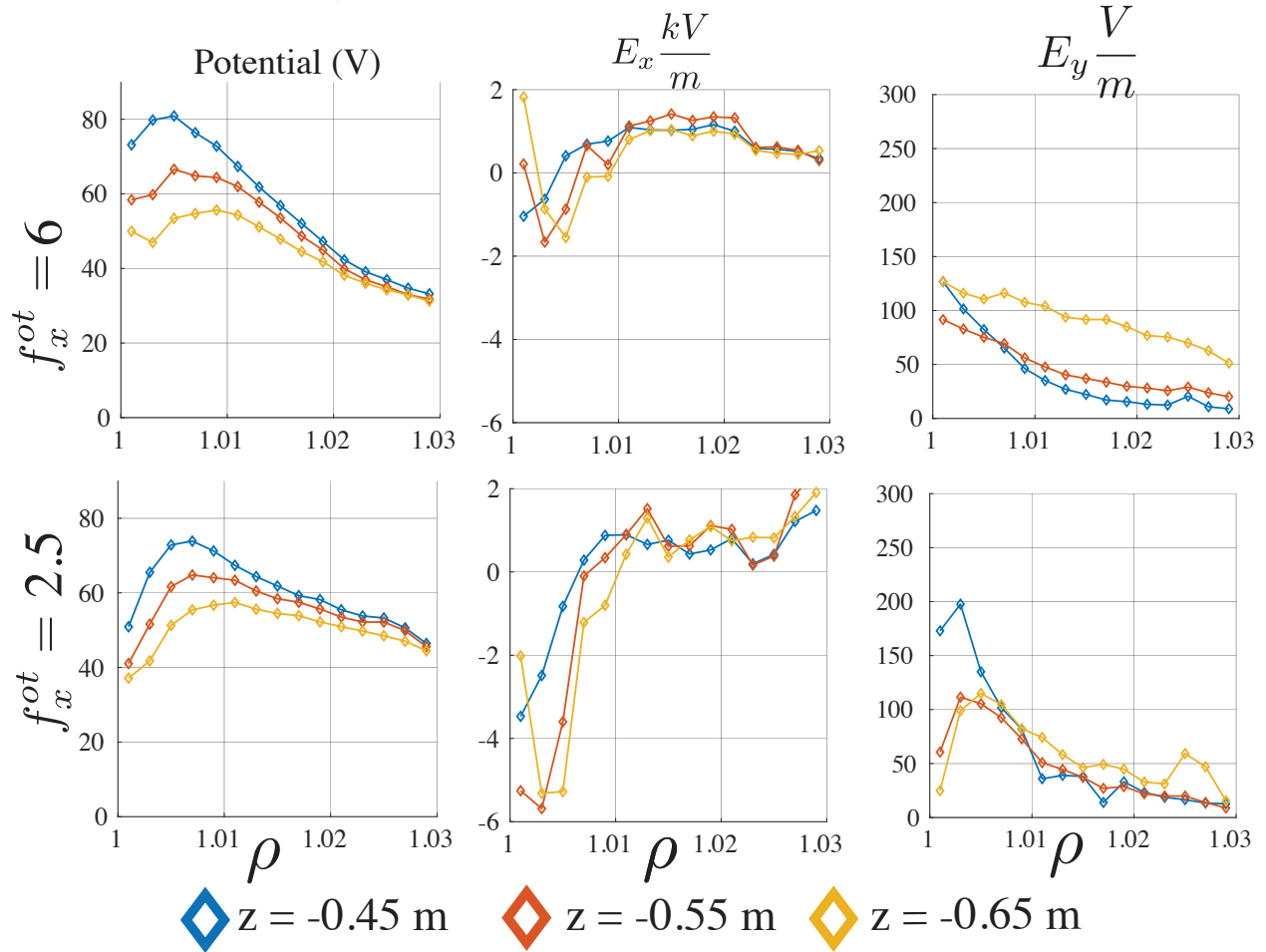
Figure 4.25: The electric potential and electric field for reverse field discharges of $f_x^{ot} = 6$ and $f_x^{ot} = 2.5$.

4.5.4 Power and Particle Balance

Total Power Flow Along the Outer Leg

To evaluate the particle and heat transport, the region between $1 < \rho < 1.03$ along the outer leg is broken up into individual flux surfaces of widths $0.002\Delta\rho$. The heat and ion fluxes crossing each annulus of width $dx = \frac{dx}{d\rho}d\rho$ are then calculated. See Figure 4.5 for a depiction of the x and y coordinates.

The heat fluxes along each flux surface as a function of height in the vessel due to Spitzer heat conduction are shown in Figures 4.26 and 4.27 for forward and reverse fields, respectively. In all cases, when going from the top of the divertor to the divertor plate, the heat carried via electron heat conduction decreases rapidly for the flux tubes immediately outside the separatrix. Farther out into the CFR, the conducted power increases along several flux surfaces while traversing from x-point to the target. This observation is consistent with the hypothesis that power from the near-separatrix CFR is spilling out

away from the separatrix and into the CFR.

The total poloidal heat transport between $1 < \rho < 1.03$ is shown in Figures 4.28 and 4.29 for forward and reverse field discharges, respectively. The power is broken into four components: Spitzer conductivity, heat convection, recombination potential, and radiation losses. The first three quantities are fluxes integrated across the annulus area, while radiation losses are integrated over the test volume between the top of the divertor and the current z position. The sum of all these terms is also shown and is expected to be constant, assuming cross-field losses to the region outside $1 < \rho < 1.03$ are negligible. The total power is constant within an estimated uncertainty of 30%. This uncertainty is calculated by assuming a 20% uncertainty in the measured n_e and a 10% uncertainty in T_e [27]. For discharges #2, #3, and #6, the power flux at the plate ($z = -0.75$) was measured using IR thermography. In these cases, the power arriving between $1 < \rho < 1.03$ and that over the whole plate is also shown in Figures 4.28 and 4.29. The total power accounted for via the HeMSI analysis should always fall between these two values, and the total power at the top of the divertor should equal all the power arriving at the plate. This relation is satisfied for all discharges within the estimated uncertainties.

Electron heat conduction is observed to be the largest component of the total poloidal heat flux in Figures 4.28 and 4.29. However, convection is of the same order of magnitude in all cases, even though large temperature gradients exist at the separatrix. Therefore, the two-point modeling as described in Section 4.1 (which assumes very dominant heat conduction) is not valid.

Radiation losses increase with flux expansion for each field direction. These losses are typically negligible except in the cases of discharges # 1 and # 5. In both these cases, the total power loss from radiation between $-0.65 < z(m) < -0.45$ approaches the flux at the bottom of the observation region.

The poloidal heat fluxes are further resolved in Figures 4.31 and 4.32 for forward and reverse fields, respectively. In them, the total power is resolved into both conduction and convection components, and the convection component is further resolved into convection via parallel transport and transport via the poloidal E × B drift. In these figures, fluxes toward the outer target are positive, and those toward the OMP are negative. The figures show that convection is always comparable to conduction in these TCV discharges and represents one of the major conclusions from this work. However, near the separatrix, the E × B drift comprises the majority of the convected heat, while further into the CFR, the convected power due to the parallel flow is roughly of the same magnitude as that due to the drift. These differences between transport from parallel flow and E × B flow result in distinct heat flux profiles between the forward and reverse field cases. In the forward field cases, the drift is away from the target near the separatrix and towards the target farther out into the CFR. This flips in the reverse field direction. The heat flux due to conduction and parallel flow is always towards the target. Therefore, the heat flux near the separatrix is larger in reverse field than in forward field, but the heat flux farther out into the CFR is larger in forward field due to the poloidal drift switching directions.
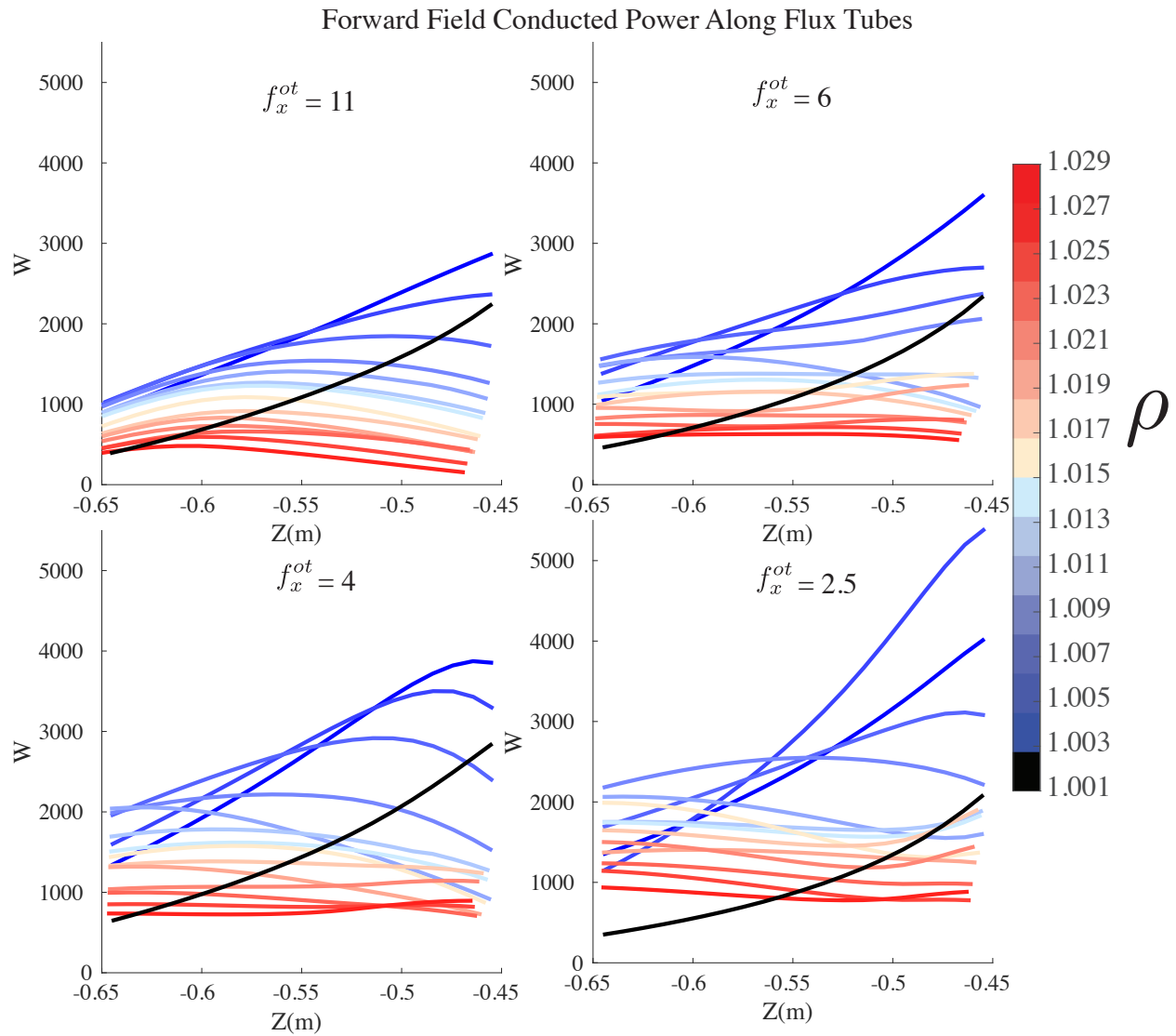
Figure 4.26: Power from electron heat conduction crossing toroidal annulus for forward field discharge. The z coordinate (abscissa axis) in these figures refers to the point at which the x coordinate intercepts the y coordinate along the separatrix.
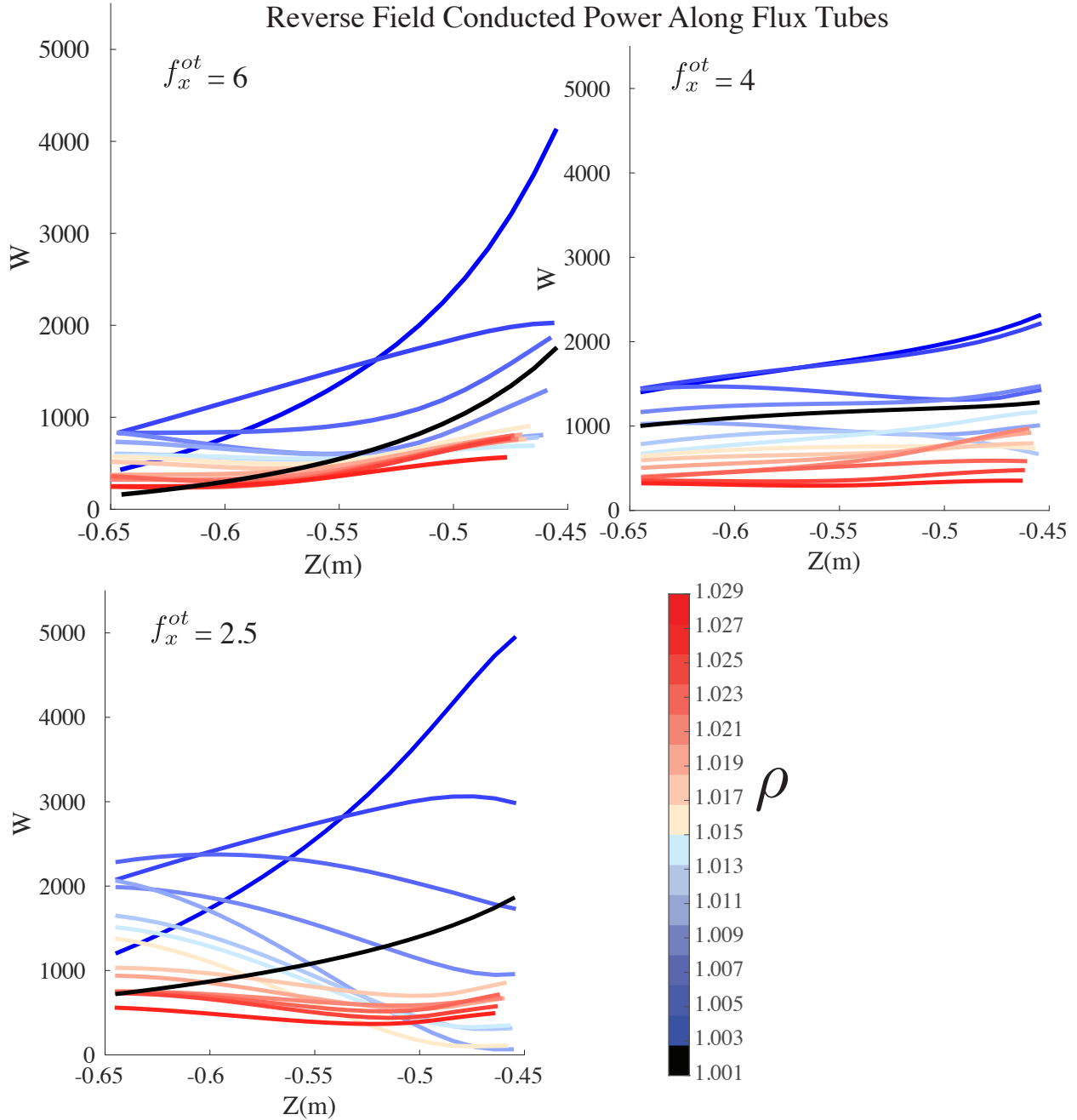
Figure 4.27: Power from electron heat conduction crossing toroidal annulus for reverse field discharge. The z coordinate (abscissa axis) in these figures refers to the point at which the x coordinate intercepts the y coordinate along the separatrix.

The net poloidal heat transport between $1 < \rho < 1.03$ is shown in Figures 4.28 and 4.29 for forward and reverse field discharges, respectively. The figures display the total poloidal heat flux as well as its components. While conduction is the largest heat transport mechanism, heat convection is still significant. Note that the heat flux calculated from the HeMSI measurements is consistent with the IR measurements at the divertor plate.

Figure 4.28: The net heat flux passing through an annulus bound between $1 < \rho < 1.03$ as a function of z position for forward field discharges. q_U refers to the potential recombination energy flowing through the annulus recouped when the ions recombine at the plate. The recombination energy is calculated as n_e multiplied by the average recombination energy of He^+ and D^+.

Reverse Field Power Through Annulus $1 < \rho < 1.03$
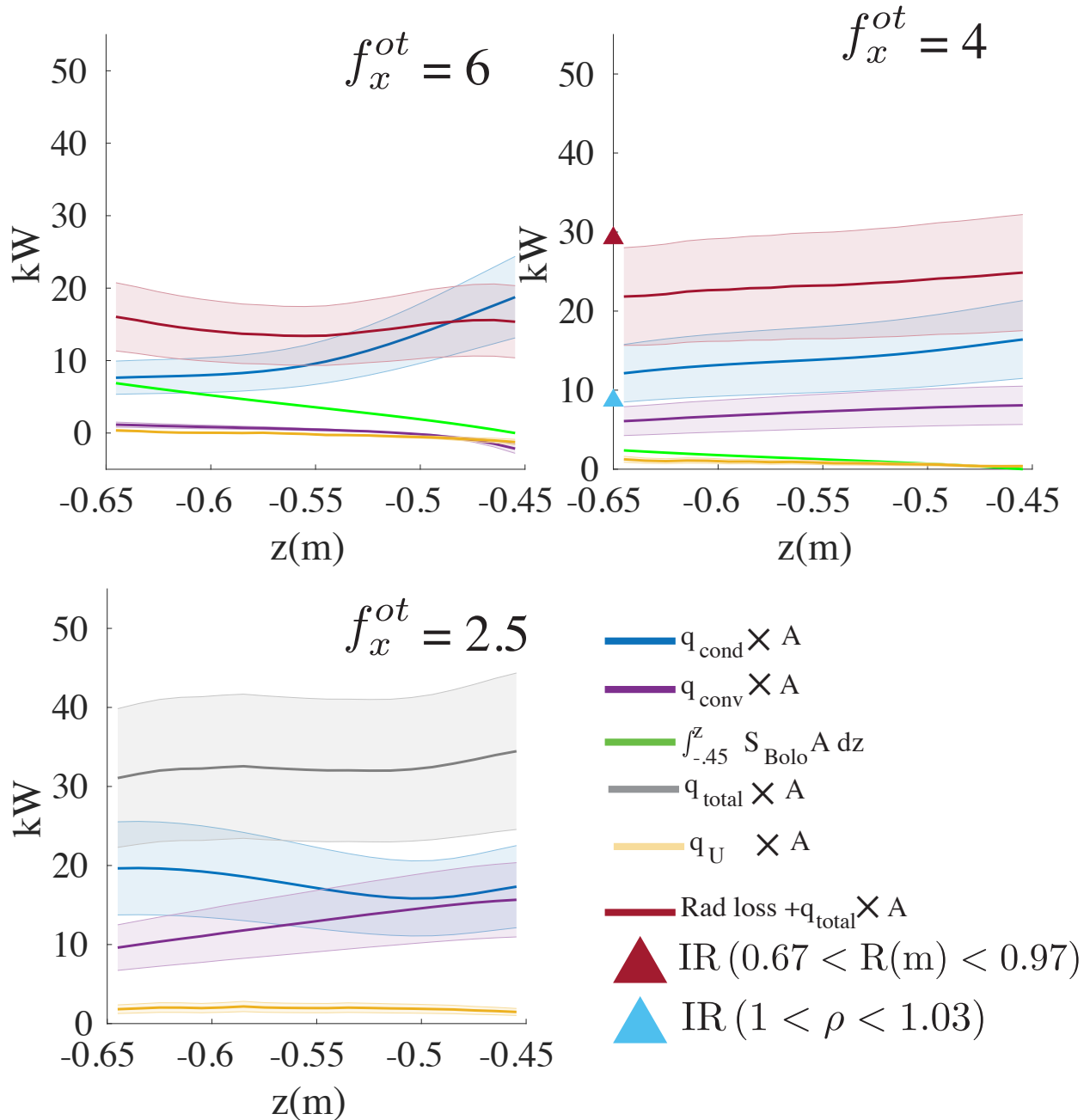
Figure 4.29: The net heat flux passing through an annulus bound between $1 < \rho < 1.03$ as a function of z position for reverse field discharges. q_U refers to the potential recombination energy flowing through the annulus recouped when the ions recombine at the plate.

Poloidal and Radial Heat Transport During Conduction-Limited Regime

Figures 4.31 and 4.32 show the poloidal heat flux along the flux surfaces for the forward and reverse field discharges, respectively. Both the total heat fluxes are shown, as well

as the heat fluxes from individual mechanisms. Positive values indicate fluxes in the direction of the outer target, and negative values indicate fluxes towards the x-point. The most prominent difference among the different discharges is observed in comparing the forward and reverse field cases. This is a direct consequence of the different drift directions. In the forward field cases, the drifts are directed towards the x-point in the region near the separatrix, and towards the plate farther into the CFR. This scenario flips in the reverse field case. The heat conveyed through parallel convection and conduction is always directed toward the target. Consequently, the peak heat flux, which is about the separatrix, is strongest in the case of the reverse field discharges. This is because the drifts and parallel heat flux are in the same direction immediately about the separatrix.

Flux expansion has a small effect on the profiles. Increasing flux expansion causes flux tubes to have greater spatial separation. Since the potential at the plate is nearly a flux function, this causes the electric field to vary as $\frac{1}{f_x}$. The result is that smaller flux expansions have larger poloidal drifts.

Increasing poloidal flux expansion increases the amount of cross-field drift transport at the separatrix, as shown in Figure 4.30.
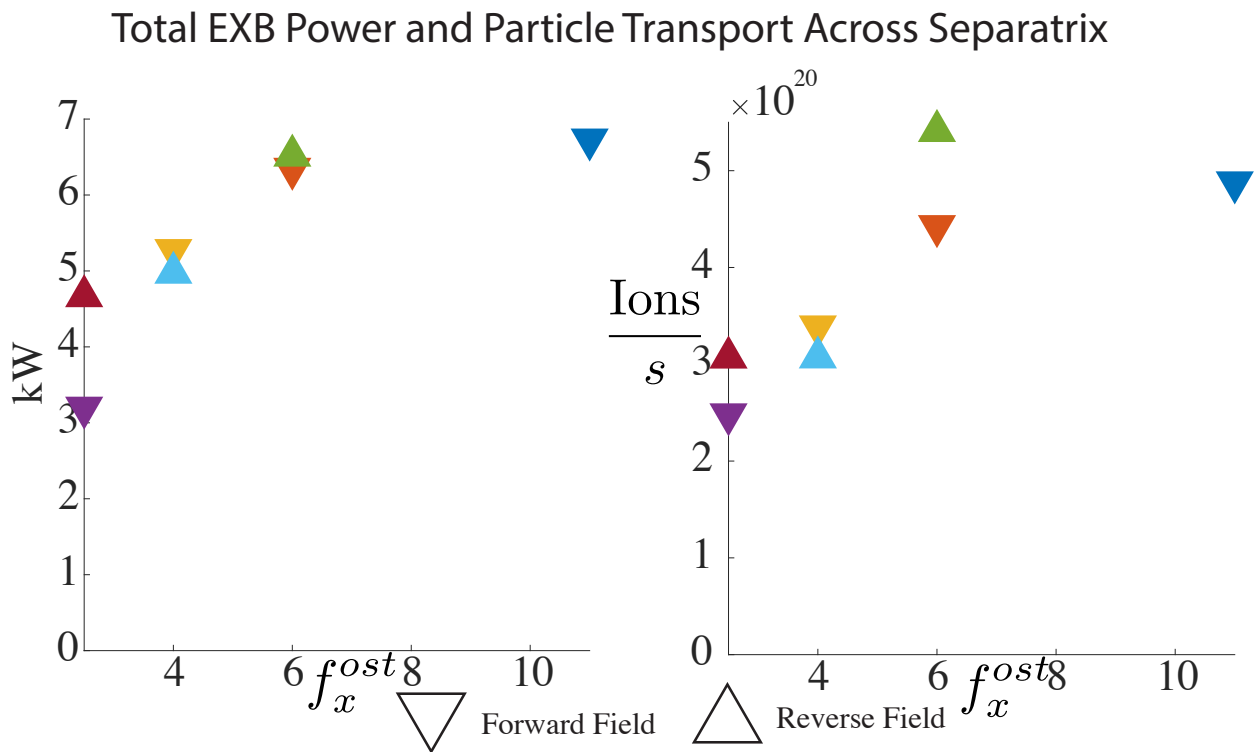
Figure 4.30: Magnitudes of power and particle fluxes crossing the separatrix due to the $v_{E\times B}$ drift over the outer leg. The totals are plotted by poloidal flux expansion at the target. For the forward field cases, the fluxes are directed towards the private flux region. For the reverse field cases they are directed toward the CFR.

Forward Field Poloidal Heat Transport
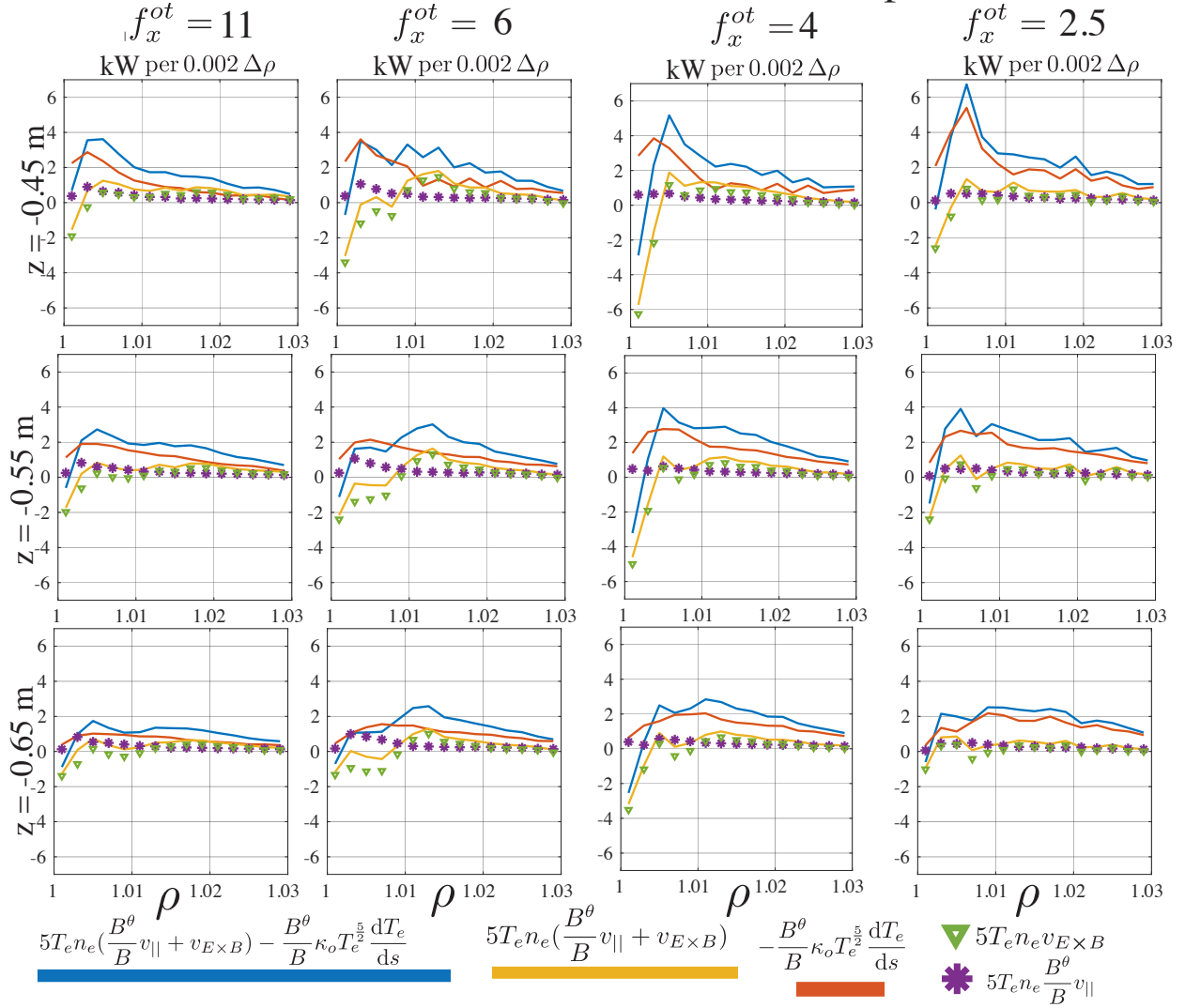
Figure 4.31: Heat flowing through annuluses with widths of $0.002\Delta\rho$ for the discharges in the forward field direction.

Reverse Field Poloidal Heat Transport
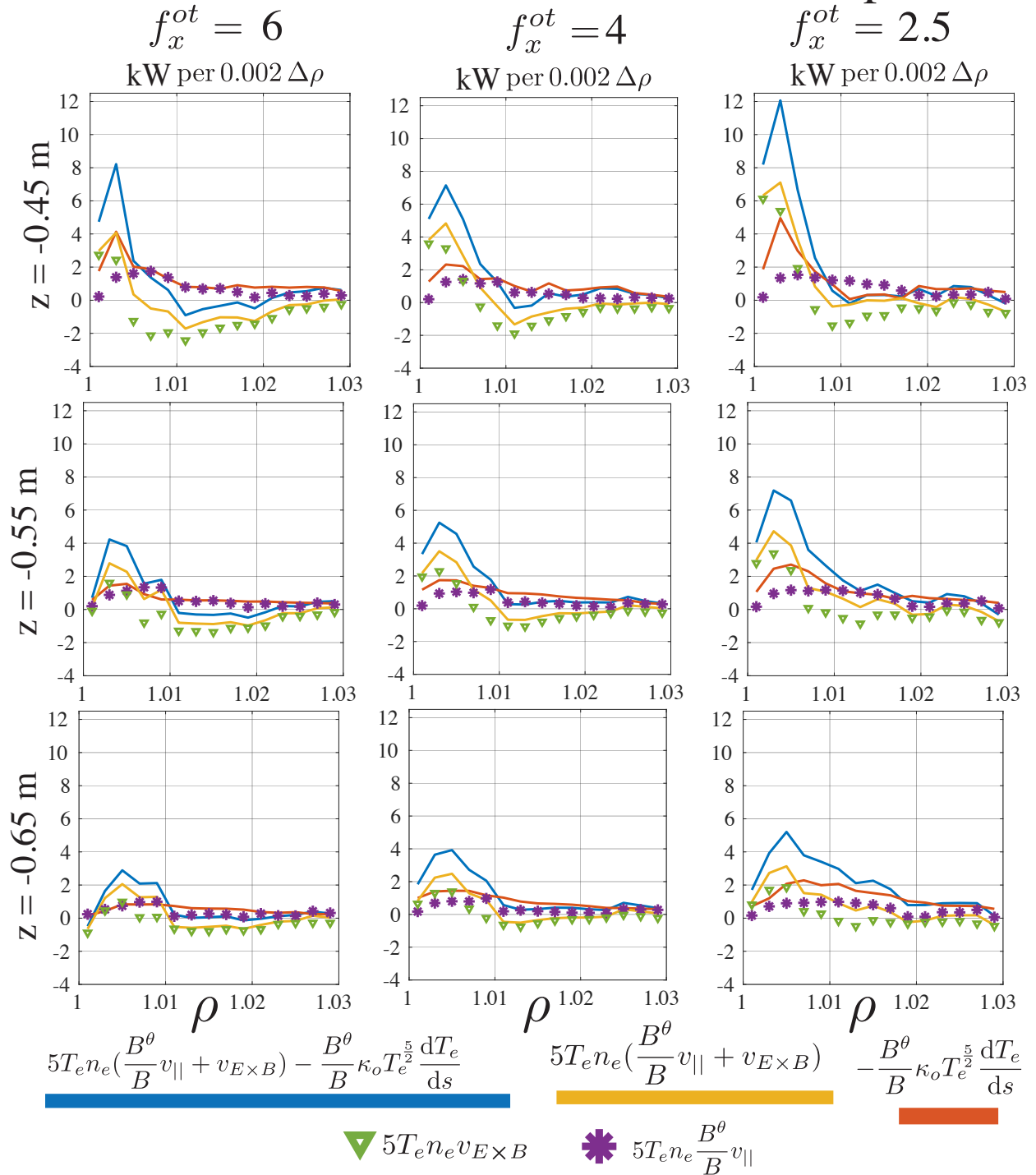
Figure 4.32: Heat flowing through annuluses with widths of $0.002\Delta\rho$ for the discharges in the reverse field direction.

While the total heat flux along the leg is approximately constant, as seen in Section 4.5.4, the heat flowing along each flux tube varies significantly. Figures 4.26 and 4.27 show the

total power conducted in the poloidal direction for individual flux surfaces in the forward and reverse field cases, respectively. As shown in them, the power is concentrated within the flux tubes immediately outside the separatrix $\rho < 1.005$ at the top of the divertor ($z = 0.45$m). However, traversing from the top of the divertor towards the target, the power conducted along these near separatrix flux tubes falls off dramatically. In contrast, the power conveyed along flux tubes with $\rho > 1.005$ increases. Nonetheless, as observed in Figures 4.28-4.29, the total power conducted along the leg remains constant. The power is dispersed from the separatrix outward further into the CFR. Comparing the cases of the forward field with $f_x^{ot} = 11$ and $f_x^{ot} = 2.5$ reveals the effects of poloidal flux expansion. In the case of larger flux expansion, the power in each flux tube begins to decrease (rolls over) as it approaches the target. However, in the cases of lower flux expansion, the power being transported via conduction in regions with $\rho > 1.008$ is still rising. Thus, increasing flux expansion allows for better cross-field heat transport.

Forward Field $f_x^{ot} = 11$ $-0.49 < z(m) < -0.48$

a)

T_e

eV

- data $-0.49 < z(m) < -0.48$
- $A\left(e^{\frac{-(x-x_o)}{\lambda_1}} - e^{\frac{-(x-x_o)}{\lambda_2}}\right) + B$

$\lambda_1 = 4\,\mathrm{mm}$ $x_o = 3\,\mathrm{mm}$
$\lambda_2 = 91\,\mathrm{mm}$ $B = 6\,\mathrm{eV}$
$A = 22\,\mathrm{eV}$

x (distance from separatrix) (m)

b)

n_e

- data $-0.49 < z(m) < -0.48$
- $Ae^{\frac{-x}{\lambda_1}} + Be^{\frac{-x}{\lambda_2}} + C$

$\times 10^{18}\ \mathrm{m}^{-3}$

$A = 2\times10^{18}\,\mathrm{m}^{-3}$
$B = 7\times10^{18}\,\mathrm{m}^{-3}$ $\lambda_1 = 3\,\mathrm{mm}$
$C = 2\times10^{18}\,\mathrm{m}^{-3}$ $\lambda_2 = 43\,\mathrm{mm}$

x (distance from separatrix) (m)

c)

$\frac{eV}{m}$ $\frac{eV}{m^2}$

$\frac{dT_e}{ds}\left(\frac{eV}{m}\right)$
$\frac{d^2T_e}{ds^2}\left(\frac{eV}{m^2}\right)$

x (m)

d)

q_{sp}
q_{conv}

$\times10^6\ \frac{W}{m^2}$

x(m)

e)

$\nabla\cdot q_{sp}$
$\nabla\cdot q_{conv}$

$\times10^5\ \frac{W}{m^3}$

x(m)

f)

w/o Flux Limitor or Q_{ei}
with Flux Limitor & Q_{ei}

ρ

$\chi_\perp\ \frac{m^2}{s}$

x (distance from separatrix) (m)

g)

w/o Flux Limitor or Q_{ei}
with Flux Limitor & Q_{ei}

ρ

$\chi_\perp\ \frac{m^2}{s}$

$\chi_\perp = 10\frac{m^2}{s}$

x (m)

Figure 4.33: Cross-field profiles where the top horizontal axis gives coordinates in ρ and the bottom in $x(m)$. **a)** HeMSI T_e data and fitted profile using Eq 4.60. **b)** HeMSI n_e data and fitted profile using Eq 4.61. **c)** $\frac{dT_e}{ds}$ and $\frac{d^2T_e}{ds^2}$. **d)** Magnitude of conducted heat flux $|\vec{q}_{sp}|$ and convected heat flux $|\vec{q}_{conv}|$. **e)** Divergence of conducted and convected heat fluxes. **f-g)** Inferred value of $\chi_\perp$ for $1 < \rho < 1.005$ and $\rho > 1.005$.

Calculations of $\chi_\perp$ and $D_\perp$

Rewriting Eq 4.58, $\chi_\perp$ can be expressed as

$$\chi_\perp = -\frac{Q_{\rm rad} + Q_{\rm Sion} - \boldsymbol{\nabla} \cdot \mathbf{q}_{\rm sp} - \boldsymbol{\nabla} \cdot \vec{q}_{\rm conv} - \boldsymbol{\nabla} \cdot \vec{q}_D}{\boldsymbol{\nabla} \cdot n_{\rm e} \boldsymbol{\nabla} T_{\rm e}} \tag{4.63}$$

Having calculated $T_{\rm e}$, $n_{\rm e}$, $\mathbf{v}$, $Q_{\rm rad}$, $Q_{\rm Sion}$ using the HeMSI, bolometry, and Langmuir probes measurements, $\chi_\perp$ can be calculated. However, this calculation produces $\chi_\perp$ values inconsistent with the assumption of constant χ. Furthermore, the calculations of $\chi_\perp$ in the far CFR are two orders of magnitude larger than those in the customary range of $0 < \chi_\perp < 10$, as typically assumed in boundary codes.

Figure 4.33 shows an example of this calculation. Figure 4.33 a) and 4.33 b) show the fits of $T_{\rm e}$ and $n_{\rm e}$ along the x coordinate. Figure 4.33 c) displays how $\frac{dT_{\rm e}}{ds}$ and $\frac{d^2 T_{\rm e}}{ds^2}$ vary along x. Figure 4.33 d) shows q_{sp} and $q_{\rm conv}$, while 4.33 e) displays the divergence of both heat flux terms. Finally, Figure 4.33 f) shows the calculated $\chi_\perp$ from Eq 4.63 for the $\rho < 1.005$ region with the blue markers, and Figure 4.33 g) displays it for $\rho > 1.005$. The uncertainty range assigned to $\chi_\perp$ reflects the 10% uncertainty in $T_{\rm e}$, 20% uncertainty in $n_{\rm e}$, and the uncertainty associated with each of the profiles along x as discussed in Section 4.4.3.

While the values of $\chi_\perp$ for $\rho < 1.005$ are within expectations, the unphysically large values of $\chi_\perp$ in the CFR prompt further review of the assumption of Spitzer conductivity, and $T_{\rm e} = T_{\rm i}$. To test the sensitivity of $\chi_\perp$ to these assumptions, a flux limiter value of $\alpha_e = 0.1$ was used to modify the electron heat flux given by Spitzer conductivity. The flux-limited parallel heat flux is given by [98]

$$\frac{1}{q_\parallel^*} = \frac{1}{q_{e\,\rm limit}} + \frac{1}{q_{sp}} \tag{4.64}$$

$$\text{where } q_{e\,\rm limit} = \alpha_e n_{\rm e} v_{e\,\rm thermal} T_{\rm e} \tag{4.65}$$

Furthermore, it is assumed that the ions heat the electrons, with an effective ion temperature of $3T_{\rm e}$. The changes to the convection calculations from such an assumption are ignored. The resultant heating of the electrons is given by [98]

$$Q_{eq} = \frac{6m_e}{m_i} n_{\rm e} \nu_{eq} T_{\rm e} \tag{4.66}$$

where ν_{eq} is the energy exchange collisional time. Accounting for heat flux limiters and ion heating of the electrons, Eq 4.63 becomes

$$\chi_\perp^* = -\frac{Q_{\rm rad} + Q_{\rm Sion} + \frac{6m_e}{m_i} n_{\rm e} \nu_{eq} T_{\rm e} - \boldsymbol{\nabla} \cdot \mathbf{q}_{\rm sp}^* - \boldsymbol{\nabla} \cdot \vec{q}_{\rm conv} - \boldsymbol{\nabla} \cdot \vec{q}_D}{\boldsymbol{\nabla} \cdot n_{\rm e} \boldsymbol{\nabla} T_{\rm e}} \tag{4.67}$$

Accounting for these changes, the calculated $\chi_\perp^*$ are shown in Figures 4.33 e) and h) by the orange markers. Despite these changes, $\chi_\perp^* > 10$ for $\rho > 1.008$. Doppler broadening measurements of $T_{\rm i}$ along the leg show that $T_{\rm e} \approx T_{\rm i}$, and a flux limiting coefficient of $\alpha_e = 0.1$ is smaller than values typically used in modeling. Thus, an ansatz of $q_{\chi_\perp} =$
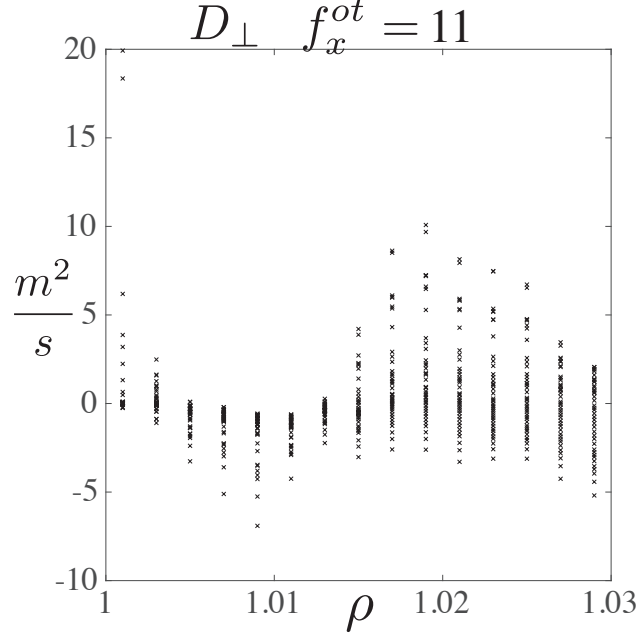
Figure 4.34: Calculation of $D_\perp$ for the largest flux expansion case in forward field. Each marker at a given ρ was calculated at specific z value between $-0.65 < z(m) < -0.45$.

$\chi_\perp n_e \boldsymbol{\nabla} T_e$ with constant $\chi_\perp < 10 \frac{m^2}{s}$ is observed to be inconsistent with the data, another major conclusion of this work.

Calculations of $D_\perp$ via

$$D_\perp = -\frac{S_p - \boldsymbol{\nabla} \cdot \left(n\mathbf{v}_{||} + n\mathbf{v}_{E\times B} \right)}{\boldsymbol{\nabla}^2 n_e}$$

yield values of $-5 < D_\perp(\frac{m^2}{s}) < 5$. Of course, a negative value of $D_\perp$ is unphysical and reflects the uncertainty in the measurements of S_p or in the calculations of $v_{E\times B}$ or $v_{||}$. Unlike the case for $\chi_\perp$, the typical assumption of $0.1 < D_\perp < 2$ is consistent with the uncertainty of the measurements presented here. An example of $D_\perp$ calculated for Discharge #1 is shown in Figure 4.34

4.6 Discussion and Conclusion

4.6.1 Discussion on $\chi_\perp$ and $D_\perp$

This discussion begins with the large values of $\chi_\perp$ calculated for $\rho > 1.008$. This result deviates from the common assumption used in modeling, i.e. $\chi_\perp$ is of order $1\frac{m^2}{s}$ [109][110]. As was shown in Section 4.5.4, this deviation lies outside the conservative estimates of the uncertainty. The consistency of the heat flux calculations between HeMSI and the IR thermography, shown in Figures 4.28 and 4.29, bolsters confidence that this result is not due to errors in the heat flux calculation. Thus, the cross-field heat transport in the far

SOL cannot be described assuming a constant $\chi_\perp \sim 1$ in L-mode TCV plasmas. However, $\chi \sim 1\frac{m^2}{s}$ for $\rho < 1.005$ which is roughly consistent with standard modeling practices.

This result should inform the modeling of L-mode TCV discharges going forward. As an example, consider SOLPS #166579 for discharge 65477 which uses $\chi_{e,\perp} = 0.7\frac{m^2}{s}$, $D_\perp = 0.1\frac{m^2}{s}$, and accounts for drifts. Simulated and measured T_e and n_e profiles are shown for this scenario in Figure 4.35.[1]
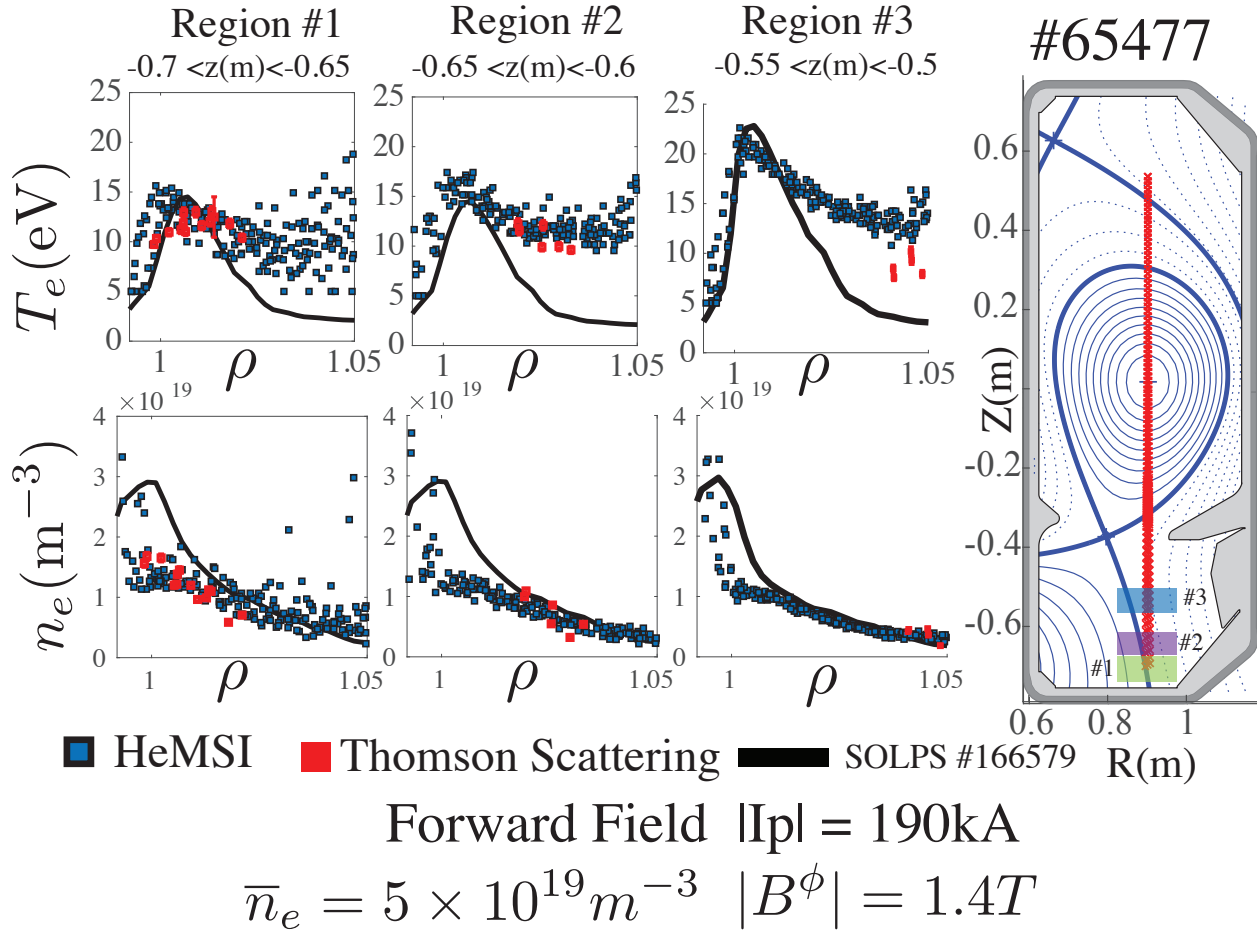
Figure 4.35: Comparison between SOLPS simulation mds#166579 and discharge 65477.

In the figure, the measured T_e falloff length is much longer than what is predicted by SOLPS. However, the measurements of T_e show good agreement with SOLPS near the separatrix. This is consistent with the inferences of $\chi_\perp$ from Section 4.5.4 which showed $\chi_\perp \sim 1\frac{m^2}{s}$ near the separatrix but $\chi_\perp \sim 100\frac{m^2}{s}$ farther into the CFR. In order for the simulation to reproduce the long falloff length of T_e, the anomalous cross-field transport needs to be increased. How this should be done is a matter for future work.

---

[1]SOLPS modeling was not available for the flux expansion discharges reviewed in this report.

4.6.2 Discussion on the Effects of Poloidal Flux Expansion

Increasing poloidal flux expansion is expected to lower the temperature at the divertor target because it increases the connection length and the divertor volume as discussed in Section 4.1. As expected, increasing poloidal flux expansion did produce lower temperatures at the target for plasmas in the conduction-limited regime. However, flux expansion was shown to have a negligible effect on the evolution of the C-III emission front or ion flux to the divertor plate during a density ramp. This latter result is surprising but consistent with previous results [14]. To understand these results, the two benefits of poloidal flux expansion will now be considered separately along with the experimental results.

Increasing the Connection Length

The benefits of increasing the connection length follow from the 2PM. However, the assumptions of the 2PM were shown to be invalid for the plasmas observed here. Drifts and parallel flow transported heat in amounts comparable to Spitzer conduction. Thus, while conducting heat over longer flux tubes may contribute to the lowering T_e in the conduction-limited regime, the effects of poloidal flux expansion on drifts and parallel convection must be considered as well.

Radiation Losses

In this section, the radiation losses are further examined. As discussed in Section 4.5.4, Figures 4.28 and 4.29 showed that radiation losses are typically negligible between $-0.65 < z(m) < -0.45$ except in the cases of discharges # 1 and # 5. This suggests that radiation losses may be responsible for the lower temperatures at the plate achieved with larger poloidal flux expansion. This conjecture is strengthened by further examination of the bolometry data. Figures 4.36 and 4.37 present the 2D reconstructions of the local radiation losses measured with bolometric tomography. They highlight that a significant amount of the radiative losses in the conduction-limited regime occur for $z < -0.65m$ which is below the region over which HeMSI is applied. Figure 4.38 presents the integration of these losses between $z = -0.5m$ and the variable floor of the test volume. The integration in Figure 4.38 is performed over the whole lower divertor volume, i.e., $.62 < R(m) < 1.2$. The top of the test volume is adjusted from the previous case of $-0.45m$ to -0.5 in order to avoid the radiative losses incurred at the inner target. As can be seen in Figure 4.38, a significant amount of the radiative losses are incurred below $Z(m) < -0.65m$ for the high poloidal flux expansion cases. This is particularly clear when observing the highest poloidal flux expansion case in Figure 4.36.

The radiation losses show less variation in the partially detached regime. Figures 4.39, 4.40, and 4.38 show the 2D reconstructions of the bolometry data during the partially detached regime, $\bar{n}_e = 5 \times 10^{19} m^{-3}$. Comparing these figures with those of the conduction-limited regime (Figures 4.36 and 4.37) demonstrates the decrease in radiative losses along the outer leg. Like in Figure 4.38 for the conduction-limited regime, Figure 4.41 shows the integration of these losses from $z = -0.5m$ to the floor of a test volume. In all cases, the radiative losses have decreased from the conduction-limited regime. However, the decreases in radiative losses are most stark for the cases of larger poloidal flux expansion. This may

128

explain why the benefits of larger flux expansion are only observed in the conduction-limited regime. In the colder, partially detached regime, radiative losses decrease, and the larger plasma volume exhausts power less effectively through radiation.
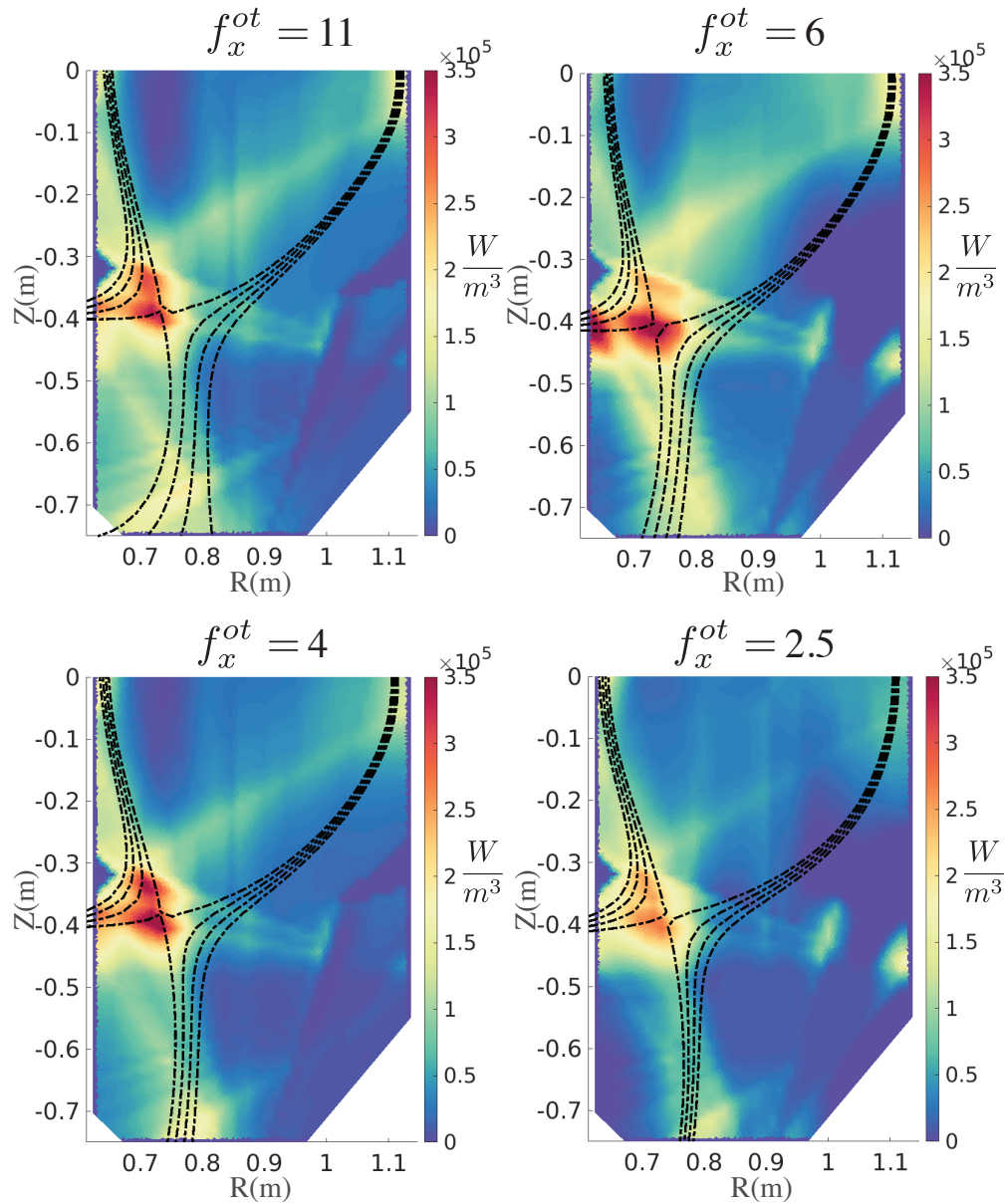
Figure 4.36: 2D reconstruction of volumetric radiation losses for forward field shots in the conduction-limited regime.
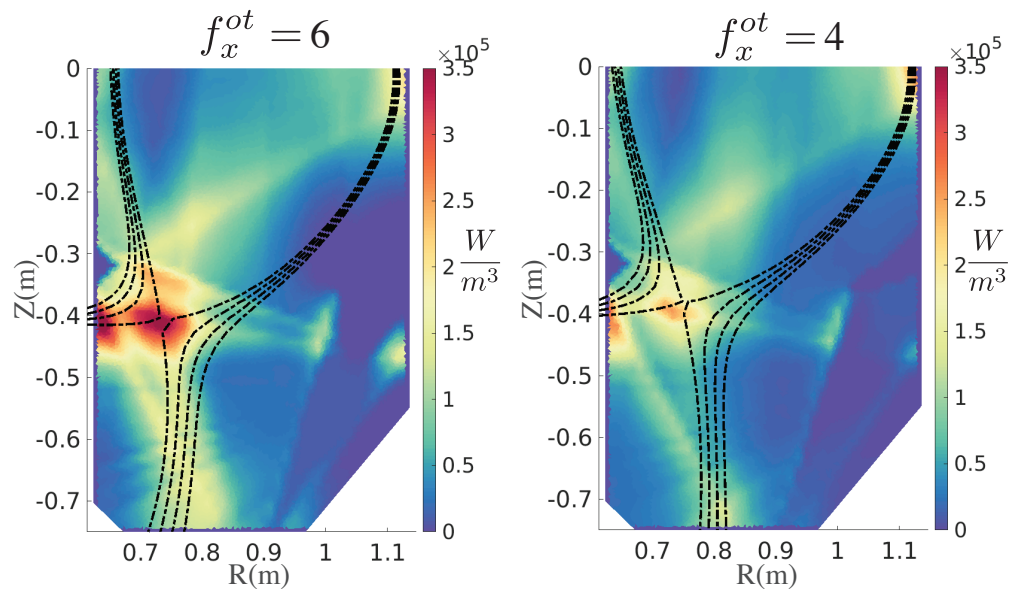
Figure 4.37: 2D reconstruction of volumetric radiation losses for reverse field shots in the conduction-limited regime.
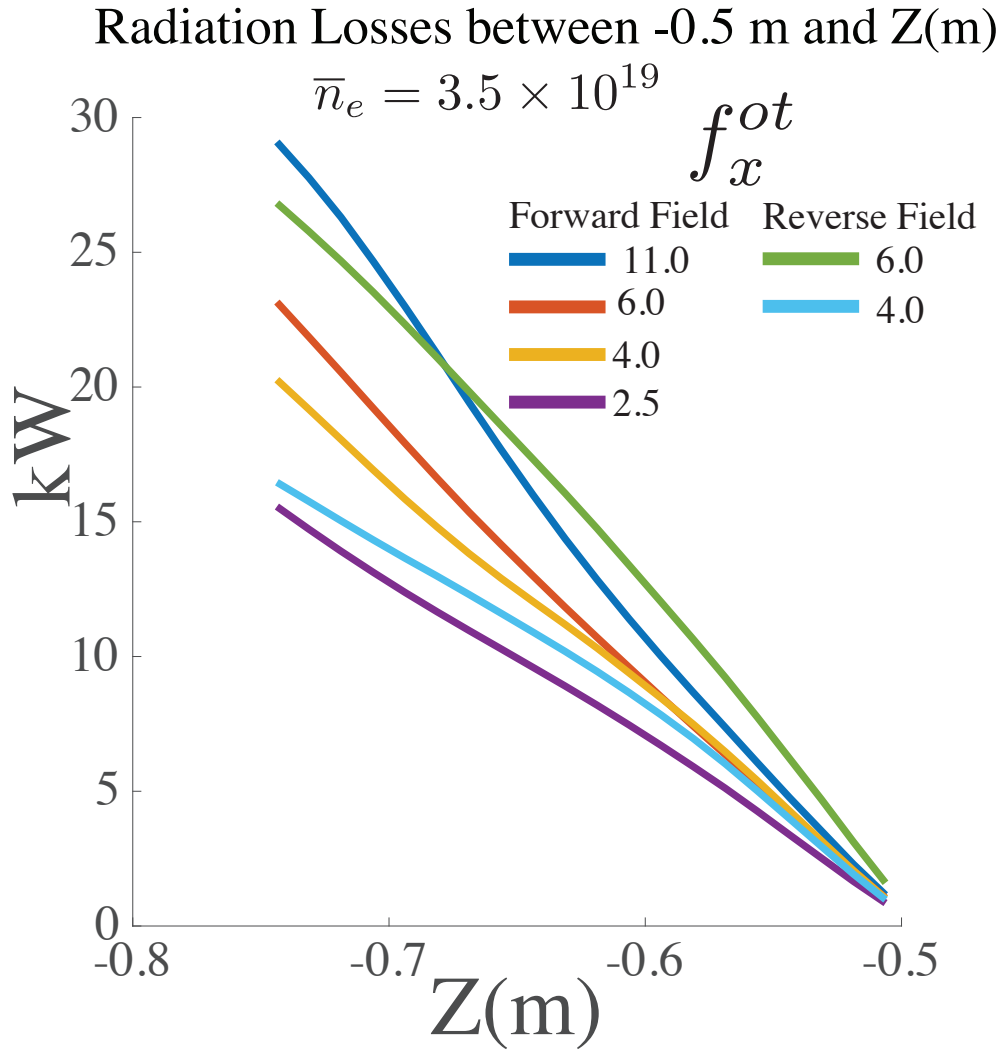
Figure 4.38: Integration of volumetric radiation losses between $-0.75 < z(m) < -0.50$ during the conduction-limited regime.
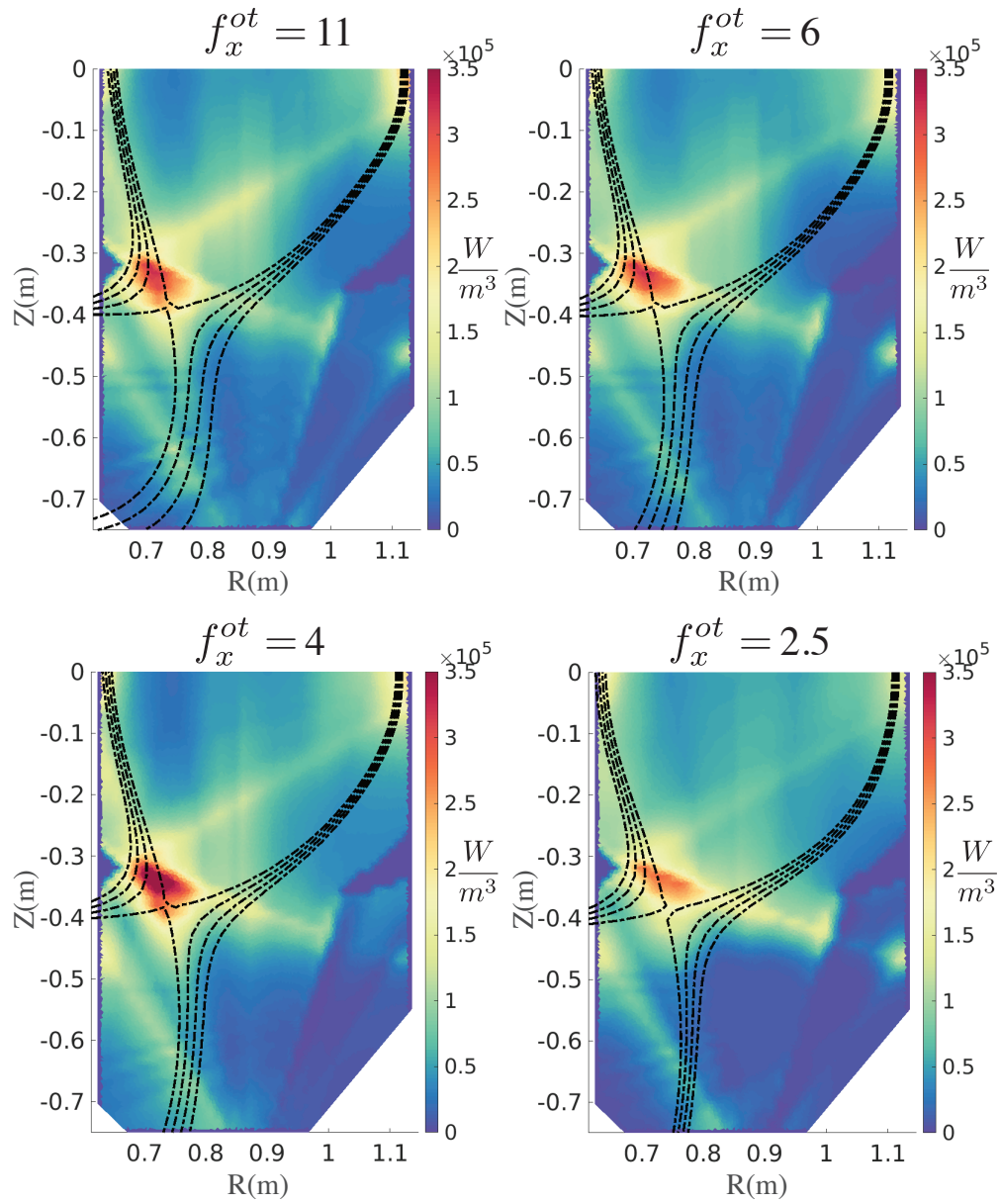
Figure 4.39: 2D reconstruction of volumetric radiation losses for forward field shots during partial detachment, $\bar{n}_e = 5 \times 10^{19} m^{-3}$.
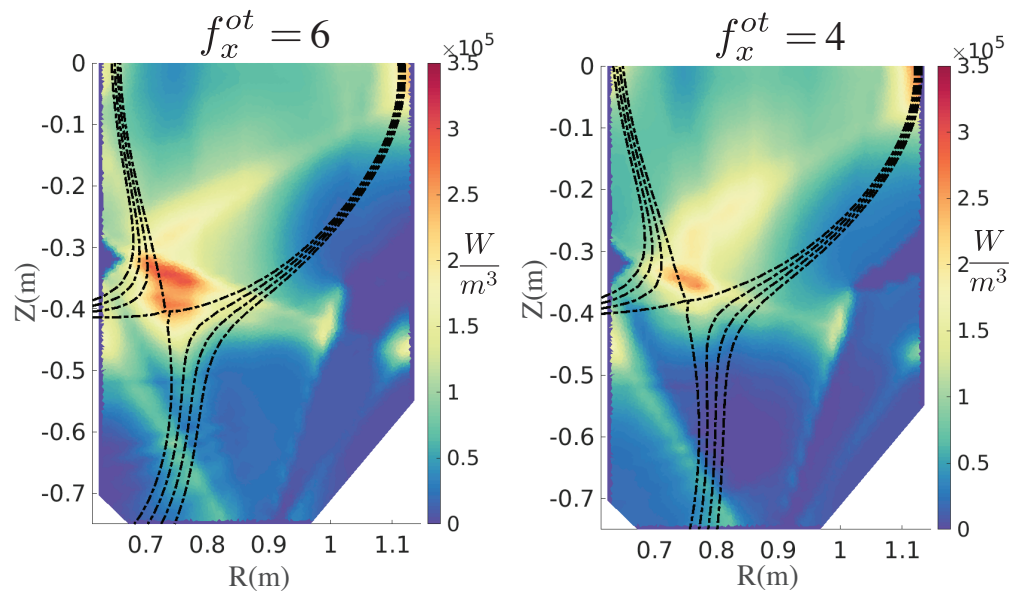
Figure 4.40: 2D reconstruction of volumetric radiation losses for reverse field shots during partial detachment, $\bar{n}_e = 5 \times 10^{19} m^{-3}$.
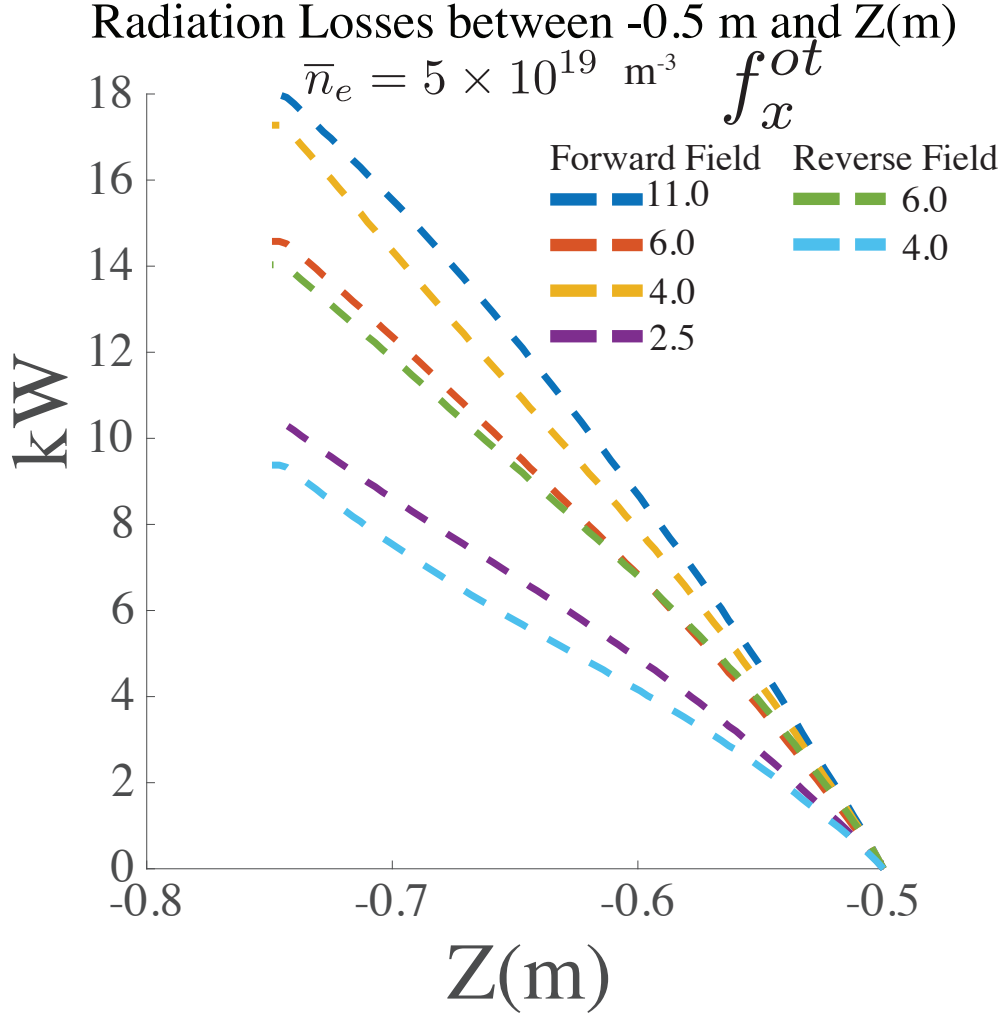
Figure 4.41: Integration of volumetric radiation losses between $-0.75 < z(m) < -0.50$ during the conduction-limited regime.

4.6.3 Conclusion

In conclusion, this chapter describes the effects of poloidal flux expansion on lower single-null L-mode TCV plasmas in both field directions using the HeMSI 2D measurements of T_e and n_e. These measurements were used to calculate particle and heat transport in 2D. These calculations highlighted the shortcomings of the basic two-point model by showing that a significant amount of heat was transported via drift and parallel convection. Convection prevents the plasma along a flux tubes from falling to the temperature predicted by the 2PM, which assumes all heat is transported via conduction. This limits the effectiveness of poloidal flux expansion. Nonetheless, increasing poloidal flux expansion was shown to lower target temperatures in the conduction-limited regime, but not in the partially detached regime like in [14]. The difference in behavior may be explained by the radiation losses as described in Section 4.6.2. Lastly, $\chi_\perp$ and $D_\perp$ were inferred. It was found that $D_\perp$ was consistent with current modeling practices, but $\chi_\perp$ was significantly

larger in the far CFR than what is typically assumed in modeling.

Chapter 5

Conclusion and Future Work

This thesis work has made several contributions to the field of magnetic confinement fusion through the development and implementation of multi-spectral imaging. First, as discussed in Chapter 2, this work implemented a polychromator-based multi-spectral imaging system on a tokamak for the first time and improved the diagnostic by removing the ghosting artifacts. Then, as discussed in Chapter 3, the MANTIS diagnostic was used to create 2D poloidal maps of T_e and n_e via the collisional radiative modeling of 2D helium line ratios, HeMSI. These measurements were validated against co-local Thomson scattering measurements for the regime of an ionizing plasma when using the atomic rates from the Goto code. As a corollary, the atomic rates from the ADAS code were shown to be inaccurate. However, 2D measurements of T_e and n_e were shown to be inaccurate in deuterium plasmas for $T_e < 10$eV.

The HeMSI measurements are a powerful new tool that allows for T_e and n_e to be measured in 2D for arbitrary geometries. Thus, for the final act of this thesis, as discussed in Chapter 4, HeMSI was applied to a study of flux expansion of L-mode plasmas in TCV. Poloidal flux expansion is expected to lower the temperature at the divertor target by increasing the connection length and radiating volume of the divertor plasma. Previous experiments [14] showed that flux expansion did not enhance the cooling of the plasma in reverse field plasmas in the partially detached regime. This was inferred via the C-III radiation front. In the experiments performed for this thesis, poloidal flux expansion was shown to produce lower temperatures at the outer target in the conduction-limited regime but not in the partially detached regime for both field directions. HeMSI was used to assess the local power balance in 2D to understand this behavior better. The analysis highlighted the effects of drifts, which transport a significant amount of heat and break the assumptions of the 2PM. In accord with expectations, measurements of the total radiated power were found to increase with poloidal flux expansion. This increase was greatest in the case of the conduction-limited regime. In the partially detached regime, this difference was less pronounced as the radiated power significantly decreased. The contrast of poloidal flux expansion being effective in the conduction-limited regime but not the partially detached regime may be explained by this change in the radiated power. The plasma radiates less as it cools, so the extra radiating volume gained by increasing the flux expansion is less efficacious in cooling the plasma.

Finally, the HeMSI measurements, along with measurements from Langmuir probes

and the 2D reconstructions of the radiated power, were used to infer values of $\chi_\perp$ and $D_\perp$ under the assumption that $\chi_\perp$ and $D_\perp$ were constant in space. $D_\perp$ was found to be consistent with current modeling assumptions. However, $\chi_\perp$ in the far common flux region was found to be two orders of magnitude larger than what is typically assumed. The effect of this difference was shown to be present when comparing SOLPS temperature profiles to measurements. SOLPS produced a T_e profile with a much shorter fall-off length than what was actually measured.

Having developed and applied novel analysis techniques, this thesis work represents the tip of the spear of what can be done going forward with multi-spectral imaging. Therefore, this work concludes by discussing suggestions for future work. First, as discussed in Chapter 3, improving atomic and molecular emission modeling would increase the utility of multi-spectral imaging devices. This is particularly important for interpreting emission for $T_e < 10\text{eV}$ when neutral ion and molecular ion reactions may be important. This is important not only for interpreting helium emission but also emission from other species, particularly from atomic and molecular deuterium [115]. While these colder scenarios are more complicated, they also offer an opportunity to reap the full benefits of imaging 6 or more wavelengths simultaneously. The ability to localize each emitter and reacting species could be extremely beneficial for improving the understanding of transport processes in detached plasmas. However, it is suggested that future testing and verification of atomic and molecular emission models be performed on smaller tabletop devices with access to high-resolution spectrometers and laser-induced fluorescence. Such a benchtop setup would allow for more detailed analysis of atomic populations.

Next, the multi-spectral imaging profiles should be better integrated with computational modeling. The 2D emission profiles and/or T_e and n_e offer an unprecedented wealth of 2D quantitative data. Adapting 2D boundary codes to fit the 2D data from multi-spectral imaging actively is one avenue for advancement. More robust and general onion-skin solvers could also be developed to extract anomalous transport coefficients from the 2D profiles as well. However, such onion-skin solvers would benefit from direct measurements of the parallel velocity. This can be done by incorporating measurements from reciprocating probes or using coherence imaging. There are currently plans to outfit the MANTIS diagnostics with coherence imaging in the near future to measure parallel flows in 2D.

Another option for future work is the improvement of the time resolution of the images. There is currently one phantom fast camera resolving filaments for the He I 587 nm line on MANTIS [116]. Resolving multiple lines at such time scales may allow insight into the fluctuations of local plasma parameters. If emission fluctuations are significantly localized, T_e and n_e fluctuations could possibly be resolved on the level of filaments. Nonetheless, understanding the fluctuations in emission will still be important to interpreting the steady time-averaged emission analyzed in this thesis.

Next, the analysis presented in this thesis and the improvements suggested above should be applied over the whole plasma edge. This work focused on the outer leg. However, TCV is now equipped with MANTIS cameras in the main chamber and upper divertor. Such a comprehensive edge analysis would be a substantial benefit to the field, especially if it is performed with the improved integration of the modeling suggested above.

Lastly, multi-spectral imaging and the analysis discussed here should be extended to

high-power and metal wall devices. These devices are fundamental to extrapolating the performance of future reactors, and would benefit from the novel research presented in this thesis and the suggestions for future work presented above.

In conclusion, this work has made a substantial contribution to the field of tokamak heat exhaust research and has set the stage for further advancement.

.1 Divergence In Frenet-Serret Frame

The following derivation was adopted from Appendix of [117].

A Frenet-Serret frame maps space to a curve's arclength and normal vectors. At a given point p, two such frames intersect at p are used to calculate the divergence. The first is from a curve that traverses exclusively along y, and the other excursively along x. These coordinates will be written as $\{y, n_y\}$, $\{x, n_x\}$, respectively, and are illustrated in Figure 1.

First, consider the Frenet-Serret frame generated by the poloidal flux surface, $\gamma_y(y) = (R_o(y), Z_o(y))$, where y is the arclength of the curve. Define $n_y(y)$ as the signed perpendicular distance from γ_y at y such that:

$$R(y, n_y) = R_o(y) + n_y \frac{\partial Z_o}{\partial y} \tag{1}$$

$$Z(y, n_y) = Z_o(y) - n_y \frac{\partial R_o}{\partial y} \tag{2}$$

Because y is an arc-length parameter, it follows that Eq 1 can be expressed with trigonometric functions:

$$R(y, n_y) = R_o(y) - n_y \sin(\xi(y)) \tag{3}$$
$$Z(y, n_y) = Z_o(y) - n_y \cos(\xi(y)) \tag{4}$$

Define $\kappa(y) \equiv \xi'(y)$ and $J \equiv 1 - \kappa(y)n_y$. Then:

$$\begin{pmatrix} dR \\ dZ \\ d\phi \end{pmatrix} = \begin{pmatrix} J_y \cos(\xi) & -\sin(\xi) & 0 \\ -J_y \sin(\xi) & -\cos(\xi) & 0 \\ 0 & 0 & 1 \end{pmatrix} \begin{pmatrix} dy \\ dn \\ d\phi \end{pmatrix} \tag{5}$$

For a sufficiently small n_y the mapping of $M(\gamma_y, n_y) \to (R, Z)$ is invertable, so $\{y, n_y, \phi\}$ is a well-defined coordinate system. From Eq 5 the metric tensor for $\{y, n_y, \phi\}$ coordinates can be shown from Eq 5 to be

$$g_{ij} = \begin{pmatrix} J_y^2 & 0 & 0 \\ 0 & 1 & 0 \\ 0 & 0 & R^2 \end{pmatrix} \tag{6}$$

As a 2D Frenet-Serret frame note that along γ_y the following relationships are satisfied:

$$\frac{\partial \mathbf{e}_y}{\partial y} = \kappa_y(y)\mathbf{e}_{n_y} \tag{7}$$

$$\frac{\partial \mathbf{e}_{n_y}}{\partial y} = -\kappa_y(y)\mathbf{e}_y \tag{8}$$

Next, for a toroidally symmetric scalar field A:

$$\boldsymbol{\nabla} A = \frac{1}{J}\frac{\partial A}{\partial y}\hat{\mathbf{e}}_y + \frac{\partial A}{\partial n_y}\hat{\mathbf{e}}_{n_y} + \frac{1}{R}\frac{\overset{0}{\cancel{\partial A}}}{\partial n_\phi}\mathbf{e}_\phi = \frac{1}{J}\frac{\partial A}{\partial y}\hat{\mathbf{e}}_y + \frac{\partial A}{\partial n_y}\mathbf{e}_{n_y} \tag{9}$$

The formula for the divergence of a vector field $F^i\hat{\mathbf{e}}_i$ (summation implied) is:

$$\boldsymbol{\nabla}\cdot F = \frac{1}{\sqrt{|g|}}\frac{\partial}{\partial x_j}\left(\frac{\sqrt{|g|}}{\sqrt{g_{jj}}}F^j\right) \tag{10}$$

In $\{y, n_y, \phi\}$ coordinate system $\sqrt{|g|} = J_y R$ so $\boldsymbol{\nabla}^2 A$ becomes

$$\nabla^2 A = \frac{1}{J_y R}\frac{\partial}{\partial y}\left(\frac{R}{J_y}\frac{\partial A}{\partial y}\right) + \frac{1}{J_y R}\frac{\partial}{\partial n_y}\left(J_y R\frac{\partial A}{\partial n_y}\right) \tag{11}$$

$$\nabla^2 A = \frac{1}{J_y^2}\frac{\partial^2 A}{\partial y^2} + \frac{1}{J_y^2 R}\frac{\partial R}{\partial y}\frac{\partial A}{\partial y} - \frac{1}{J_y^3}\frac{\partial J_y}{\partial y}\frac{\partial A}{\partial y}\cdots \tag{12}$$

$$+ \frac{\partial^2 A}{\partial n_y^2} + \frac{1}{R}\frac{\partial R}{\partial n_y}\frac{\partial A}{\partial n_y} + \frac{1}{J_y}\frac{\partial J_y}{\partial n_y}\frac{\partial A}{\partial n_y} \tag{13}$$

At this point p, $\mathbf{e}_x = \frac{\partial \vec{r}}{\partial x} = \frac{\partial \vec{r}}{\partial n_y} = \mathbf{e}_y$. Thus, the n_y derivatives must be reformatted into x derivatives. To accomplish this task, note that A can be parameterized as $A = A(x, n_x)$ and apply the chain rule.

$$\frac{\partial A(x, n_x)}{\partial n_y} = \frac{\partial A}{\partial x}\frac{\partial x}{\partial n_y} + \frac{\partial A}{\partial n_x}\frac{\partial n_x}{\partial n_y} = \frac{\partial A}{\partial x}\mathbf{e}^x\cdot\mathbf{e}_{n_y} + \frac{\partial A}{\partial n_x}\mathbf{e}^{n_x}\cdot\mathbf{e}_{n_y} \tag{14}$$

$$= \frac{\partial A}{\partial x}\frac{\mathbf{e}_x\cdot\mathbf{e}_{n_y}}{J_x^2} + \frac{\partial A}{\partial n_x}\mathbf{e}_{n_x}\cdot\mathbf{e}_{n_y} \tag{15}$$

At the intersection of the two curves:

$$\mathbf{e}_{n_y} = \mathbf{e}_x \tag{16}$$
$$\mathbf{e}_{n_x} = -\mathbf{e}_y \tag{17}$$
$$J_y = J_x = 1 \tag{18}$$
$$\frac{\partial J_x}{\partial n_y} = \frac{\partial J_x}{\partial x} = n_x\frac{\partial k_x}{\partial x} = 0 \tag{19}$$

$$\frac{\partial A(x, n_x)}{\partial n_y} = \frac{\partial^2 A}{\partial x^2}\left(\frac{\mathbf{e}_x\cdot\mathbf{e}_{n_y}}{J_x^2}\right)^2 + \frac{1}{J_x^2}\frac{\partial A}{\partial x}\frac{\partial \mathbf{e}_x}{\partial n_y}\cdot\mathbf{e}_{n_y} - 2\frac{\frac{\partial J_x}{\partial n_y}}{J_x^3}\frac{\partial A}{\partial x}\mathbf{e}_x\cdot\mathbf{e}_{n_y} \tag{20}$$

$$+ \frac{1}{J_x^2}\frac{\partial A}{\partial x}\mathbf{e}_x\cdot\frac{\partial \mathbf{e}_{n_y}}{\partial n_y} + \frac{\partial^2 A}{\partial n_x^2}\left(\mathbf{e}_{n_x}\cdot\mathbf{e}_{n_y}\right)^2 \tag{21}$$

$$+ \frac{\partial A}{\partial n_x}\frac{\partial \mathbf{e}_{n_x}}{\partial n_y}\cdot\mathbf{e}_{n_y} + \frac{\partial A}{\partial n_x}\mathbf{e}_x\cdot\frac{\partial \mathbf{e}_{n_y}}{\partial n_y} \tag{22}$$

$$\frac{\partial A(x, n_x)}{\partial n_y} = \frac{\partial^2 A}{\partial x^2} + \frac{\partial A}{\partial n_x}\frac{\partial \mathbf{e}_{n_x}}{\partial n_y} \cdot \mathbf{e}_{n_y} = \frac{\partial^2 A}{\partial x^2} + \frac{\partial A}{\partial y}\kappa(x) \tag{23}$$

Now Eq 23 is substituted into 12, and evaulated at p i.e. $n_y = n_x = 0$. Thus, $\frac{\partial}{\partial n_y} = \frac{\partial}{\partial x}$ and $J_x = J_y = 1$, yielding

$$\nabla^2 A = \frac{\partial^2 A}{\partial y^2} + \frac{\partial^2 A}{\partial x^2} + \frac{1}{R}\frac{\partial R}{\partial y}\frac{\partial A}{\partial y} + \frac{\partial A}{\partial y}\kappa_x(x) + \frac{1}{R}\frac{\partial R}{\partial x}\frac{\partial A}{\partial x} - \kappa_y(y)\frac{\partial A}{\partial x} \tag{24}$$
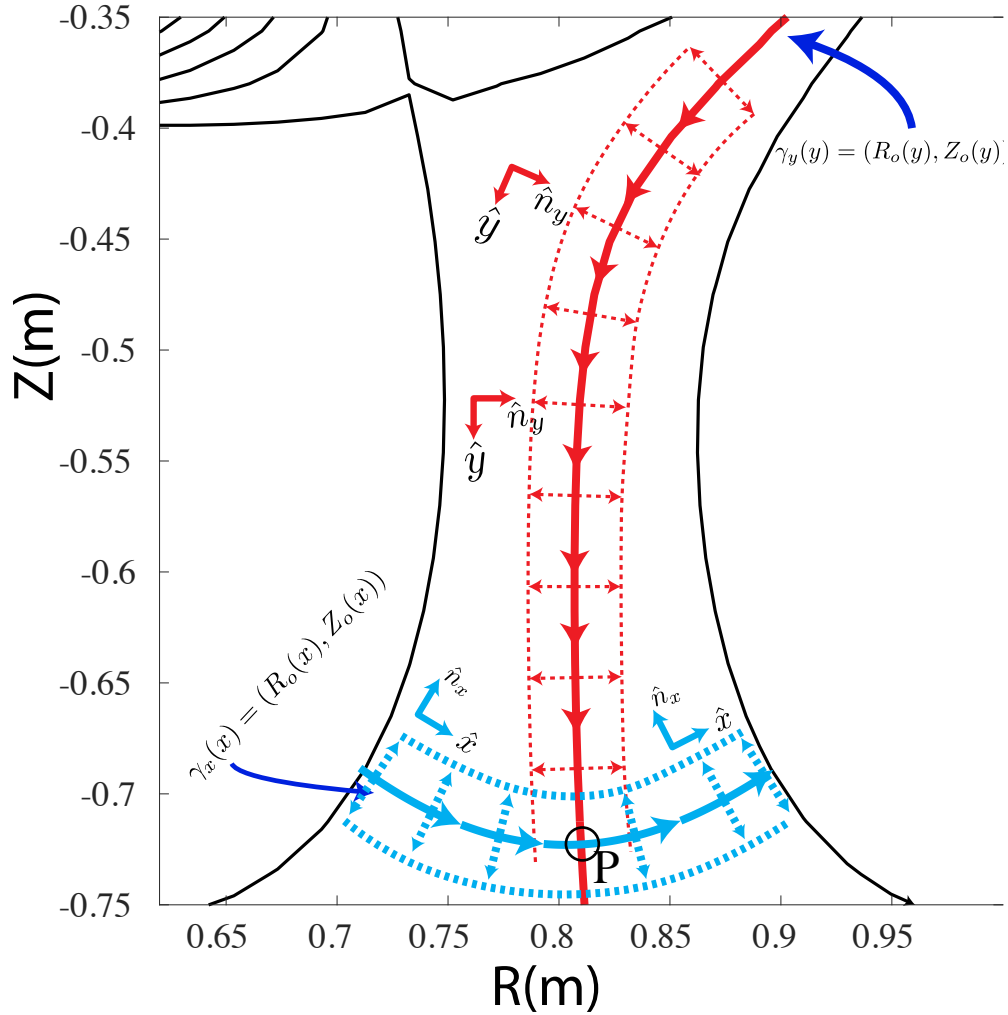
Figure 1: Illustration of Frenet-Serret frames about contours used to fit the data. The curves intersect at at point P where $\mathbf{e}_x = \mathbf{e}_{n_y}$ and $\mathbf{e}_y = -\mathbf{e}_{n_x}$.

.1.1 Evaluation of ∇ and ∇^2

the ∇ and ∇^2 operators are evaluted via the derivtives from the x and y coordinates. The coordinates x and y are non-euclidean and require the calculation of a non-standard metric

141

tensor. After calculating the metric, it follows, for a scalar function of the form $A(x, y)$, that the ∇ and ∇^2 operators are

$$\nabla A = \frac{\partial A}{\partial y}\mathbf{e}_y + \frac{\partial A}{\partial x}\mathbf{e}_x \tag{25}$$

$$\nabla^2 A = \frac{\partial A^2}{\partial^2 y} + \frac{\partial A^2}{\partial^2 x} + \frac{1}{R}\frac{\partial R}{\partial x}\frac{\partial A}{\partial x} + \frac{1}{R}\frac{\partial R}{\partial y}\frac{\partial A}{\partial y} - \kappa_y\frac{\partial A}{\partial x} + \kappa_x\frac{\partial A}{\partial y} \tag{26}$$

Where $\kappa_{x,y}$ indicates the curvature of either x or y contour (see Figure 4.5). Equations 25 - 26 are derived in .1. Note that in the case where a vector function is fully aligned with the magnetic field, $\mathbf{V} = V(s, \rho)\hat{s}$, the divergence operator simplifies to:

$$\nabla \cdot (V(s, \rho)\hat{s}) = B\frac{\partial}{\partial s}\left(\frac{V(s, \rho)}{B}\right) \tag{27}$$

References

[1] Smithsonian Institution's Human Origins Program, *Human evolution interactive timeline*, https://humanorigins.si.edu/evidence/human-evolution-interactive-timeline, Accessed: December 18, 2023, 2021. (visited on 04/27/2021).

[2] NASA's Goddard Institute for Space Studies (GISS), *Global land-ocean temperature index*, NASA Goddard Institute for Space Studies, Dataset accessed 2023-12-19, 2024. [Online]. Available: https://climate.nasa.gov/vital-signs/global-temperature/.

[3] N. Lenssen, G. Schmidt, J. Hansen, M. Menne, A. Persin, R. Ruedy, and D. Zyss, "Improvements in the gistemp uncertainty model," *J. Geophys. Res. Atmos.*, vol. 124, no. 12, pp. 6307–6326, 2019. DOI: 10.1029/2018JD029522.

[4] X. Lan, *Global carbon dioxide trends*, NOAA Global Monitoring Laboratory, Accessed: 2024-02-16, 2024. [Online]. Available: https://gml.noaa.gov/ccgg/trends/.

[5] R. Keeling, *Atmospheric carbon dioxide record from scripps institution of oceanography*, Scripps Institution of Oceanography, Accessed: 2024-02-16, 2024. [Online]. Available: https://scrippsco2.ucsd.edu/.

[6] J. Wesson and D. J. Campbell, *Tokamaks*. Oxford university press, 2011, vol. 149.

[7] B. Sorbom, J. Ball, T. Palmer, F. Mangiarotti, J. Sierchio, P. Bonoli, C. Kasten, D. Sutherland, H. Barnard, C. Haakonsen, *et al.*, "Arc: A compact, high-field, fusion nuclear science facility and demonstration power plant with demountable magnets," *Fusion Engineering and Design*, vol. 100, pp. 378–405, 2015.

[8] S. Li, H. Jiang, Z. Ren, C. Xu, *et al.*, "Optimal tracking for a divergent-type parabolic pde system in current profile control," in *Abstract and Applied Analysis*, Hindawi, vol. 2014, 2014.

[9] A. Loarte, B. Lipschultz, A. Kukushkin, *et al.*, "Chapter 4: Power and particle control," *Nuclear Fusion*, vol. 47, no. 6, S203, Jun. 2007. DOI: 10.1088/0029-5515/47/6/S04. [Online]. Available: https://dx.doi.org/10.1088/0029-5515/47/6/S04.

[10] A. Q. Kuang, S. Ballinger, D. Brunner, *et al.*, "Divertor heat flux challenge and mitigation in SPARC," en, *Journal of Plasma Physics*, vol. 86, no. 5, p. 865 860 505, Oct. 2020, ISSN: 0022-3778, 1469-7807. DOI: 10.1017/S0022377820001117. [Online]. Available: https://www.cambridge.org/core/product/identifier/ S0022377820001117/type/journal_article (visited on 11/20/2023).

[11] S. Coda, J. Ahn, R. Albanese, S. Alberti, E. Alessi, S. Allan, H. Anand, G. Anastassiou, Y. Andrèbe, C. Angioni, *et al.*, "Overview of the tcv tokamak program: Scientific progress and facility upgrades," *Nuclear Fusion*, vol. 57, no. 10, p. 102 011, 2017.

[12] H. Reimerdes, B. Duval, J. Harrison, *et al.*, "TCV experiments towards the development of a plasma exhaust solution," *Nuclear Fusion*, vol. 57, no. 12, p. 126 007, Sep. 2017. DOI: 10.1088/1741-4326/aa82c2. [Online]. Available: https://doi.org/10.1088/1741-4326/aa82c2.

[13] B. Labit, G. Canal, N. Christen, *et al.*, "Experimental studies of the snowflake divertor in tcv," *Nuclear Materials and Energy*, vol. 12, pp. 1015–1019, 2017, Proceedings of the 22nd International Conference on Plasma Surface Interactions 2016, 22nd PSI, ISSN: 2352-1791. DOI: https://doi.org/10.1016/j.nme.2017.03.013. [Online]. Available: https://www.sciencedirect.com/science/article/pii/S235217911630179X.

[14] C. Theiler, B. Lipschultz, J. Harrison, B. Labit, H. Reimerdes, C. Tsui, W. Vijvers, J. Boedo, B. Duval, S. Elmore, *et al.*, "Results from recent detachment experiments in alternative divertor configurations on tcv," *Nuclear Fusion*, vol. 57, no. 7, p. 072 008, 2017.

[15] A. Perek, W. Vijvers, Y. Andrebe, I. Classen, B. Duval, C. Galperti, J. Harrison, B. Linehan, T. Ravensbergen, K. Verhaegh, *et al.*, "Mantis: A real-time quantitative multispectral imaging system for fusion plasmas," *Review of Scientific Instruments*, vol. 90, no. 12, p. 123 514, 2019.

[16] A. Huber, S. Brezinsek, P. Mertens, *et al.*, "Development of a mirror-based endoscope for divertor spectroscopy on JET with the new ITER-like wall (invited)a)," *Review of Scientific Instruments*, vol. 83, no. 10, p. 10D511, Jul. 2012, ISSN: 0034-6748. DOI: 10.1063/1.4731759. [Online]. Available: https://doi.org/10.1063/1.4731759 (visited on 03/06/2024).

[17] M. E. Fenstermacher, R. D. Wood, S. L. Allen, *et al.*, "Comprehensive 2D measurements of radiative divertor plasmas in DIII-D," *Journal of Nuclear Materials*, vol. 241-243, pp. 666–671, Feb. 1997, ISSN: 0022-3115. DOI: 10.1016/S0022-3115(97)80119-5. [Online]. Available: https://www.sciencedirect.com/science/article/pii/S0022311597801195 (visited on 03/07/2024).

[18] M. E. Fenstermacher, W. H. Meyer, R. D. Wood, D. G. Nilson, R. Ellis, and N. H. Brooks, "A tangentially viewing visible TV system for the DIII-D divertor," *Review of Scientific Instruments*, vol. 68, no. 1, pp. 974–977, Jan. 1997, ISSN:

0034-6748. DOI: 10.1063/1.1147729. [Online]. Available:
https://doi.org/10.1063/1.1147729 (visited on 03/07/2024).

[19] C. J. Boswell, "Visible Spectroscopic Imaging on the Alcator C-Mod Tokamak,"
      en, Ph.D, Massachusetts Institute of Technology, 2003.

[20] C. J. Boswell, J. L. Terry, B. Lipschultz, and J. Stillerman, "Applications of visible
      CCD cameras on the Alcator C-Mod tokamak," *Review of Scientific Instruments*,
      vol. 72, no. 1, pp. 935–939, Jan. 2001, ISSN: 0034-6748. DOI: 10.1063/1.1321010.
      [Online]. Available: https://doi.org/10.1063/1.1321010 (visited on 03/07/2024).

[21] F. Scotti and V. A. Soukhanovskii, "A dual wavelength imaging system for
      plasma-surface interaction studies on the National Spherical Torus Experiment
      Upgrade," *Review of Scientific Instruments*, vol. 86, no. 12, p. 123103, Dec. 2015,
      ISSN: 0034-6748. DOI: 10.1063/1.4935609. [Online]. Available:
      https://doi.org/10.1063/1.4935609 (visited on 03/07/2024).

[22] T. N. Carlstrom, J. C. DeBoo, R. Evanko, C. M. Greenfield, C.-L. Hsieh,
      R. T. Snider, and P. Trost, "A compact, low cost, seven channel polychromator for
      Thomson scattering measurements," *Review of Scientific Instruments*, vol. 61,
      no. 10, pp. 2858–2860, Oct. 1990, ISSN: 0034-6748. DOI: 10.1063/1.1141806. [Online].
      Available: https://doi.org/10.1063/1.1141806 (visited on 03/08/2024).

[23] R. T. Mumgaard, "Engineering upgrades to the Motional Stark Effect diagnostic
      on Alcator C-Mod," eng, Accepted: 2016-07-18T19:10:20Z Journal Abbreviation:
      Engineering upgrades to the MSE diagnostic on Alcator C-Mod, Thesis,
      Massachusetts Institute of Technology, 2015. [Online]. Available:
      https://dspace.mit.edu/handle/1721.1/103655 (visited on 03/05/2024).

[24] B. Linehan, R. Mumgaard, M. Wensing, K. Verhaegh, Y. Andrebe, J. Harrison,
      B. Duval, C. Theiler, T. Team, *et al.*, "The multi-spectral imaging diagnostic,"
      Review of Scientific Instruments, vol. 89, no. 10, 2018.

[25] S. Silburn, J. Harrison, T. Farley, *et al.*, *Calcam*, version 2.7.0, 2021. DOI:
      10.5281/zenodo.4698377. [Online]. Available:
      https://doi.org/10.5281/zenodo.4698377.

[26] A. H. Andersen and A. C. Kak, "Simultaneous Algebraic Reconstruction
      Technique (SART): A Superior Implementation of the Art Algorithm," *Ultrasonic
      Imaging*, vol. 6, no. 1, pp. 81–94, Jan. 1984, ISSN: 0161-7346. DOI:
      10.1177/016173468400600107. [Online]. Available:
      https://doi.org/10.1177/016173468400600107.

[27] B. Linehan, A. Perek, B. Duval, *et al.*, "Validation of 2d T_e and n_e measurements
      made with helium imaging spectroscopy in the volume of the tcv divertor,"
      Nuclear Fusion, vol. 63, no. 3, p. 036021, Feb. 2023. DOI: 10.1088/1741-4326/acb5b0.
      [Online]. Available: https://dx.doi.org/10.1088/1741-4326/acb5b0.

[28] S. P. Cunningham, R. J. Beaver, and R. C. Waugh, "US Atomic Energy
      Commission Rep," *WASH-289*, p. 279, 1955.

[29] D. Wendler, R. Dux, R. Fischer, M. Griener, E. Wolfrum, G. Birkenmeier, and U. Stroth, "Collisional radiative model for the evaluation of the thermal helium beam diagnostic at ASDEX upgrade," *Plasma Physics and Controlled Fusion*, vol. 64, no. 4, p. 045 004, 2022, ISSN: 0741-3335. DOI: 10.1088/1361-6587/ac49f8.

[30] M. Griener, E. Wolfrum, M. Cavedon, R. Dux, V. Rohde, M. Sochor, J. M. Muñoz Burgos, O. Schmitz, and U. Stroth, *Review of Scientific Instruments*, vol. 89, no. 10, 2018, ISSN: 10897623. DOI: 10.1063/1.5034446. [Online]. Available: http://dx.doi.org/10.1063/1.5034446.

[31] S. Kajita, D. Nishijima, K. Fujii, G. Akkermans, and H. Van Der Meiden, "Application of multiple regression for sensitivity analysis of helium line emissions to the electron density and temperature in Magnum-PSI," *Plasma Physics and Controlled Fusion*, vol. 63, no. 5, 2021, ISSN: 13616587. DOI: 10.1088/1361-6587/abf36e.

[32] D. Nishijima, S. Kajita, and G. R. Tynan, "Machine learning prediction of electron density and temperature from He i line ratios," *Review of Scientific Instruments*, vol. 92, no. 2, 2021, ISSN: 10897623. DOI: 10.1063/5.0028000. [Online]. Available: https://doi.org/10.1063/5.0028000.

[33] W. Zholobenko, M. Rack, and D. Reiter, "Development and evaluation of a synthetic helium beam diagnostic for Wendelstein 7-X," Jülich, Tech. Rep. Juel-4407, 2018, 63 p. [Online]. Available: https://juser.fz-juelich.de/record/844035.

[34] W. Zholobenko, M. Rack, D. Reiter, M. Goto, Y. Feng, B. Küppers, and P. Börner, "Synthetic helium beam diagnostic and underlying atomic data," *Nuclear Fusion*, vol. 58, no. 12, 2018, ISSN: 17414326. DOI: 10.1088/1741-4326/aadda9.

[35] O. Schmitz, I. L. Beigman, L. A. Vainshtein, *et al.*, "Status of electron temperature and density measurement with beam emission spectroscopy on thermal helium at TEXTOR," *Plasma Physics and Controlled Fusion*, vol. 50, no. 11, 2008, ISSN: 07413335. DOI: 10.1088/0741-3335/50/11/115004.

[36] M. Goto and K. Sawada, "Determination of electron temperature and density at plasma edge in the Large Helical Device with opacity-incorporated helium collisional-radiative model," *Journal of Quantitative Spectroscopy and Radiative Transfer*, vol. 137, pp. 23–28, 2014, ISSN: 00224073. DOI: 10.1016/j.jqsrt.2013.12.003. [Online]. Available: http://dx.doi.org/10.1016/j.jqsrt.2013.12.003.

[37] Y. Iida, S. Kado, and S. Tanaka, "On the application of He I collisional-radiative model to the He-H 2 mixture plasmas in MAP-II divertor simulator," *Journal of Nuclear Materials*, vol. 438, no. SUPPL, S1237–S1240, 2013, ISSN: 00223115. DOI: 10.1016/j.jnucmat.2013.01.274. [Online]. Available: http://dx.doi.org/10.1016/j.jnucmat.2013.01.274.

[38] A. Okamoto, S. Kado, K. Sawada, Y. Kuwahara, Y. Iida, and S. Tanaka, "Contribution of hydrogen molecular assisted recombination processes to population of hydrogen atom in divertor simulator MAP-II," *Journal of Nuclear Materials*, vol. 363-365, no. 1-3, pp. 395–399, 2007, ISSN: 00223115. DOI: 10.1016/j.jnucmat.2007.01.033.

[39] S. Ma, J. Howard, B. D. Blackwell, and N. Thapar, "Measurements of electron density and temperature in the H-1 heliac plasma by helium line intensity ratios," *Review of Scientific Instruments*, vol. 83, no. 3, 2012, ISSN: 00346748. DOI: [10.1063/1.3692756](10.1063/1.3692756).

[40] E. De La Cal and J. Guasp, "Two-dimensional imaging of edge plasma electron density and temperature by the passive helium emission ratio technique in TJ-II," *Plasma Physics and Controlled Fusion*, vol. 53, no. 8, 2011, ISSN: 07413335. DOI: [10.1088/0741-3335/53/8/085006](10.1088/0741-3335/53/8/085006).

[41] S. Lisgo, P. Börner, G. F. Counsell, J. Dowling, A. Kirk, R. Scannell, M. O'Mullane, and D. Reiter, "Interpretation of spatially resolved helium line ratios on MAST," *Journal of Nuclear Materials*, vol. 390-391, no. 1, pp. 1078–1080, 2009, ISSN: 00223115. DOI: 10.1016/j.jnucmat.2009.01.292.

[42] S. Kajita, N. Ohno, S. Takamura, and T. Nakano, "Comparison of He I line intensity ratio method and electrostatic probe for electron density and temperature measurements in NAGDIS-II," *Physics of Plasmas*, vol. 13, no. 1, pp. 1–9, Jan. 2006, ISSN: 1070664X. DOI: [10.1063/1.2164461](10.1063/1.2164461). [Online]. Available: http://aip.scitation.org/doi/10.1063/1.2164461.

[43] L. Carraro, G. De Pol, M. E. Puiatti, F. Sattin, P. Scarin, and M. Valisa, "Edge temperature and density measurements with a thermal helium beam in the RFX reversed field pinch," *Plasma Physics and Controlled Fusion*, vol. 42, no. 1, pp. 1–14, 2000, ISSN: 07413335. DOI: [10.1088/0741-3335/42/1/301](10.1088/0741-3335/42/1/301).

[44] a. R. Field, P. G. Carolan, N. J. Conway, and M. G. O'Mullane, "Optimized instrumentation for edge T[sub e] and n[sub e] measurements on COMPASS-D tokamak from He I line intensity ratios," *Review of Scientific Instruments*, vol. 70, no. 1, pp. 355–358, 1999, ISSN: 00346748. DOI: [10.1063/1.1149504](10.1063/1.1149504). [Online]. Available: http://link.aip.org/link/RSINAK/v70/i1/p355/s1&Agg=doi.

[45] H. KUBO, M. GOTO, H. TAKENAGA, A. KUMAGAI, T. SUGIE, S. SAKURAI, N. ASAKURA, S. HIGASHIJIMA, and Akira SAKASAI, "Study of Intesity Ratios of He I Line (668 nm, 706 nm and 728 nm) for Measurement of Electron Temperature and Density in JT-60U Divertor Plasma," *Journal of Plasma and Fusion Research*, vol. 75, no. 8, pp. 945–966, 1999. DOI: 10.1585/jspf.75.945.

[46] S. J. Davies, P. D. Morgan, Y. Ul'Haq, *et al.*, "Parallel electron temperature and density gradients measured in the JET MkI divertor using thermal helium beams," *Journal of Nuclear Materials*, vol. 241-243, pp. 426–432, 1997, ISSN: 00223115. DOI: [10.1016/s0022-3115(97)80076-1](10.1016/s0022-3115(97)80076-1).

[47] D. Bates, A. Kingston, and R. McWhirter, "Recombination between electrons and atomic ions I. Optically thin plasmas," *Proc. Roy. Soc. A.*, vol. 301, no. 1413, pp. 355–361, 1962.

[48] T. Fujimoto, *Plasma Spectroscopy* (International Series of Monographs on Physics). Clarendon Press, 2004, ISBN: 9780191523892. [Online]. Available: https://books.google.com/books?id=BQpREAAAQBAJ.

[49] H. P. Summers, W. J. Dickson, M. G. O'Mullane, N. R. Badnell, A. D. Whiteford, D. H. Brooks, J. Lang, S. D. Loch, and D. C. Griffin, "Ionization state, excited populations and emission of impurities in dynamic finite density plasmas: I. The generalized collisional-radiative model for light elements," *Plasma Physics and Controlled Fusion*, vol. 48, no. 2, pp. 263–293, 2006, ISSN: 07413335. DOI: 10.1088/0741-3335/48/2/007. arXiv: 0511561 [astro-ph].

[50] T. Fujimoto, "A collisional-radiative model for helium and its application to a discharge plasma," *Journal of Quantitative Spectroscopy and Radiative Transfer*, vol. 21, no. 5, pp. 439–455, May 1979, ISSN: 00224073. DOI: 10.1016/0022-4073(79)90004-9.

[51] M. Goto, "Collisional-radiative model for neutral helium in plasma revisited," *Journal of Quantitative Spectroscopy and Radiative Transfer*, vol. 76, no. 3-4, pp. 331–344, 2003, ISSN: 00224073. DOI: 10.1016/S0022-4073(02)00060-2.

[52] J. M. Muñoz Burgos, O. Schmitz, S. D. Loch, and C. P. Ballance, "Hybrid time dependent/independent solution for the He i line ratio temperature and density diagnostic for a thermal helium beam with applications in the scrape-off layer-edge regions in tokamaks," *Physics of Plasmas*, vol. 19, no. 1, 2012, ISSN: 1070664X. DOI: 10.1063/1.3672230.

[53] T. FUJIMOTO, *Plasma Spectroscopy*. 2004.

[54] G. W. F. Drake and Z.-C. Yan, "Energies and relativistic corrections for the rydberg states of helium: Variational results and asymptotic analysis," *Phys. Rev. A*, vol. 46, pp. 2378–2409, 5 Sep. 1992. DOI: 10.1103/PhysRevA.46.2378. [Online]. Available: https://link.aps.org/doi/10.1103/PhysRevA.46.2378.

[55] A. Kramida, Yu. Ralchenko, J. Reader, and and NIST ASD Team, NIST Atomic Spectra Database (ver. 5.9), [Online]. Available: https://physics.nist.gov/asd [2017, April 9]. National Institute of Standards and Technology, Gaithersburg, MD. 2021.

[56] Y. Ralchenko, R. K. Janev, T. Kato, D. V. Fursa, I. Bray, and F. J. de Heer, "Electron-impact excitation and ionization cross sections for ground state and excited helium atoms," *Atomic Data and Nuclear Data Tables*, vol. 94, no. 4, pp. 603–622, 2008, ISSN: 0092640X. DOI: 10.1016/j.adt.2007.11.003.

[57] C. P. Ballance, D. C. Griffin, S. D. Loch, R. F. Boivin, and M. S. Pindzola, "Collisional-radiative calculations of He line emission in low-temperature plasmas," *Physical Review A - Atomic, Molecular, and Optical Physics*, vol. 74, no. 1, pp. 1–8, 2006, ISSN: 10502947. DOI: 10.1103/PhysRevA.74.012719.

[58] A. Burgess and H. P. Summers, "The Recombination and Level Populations of Ions—I HYDROGEN AND HYDROGENIC IONS," *Monthly Notices of the Royal Astronomical Society*, vol. 174, no. 2, pp. 345–391, 1976, ISSN: 0035-8711. DOI: 10.1093/mnras/174.2.345. [Online]. Available: https://doi.org/10.1093/mnras/174.2.345.

[59] *Adas-atomic data and analysis structure*. [Online]. Available: http://www.adas.ac.uk/.

[60] S. Sasaki, S. Takamura, S. Watanabe, S. Masuzaki, T. Kato, and K. Kadota, "Helium I line intensity ratios in a plasma for the diagnostics of fusion edge plasmas," *Review of Scientific Instruments*, vol. 67, no. 10, pp. 3521–3529, 1996, ISSN: 00346748. DOI: 10.1063/1.1147060.

[61] M. Fujimoto and T., "collisional-radiative model for neutral helium in plasma: Excitation cross section and singlet-triplet wavefunction mixing (NIFS-DATA-43)," 1997.

[62] M. Goto and T. Fujimoto, "Collisional-radiative model for helium and its application to a tokamak plasma," *Fusion Engineering and Design*, vol. 34-35, no. 16, pp. 759–762, 1997, ISSN: 09203796. DOI: 10.1016/S0920-3796(96)00549-2.

[63] Y. Iida, S. Kado, A. Okamoto, and S. Kajita, "Effect of Radiation Trapping on an He I CR Model for a Divertor Simulator MAP-II.pdf," *Journal of Plasma and Fusion Research*, vol. 7, pp. 123–126, 2006.

[64] D. Nishijima, R. P. Doerner, M. J. Baldwin, E. M. Hollmann, R. P. Seraydarian, and Y. Ueda, "Spectroscopic determination of the singly ionized helium density in low electron temperature plasmas mixed with helium in a linear divertor plasma simulator," *Physics of Plasmas*, vol. 14, no. 10, 2007, ISSN: 1070664X. DOI: 10.1063/1.2786063.

[65] D. P. Stotler, J. Boedo, B. LeBlanc, R. J. Maqueda, and S. J. Zweben, "Progress towards the validation of models of the behavior of neutral helium in gas puff imaging experiments," *Journal of Nuclear Materials*, vol. 363-365, no. 1-3, pp. 686–692, 2007, ISSN: 00223115. DOI: 10.1016/j.jnucmat.2007.01.276.

[66] L. Cai, G. R. Tynan, and E. M. Hollmann, "Evidence for molecular-assisted recombination of He+ from particle balance measurements in helium-hydrogen mixture plasmas in PISCES-A," *Physics of Plasmas*, vol. 15, no. 10, 2008, ISSN: 1070664X. DOI: 10.1063/1.2991396.

[67] F. B. Rosmej, N. Ohno, S. Takamura, and S. Kajita, "Fluctuating helium emission in optically thick divertor plasmas," *Contributions to Plasma Physics*, vol. 48, no. 1-3, pp. 243–248, 2008, ISSN: 08631042. DOI: 10.1002/ctpp.200810042.

[68] S. Kajita, D. Nishijima, E. M. Hollmann, and N. Ohno, "Ray tracing simulation for radiation trapping of the He i resonance transitions in a linear plasma device," *Physics of Plasmas*, vol. 16, no. 6, 2009, ISSN: 1070664X. DOI: 10.1063/1.3157248.

[69] Y. Iida, S. Kado, A. Muraki, and S. Tanaka, "Application of optical emission spectroscopy for He i considering the spatial structure of radiation trapping in MAP-II divertor simulator," *Review of Scientific Instruments*, vol. 81, no. 10, 2010, ISSN: 00346748. DOI: 10.1063/1.3475789.

[70] Y. Iida, S. Kado, and S. Tanaka, "Calculation of spatial distribution of optical escape factor and its application to He i collisional-radiative model," *Physics of Plasmas*, vol. 17, no. 12, 2010, ISSN: 1070664X. DOI: 10.1063/1.3506822.

[71] K. SAWADA, Y. YAMADA, T. MIYACHIKA, N. EZUMI, A. IWAMAE, and M. GOTO, "Collisional-Radiative Model for Spectroscopic Diagnostic of Optically Thick Helium Plasma," *Plasma and Fusion Research*, vol. 5, pp. 001–001, 2010, ISSN: 1880-6821. DOI: 10.1585/pfr.5.001.

[72] S. Kajita and N. Ohno, "Practical selection of emission lines of He i to determine the photon absorption rate," *Review of Scientific Instruments*, vol. 82, no. 2, 2011, ISSN: 00346748. DOI: 10.1063/1.3548923.

[73] S. Ma, J. Howard, and N. Thapar, "Relations between light emission and electron density and temperature fluctuations in a helium plasma," *Physics of Plasmas*, vol. 18, no. 8, 2011, ISSN: 1070664X. DOI: 10.1063/1.3620403.

[74] S. Kajita, T. Tsujihara, M. Aramaki, *et al.*, "Behavior of 23S metastable state He atoms in low-temperature recombining plasmas," *Physics of Plasmas*, vol. 24, no. 7, 2017, ISSN: 10897674. DOI: 10.1063/1.4990077. [Online]. Available: http://dx.doi.org/10.1063/1.4990077.

[75] W. Lee, K. Park, and C. H. Oh, "Study on the radiative excitation rate coefficient of collisional radiative model," *Physics of Plasmas*, vol. 24, no. 6, 2017, ISSN: 10897674. DOI: 10.1063/1.4984987. [Online]. Available: http://dx.doi.org/10.1063/1.4984987.

[76] S. Kajita, K. Suzuki, H. Tanaka, and N. Ohno, "Helium line emission spectroscopy in recombining detached plasmas," *Physics of Plasmas*, vol. 25, no. 6, 2018, ISSN: 10897674. DOI: 10.1063/1.5029414. [Online]. Available: http://dx.doi.org/10.1063/1.5029414.

[77] W. Lee and C. H. Oh, "Optical diagnostics of helium recombining plasmas with collisional radiative model," *Physics of Plasmas*, vol. 25, no. 11, 2018, ISSN: 10897674. DOI: 10.1063/1.5051569. [Online]. Available: http://dx.doi.org/10.1063/1.5051569.

[78] S. Kajita, G. Akkermans, K. Fujii, H. Van Der Meiden, and M. C. Van De Sanden, "Emission spectroscopy of He lines in high-density plasmas in Magnum-PSI," *AIP Advances*, vol. 10, no. 2, 2020, ISSN: 21583226. DOI: 10.1063/1.5143481. [Online]. Available: https://doi.org/10.1063/1.5143481.

[79] D. Nishijima, M. I. Patino, and R. P. Doerner, "New application of hyperspectral imaging to steady-state plasma observations," *Review of Scientific Instruments*, vol. 91, no. 8, 2020, ISSN: 10897623. DOI: 10.1063/5.0011640. [Online]. Available: https://doi.org/10.1063/5.0011640.

[80] A. Mathews, J. L. Terry, S. G. Baek, *et al.*, *Deep modelling of plasma and neutral fluctuations from gas puff turbulence imaging*, 2022. DOI: 10.48550/ARXIV.2201.09988. [Online]. Available: https://arxiv.org/abs/2201.09988.

[81] J. M. Muñoz Burgos, O. Schmitz, E. A. Unterberg, S. D. Loch, and C. P. Ballance, "Implementation of a new atomic basis for the He i equilibrium line ratio technique for electron temperature and density diagnostic in the SOL for H-mode plasmas in DIII-D," *Journal of Nuclear Materials*, vol. 415, no. 1 SUPPL, pp. 1155–1158, 2011, ISSN: 00223115. DOI: 10.1016/j.jnucmat.2010.11.052.

[82] E. M. Hollmann, C. Brandt, B. Hudson, D. Kumar, D. Nishijima, and A. Y. Pigarov, "Investigation of mechanisms for He-I emission radial profile broadening in a weakly ionized cylindrical helium plasma with recombining edge," *Physics of Plasmas*, vol. 20, no. 9, 2013, ISSN: 1070664X. DOI: 10.1063/1.4821610.

[83] J. M. Muñoz Burgos, T. Barbui, O. Schmitz, D. Stutman, and K. Tritz, "Time-dependent analysis of visible helium line-ratios for electron temperature and density diagnostic using synthetic simulations on NSTX-U," *Review of Scientific Instruments*, vol. 87, no. 11, pp. 1–5, 2016, ISSN: 10897623. DOI: 10.1063/1.4955286. [Online]. Available: http://dx.doi.org/10.1063/1.4955286.

[84] "Evaluation of thermal helium beam and line-ratio fast diagnostic on the National Spherical Torus Experiment-Upgrade," *Physics of Plasmas*, vol. 23, no. 5, p. 53 302, May 2016, ISSN: 10897674. DOI: 10.1063/1.4948554. [Online]. Available: https://doi.org/10.1063/1.4948554.

[85] M. Griener, J. M. M. Burgos, M. Cavedon, *et al.*, "Qualification and implementation of line ratio spectroscopy on helium as plasma edge diagnostic at ASDEX Upgrade," *Plasma Physics and Controlled Fusion*, vol. 60, no. 2, p. 025 008, 2018, ISSN: 0741-3335. DOI: 10.1088/1361-6587/aa97e8. [Online]. Available: http://stacks.iop.org/0741-3335/60/i=2/a=025008?key=crossref.0d3828aef314393c745d2c2fbb4738d3.

[86] E. Flom, M. Krychowiak, O. Schmitz, *et al.*, "Bayesian modeling of collisional-radiative models applicable to thermal helium beam plasma diagnostics," *Nuclear Materials and Energy*, vol. 33, p. 101 269, 2022, ISSN: 2352-1791. DOI: https://doi.org/10.1016/j.nme.2022.101269. [Online]. Available: https://www.sciencedirect.com/science/article/pii/S2352179122001508.

[87] T. Nakano, H. Kubo, N. Asakura, K. Shimizu, H. Kawashima, and S. Higashijima, "Radiation process of carbon ions in jt-60u detached divertor plasmas," *Journal of Nuclear Materials*, vol. 390-391, pp. 255–258, 2009, Proceedings of the 18th International Conference on Plasma-Surface Interactions in Controlled Fusion Device, ISSN: 0022-3115. DOI: https://doi.org/10.1016/j.jnucmat.2009.01.085. [Online]. Available: https://www.sciencedirect.com/science/article/pii/S0022311509001081.

[88] P. Blanchard, Y. Andrebe, H. Arnichand, R. Agnello, S. Antonioni, S. Couturier, J. Decker, T. D. K. D'Exaerde, B. Duval, I. Furno, *et al.*, "Thomson scattering measurements in the divertor region of the TCV tokamak plasmas," *Journal of Instrumentation*, vol. 14, no. 10, p. C10038 C10038, Oct. 2019. DOI: 10.1088/17480221/14/10/c10038. [Online]. Available: https://doi.org/10.1088/1748%200221/14/10/c10038.

[89] L. Martinelli, D. Mikitchuck, B. P. Duval, *et al.*, "Implementation of high-resolution spectroscopy for ion (and electron) temperature measurements of the divertor plasma in the tokamak à configuration variable," *Review of Scientific Instruments*, vol. 93, no. 12, p. 123 505, 2022. DOI: 10.1063/5.0114538. [Online]. Available: https://doi.org/10.1063/5.0114538.

[90] F. E. Irons, "The escape factor in plasma spectroscopy-I. The escape factor defined and evaluated," *Journal of Quantitative Spectroscopy and Radiative Transfer*, vol. 22, no. 1, pp. 1–20, 1979, ISSN: 00224073. DOI: 10.1016/0022-4073(79)90102-X.

[91] M. Wensing, J. Loizu, H. Reimerdes, B. P. Duval, and M. Wischmeier, "X-point potential well formation in diverted tokamaks with unfavorable magnetic field direction," *Nuclear Fusion*, vol. 60, no. 5, pp. 1–8, 2020, ISSN: 17414326. DOI: 10.1088/1741-4326/ab7d4f.

[92] A. Jaervinen, S. Allen, M. Groth, *et al.*, "Interpretations of the impact of cross-field drifts on divertor flows in diii-d with uedge," *Nuclear Materials and Energy*, vol. 12, pp. 1136–1140, 2017, Proceedings of the 22nd International Conference on Plasma Surface Interactions 2016, 22nd PSI, ISSN: 2352-1791. DOI: https://doi.org/10.1016/j.nme.2016.11.014. [Online]. Available: https://www.sciencedirect.com/science/article/pii/S2352179116302447.

[93] "SOLPS-ITER simulations of the TCV divertor upgrade," *Plasma Physics and Controlled Fusion*, vol. 61, no. 8, 2019, ISSN: 13616587. DOI: 10.1088/1361-6587/ab2b1f.

[94] O. Février, H. Reimerdes, C. Theiler, *et al.*, "Divertor closure effects on the TCV boundary plasma," *Nuclear Materials and Energy*, vol. 27, 2021, ISSN: 23521791. DOI: 10.1016/j.nme.2021.100977.

[95] N. Ohno, N. Ezumi, S. Takamura, S. I. Krasheninnikov, and A. Y. Pigarov, "Experimental evidence of molecular activated recombination in detached recombining plasmas," *Physical Review Letters*, vol. 81, no. 4, pp. 818–821, 1998, ISSN: 10797114. DOI: 10.1103/PhysRevLett.81.818.

[96] D. Nishijima, U. Wenzel, K. Ohsumi, N. Ohno, Y. Uesugi, and S. Takamura, "Characteristics of detached plasmas associated with electron-ion and molecular assisted recombinations in NAGDIS-II," *Plasma Physics and Controlled Fusion*, vol. 44, no. 5, pp. 597–610, 2002, ISSN: 07413335. DOI: 10.1088/0741-3335/44/5/307.

[97] K. Verhaegh, B. Lipschultz, J. Harrison, *et al.*, "The role of plasma-molecule interactions on power and particle balance during detachment on the TCV tokamak," *Nuclear Fusion*, vol. 61, no. 10, p. 106 014, Sep. 2021.

[98] P. C. Stangeby, *The plasma boundary of magnetic fusion devices / Peter C. Stangeby.* (Plasma physics series), eng. Bristol, UK ; Institute of Physics Pub., 2000, ISBN: 0750305592.

[99] C. Tsui, J. Boedo, O. Février, H. Reimerdes, C. Colandrea, S. Gorno, T. Team, *et al.*, "Relevance of e× b drifts for particle and heat transport in divertors," *Plasma Physics and Controlled Fusion*, vol. 64, no. 6, p. 065 008, 2022.

[100] H. D. Oliveira, C. Theiler, O. Février, H. Reimerdes, B. P. Duval, C. K. Tsui, S. Gorno, D. S. Oliveira, A. Perek, and t. T. Team, "New insights on divertor parallel flows,E × B drifts, and fluctuations from in situ, two-dimensional probe measurement in the Tokamak à Configuration Variable," en, *Nuclear Fusion*, vol. 62, no. 9, p. 096 028, Aug. 2022, Publisher: IOP Publishing, ISSN: 0029-5515. DOI: 10.1088/1741-4326/ac82fd. [Online]. Available: https://dx.doi.org/10.1088/1741-4326/ac82fd (visited on 01/28/2024).

[101] A. Perek, B. Linehan, M. Wensing, *et al.*, "Measurement of the 2d emission profiles of hydrogen and impurity ions in the tcv divertor," *Nuclear Materials and Energy*, vol. 26, p. 100 858, 2021, ISSN: 2352-1791. DOI: https://doi.org/10.1016/j.nme.2020.100858. [Online]. Available: https://www.sciencedirect.com/science/article/pii/S2352179120301253.

[102] O. Février, C. Theiler, H. De Oliveira, B. Labit, N. Fedorczak, and A. Baillod, "Analysis of wall embedded langmuir probe signals in different conditions on the tokamak à configuration variable," *Review of Scientific Instruments*, vol. 89, no. 5, p. 053 502, 2018. DOI: 10.1063/1.5022459. eprint: https://doi.org/10.1063/1.5022459. [Online]. Available: https://doi.org/10.1063/1.5022459.

[103] U. Sheikh, L. Simons, B. Duval, O. Février, D. Moret, A. Allegrucci, M. Bernert, F. Crisinel, T. Tersztyánszky, and O. Villinger, "Radcam—a radiation camera system combining foil bolometers, axuv diodes, and filtered soft x-ray diodes," *Review of Scientific Instruments*, vol. 93, no. 11, 2022.

[104] R. Maurizio, S. Elmore, N. Fedorczak, A. Gallo, H. Reimerdes, B. Labit, C. Theiler, C. Tsui, W. Vijvers, T. Team, *et al.*, "Divertor power load studies for attached l-mode single-null plasmas in tcv," *Nuclear Fusion*, vol. 58, no. 1, p. 016 052, 2017.

[105] S. Braginskii, "Transport processes in a plasma," *Reviews of plasma physics*, vol. 1, p. 205, 1965.

[106] M. Schaffer, A. Chankin, H. Guo, G. Matthews, and R. Monk, "Pfirsch-schluter currents in the jet divertor," *Nuclear fusion*, vol. 37, no. 1, p. 83, 1997.

[107] A. Chankin and P. Stangeby, "The effect of diamagnetic drift on the boundary conditions in tokamak scrape-off layers and the distribution of plasma fluxes near the target," *Plasma physics and controlled fusion*, vol. 36, no. 9, p. 1485, 1994.

[108] T. Rognlien, D. Ryutov, and N. Mattor, "Calculation of 2-d profiles for the plasma and electric field near a tokamak separatrix," *Czechoslovak journal of physics*, vol. 48, no. Suppl 2, pp. 201–206, 1998.

[109] M. Wensing, "Drift-related transport and plasma-neutral interaction in the TCV divertor," Ph.D. dissertation, 2021.

[110] M. Wensing, H. Reimerdes, O. Février, *et al.*, "SOLPS-ITER validation with TCV L-mode discharges," *Physics of Plasmas*, vol. 28, no. 8, 2021, Publisher: AIP Publishing LLC, ISSN: 10897674. DOI: 10.1063/5.0056216.

[111] B. LaBombard, M. V. Umansky, R. L. Boivin, J. A. Goetz, J. Hughes, B. Lipschultz, D. Mossessian, C. S. Pitcher, J. L. Terry, and A. Group, "Cross-field plasma transport and main-chamber recycling in diverted plasmas on Alcator C-Mod," en, *Nuclear Fusion*, vol. 40, no. 12, p. 2041, Dec. 2000, ISSN: 0029-5515. DOI: 10.1088/0029-5515/40/12/308. [Online]. Available: https://dx.doi.org/10.1088/0029-5515/40/12/308 (visited on 04/14/2024).

[112] B. LaBombard, R. L. Boivin, M. Greenwald, J. Hughes, B. Lipschultz, D. Mossessian, C. S. Pitcher, J. L. Terry, and S. J. Zweben, "Particle transport in the scrape-off layer and its relationship to discharge density limit in Alcator C-Mod," *Physics of Plasmas*, vol. 8, no. 5 II, pp. 2107–2117, 2001, ISSN: 1070664X. DOI: 10.1063/1.1352596.

[113] M. V. Umansky, S. I. Krasheninnikov, B. LaBombard, B. Lipschultz, and J. L. Terry, "Modeling of particle and energy transport in the edge plasma of Alcator C-Mod," en, *Physics of Plasmas*, vol. 6, no. 7, pp. 2791–2796, Jul. 1999, ISSN: 1070-664X, 1089-7674. DOI: 10.1063/1.873236. [Online]. Available: https://pubs.aip.org/pop/article/6/7/2791/465040/Modeling-of-particle-and-energy-transport-in-the (visited on 04/14/2024).

[114] A. Smolders, M. Wensing, S. Carli, *et al.*, "Comparison of high density and nitrogen seeded detachment using SOLPS-ITER simulations of the tokamak á configuration variable," *Plasma Physics and Controlled Fusion*, vol. 62, no. 12, 2020, ISSN: 13616587. DOI: 10.1088/1361-6587/abbcc5.

[115] J. Karhunen, A. Holm, B. Lomanowski, V. Solokha, S. Aleiferis, P. Carvalho, M. Groth, K. D. Lawson, A. G. Meigs, and A. Shaw, "Experimental distinction of the molecularly induced Balmer emission contribution and its application for inferring molecular divertor density with 2D filtered camera measurements during detachment in JET L-mode plasmas," en, *Plasma Physics and Controlled Fusion*, vol. 64, no. 7, p. 075 001, Jul. 2022, ISSN: 0741-3335, 1361-6587. DOI: 10.1088/1361-6587/ac6ae3. [Online]. Available: https://iopscience.iop.org/article/10.1088/1361-6587/ac6ae3 (visited on 04/14/2024).

[116] C. Wüthrich, C. Theiler, N. Offeddu, D. Galassi, D. Oliveira, B. Duval, O. Février, T. Golfinopoulos, W. Han, E. Marmar, *et al.*, "X-point and divertor filament dynamics from gas puff imaging on tcv," *Nuclear Fusion*, vol. 62, no. 10, p. 106 022, 2022.

[117] X. Garbet, "Magnetic coordinates and equilibrium magnetic field," Doctoral, Lecture, France, Feb. 2023. [Online]. Available: https://hal.science/hal-03974960.